

Design de nanocomposites à hautes propriétés barrière par la combinaison d'approches expérimentales, de modélisation et d'apprentissage automatique

Aurore Jullin

▶ **To cite this version:**

Aurore Jullin. Design de nanocomposites à hautes propriétés barrière par la combinaison d'approches expérimentales, de modélisation et d'apprentissage automatique. Matériaux. Université Claude Bernard - Lyon I, 2025. Français. ⟨NNT : 2025LYO10017⟩. ⟨tel-05127358⟩

HAL Id: tel-05127358

https://theses.hal.science/tel-05127358v1

Submitted on 24 Jun 2025

HAL is a multi-disciplinary open access archive for the deposit and dissemination of scientific research documents, whether they are published or not. The documents may come from teaching and research institutions in France or abroad, or from public or private research centers.

L'archive ouverte pluridisciplinaire **HAL**, est destinée au dépôt et à la diffusion de documents scientifiques de niveau recherche, publiés ou non, émanant des établissements d'enseignement et de recherche français ou étrangers, des laboratoires publics ou privés.



Distributed under a Creative Commons CC BY 4.0 - Attribution - International License

Université Claude Bernard Lyon 1

THESE de DOCTORAT DE
L'UNIVERSITE CLAUDE BERNARD LYON 1

Ecole Doctorale N° 34
Matériaux

Discipline :
Matériaux polymères et composites

Soutenue publiquement le 27/01/2025, par :
Aurore JULLIN

Design de nanocomposites à hautes propriétés barrière par la combinaison d'approches expérimentales, de modélisation et d'apprentissage automatique

---

Devant le jury composé de :

M^me GAUCHER, Valérie	Professeure Université Lille	Rapporteure
M^me DOMENEK, Sandra	Professeure AgroParisTech	Rapporteure
M. CASSAGNAU, Philippe	Professeur Université Lyon 1	Président du jury
M. DANTRAS, Eric	Professeur Université Toulouse III	Examinateur
M. GONON, Laurent	Professeur Grenoble INP-UGA	Examinateur
M^me ESPUCHE, Eliane	Professeure Université Lyon 1	Directrice de thèse
M. CHINESTA, Francisco	Professeur, ENSAM Paris	Co-directeur de thèse
M. HASCOET, Nicolas	Maître de conférences, ENSAM Paris	Examinateur

CC BY

UNIVERSITE CLAUDE BERNARD – LYON 1

Président de l'Université	Frédéric FLEURY
Président du Conseil Académique	Hamda BEN HADID
Vice-Président du Conseil d'Administration	Philippe CHEVALIER
Vice-Président de la Commission de la Formation et de la Vie Universitaire	Christophe VITON
Vice-Président de la Commission de Recherche	Philippe CASSAGNAU
Directeur Général des Services	Pierre ROLLAND

COMPOSANTES SANTE

Directrice Administrative du Département de Formation et Centre de Recherche en Biologie Humaine	Laeticia BIGNON
Doyen de la Faculté d'Odontologie	Jean-Christophe MAURIN
Doyen de la Faculté de Médecine et Maïeutique Lyon Sud - Charles Mérieux	Philippe PAPAREL
Doyen de la Faculté de Médecine Lyon Est	Gilles RODE
Directeur de l'Institut des Sciences et Techniques de la Réadaptation	Jacques LUAUTE
Directeur de l'Institut des Sciences Pharmaceutiques et Biologiques	Claude DUSSART

COMPOSANTES ET DEPARTEMENTS DE SCIENCES ET TECHNOLOGIE

Directrice du Département de Génie Electrique et des Procédés	Sophie CAVASSILA
Directrice du Département Informatique	Saïda BOUAKAZ BRONDEL
Directeur du Département Mécanique	Marc BUFFAT
Directeur de l'Ecole Supérieure de Chimie, Physique, Electronique	Gérard PIGNAULT
Directeur de l'Institut de Science Financière et d'Assurances	Christian ROBERT
Directeur de l'Institut National du Professorat et de l'Education	Pierre CHAREYRON
Directeur de l'Institut Universitaire de Technologie de Lyon 1	Michel MASSENZIO
Directeur de l'Observatoire de Lyon	Bruno GUIDERDONI
Directeur de Polytech Lyon	Emmanuel PERRIN
Directrice de l'UFR Biosciences	Kathrin GIESELER
Directeur de l'UFR des Sciences et Techniques des Activités Physiques et Sportives	Guillaume BODET
Directeur de l'UFR Faculté des Sciences	Bruno ANDRIOLETTI

Remerciements

Ce travail de thèse a été possible grâce à de nombreuses personnes que je voudrais remercier ici.

Tout d'abord je souhaite remercier M^{me} Valérie Gaucher et M^{me} Sandra Domenek pour l'intérêt que vous portez à ce travail et pour le temps que vous y avez consacré en tant que rapporteures de cette thèse. Je remercie également, M. Philippe Cassagnau, M. Eric Dantras et M. Laurent Gonon pour avoir accepté de juger ce travail en tant qu'examinateurs.

Je voudrais ensuite remercier chaleureusement Eliane, ma directrice de thèse, pour son soutien constant et ses encouragements tout au long de ces 3 années. Merci d'avoir fait de cette thèse une aventure passionnante. Merci également à Paco, mon co-directeur de thèse pour son enthousiasme et son grain de folie, et à Nicolas pour sa disponibilité et qui a toujours su répondre à mes appels au secours sur Python.

Merci à Véronique, Fabrice, Guillaume et Matthieu pour leur participation à ce projet, ainsi qu'à l'équipe du PIMM pour leur accueil lors de mon séjour à l'ENSAM. Je voudrais également remercier l'ensemble du personnel technique de l'IMP, notamment Pierre pour ses nombreux conseils en microscopie et sa patience pour me former en ultramicrotomie et Olivier grâce à qui je suis (presque) devenue une experte de l'ATG ! Merci également à Noëllie, sans qui je n'aurai jamais eu la chance de faire la connaissance du Haake !

Merci à Gabriel pour ta contribution à ce travail pendant les quelques mois que tu as passé à l'IMP.

Je remercie tous les doctorants et post-doctorants (les vieux et les moins vieux) pour ces bons moments partagés au labo, les fous rires, les débats sans fin, les pauses croissants, les pauses goûter et les coups de main pour les manips, sans oublier bien sûr la team MDP (midi ?). Je voudrais notamment remercier les copains de promo : Pauline, Gabi, Chloé, Alex et Théo avec qui j'ai passé 3 belles années de thèse. Merci au bureau 326 et tout particulièrement Bene et Alex avec qui j'ai tout partagé du début à la fin !

Merci à Camille, mon incontournable soutien depuis si longtemps maintenant (ah quand je repense aux pompoms et à la métallurgie…) ! Je crois que sans toi je n'aurai jamais couru ces deux semis !

Merci à mes amis, qui m'ont encouragée durant ces années.

Enfin merci à mes parents qui n'ont jamais vraiment compris ce que je faisais, mais qui ont su m'encourager et me soutenir pendant toutes mes études et merci à ma sœur, avec qui je partage tout depuis 23 ans !

Finalement merci à Victor, sans qui je n'aurai peut-être jamais commencé cette belle aventure ! Merci pour ton soutien quotidien inestimable et pour tout le reste…

« La meilleure façon de prédire l'avenir c'est de le créer. »

Peter Drucker

Résumé

Design de nanocomposites à hautes propriétés barrière par la combinaison d'approches expérimentales, de modélisation et d'apprentissage automatique.

Les nanocomposites à base de polymère et de charges imperméables suscitent un grand intérêt pour les applications barrière mais ils représentent des matériaux complexes. En effet, les propriétés fonctionnelles de ces matériaux dépendent d'un nombre important de paramètres liés aux charges et à leur état de dispersion, à la matrice polymère, aux interactions charge/matrice pouvant conduire à des propriétés interfaciales variées ainsi qu'à des effets indirects potentiels des charges sur la matrice ; ces paramètres pouvant jouer des rôles additifs ou au contraire antagonistes. Ainsi, les objectifs de ce travail de thèse sont de définir des voies de développement robustes de nanocomposites à propriétés barrière optimisées sur la base d'approches expérimentales, théoriques et d'apprentissage automatique. Dans un premier temps, les études se sont focalisées sur une plateforme de nanocomposites à matrice acide polylactique (PLA), qui permet de faire varier aisément la microstructure de la matrice, le procédé de mise en œuvre et le type de domaines imperméables. L'analyse détaillée des paramètres matériaux et des propriétés fonctionnelles est exploitée par des modèles théoriques mais également dans une approche d'apprentissage automatique. Ainsi les relations entre paramètres matériaux et propriétés barrière ont pu être établies et les différents paramètres hiérarchisés. À l'issue de ces résultats, l'étude a été étendue à un grand nombre de matrices et de charges, permettant ainsi de couvrir une large gamme de niveaux de perméabilité. Pour l'ensemble des plateformes de nanocomposites, une hiérarchisation pertinente des paramètres matériaux a pu être réalisée mettant en lumière les facteurs gouvernant la perméabilité. Des modèles d'apprentissage automatique ont été entrainés avec succès à partir de ces facteurs, permettant d'une part de prédire les valeurs de perméabilité relative pour cette famille étendue de matériaux mais aussi de proposer des designs de matériaux répondant à des propriétés fonctionnelles choisies.

Mots-clés : nanocomposites, propriétés barrière, morphologie, apprentissage automatique

Abstract

Design of nanocomposites with high barrier properties using a combination of experimental, modelling and machine learning

Nanocomposites based on polymer and impermeable fillers are of great interest for barrier properties, but they are complex materials. Indeed, the functional properties of these materials depend on many parameters linked to the fillers and their dispersion state, the polymer matrix, the filler/matrix interactions that can lead to different interfacial properties, as well as potential indirect effects of the fillers on the matrix, which can play additive or, on the contrary, antagonistic roles. Thus, the objectives of this thesis work are to define robust development routes for nanocomposites with optimized barrier properties based on experimental, theoretical and machine-learning approaches. The studies first focused on a platform of nanocomposites with a polylactic acid (PLA) matrix, allowing easy variation of matrix microstructure, processing method and type of impermeable domains. The detailed analysis of material parameters and functional properties is exploited both by theoretical models and through a machine learning approach. In this way, relationships between material parameters and barrier properties could be established, and the various parameters ranked in order of importance. Based on these results, the study was extended to a large number of matrices and fillers, covering a wide range of permeability levels. For the whole nanocomposite platform, a relevant hierarchy of material parameters was achieved, highlighting the factors governing permeability. Machine learning models were successfully trained using these factors, enabling not only the prediction of relative permeability values for this extended family of materials, but also the proposal of material designs able to meet selected functional properties.

Key-words: nanocomposites, barrier properties, morphology, machine learning

Sommaire

Abbreviations 14

Introduction générale 17

Chapitre I – Etude bibliographique 23

1. Introduction 25
2. Approche théorique du transport de petites molécules dans le cas de films polymères denses 25
3. Le machine learning et ses applications pour la prédiction de propriétés spécifiques 39
4. Approche expérimentale de la permeabilité appliquée à des matrices PLA contenant une ou plusieures phases imperméables 46
5. Conclusion 66
6. Références 69

Chapitre II - Matériel et méthodes 79

1. Matériel 80
2. Caractérisations 83

Chapitre III - Design de matériaux à matrice PLA contenant une phase impermeable 87

Introduction 89

Chaptitre III.A - Influence of different type of impermeable phase on the permeability of PLA films: nanofillers versus crystalline phase 91

1. Abstract 92
2. Introduction 92
3. Experimental 94
4. Results and discussion 100
5. Conclusion 128
6. References 130

Chapitre III.B – PLA nanocomposites based silica and organo-modified montmorillonite: a comparative investigation of different solvent-free synthesis routes on morphology and water permeability 137

1. Abstract 138
2. Introduction 138
3. Experimental 141
4. Results and discussion 147
5. Conclusion 166
6. References 168

Chapitre III.C – Data Driven modelling as a new route to design PLA based materials with high barrier properties ____ 173

1. *Abstract* *174*
2. *Introduction* *174*
3. *Methods* *176*
4. *Results and discussion* *180*
5. *Conclusion* *193*
6. *References* *194*

Conclusion ____ 197

Supplementary information ____ 199

Chapitre IV – Design de nanocomposites PLA à deux phases imperméables ____ 219

Introduction ____ 221

Chapitre IV.A – Influence of the process on the permeability of semi-crystalline PLA nanocomposites : solvent casting versus annealing of melt-blended films ____ 223

1. *Abstract* *224*
2. *Introduction* *224*
3. *Experimental* *226*
4. *Results and discussion* *232*
5. *Conclusion* *250*
6. *References* *251*

Chapitre IV.B - Adding montmorillonite in PLA/silica and PLA/graphene nanocomposites : influence on nanocomposite's morphology and barrier properties ____ 259

1. *Abstract* *260*
2. *Introduction* *260*
3. *Experimental* *262*
4. *Results* *266*
5. *Discussion* *275*
6. *Conclusion* *277*
7. *References* *280*

Conclusion ____ 283

Supporting information ____ 285

Chapitre V - Design of high barrier properties polymer nanocomposites with machine learning _____ 293

1. Objectif 295
2. Abstract 296
3. Introduction 296
4. Methods 298
5. Results and discussion 302
6. Conclusion 311
7. References 313

Conclusion générale _____ 319

Abréviations

Acronyme	Description (FR)	Description (EN)
α	Facteur de forme	Aspect ratio
β	Facteur d'immobilisation des chaines	Chains immobilization factor
δ	Déplacement chimique	Chemical shift
θ	Angle de diffusion	Diffusion angle
μ	Masse volumique	Density
τ	Facteur de tortuosité	Tortuosity factor
Φ_a	Fraction de phase amorphe	Amorphous phase fraction
Φ_m	Fraction massique	Weigh fraction
Φ_v	Fraction volumique	Volume fraction
χ_c	Taux de cristallinité	Degree of crystallinity
Ag	Nanoparticules d'argent	Silver nanoparticles
ΔC_p	Différence de capacité calorifique au niveau de la transition vitreuse	Heat capacity change at the glass transition
ΔC_{p0}	Différence de capacité calorifique au niveau de la transition vitreuse pour le PLA amorphe	Heat capacity change at the glass transition for the amorphous PLA
d	Diamètre	Diameter
e	Épaisseur de film	Thickness of the film
GNP	Plaquette d'oxyde de graphène	Graphene oxide platelet
HNT	Nanotube d'halloysite	Halloysite nanotube
ΔH_{cc}	Enthalpie de cristallisation froide	Cold crystallization enthalpy
ΔH_m	Enthalpie de fusion	Melting enthalpy
$\Delta H_{m\infty}$	Enthalpie de fusion théorique d'un PLA 100% cristallin	Theoretical melting enthalpy of a 100% crystalline PLA
I	Intensité	Intensity
J	Flux d'espèce diffusante	Diffusing molecule flux
L	Longueur des charges	Fillers length
L_a	Epaisseur de zone amorphe entre les lamelles cristallines	Thickness of the amorphous area between the crystalline lamellae
L_c	Epaisseur des lamelles cristallines	Thickness of the crystalline lamellae
L_p	Longue période cristalline	Crystalline long period
m	Masse	Mass

M_n	Masse molaire moyenne en nombre	Average number molar masse
MAE	Erreur moyenne absolue	Mean absolute error
MAF	Fraction amorphe mobile	Mobile amorphous fraction
MMT	Montmorillonite	Montmorillonite
ML	Machine learning	Machine learning
OMMT	Montmorillonite modifiée avec un cation organique	Montmorillonite modified with an organic cation
P	Perméablité de l'échantillon	Sample permeability
P_0	Permeabilité du PLA amorphe	Permeability of the amorphous PLA
P_{matrix}	Perméablitité de la matrice	Permeability of the matrix
PLA	Acide polylactique	Polylactic acid
q	Vecteur de diffusion	Diffusion vector
R^2	Coefficient de corrélation	Correlation coefficient
RAF	Fraction amorphe rigide	Rigid amorphous fraction
RAFa	Fraction amorphe rigide dans la phase amorphe	Rigid amorphous fraction over the amorphous phase
RMSD	Racine carrée de la distance	Root mean square deviation
RF	Forêt aléatoire	Random Forest
S	Facteur d'orientation des charges	Filler orientation factor
s	Coefficient de solubilité	Solubility coefficient
SiOH	Silice non traitée	Non modified silica
$SiCH_3$	Silice traitée avec dimethyl dichlorosilane	Silica modified with dimethyl dichlorosilane
SVM	Machine à vecteurs de support	Support Vector Machine
T	Température	Temperature
T_a	Température de recuit	Annealing temperature
T_{cc}	Température de cristallisation froide	Cold crystallization temperature
T_g	Température de transition vitreuse	Glass transition temperature
T_m	Température de fusion	Melting temperature
w	Epaisseur des charges/domaines de charges	Fillers / fillers domains thickness
%vol / vol%	Pourcentage volumique	Volume percentage
%mass/wt %	Pourcentage massique	Weight percentage

Introduction générale

Le développement de matériaux flexibles ayant de bonnes propriétés barrière est actuellement un défi majeur pour diverses applications telles que l'emballage alimentaire et pharmaceutique ou encore le secteur de l'énergie (stockage d'hydrogène, membrane de pile à combustible, revêtement de protection…). Les polymères sont d'intéressants candidats en raison de leur facilité de mise en œuvre, leur faible coût et la large gamme de propriétés mécaniques qu'ils peuvent couvrir. Toutefois, leurs propriétés barrière sont généralement trop faibles pour répondre aux exigences des cahiers des charges requis par ces diverses applications. En effet, les valeurs de transmission à la vapeur d'eau (WTR) de ces matériaux sont de l'ordre de 1 à 100 $g.m^{-2}.j^{-1}$ pour un film d'une centaine de microns d'épaisseur ce qui est bien supérieur aux niveaux requis dans le domaine de l'emballage alimentaire et médical (WTR < 10^{-1} à 10^{-3} $g.m^{-2}.j^{-1}$) ainsi que pour des applications nécessitant de hautes propriétés barrière comme l'optoélectronique organique (10^{-3} à 10^{-6} $g.m^{-2}.j^{-1}$) [1]. Pour le taux de transmission à l'oxygène (OTR) les valeurs recherchées sont de l'ordre de 1,5 à 3 $cm^3_{STP}.cm^{-2}.j^{-1}$ dans le domaine de l'emballage et inférieures à 10^{-5} $cm^3_{STP}.cm^{-2}.j^{-1}$ pour des applications de pointe [2]. Il existe donc différentes gammes de propriétés barrière requises en fonction des applications visées. Ainsi, l'amélioration des propriétés barrière de polymères pourrait permettre l'utilisation de nouveaux matériaux pour certaines applications ou bien la diminution de la quantité de matière utilisée.

Dans ce contexte, l'élaboration de matériaux nanocomposites à matrice polymère contenant des nanocharges imperméables a suscité un vif intérêt ces dernières années. En effet, l'ajout de nanocharges, c'est-à-dire des charges ayant au moins une dimension inférieure à 100 nm, s'est avéré être particulièrement efficace pour améliorer les propriétés barrière des polymères. La présence de domaines imperméables représente un obstacle pour la diffusion de petites molécules dans la matrice polymère qui doivent alors emprunter un chemin plus tortueux. On parle d'effet de tortuosité. Par ailleurs, les nanocharges permettent de pouvoir préserver la transparence du matériau si la dispersion des charges est bien maitrisée. De plus, ces matériaux généralement composés d'un taux de charges faible devraient permettre un recyclage ou une fin de vie facile à maitriser. Pour les années à venir, l'enjeu est de concevoir

des matériaux nanocomposites répondant aux valeurs de perméabilité requises mais aussi à d'autres critères liés à l'écoconception et à la minimisation de l'impact environnemental. Ainsi, en visant des propriétés finales identiques, il est intéressant de pouvoir proposer des procédés de mise en œuvre et des matrices polymères à moindre impact environnemental.

Il est aujourd'hui évident que les propriétés barrière dépendent d'une multitude de paramètres liés aux charges introduites dans le système (forme, facteur de forme, orientation, dispersion, fraction volumique…) [3], à la matrice polymère (nature chimique, mobilité des chaines, volume libre, cristallinité…) ainsi qu'à l'interface charge/matrice et à l'effet indirect des charges sur la structure de la matrice [4]. Il semble donc pertinent d'utiliser de nouveaux outils, comme l'apprentissage automatique dénommé de façon courante « machine learning », en complément d'approches expérimentales et théoriques, pour effectuer une analyse détaillée des différents facteurs influençant la perméabilité et de mettre également en évidence leurs éventuelles interrelations. Le but étant de pouvoir identifier les facteurs clés du transport et aboutir *in fine* à définir des microstructures optimales pour une gamme de perméabilité souhaitée.

C'est dans ce cadre que s'inscrit ce travail de thèse qui fait partie du projet ANR BANCODEMM et qui le fruit d'une collaboration entre le laboratoire Ingénierie des Matériaux Polymères (IMP) et le laboratoire Procédés et Ingénierie en Mécanique et Matériaux (PIMM). Ce manuscrit est constitué de cinq chapitres qui rendent compte de la progression du travail mené initialement sur une plateforme de matériaux à base d'acide polylactique (PLA) puis élargie à une large gamme de matrices polymères, liant intimement approches expérimentales, théoriques et machine learning.

Le premier chapitre est une synthèse bibliographique qui présente dans un premier temps les mécanismes de transport de petites molécules au sein de polymères denses puis dans des systèmes plus complexes tels que ceux formés par une matrice polymère contenant une phase imperméable. Cette phase imperméable pouvant être la phase cristalline ou des nanocharges. Une deuxième partie consiste en une brève présentation de l'approche machine learning incluant les méthodes de mise en œuvre et leurs applications notamment pour la conception de matériaux polymères à propriétés spécifiques. La troisième partie se focalise sur une matrice d'intérêt, le PLA. Elle consiste en une analyse exhaustive des données expérimentales

de l'ajout d'une phase imperméable dans une matrice (la phase cristalline du PLA ou différents types de charges imperméables). Les principales voies d'élaboration de nanocomposites seront également présentées dans cette troisième partie.

Le second chapitre présente brièvement les matériaux de base utilisés dans ce travail ainsi que l'ensemble des systèmes qui ont été préparés et caractérisés expérimentalement.

Les trois chapitres suivants synthétisent les résultats obtenus au cours de cette thèse. Ces résultats sont présentés sous forme de publications rédigées en anglais qui ont été ou seront soumises dans des journaux internationaux. Pour chaque chapitre, une introduction est rédigée en français ainsi que les transitions entre chaque sous-chapitre et la conclusion.

Ainsi, le troisième chapitre s'intéresse à la perméabilité de matériaux PLA contentant une phase imperméable. Ce chapitre est composé d'une première partie qui compare l'effet de la phase cristalline et de différentes charges imperméables sur la perméabilité du PLA, à travers une approche expérimentale et de modélisation. Une deuxième partie s'intéresse à l'influence du procédé d'élaboration sur la microstructure et la perméabilité de nanocomposites PLA en utilisant la silice ou la montmorillonite comme charges imperméables. Enfin, une troisième partie s'appuyant sur les deux premières parties, propose une approche en machine learning permettant d'identifier les paramètres les plus pertinents pour prédire la perméabilité de système PLA à une phase imperméable. L'approche est également exploitée pour l'objectif de proposer des designs de matériaux à matrice PLA pour des niveaux de propriétés barrière choisis.

Le quatrième chapitre présente l'effet de deux phases imperméables différentes sur la perméabilité du PLA. Une première partie traite du cas de nanocomposites semi-cristallins, contenant une charge imperméable. Cette étude compare les résultats obtenus avec deux procédés de mise en œuvre différents pour une large gamme de charges imperméables. Une seconde partie porte sur l'ajout de deux charges imperméables (silice/montmorillonite et graphène/montmorillonite) dans une matrice PLA amorphe et étudie leur influence sur la perméabilité.

Le dernier chapitre propose d'étendre l'approche développée par machine learning sur un large éventail de matrices polymères permettant de couvrir une large gamme de

perméabilités initiales. Ce chapitre a pour objectif de voir, dans un premier temps, si les modèles utilisés dans le cas du PLA sont également adaptés pour une gamme étendue de matériaux. Après cette validation, l'enjeu est de pouvoir proposer des combinaisons (matrice, procédé, charge) permettant de concevoir des matériaux répondant à des propriétés barrière données.

Enfin, une conclusion générale reprenant les résultats et les avancées principales issus de ce travail de thèse ainsi que des perspectives sera présentée à la fin de ce manuscrit.

[1] S. Cros, Polymères et effet barrière, Techniques de l'ingénieur (2007). https://www.techniques-ingenieur.fr/base-documentaire/materiaux-th11/applications-des-plastiques-42141210/proprietes-barrieres-des-polymeres-utilises-en-emballage-am3160/polymeres-et-effet-barriere-am3160niv10002.html (accessed October 31, 2024).
[2] F. Wu, M. Misra, A.K. Mohanty, Challenges and new opportunities on barrier performance of biodegradable polymers for sustainable packaging, Progress in Polymer Science 117 (2021) 101395. https://doi.org/10.1016/j.progpolymsci.2021.101395.
[3] C. Wolf, H. Angellier-Coussy, N. Gontard, F. Doghieri, V. Guillard, How the shape of fillers affects the barrier properties of polymer/non-porous particles nanocomposites: A review, Journal of Membrane Science 556 (2018) 393–418. https://doi.org/10.1016/j.memsci.2018.03.085.
[4] E. Espuche, Nanocomposites for gas barrier applications: Governing factors, single and coupled effects, new routes to optimise the function properties, Polymer Testing 125 (2023) 108124. https://doi.org/10.1016/j.polymertesting.2023.108124.

Chapitre I

Etude bibliographique

Chapitre I – Etude bibliographique

1. Introduction ____ *25*

2. Approche théorique du transport de petites molécules dans le cas de films polymères denses ____ *25*

2.1. Généralités ____ **25**

2.2. Cas des films polymères contenant une phase imperméable dispersée ____ **2G**

2.2.a) Approche théorique du rôle de la phase cristalline sur la perméabilité ____ 29

2.2. b) Approche théorique de la perméabilité dans les nanocomposites ____ 31

3. Le machine learning et ses applications pour la prédiction de propriétés spécifiques ____ *33*

3.1. Méthodes de machine learning ____ **3G**

3.1.a) Les forêts d'arbres décisionnels (*Random Forest*) ____ 42

3.1. b) Les machines à vecteurs de support (*Support Vector Machine*) ____ 43

3.2. Utilisation des méthodes de machine learning pour la prédiction de propriétés spécifiques de matériaux polymères et nanocomposites ____ **44**

4. Approche expérimentale de la perméabilité appliquée à des matrices PLA contenant une ou plusieurs phases imperméables ____ *4C*

4.1. Synthèse du PLA ____ **47**

4.2. Microstructure du PLA ____ **4G**

4.1. Influence de la cristallinité sur les propriétés barrière du PLA ____ **54**

4.2. Influence de nanocharges imperméables sur les propriétés barrière du PLA ____ **56**

4.2. a) Élaboration de nanocomposites PLA à partir de charges préformées ____ 56

4.2. b) Nanocomposites PLA à charges sphériques ____ 57

4.2. c) Nanocomposites PLA à charges de formes allongées ____ 58

4.2. d) Nanocomposites PLA à charges lamellaires ____ 60

4.2. e) Discussion ____ 64

5. Conclusion ____ *CC*

C. Références ____ *C3*

1. Introduction

L'objectif de cette thèse est d'exploiter la complémentarité et la synergie potentielle d'approches expérimentales, de modélisation et de machine learning pour concevoir des nanocomposites ayant de hautes propriétés barrière et d'identifier les paramètres gouvernant la perméabilité dans une approche globale, allant de la mise en œuvre à la microstructure jusqu'aux propriétés fonctionnelles. Dans ce contexte, ce premier chapitre bibliographique a pour but de présenter les différentes approches d'intérêt permettant, entre autres, de relier la microstructure de matériaux contenant une phase imperméable et leurs propriétés barrière.

La première partie de ce chapitre rappelle les bases théoriques des phénomènes de transport de petites molécules au sein de polymères denses, puis détaille le cas des matériaux à matrice polymère contenant une phase imperméable dispersée, en incluant la présentation de modèles empiriques. La deuxième partie présente le principe général et les méthodes d'une approche innovante et jusqu'alors non encore utilisée pour étudier la perméabilité de polymères contenant une phase imperméable : le machine learning. Enfin, une analyse critique des données de la littérature concernant la perméabilité de matrices PLA contenant une phase imperméable est proposée au travers du recensement et de l'étude d'un nombre conséquent de travaux. Ainsi, les données relatives à l'influence de la phase cristalline et de différents types de charges imperméables (de forme sphériques, allongées ou lamellaires) sur la perméabilité ont été collectées, comparées et analysées afin d'identifier de potentielles tendances.

2. Approche théorique du transport de petites molécules dans le cas de films polymères denses

2.1. Généralités

Le transport de petites molécules au sein d'un film polymère dense (non poreux) soumis à un gradient de pression est généralement décrit comme le déplacement aléatoire des molécules de la face amont du film soumise à la pression plus élevée (p_1) à sa face avale soumise à la pression plus faible (p_2) par le biais des volumes libres présents entre les chaines polymères,

appelés sites de sorption. En effet, un matériau polymère est constitué d'un agencement plus ou moins ordonné et compact c de séquences de chaînes polymères mobiles les unes par rapport aux autres. Les molécules diffusantes peuvent alors se déplacer de volume libre en volume libre, en s'adaptant à la potentielle redistribution des volumes libres au sein du matériau lors de phénomènes de relaxations des chaines [1], [2]. La force motrice de la diffusion est le gradient de concentration en molécules diffusantes de part et d'autre de la membrane polymère. Le transport est ainsi décrit par un mécanisme de solubilité-diffusion [3], [4], [5] qui se traduit en trois étapes principales comme illustré sur la **Figure 1** :

- L'absorption des molécules diffusantes sur la partie amont de la membrane
- La diffusion des molécules au sein de la membrane polymère
- La désorption des molécules du côté aval de la membrane

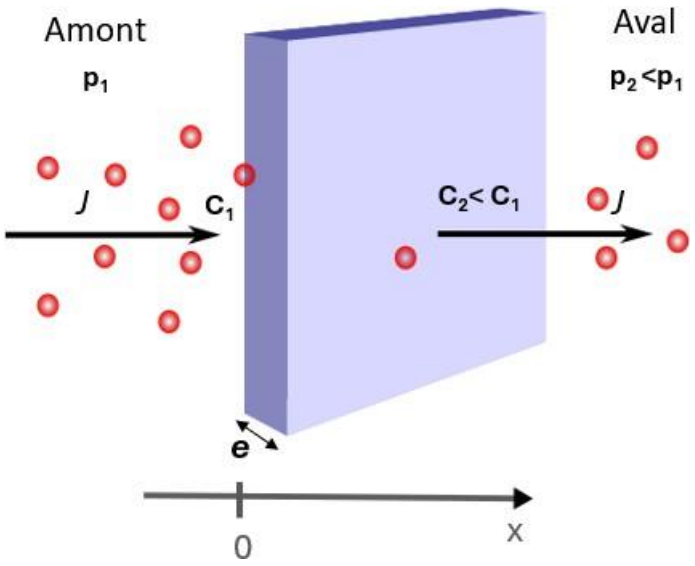


Figure 1 - Schéma du phénomène de transport de petites molécules à travers un film polymère mince.

Ce phénomène fait ainsi intervenir trois paramètres : le coefficient de diffusion (*D*), le coefficient de solubilité (*s*) et le coefficient de perméabilité (*P*).

Le coefficient de solubilité traduit l'affinité des molécules diffusantes pour le matériau : il s'exprime en ($cm^3{}_{STP}/(cm^3.cm_{Hg})$) selon l'équation (1) :

$$s = \frac{c}{p} \qquad (1)$$

Où *p* est la pression et *c* la concentration de molécules sorbées à l'équilibre à la pression *p*.

Le coefficient de diffusion est un facteur cinétique qui traduit la vitesse de déplacement des molécules diffusantes au sein de la membrane : il est exprimé en $cm^2.s^{-1}$. La diffusion au sein de la membrane est le plus généralement régie par les lois de Fick établies en 1855 [6]. Dans le cas où l'on considère un film mince pour lequel la diffusion s'effectue uniquement dans l'épaisseur, la première loi de Fick relie le flux de matière traversant la membrane (*J*) et le gradient de concentration en molécules diffusantes de la face amont à la face aval de la membrane. Cette loi s'écrit selon l'équation (2) :

$$J = -D\frac{\partial c}{\partial x} \qquad (2)$$

Avec :

J : le flux d'espèce diffusante à travers la membrane ($cm^3_{STP}.cm^{-2}.s^{-1}$)

c : la concentration locale d'espèce diffusante (cm^3)

D : le coefficient de diffusion ($cm^2.s^{-1}$)

En se plaçant toujours dans le cas d'un film mince, la seconde loi de Fick décrit l'évolution de la concentration en fonction du temps pour un point donné dans l'épaisseur selon l'équation (3):

$$\frac{\partial c}{\partial t} = D\frac{\partial^2 c}{\partial^2 x} \qquad (3)$$

En régime stationnaire, le gradient de concentration en espèce diffusante à travers le film est constant ce qui permet décrire le coefficient de diffusion (D) selon l'équation (4) :

$$D = \frac{J.e}{c_1 - c_2} \qquad (4)$$

Avec :

c_1 : la concentration d'espèces diffusantes sur la face amont du film (cm^3_{STP})

c_2 : la concentration d'espèces diffusantes sur la face aval du film (cm^3_{STP})

e : l'épaisseur du film (cm)

Enfin, le coefficient de perméabilité (*P*) caractérise la capacité d'un matériau à se laisser traverser par un gaz (ou une vapeur) quand il est soumis à un gradient de pression ($\Delta \mathrm{p}$). Il se

calcule à partir du flux de molécules diffusantes mesuré en régime stationnaire (*J*) par l'équation (4).

$$P = \frac{J.e}{\Delta p} \quad (4)$$

Avec *J* le flux d'espèce diffusante ($cm^3_{STP}.cm^{-2}.s^{-1}$), *e* l'épaisseur du fim (cm) et Δp le gradient de pression (cm_{Hg}).

La perméabilité à un gaz donné est un paramètre intrinsèque du matériau, indépendant de l'épaisseur de la membrane, si aucune modification de sa morphologie n'en découle.

Le coefficient de perméabilité est souvent exprimé en Barrer :

$$1\ Barrer = 10^{-10}\ \frac{cm^3_{STP}.cm}{cm^2.s.cm_{Hg}} = 3.36 \text{ x } 10^{-16}\ \frac{mol.m}{m^2.s.Pa}$$

Dans le cas d'un transport fickien, le coefficient de perméabilité peut s'exprimer par le produit du coefficient de solubilité et du coefficient de diffusion selon l'équation (5) :

$$P = D.s \quad (5)$$

Dans un film polymère, il a été montré que l'augmentation de l'encombrement stérique [7], de la cristallinité ainsi que la diminution de la mobilité des chaines et la diminution des volumes libres [8] entrainent généralement une diminution du coefficient de perméabilité. Les propriétés de transport d'un polymère peuvent aussi être modulées par l'incorporation de domaines imperméables conduisant, entre autres, à créer un effet de tortuosité au sein du matériau en allongeant le chemin de diffusion du pénétrant [9], [10], [11]. Ces domaines imperméables peuvent être des charges nanométriques ou des domaines organiques tels que la phase cristalline du polymère qui est pour la majorité des polymères considérée comme imperméable aux petites molécules telles que les gaz [8]. Par ailleurs, ces phases imperméables peuvent également jouer sur d'autres paramètres influençant la perméabilité comme la mobilité des chaines [8] qui se manifeste notamment par une évolution de la température de transition vitreuse [5]. Ainsi, la partie suivante va s'attacher à décrire, par une approche théorique, le transport de petites molécules dans les films polymères contenant une phase imperméable dispersée.

2.2. Cas des films polymères contenant une phase imperméable dispersée

La présence de domaines imperméables dispersés au sein d'une matrice polymère représente un obstacle pour les molécules diffusantes (**Figure 2**).

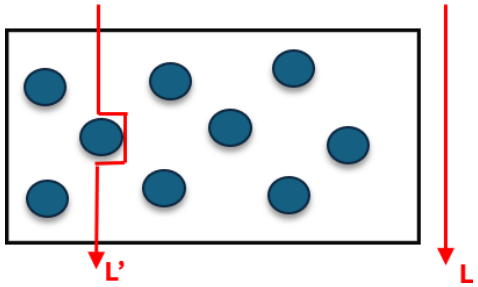


Figure 2 - Schéma du parcours d'une molécule diffusante au sein d'un nanocomposite.

On définit ainsi un facteur de tortuosité τ associé au chemin supplémentaire que doit parcourir une molécule pour traverser le matériau selon l'équation (6)

$$\tau = \frac{chemin\ parcouru\ en\ présence\ de\ phase\ imperméable}{chemin\ parcouru\ sans\ phase\ imperméable} = \frac{L'}{L} \qquad (6)$$

La distance *L' peut* être estimée comme suit :

$$L' = L + < N > * d \qquad (7)$$

Avec:

<*N*> : Nombre d'obstacles rencontrés sur le chemin *L'*

d : chemin supplémentaire parcouru au niveau de chaque obstacle

Ainsi, le facteur de tortuosité peut s'écrire sous la forme générale (équation (8)) :

$$\tau = 1 + \frac{< N > * d}{L} \qquad (8)$$

2.2. a) Approche théorique du rôle de la phase cristalline sur la perméabilité

Du fait de sa densité plus élevée que la phase amorphe et de son organisation, la phase cristalline est généralement assimilée à une entité imperméable. Par conséquent, le phénomène de sorption se fait uniquement dans la phase amorphe [3], [12]. Ainsi au sein d'un polymère semi-cristallin, le coefficient de solubilité s'exprime en fonction du taux de cristallinité (χ_c)[8] selon l'équation (9) :

$$s = s_0 (1 - \chi_c) \quad (9)$$

Avec :

s : le coefficient de solubilité dans le polymère semi-cristallin

s_0 : le coefficient de solubilité dans la phase amorphe

χ_c : le taux de cristallinité du polymère

De plus, les lamelles cristallines représentent un obstacle aux molécules diffusantes, ce qui crée un effet de tortuosité. Deux mécanismes de diffusion ont été envisagés dans le cas où la phase cristalline est organisée sous forme de sphérolites. La diffusion peut s'effectuer en contournant le sphérolite, ou se faire via la phase amorphe présente entre les lamelles cristallines qui composent le sphérolite. Toutefois, il a été montré que la contribution de la diffusion entre les lamelles cristallines au sein d'un sphérolite est minime comparée à la diffusion autour des sphérolites [8], [13]. Par ailleurs, la phase cristalline peut participer à l'immobilisation des chaines polymères à l'interface lamelles cristallines/phase amorphe, ce qui demande une énergie d'activation supplémentaire pour que les molécules diffusent dans les volumes libres de cette zone. Pour prendre en compte cet effet, Michaels *et al.* ont introduit un facteur β lié à l'immobilisation d'une partie des chaines de la phase amorphe [8]. Ce facteur β est dépendant de la température selon une loi d'Arrhenius. Ainsi, au sein d'un polymère semi-cristallin, le coefficient de diffusion peut s'exprimer en fonction de la tortuosité τ et d'un facteur d'immobilisation des chaines β selon l'équation (10) :

$$D = \frac{D_0}{\tau\beta} \quad (10)$$

Avec :

D : le coefficient de diffusion dans le polymère semi-cristallin

D_0 : le coefficient de diffusion dans la phase amorphe

τ : le facteur de tortuosité

β : le facteur d'immobilisation des chaines

Pour un transport fickien, en combinant les deux équations précédentes, on obtient l'expression du coefficient de perméabilité pour un polymère semi-cristallin selon l'équation (11) :

$$P = P_0 \frac{1 - \chi_c}{\tau\beta} \quad (11)$$

Avec :

P : le coefficient de perméabilité relatif au polymère semi-cristallin

P_0 : le coefficient de perméabilité relatif à la phase amorphe

Dans le cas où l'on considère que la diffusion s'effectue exclusivement autour des sphérolites, le facteur de tortuosité τ peut s'exprimer en fonction du taux de cristallinité [8], [14], [15] selon l'équation (12) :

$$\tau = 1 + \frac{\chi_c}{2} \quad (12)$$

D'autres expressions de la perméabilité dans le cas de polymères semi-cristallins ont également été proposées. Par exemple, Petterlin *et al* [16] ont choisi d'exprimer la perméabilité en fonction d'un « ratio de détour » ψ compris entre 0 et 1 et du facteur bloquant *B* (équation (13)). Le facteur bloquant est associé aux zones amorphes très fines entre les lamelles cristallines non accessibles aux molécules diffusantes. Cet effet bloquant est plus marqué pour les molécules ayant des diamètres cinétiques importants.

$$P = P_0 \frac{(1 - \chi_c)\psi}{B} \quad (13)$$

2.2. b) Approche théorique de la perméabilité dans les nanocomposites

Un deuxième moyen d'améliorer les propriétés barrière est d'introduire des charges imperméables dans la matrice polymère. Plusieurs modèles théoriques ont été établis pour décrire la perméabilité dans les nanocomposites [10], [17]. Ces modèles font principalement intervenir la fraction volumique de charges, le facteur de forme des charges, leur état de dispersion et leur orientation. Comme dans le cas d'une phase cristalline imperméable, le coefficient de solubilité (*s*) au sein du nanocomposite s'exprime selon l'équation (14) :

$$s = s_0 (1 - \Phi_v) \quad (14)$$

Avec s_0 le coefficient de solubilité de la matrice polymère et Φ_v la fraction volumique de phase imperméable.

Le coefficient de diffusion (D) du matériau est également amoindri et s'exprime en fonction du coefficient de diffusion de la matrice polymère (D_0) et de la tortuosité (τ) selon l'équation (15) :

$$D = \frac{D_0}{\tau} \tag{15}$$

Dans le cas d'un transport fickien, on obtient l'expression du coefficient de perméabilité du matériau en combinant les équations (14) et (15) selon l'équation (16).

$$P = P_0 \frac{(1 - \Phi_v)}{\tau} \tag{16}$$

Avec P_0 le coefficient de perméabilité de la matrice polymère, $\mathbf{\Phi}_v$ la fraction volumique de phase imperméable et τ la tortuosité. Les équations présentées ci-après ont été à l'origine développées pour des charges dispersées unitairement.

Pour le cas des nanocomposites à charges sphériques, il n'y a pas de facteur d'orientation à prendre en compte et le facteur de forme est considéré égal à 1. Le facteur de tortuosité est donc de la forme (équation (17)) :

$$\tau = 1 + \frac{\Phi_v}{2} \tag{17}$$

Les lois expriment souvent la perméabilité relative définie par le rapport de la perméabilité du matériau (*P*) sur la perméabilité de la matrice (P_0). Ainsi, la perméabilité relative pour un nanocomposite à base de sphères imperméables peut être décrite avec l'équation (18) correspondant au modèle de Maxwell :

$$\frac{P}{P_0} = \frac{1 - \Phi_v}{(1 + 0.5\,\Phi_v)} \tag{18}$$

A notre connaissance un seul modèle a été proposé dans le cas de charges tubulaires. Guo *et al.* [18] ont exprimé le chemin supplémentaire parcouru au niveau de chaque tube (*d*) et le nombre d'obstacles franchis <*N*> selon les équations (19) et (20) en fonction du rayon *R* du tube et de l'angle θ défini sur la **Figure 3**:

$$d = R \int_0^{\frac{\pi}{2}} (\theta - sin\theta) d\theta \tag{19}$$

$$< N > = \frac{L}{2R} \Phi_v \qquad (20)$$

En intégrant et combinant les équations (19) et (20), la tortuosité a pu être exprimée à partir de la fraction volumique de tubes dans le cas de tubes orientés aléatoirement dans le plan perpendiculairement à la diffusion (**Figure 3**) selon l'équation (21) :

$$\tau = 1 + \frac{\pi^2 - 8}{16} \Phi_v \qquad (21)$$

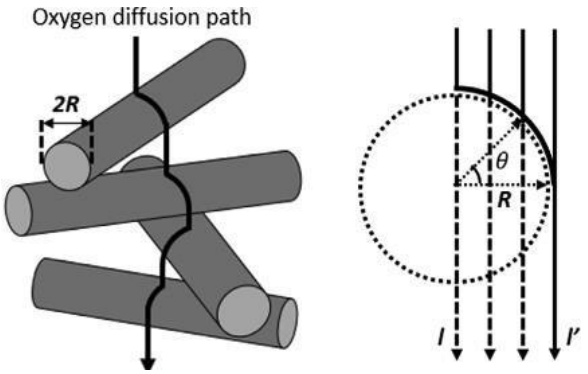


Figure 3 - Représentation schématique de la tortuosité dans le cas d'un arrangement aléatoire de tubes dans le plan perpendiculaire à la direction de diffusion.

Dans le cas de plaquettes ou de disques, le facteur de forme et l'orientation des charges sont des facteurs à prendre en compte. Certains modèles considèrent une dispersion homogène de plaquettes unitaires orientées perpendiculairement au flux gazeux (**Figure 4**).

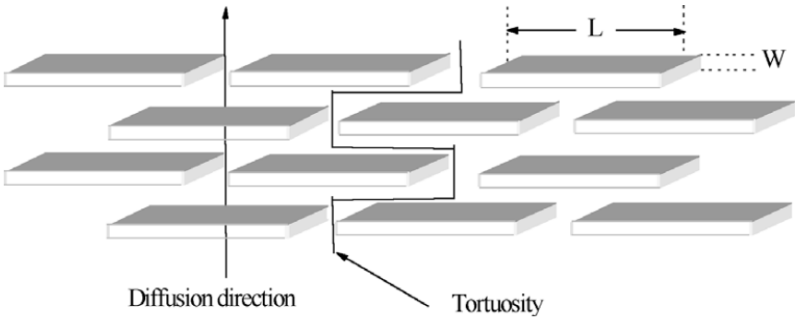


Figure 4 - Représentation schématique de la tortuosité dans le cas d'un arrangement de plaquettes (L x w) organisées de façon régulière et perpendiculairement au flux de diffusion [10].

C'est notamment le cas du modèle de Nielsen [9] qui propose l'équation (22) pour décrire la perméabilité relative.

$$\frac{P}{P_0} = \frac{1 - \Phi_v}{1 + \frac{\alpha}{2}\,\Phi_v} \tag{22}$$

Avec α le facteur de forme des charges correspondant au rapport entre la longueur et l'épaisseur des charges. Ce modèle assez simple permet de décrire la perméabilité seulement à partir du taux de charges et du facteur de forme.

Cussler *et al.* [19] ont également proposé un modèle à partir des mêmes paramètres (équation (23)).

$$\frac{P}{P_0} = \frac{1}{1 + \frac{\alpha^2 {\Phi_v}^2}{1 - \Phi_v}} \tag{23}$$

D'autres modèles prennent en compte l'effet d'un arrangement irrégulier de charges uniformes et orientées perpendiculairement au flux. Ainsi Brydges *et al.* [20] ont calculé la perméabilité relative en fonction d'un paramètre d'empilement Υ qui tient compte de la position d'une plaquette par rapport à celle du plan inférieur (**Figure 5**). Ce modèle est valable uniquement si $\Upsilon < 1$ et dans le cas de grands facteurs de forme ($\alpha > 100$). L'expression de la perméabilité relative est donnée par l'équation (24) :

$$\frac{P}{P_0} = \frac{1}{1 + \frac{\alpha^2 {\Phi_v}^2}{1 - \Phi_v}\,\gamma(1 - \gamma)} \tag{24}$$

Ce modèle nécessite de connaitre et mesurer le paramètre d'empilement Υ à partir d'images prises en microscopie électronique, ce qui peut s'avérer compliqué en pratique.

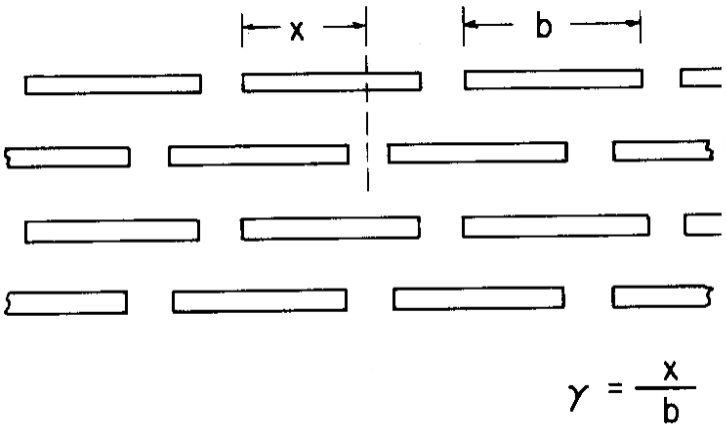


Figure 5 - Schéma d'un arrangement régulier de charges uniformes et orientées perpendiculairement définissant les paramètres utilisés dans le modèle de Brydges [20].

De façon similaire, Lape *et al.* [21] ont établi un modèle pour un arrangement aléatoire de plaquettes uniformes parallèles les unes aux autres et orientées perpendiculairement au flux. La perméabilité relative a été décrite en fonction de la réduction de l'aire disponible pour la diffusion dans le composite par rapport à celle de la matrice seule et en fonction de la tortuosité selon l'équation (25).

$$\frac{P}{P_0} = \frac{A}{A_0} * \frac{1}{\tau} \tag{25}$$

Avec A/A_0 le rapport d'aire disponible pour la diffusion dans le nanocomposite et dans la matrice qui est calculé selon l'équation (26) :

$$\frac{A}{A_0} = \frac{(1 - \Phi_v)}{\tau} \tag{26}$$

L'expression de la tortuosité est la même que pour le modèle de Nielsen, mais avec l'ajout d'un facteur 1/3 permettant de prendre en compte la position aléatoire des plaquettes (équation (27)), d'après des considérations statistiques.

$$\tau = (1 + \frac{\alpha}{3} \Phi_v) \tag{27}$$

Ainsi le modèle de perméabilité proposé par Lape *et al.* [21] est présenté selon l'équation (28):

$$\frac{P}{P_0} = \frac{1 - \Phi_v}{(1 + \frac{\alpha}{3} \Phi_v)^2} \tag{28}$$

La **Figure 6** compare les résultats des différents modèles présentés (e.g. : le modèle de Nielsen, le modèle de Cussler et le modèle de Lape). Pour un facteur de forme relativement faible (α=10), le modèle de Lape montre une diminution plus rapide de la perméabilité que celui de Nielsen et de Cussler. Pour des facteurs de forme plus élevés (α > 100), le modèle de Lape donne une perméabilité relative plus faible que celui de Nielsen et plus élevée que celui de Cussler.

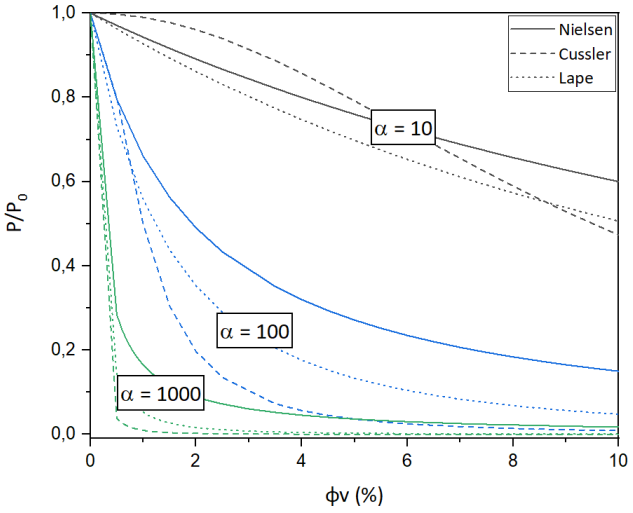


Figure 6 - Évolution de la perméabilité relative selon les modèles de Nielsen [9], de Cussler [19] et de Lape [21] pour différents facteurs de forme des domaines imperméables dispersés.

Un modèle élargi au cas où les domaines imperméables ne sont pas homogènes en longueur et en épaisseur a été proposé par Picard *et al.* [22] en s'appuyant sur les travaux de Lape *et al.* [21]. Ce modèle prend en compte la distribution des valeurs des facteurs de forme (α_i) et aboutit ainsi à l'équation (29):

$$\frac{P}{P_0} = \frac{1-\Phi_v}{[1+\frac{1}{3}\Phi_v * \frac{\sum n_i\alpha_i^2}{\sum n_i\alpha_i}]^2} \quad (29)$$

Enfin, d'autres modèles ont été proposés dans le cas où les charges ne sont pas orientées perpendiculairement à la direction du flux de diffusion. Ainsi, Bharadwaj *et al.* [23] ont proposé d'introduire un paramètre d'orientation *S* qui s'exprime en fonction de l'orientation des charges selon l'équation (30) :

$$S = \frac{1}{2}(3\,cos^2(\theta) - 1) \quad (30)$$

La perméabilité relative s'exprime alors selon l'équation (31) :

$$\frac{P}{P_0} = \frac{1-\Phi_v}{1+\frac{\alpha}{2} * \frac{2}{3}(S+\frac{1}{2})\Phi_v} \quad (31)$$

θ correspond à l'angle entre la surface des charges et la direction du flux de diffusion, en prenant la moyenne de l'ensemble des charges dans le matériau. Si les charges sont toutes

perpendiculaires au flux ($\theta = \pi/2$) alors *S* est égal à -1/2 et on retrouve l'équation de Nielsen. Au contraire si toutes les charges sont parallèles au flux ($\theta = 0$), *S* vaut 1. Enfin, si les charges n'ont pas d'orientation préférentielle, le paramètre *S* est considéré comme égal à 0.

Ainsi, un certain nombre de modèles théoriques ont été développés pour décrire au mieux l'évolution de la perméabilité en présence d'une phase imperméable. Toutefois ces modèles basés essentiellement sur une approche géométrique présentent certaines limites. En effet, l'ajout de charges peut modifier la phase cristalline de la matrice polymère qui, comme évoqué précédemment, constitue également une phase imperméable. Cela peut donc conduire à augmenter/diminuer la perméabilité (**Figure 7**). Par exemple, Olivier *et al.* [24] ont observé l'apparition d'une phase cristalline Υ et une orientation préférentielle des lamelles cristallines avec l'ajout de charges lamellaires de type α-ZrP (phosphate de zirconium) dans une matrice polyamide. Il a été montré que ces modifications ont une influence sur les propriétés barrière. Par ailleurs, l'interface charges/matrice n'est pas considérée dans les modèles décrits précédemment. Or, elle peut parfois modifier les propriétés barrière du matériau en cas d'interactions charges/matrice fortes ou au contraire faibles (**Figure 7**). Des interactions fortes peuvent en effet réduire la mobilité des chaines à l'interface et ralentir la diffusion. Ce phénomène a pu être observé avec l'ajout de compatibilisant dans le cas de nanocomposites polyethylène/montmorillonite, pour lesquels la perméabilité diminue davantage dans le cas où les interactions entre les montmorillonites et la matrice polyéthylène sont plus fortes [25]. Cette tendance a également été mise en avant dans le cas de nanocomposites polycaprolactone/montmorillonite pour lesquels le greffage de chaines polymères à la surface des charges permet d'avoir, à état de dispersion similaire, une perméabilité plus faible que dans le cas de chaines non greffées [26]. Enfin, l'effet inverse a été observé lors de l'utilisation de longues chaines alkyles en tant qu'agent modifiant pour des charges lamellaires de α-ZrP dans une matrice élastomère [27]. Les longues chaines alkyles ont mené à la création d'une interface à base de chaines mobiles autour des charges ce qui a induit une non-variation voire une augmentation de la perméabilité en regard de la matrice seule.

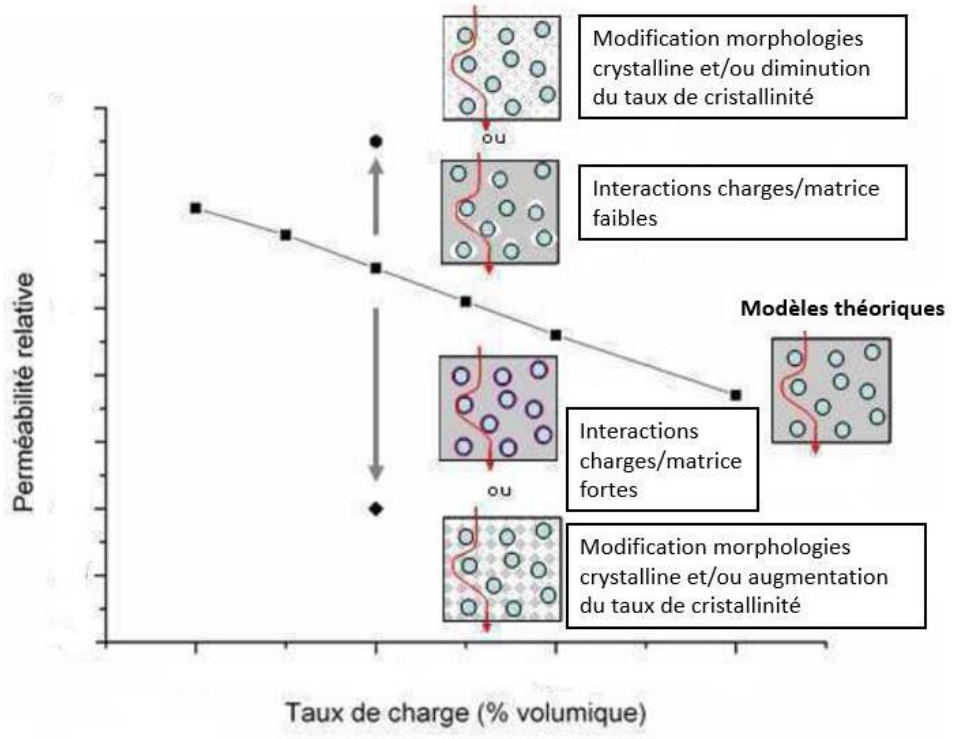


Figure 7 - Schéma représentant les limites des modèles théoriques de perméabilité (schéma adapté de F.Morel [28])

En conclusion, un intérêt croissant a ainsi été porté aux nanocomposites à matrice polymère au cours des dernières années pour des applications nécessitant de hautes propriétés barrière aux gaz et/ou à l'eau, en couvrant un grand nombre de matrices polymères et de nanocharges différentes. Cependant, les paramètres agissant sur les propriétés barrière sont nombreux et pas toujours tous pris en compte par les modèles usuels qui sont le plus souvent en deux dimensions. Par ailleurs, il est difficile de caractériser certains paramètres tels que l'effet de la présence d'agrégats ainsi que l'effet des interfaces charges/matrices. Des approches de simulation par éléments finis ont été développées pour représenter des morphologies spécifiques, ajouter de potentiels effets d'interface et prédire les propriétés barrière [29], [30], [31]. Il est toutefois difficile par cette approche de prendre en compte des effets de modification de la matrice polymère comme la cristallinité ou la rigidification de la phase amorphe. Devant la quantité de paramètres à étudier et du fait de l'existence d'un nombre important d'études expérimentales dans le domaine des propriétés barrière [32], il apparait que l'utilisation d'une nouvelle approche comme le machine learning puisse être une piste intéressante à explorer, ce qui n'a encore jamais été fait à notre connaissance en ce qui concerne les propriétés barrière des nanocomposites. La partie suivante va s'attacher à

présenter les méthodes de machine learning ainsi que des exemples de leurs utilisations pour la prédiction de propriétés spécifiques de matériaux polymères.

3. Le machine learning et ses applications pour la prédiction de propriétés spécifiques

Le machine learning est un domaine de l'Intelligence Artificielle. Il repose sur un apprentissage exclusivement à partir de données en utilisant un certain nombre d'algorithmes à partir desquels le système peut prendre des décisions et donner des prédictions à l'utilisateur.

3.1. Méthodes de machine learning

Les méthodes utilisées en machine learning se divisent en deux principales catégories : l'apprentissage supervisé et l'apprentissage non supervisé [33], [34]. L'apprentissage non supervisé est réalisé avec des données d'entrée sans connaitre la sortie correspondante [35], [36]. La séparation des données se fait donc de façon à créer des groupes ayant des caractéristiques communes, le but étant de trouver des similitudes entre les données ou des tendances dissimulées. Ce type d'apprentissage peut ainsi être utilisé pour du regroupement de données (« Clustering »), dont le principe consiste à rassembler des données selon un certain nombre de groupes à partir de caractéristiques communes comme illustré sur la **Figure 8**. L'apprentissage non supervisé est également utilisé pour la reconnaissance d'image ou la réduction de dimensions. Parmi les méthodes utilisées, on peut citer la méthode des *K-moyens* qui consiste à classer les données en k groupes, en associant chaque point au groupe dont le centre est le plus proche puis en redéfinissant le centre des groupes à chaque itération. Une deuxième méthode est le *Clustering hiérarchique* qui consiste à associer progressivement des échantillons deux à deux par similarité jusqu'au nombre de classes ou seuil de distance définis. La réduction de dimension, quant à elle, a pour objectif de regrouper plusieurs variables d'entrée et ainsi réduire le temps de calcul.

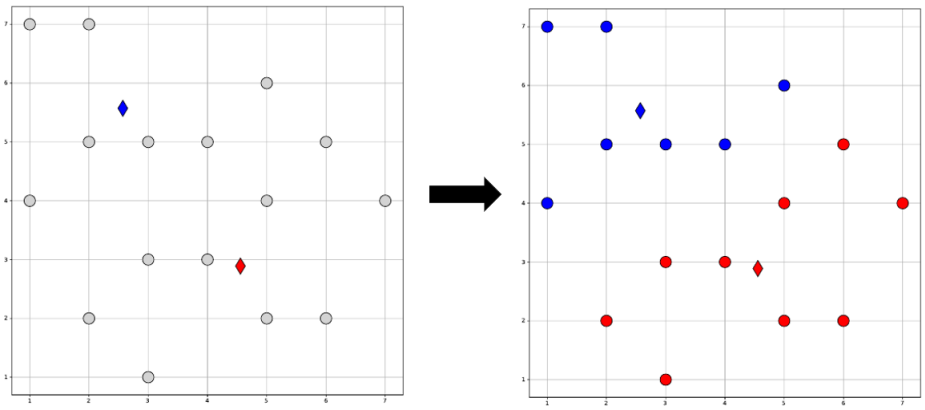


Figure 8 - Principe du regroupement de données. Les points ont été organisés en deux groupes (les rouges et les bleus) créés par rapprochement de caractéristiques communes (figure adaptée du cours « Machine Learning », Prof. F. Chinesta, Dr. N. Hascoët, ENSAM).

Le deuxième mode d'apprentissage est l'apprentissage supervisé [34], [37], [38]. Il consiste à donner au système des données d'entrée reliées à des données de sortie, c'est à dire qu'un vecteur de données d'entrée est lié à un vecteur de données de sortie. Le but est d'entrainer le système à partir de ces données (données d'entrée et de sortie) afin qu'il puisse ensuite prédire des résultats à partir de nouvelles données. Pour cela une majeure partie des données (généralement 80%) est utilisée pour entrainer le modèle choisi et aboutir à un modèle minimisant l'erreur faite sur les données d'entrainement. Puis le restant des données d'entrée est utilisé avec le modèle optimisé. Les prédictions du modèle sont alors comparées aux données de sortie correspondantes (**Figure 9**). Cela permet de valider ou non le modèle et de voir si le modèle a été surentrainé ou sous-entrainé. On dit que le modèle est sous-entrainé (ou « underfitted ») si les prédictions obtenues avec les données d'entrainement sont mauvaises. A l'inverse on dit qu'un modèle est surentrainé (ou « overfitted ») si les prédictions obtenues avec les données d'entrainement sont très bonnes mais que les prédictions obtenues avec les données de test sont mauvaises.

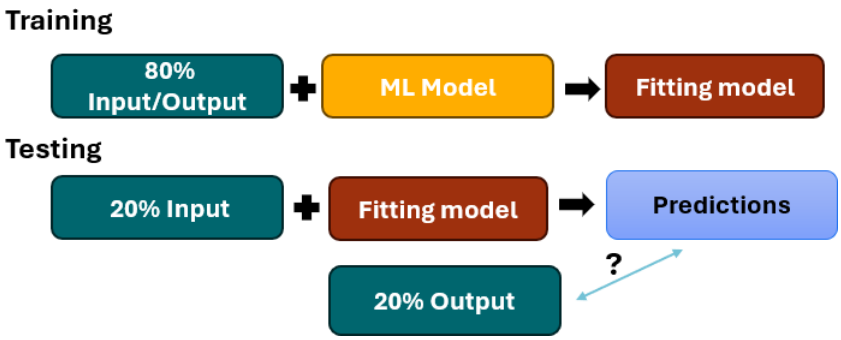


Figure 9 - Schéma du principe d'évaluation des modèles supervisés.

Dans le cas où les données de sortie sont discontinues on utilise des algorithmes de classification qui permettent de catégoriser de nouvelles données par rapport à un paramètre de sortie. Le principe consiste à trouver une tendance permettant d'attribuer une valeur de sortie à des caractéristiques d'entrée (**Figure 10**).

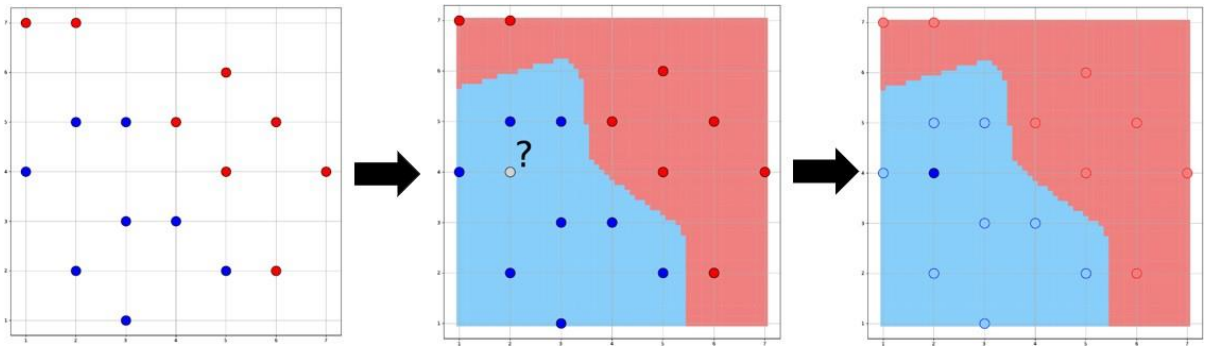


Figure 10 - Principe de la classification : lors de l'entrainement du modèle une tendance a permis de séparer les points bleus des point rouges : la couleur d'un nouveau point est attribuée en fonction de cette tendance (figure adaptée du cours « Machine Learning », Prof. F. Chinesta, Dr. N. Hascoët, ENSAM).

Au contraire, si les données de sortie sont des variables continues on utilise alors des algorithmes de régression qui permettent ensuite de prédire une valeur numérique en fonction de données d'entrée (**Figure 11**).

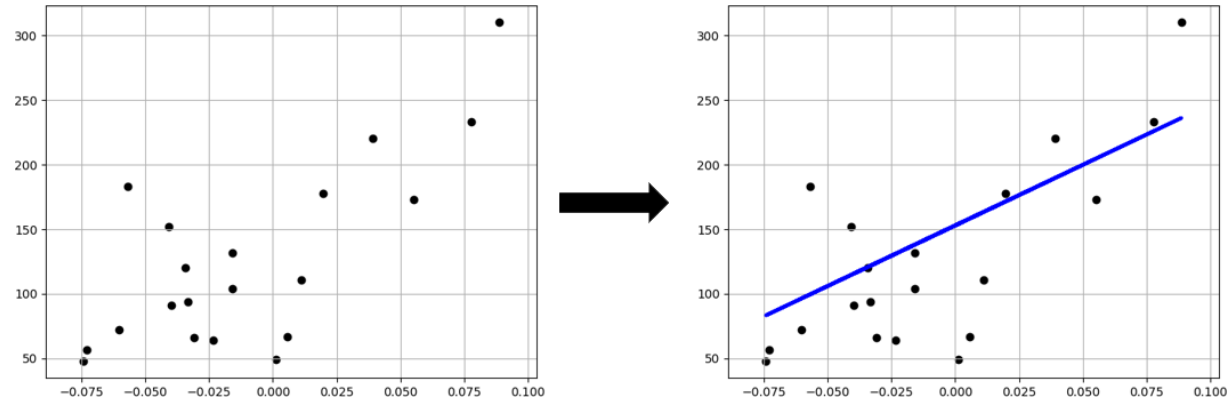


Figure 11 - Principe de la régression (figure adaptée du cours « Machine Learning », Prof. F. Chinesta, Dr. N. Hascoët, ENSAM).

Pour l'apprentissage supervisé on retrouve différentes méthodes dont les plus utilisées lorsque l'on dispose de peu de données sont les forêts d'arbres décisionnels (*Random Forest)* et les machines à vecteurs de support (*Support Vector Machine*) [37], [39], [40].

3.1. a) Les forêts d'arbres décisionnels (*Random Forest*)

Les forêts d'arbres décisionnels sont constituées d'un ensemble d'arbres de décision. Les arbres de décision sont un algorithme d'apprentissage supervisé utilisé pour la classification ou la régression. Les arbres de décision sont composés de branches, de nœuds et de feuilles : les données d'entrée sont sur les branches puis elles sont séparées au niveau de chaque nœud par une critère de discrimination et se retrouvent dans les feuilles (**Figure 12**).

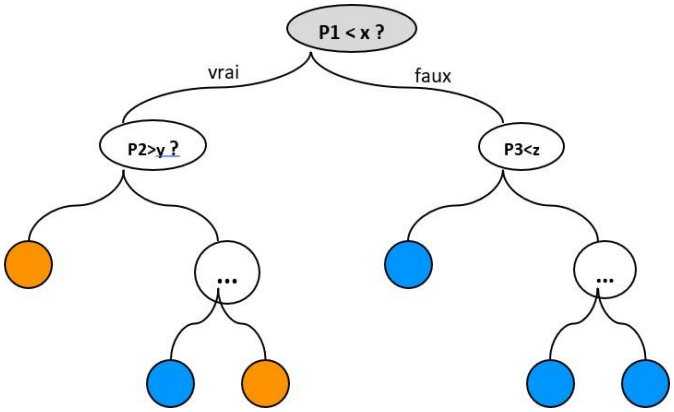


Figure 12 - Schéma d'un arbre de décision : les ronds blanc correspondent aux nœuds, les lignes aux branches et les parties colorées aux feuilles (figure adaptée du cours « Machine Learning », Prof. F. Chinesta, Dr. N. Hascoët, ENSAM).

Cette partition binaire des données en fonction des paramètres d'entrée se répète jusqu'à un certain seuil défini par l'utilisateur. Cependant ce modèle peut facilement être confronté au problème de surentrainement (*overfitting*), c'est-à-dire que l'erreur faite sur les prédictions du modèle à partir de nouvelles données sera beaucoup plus grande que celle obtenue avec les données d'entrainement. C'est pourquoi, il est préférable d'utiliser les forêts aléatoires (*Random Forest*) qui moyennent les résultats d'un certain nombre d'arbres de décision [41], [42]. Cette décision collective permet d'éviter les possibles erreurs individuelles.

3.1. b) Les machines à vecteurs de support (*Support Vector Machine*)

Les machines à vecteurs de support sont également des méthodes pour un apprentissage supervisé utilisées pour de la classification (*Support Vector Classification*) ou pour de la régression (*Support Vector Regression*) [43]. Cette méthode utilise un hyperplan pour séparer les données dans le cas d'une classification ou pour décrire au mieux les données de sortie dans le cas d'une régression. Cet hyperplan peut être linéaire, polynomiale ou radial. Un critère de pénalisation permet de définir une marge d'erreur autour de l'hyperplan et un critère de certitude est utilisé pour calculer la distance des points par rapport à cette marge. Pour la classification de données, le but est d'avoir un maximum de points de chaque côté de la marge tandis que pour la régression on cherche avoir le plus de point à l'intérieur de la marge (**Figure 13**). Les machines à support de vecteurs sont moins sensibles au phénomène d'*overfitting* mais leurs performances peuvent être affectées dans le cas d'un nombre de données très important et notamment en présence de « bruit » dans les données.

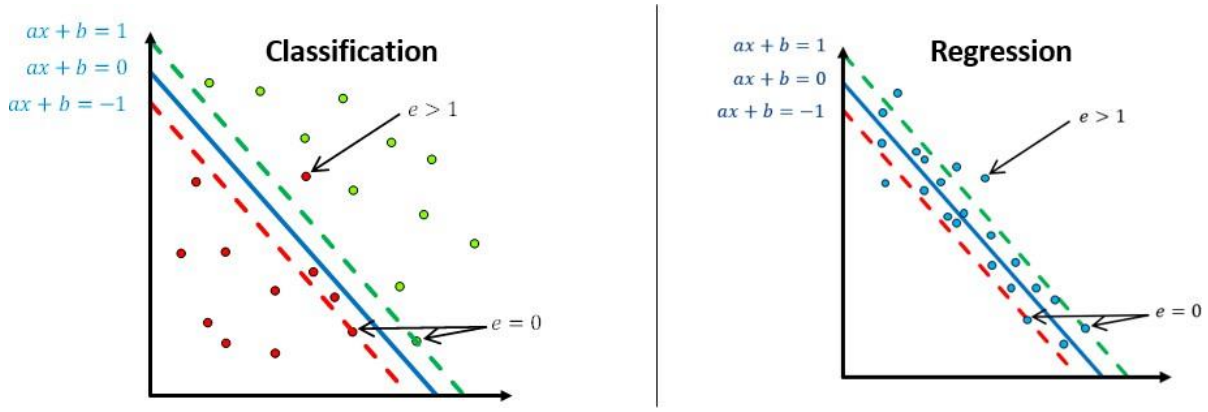


Figure 13 - Schéma du principe des machines à support de vecteurs dans le cas de classification « *Support Vector Classification* » (gauche) et de regression *« Support Vector Regression* » (droite) (figure adaptée du cours « Machine Learning », Prof. F. Chinesta, Dr. N. Hascoët, ENSAM).

3.2. Utilisation des méthodes de machine learning pour la prédiction de propriétés spécifiques de matériaux polymères et nanocomposites

Des modèles de ML ont été utilisés au cours des dernières années pour la conception de nanocomposites pour des propriétés mécaniques, thermiques, ou optiques [44]. Ainsi, on peut citer les travaux de Khanam *et al.* [45] sur la conception de nanocomposites polyéthylène/graphène qui ont utilisé les réseaux de neurones comme modèle pour prédire la conductivité thermique, la température de cristallisation, la température de dégradation et la contrainte à la rupture des échantillons à partir de la fraction massique de graphène incorporé et de la vitesse de rotation de la vis de l'extrudeuse. Les prédictions obtenues sont très bonnes avec des valeurs de R^2 supérieures à 0.9. Zakaulla *et al.* [46] se sont également servis des réseaux de neurone pour prédire les propriétés mécaniques de nanocomposites polyétheréthercétone/graphène/oxyde de titane à partir de la fraction volumique de matrice, de graphène et d'oxyde de titane. Les valeurs prédites par le modèle (eg : module d'Young, élongation à la rupture, contrainte à la rupture et dureté) sont très proches des valeurs expérimentales avec un R^2 supérieur à 0.94 comme le montre la **Figure 14**.

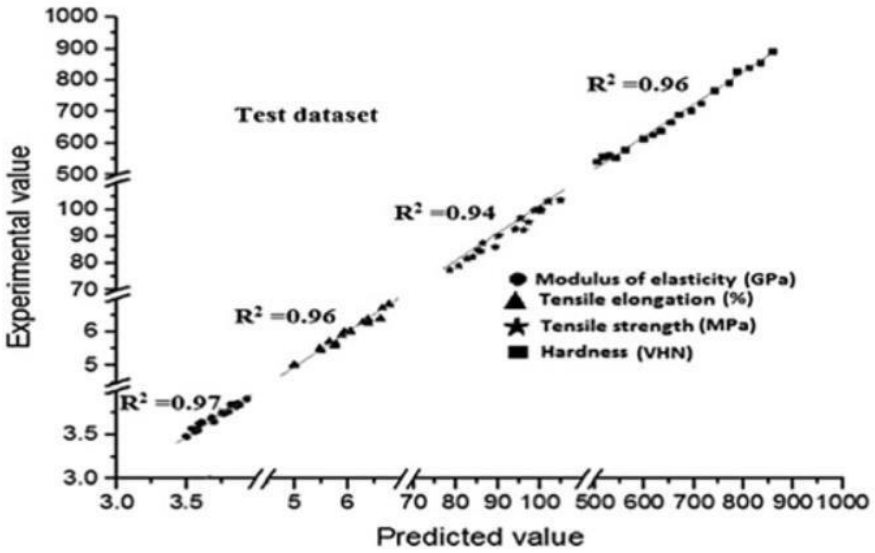


Figure 14 - Comparaison des valeurs prédites et des valeurs expérimentales de propriétés mécaniques (module d'Young, élongation à la rupture, contrainte à la rupture et dureté) par les réseaux de neurones pour un système polyétheréthercétone /graphène/oxyde de titane [46].

Par ailleurs, des études ont également été réalisées en machine learning dans le domaine du transport de petite molécules avec des homopolymères ou des copolymères non chargés [47],

[48], [49]. Pour cela, les perméabilités à différents gaz (O_2, N_2, CO_2, He, H_2, CH_4) d'une large gamme de polymères ont été prédites à partir de leur composition chimique. Les modèles de machine learning s'appuyant sur une méthode de régression Gaussienne (GPR) ont pu être entrainés et validés pour prédire de nouvelles données. Zhu *et al.* [47] ont entrainé leur modèle sur 284 polymères puis l'ont ensuite testé sur 31 autres polymères. La **Figure 15** montre que les valeurs prédites par le modèle sont très proches des valeurs expérimentales pour les points d'entrainement et de test avec un R^2 supérieur à 0.93 pour les deux cas. Ainsi ce modèle est aujourd'hui utilisé sur la plateforme en ligne *Polymer Genome* pour la conception de nouveaux polymères en fonction de critères de perméabilité souhaités envers différents gaz.

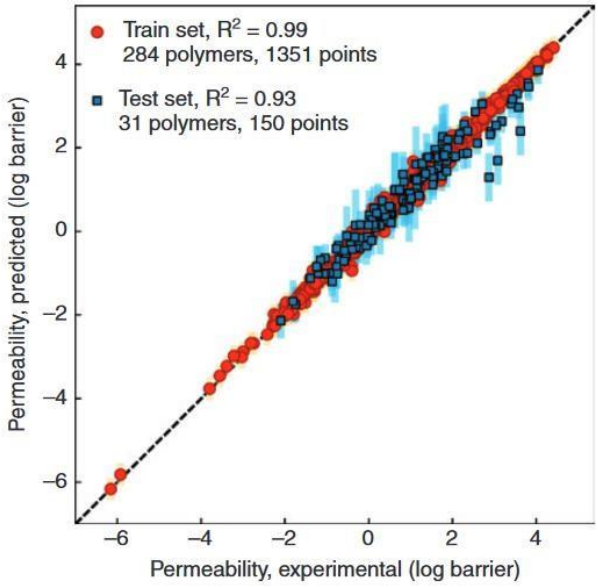


Figure 15 - Comparaison des valeurs de perméabilité prédites et expérimentales par un modèle GPR (*Gaussian Process regression*) pour des polymères. Les points bleus correspondent aux prédictions sur les données d'entrainement et les points rouges correspondent aux prédictions sur les données test [47].

Cependant, à notre connaissance, aucune étude en machine learning n'a encore été publiée sur les relations structure/propriétés de nanocomposites à matrice polymère pour des propriétés barrière, ce qui sera l'un des objectifs de ce travail de thèse.

Devant le grand nombre de facteurs pouvant influencer la perméabilité dans le cas des nanocomposites et la multitude de systèmes possibles, nous avons choisi dans un premier temps de nous focaliser sur une seule matrice afin de nous affranchir de paramètres spécifiquement liés à la structure chimique de la phase continue du nanocomposite. Toutefois,

le choix de la matrice doit permettre de faire varier un nombre de paramètres conséquents et dans une gamme suffisamment large. Ainsi l'acide polylactique (PLA) s'avère particulièrement pertinent, car il permet d'utiliser différentes voies de mise en œuvre (voie fondue, voie solvant, polymérisation *in situ* ...) et peut être amorphe ou semi-cristallin. De plus, de nombreuses études ont déjà été réalisées sur les nanocomposites à matrice PLA pour des propriétés barrière ce qui permettra de pouvoir collecter un nombre conséquent de données. Ainsi le PLA semble être une matrice modèle pertinente pour disposer d'un nombre suffisant de combinaisons permettant l'analyse et la compréhension du rôle des différents facteurs liés à la perméabilité dans les nanocomposites, ainsi que pour pouvoir réaliser une première étude en machine learning. La partie suivante s'attache donc à présenter la microstructure du PLA ainsi que l'influence de la cristallinité sur ses propriétés barrière. Enfin, une étude approfondie a été réalisée sur l'influence de la présence de nanocharges imperméables sur la perméabilité du PLA.

4. Approche expérimentale de la perméabilité appliquée à des matrices PLA contenant une ou plusieurs phases imperméables

L'acide polylactique (PLA), fait partie de la famille des polyesters. Il est obtenu à partir de l'acide lactique ou du lactide produit par la fermentation de sucres alimentaires (maïs, manioc, betterave, canne à sucre…). Le PLA est aujourd'hui le polymère biosourcé le plus produit puisqu'il représentait 31 % de la production globale de polymères biosourcés en 2023 et les projections montrent qu'il le sera encore davantage dans les années à venir (44% de la part des polymères biosourcés d'ici 2028) [50]. De plus, sa facilité de mise en œuvre, sa transparence, sa biodégradabilité et son coût relativement faible (~10€ /kg) en font un candidat particulièrement intéressant pour le secteur de l'emballage [50], [51], [52].

Pa ailleurs, concernant notre étude, le PLA présente plusieurs autres points d'intérêt. Tout d'abord les propriétés mécaniques sont suffisantes pour obtenir des films relativement fins et cohésifs afin de pouvoir mesurer sa perméabilité. Les perméabilités au dioxygène et à la vapeur d'eau du PLA sont globalement comparables aux polymères standards (PP, PE, PET, PS) [53], [54] comme le montre la **Figure 16**.

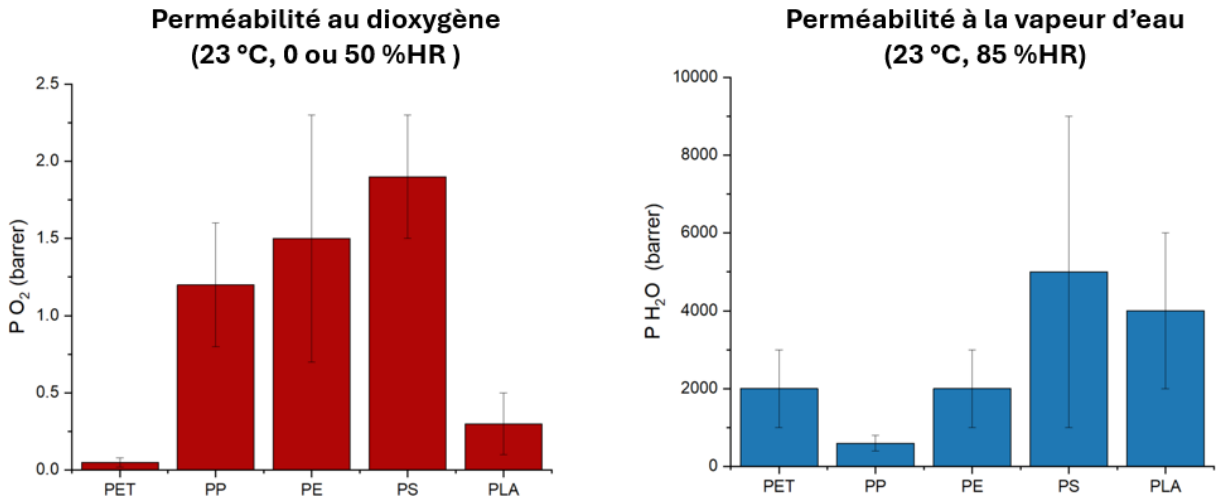


Figure 16 - Perméabilités au dioxygène et à la vapeur d'eau du PLA comparées à celles du PET, PP, PE et du PS (adaptée de l'étude Drieskens *et al.* [53]).

De plus, la cristallinité du PLA peut être facilement modulée ce qui permet d'obtenir des PLA avec différents taux de cristallinité. Enfin, le PLA est compatible avec une large gamme de procédés de mise en œuvre (voie fondue, voie solvant, polymérisation *in situ*). Le PLA présente donc de nombreux atouts pour élaborer une large plateforme de matériaux et étudier leurs propriétés barrière.

4.1. Synthèse du PLA

Deux voies de polymérisation peuvent être utilisées pour obtenir du PLA comme illustré par la **Figure 17**. La première est la polymérisation de l'acide lactique par polycondensation. Cependant, cette voie repose sur un équilibre thermodynamique et nécessite l'élimination de l'eau formée au fur et à mesure de la polymérisation pour déplacer l'équilibre de réaction. Cette méthode conduit souvent à de faibles masses molaires. La seconde voie est la polymérisation par ouverture de cycle (ROP) du lactide qui permet un meilleur contrôle de la polymérisation ainsi que l'obtention de masses molaires élevées. Cependant, elle nécessite l'utilisation d'un catalyseur ou d'un amorceur de réaction.

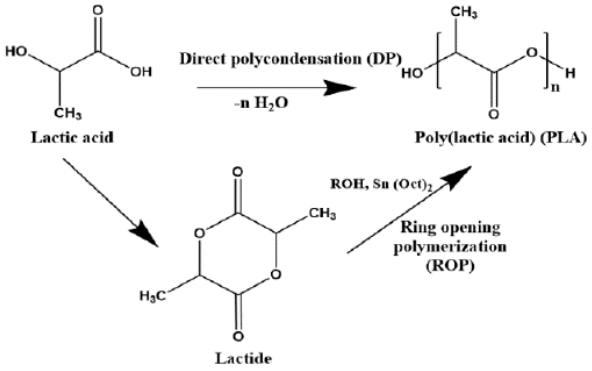


Figure 17 - Voies de polymérisation du PLA [17].

Concernant la polymérisation du PLA par ouverture de cycle, deux mécanismes existent. Le premier consiste en la complexation d'un catalyseur organométallique avec le groupement C=O du lactide puis la polymérisation est initiée par un agent nucléophile (H_2O, alcool) comme représenté sur la **Figure 18**. Le second est un mécanisme de coordination/insertion (**Figure 19**) réalisé à l'aide d'un amorceur de polymérisation, le plus souvent un alcoxyde métallique (octanoate d'étain, alcokyde d'aluminium…) [55], [56].

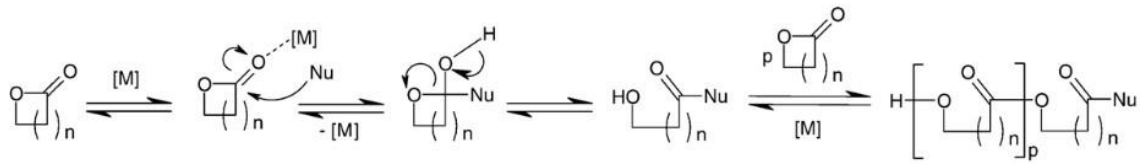


Figure 18 - Polymérisation « ROP » de lactone catalysée par un organométallique [M] en présence d'un nucléophile (Nu) [55].

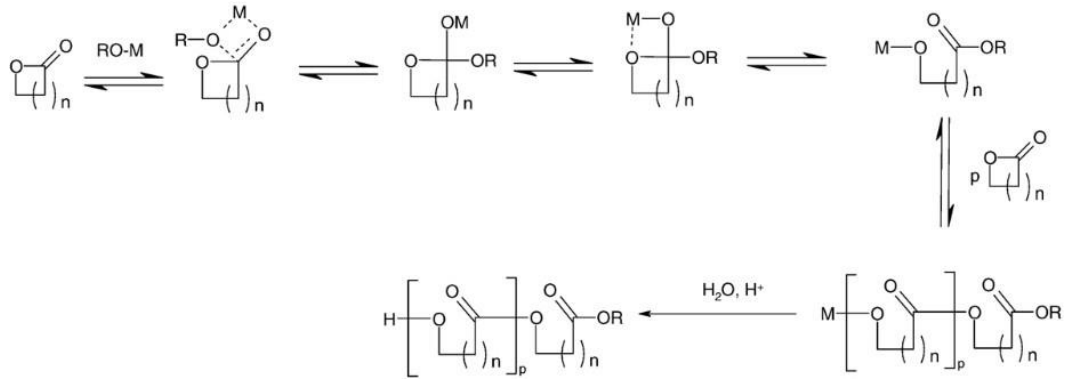


Figure 19 - Polymérisation « ROP » de lactone par un mécanisme de "coordination-insertion"[55].

La molécule d'acide lactique est une molécule chirale qui existe sous deux formes énantiomériques L et D. Le lactide existe ainsi sous 3 formes le L-Lactide, le D-lactide et le méso-lactide (LD) (**Figure 20**). De ce fait, il existe différentes formes de PLA avec des compositions en isomères L et D variables. Un PLA contenant uniquement des unités monomères L est désigné comme PLLA ; s'il contient uniquement des unités monomères D il s'agit alors de PDLA. Dans le cas d'une alternance d'unités monomères L et D, on parle de PDLLA. Dans ce manuscrit le PDLLA sera utilisé sous le nom de PLA. Cette structure chimique a une influence sur les propriétés des matériaux et notamment sur la cristallinité. En effet, une forte proportion d'unités monomères L permet d'avoir une phase cristalline tandis qu'au-delà de 8% d'unités D, le PLA reste amorphe [57].

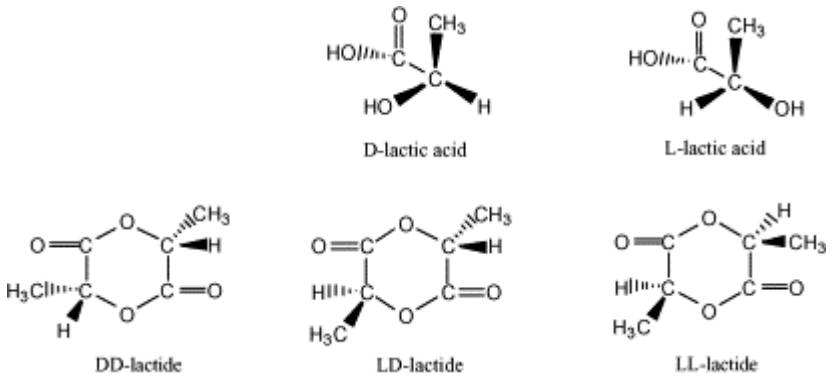


Figure 20 - Structure chimique du l'acide lactique (sous la forme L et D), du lactide (sous la forme L, D et LD) du PLA [54].

4.2. Microstructure du PLA

Le PLA peut être amorphe ou semi-cristallin selon la proportion d'unités isomères D, comme évoqué précédemment, et selon le procédé de mise en œuvre.

Un exemple de thermogramme DSC enregistré sur le PLA au cours d'une descente en température à 10 °C puis d'une montée en température à 2 °C est présenté sur la **Figure 21**. D'après ce thermogramme, la température de transition vitreuse (T_g) se situe aux environs de 50 °C et la température de fusion (T_m) aux alentours de 160 °C avec deux pics endothermiques associés au phénomène de fusion-recristallisation. Le thermogramme du PLA montre également un exotherme lors de la montée en température correspondant au phénomène de cristallisation froide pour une température (T_c) vers 110 °C. En effet, en condition non

isotherme la cristallisation du PLA s'effectue plus aisément en montée en température (cristallisation froide) à partir de l'état vitreux [58].

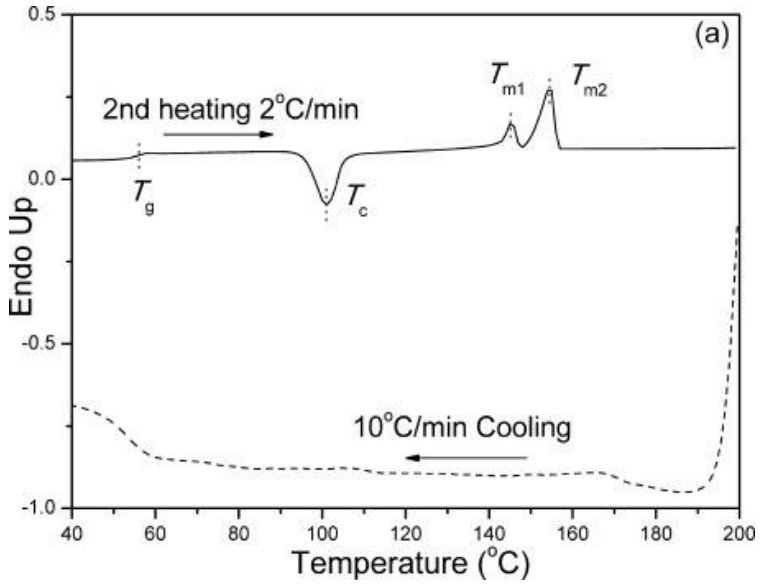


Figure 21 - Thermogramme DSC d'un PLA lors d'une descente en température depuis l'état fondu à 10 °C/min puis d'une montée en température à 2 °C/min [58].

En ce qui concerne la possibilité d'obtenir des PLA semi-cristallins, il est tout d'abord à noter que la cinétique de cristallisation est lente, ce qui conduit dans le cas de mise en œuvre par voie fondue avec refroidissement rapide à un matériau amorphe. Toutefois, il est possible de contrôler la cristallinité par des conditions de cristallisation isothermes depuis l'état fondu ou vitreux. Cependant, la cinétique de cristallisation est beaucoup plus lente depuis l'état fondu (**Figure 22**) comme l'ont montré Nassar *et al.* [59]. Ainsi dans la plupart des cas, la cristallisation du PLA est effectuée en conditions isothermes depuis l'état vitreux [53], [60], [61], [62].

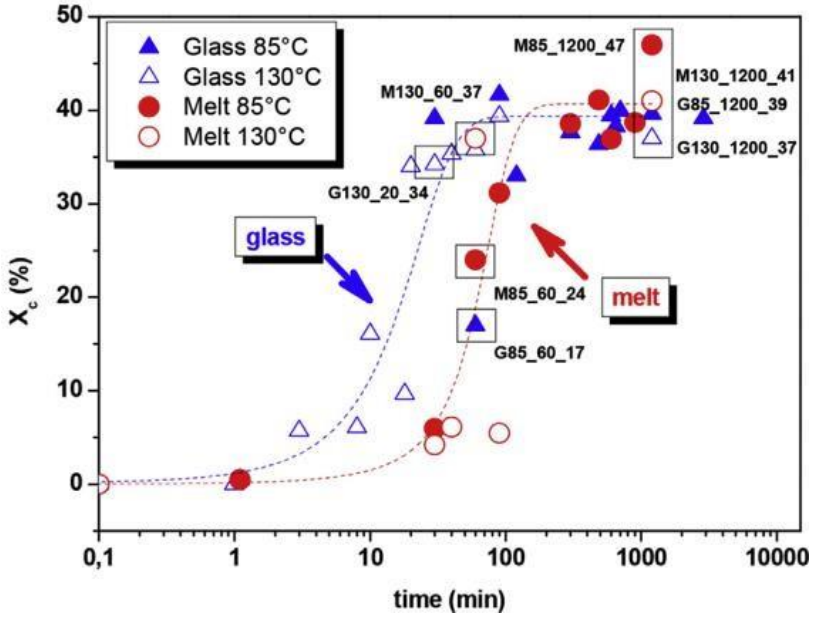


Figure 22 - Cinétique de cristallisation du PLA pour différentes températures à partir de l'état vitreux (en bleu) ou de l'état fondu (en rouge) [59].

Morel *et al.* [63] ont montré que le temps de demi-cristallisation varie, comme attendu, avec la température et passe par un minimum pour une température de 110 °C, température pour laquelle la cinétique de cristallisation est la plus rapide (**Figure 23a**). La température affecte également le taux de cristallinité qui tend vers son maximum (χ_c = 35%) pour des températures de cristallisation supérieures ou égale à 110 °C (**Figure 23b**).

Le PLA peut également cristalliser en solution par évaporation de solvant [64], [65]. Dans ce cas la cinétique de cristallisation dépend de l'évaporation du solvant [66] mais le degré de cristallinité ne peut pas être contrôlé.

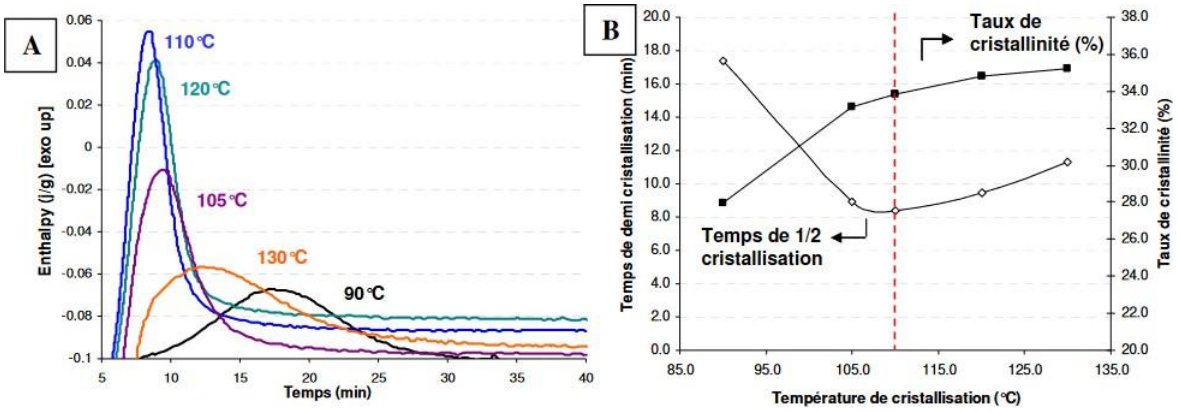


Figure 23 - (a) Évolution de l'enthalpie de cristallisation du PLA en fonction du temps et (b) évolution du temps de demi-cristallisation et du taux de cristallinité en fonction d'isotherme à différentes températures depuis l'état vitreux [28].

Le PLA peut cristalliser sous différentes formes cristallines en fonction de la température et des contraintes mécaniques. La forme la plus commune est la forme α qui est obtenue en majorité pour des températures de cristallisation froide supérieures à 100 °C et des cristallisations en solution. Des études ont également montré la présence d'une forme α', légèrement moins ordonnée que la forme α. Cette forme α' est prédominante pour des températures de cristallisation froide inférieures à 100 °C tandis qu'elle est présente de façon minoritaire pour des températures entre 100 et 120 °C [62], [67]. D'autres formes moins courantes ont été identifiées comme la forme β [68] et la forme ϒ [69], qui apparaissent lors de cristallisation sous contraintes. Les caractéristiques des différentes phases cristallines sont reportées dans le **Tableau 1.**

Tableau 1- Propriétés des différentes formes cristallines du PLA (adapté de l'étude de S. Saiellou *et al.*[70]).

Crystal type	Crystal system	Chain conformation	Cell parameters						$\rho_{theoretical}$ (g/cm^3)
			a (nm)	b (nm)	c (nm)	α (°)	β (°)	γ (°)	
α	Pseudo-orthorombic	10_3 helical	1.07	0.645	2.78	90	90	90	1.247
α	Orthorombic	10_3 helical	1.05	0.61	2.88	90	90	90	1.297
β	Orthorombic	3_1 helical	1.031	1.821	0.90	90	90	90	1.275
β	Trigonal	3_1 helical	1.052	1.052	0.88	90	90	120	1.277
γ	Orthorombic	3_1 helical	0.995	0.625	0.88	90	90	90	1.312
SC	Triclinic	3_1 helical	0.916	0.916	0.870	109.2	109.2	109.8	1.274
SC	Trigonal	3_1 helical	1.498	1.498	0.87	90	90	120	1.274

En l'absence de contraintes mécaniques lors de la cristallisation, les lamelles cristallines s'organisent sous forme de sphérolites. Lors de la cristallisation depuis l'état vitreux, la vitesse de nucléation est plus rapide que la croissance ce qui donne de plus petits sphérolites que lors

d'une cristallisation depuis l'état fondu [59], [71]. La différence de taille est illustrée par la **Figure 24** qui montre des sphérolites de PLA obtenus selon différentes conditions de cristallisation.

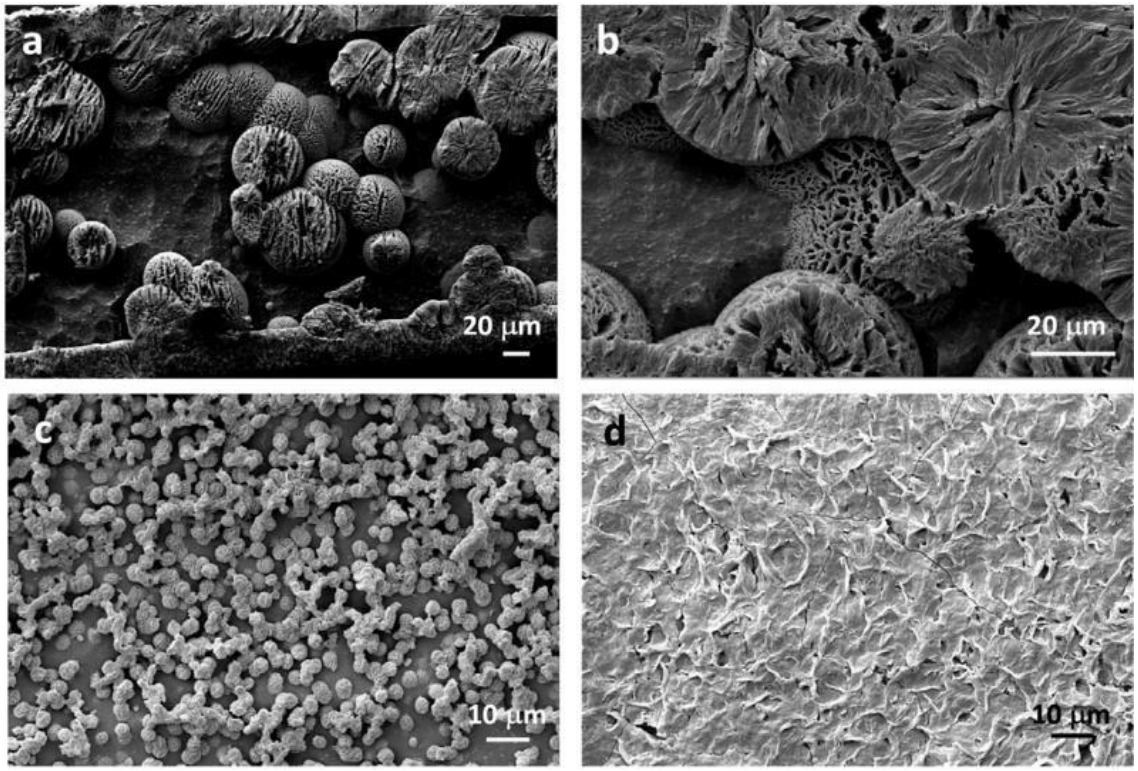


Figure 24 - Images prises en microscopie électronique à balayage de PLA semi-cristallins pour lesquels la phase amorphe a été éliminée par digestion enzymatiques. La phase cristalline a été obtenue par cristallisation soit depuis l'état fondu (a) à 85 °C pendant 24h, (b) à 130 °C soit depuis l'état vitreux (c) à 85 °C et d) à 130 °C [59].

Si les polymères semi-cristallins sont généralement considérés comme composés de deux phases, la phase cristalline et la phase amorphe, il est dans certains cas possible de distinguer ou de mettre en évidence au sein de la phase amorphe la coexistence d'une phase amorphe mobile (*MAF*) et d'une phase amorphe rigide (*RAF*). Ce modèle à trois phases a été mis en évidence pour la première fois en 1981 par Manczel et Wunderlich [72]. Généralement la fraction amorphe rigide (*RAF*) se situe à l'interface entre la phase cristalline et la phase amorphe, là où les cristaux entrainent une diminution du nombre de micro conformations que peuvent adopter les chaines amorphes, en raison de leur immobilisation progressive [73], [74]. La mobilité de cette phase étant moindre, la *RAF* et la *MAF* présentent des propriétés physiques différentes. Plusieurs études se sont intéressées à la présence de *RAF* dans le PLA [60], [61], [75]. Delpouve *et al.* [75] ont montré que la présence de *RAF* était notable

seulement pour un taux de cristallinité supérieur ou égal à 20% que ce soit pour du PLLA ou du PDLA. Ils ont également montré que la *RAF* était présente en plus grande proportion lorsque le PLA semi-cristallin est issu d'une cristallisation isotherme depuis l'état vitreux.

Concernant ses propriétés thermiques, le PLA possède une température de dégradation autour de 350 °C [76] correspondant à l'homolyse des chaines de PLA puis à une décomposition des oligomères comme l'acétaldéhyde en méthane et monoxyde de carbone [57]. De plus le PLA est sensible aux phénomènes d'hydrolyse, d'oxydation et de transestérification intra et intermoléculaire au-delà de la température de fusion [57], [76], [77]. De ce fait, il peut subir une certaine dégradation lors du procédé d'extrusion qui conduit à une diminution de la masse molaire au cours du temps comme le montre la **Figure 25**. Il est donc important de bien choisir la température et le temps de mélange lors d'un mélange par voie fondue ainsi que d'éviter toute présence d'eau.

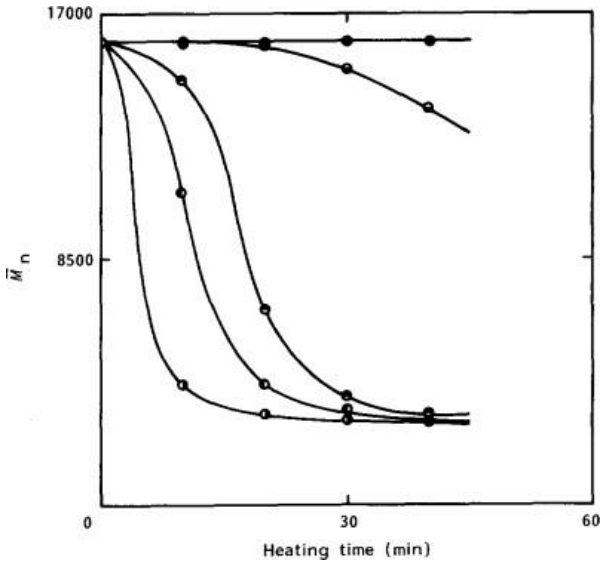


Figure 25 - Évolution de la masse molaire moyenne en nombre du PLLA pour plusieurs températures en fonction du temps : ● 180 °C, O190 °C, O 200 °C, ◐ 210 °C, ◑ 220 °C [77].

4.1. Influence de la cristallinité sur les propriétés barrière du PLA

Il a été montré dans plusieurs études [53], [59], [61], que la cristallisation du PLA depuis l'état vitreux conduit à une diminution de la perméabilité au dioxygène, comme généralement attendu (**Figure 26**). Les propriétés barrière sont améliorées lorsque le taux de cristallinité augmente et il est noté une diminution plus accentuée de la perméabilité au-delà d'un taux de cristallinité de l'ordre de 35% [53], [61]. Les auteurs ont expliqué cette plus forte diminution

de perméabilité par le phénomène de « cristallisation secondaire » correspondant à un perfectionnement de la structure cristalline au-delà d'un certain degré de cristallinité.

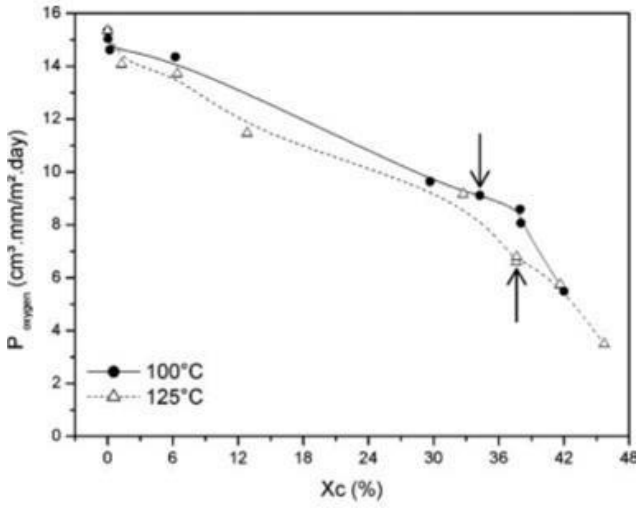


Figure 26 - Effet de la cristallinité sur le coefficient de perméabilité au dioxygène pour du PLA recuit à 100 °C et 125 °C [53].

De même, des films de PLA semi-cristallins obtenus par voie solvant et séchés à différentes température entre 90 et 120 °C, de façon à éliminer toute trace de solvant, ont montré une diminution de la perméabilité par rapport au même PLA amorphe (**Figure 27**) [28].

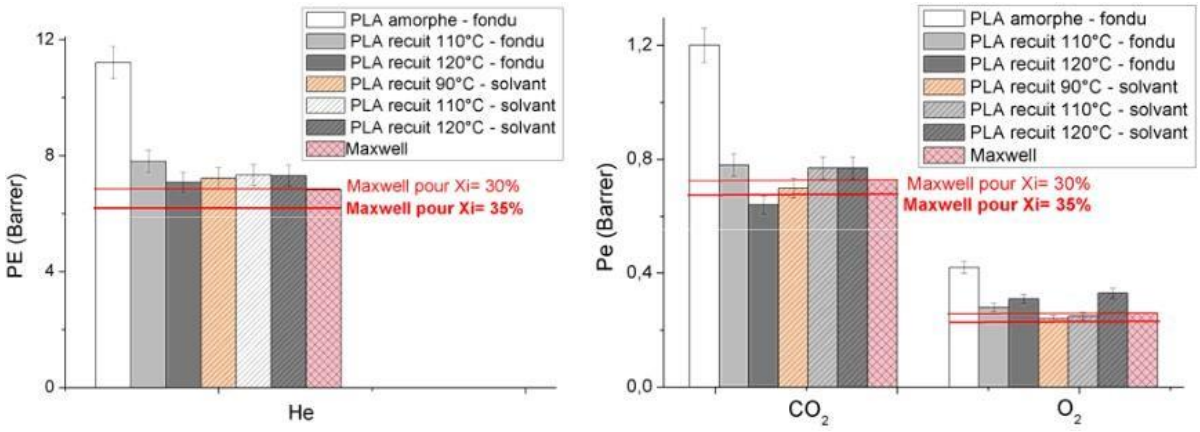


Figure 27 - Comparaison de la perméabilité à l'hélium, au dioxyde de carbone et au dioxygène de films de PLA amorphe et de films de PLA semi-cristallin obtenus par différents procédés [28].

De plus, la structure cristalline semble aussi avoir un effet sur la perméabilité. En effet, la perméabilité diminue davantage dans le cas d'une structure de type α qu'en présence de phase α' [61], [62]. Enfin, la présence d'une phase amorphe plus rigide (*RAF*) dans les PLA semi-cristallins peut avoir des conséquences sur les propriétés barrière du PLA. En effet,

Guinault *et al.* [61] ont supposé que la rigidification de la phase amorphe serait à l'origine d'une augmentation du coefficient de diffusion pour des taux de cristallinité inférieur ou égaux à 35%. Par ailleurs Sangroniz *et al.* [78] ont décrit une augmentation du coefficient de solubilité de la phase amorphe avec le taux de cristallinité (< 35%) qu'ils attribuent à l'augmentation de la *RAF*. Cependant aucune étude n'a montré d'effet de la rigidification de la phase amorphe sur la perméabilité.

Pour conclure, la perméabilité dans les systèmes PLA semi-cristallins semble dépendre d'un certain nombre de paramètres dont il sera important de considérer l'effet.

4.2. Influence de nanocharges imperméables sur les propriétés barrière du PLA

4.2. a) Élaboration de nanocomposites PLA à partir de charges préformées

Le procédé d'élaboration permet de jouer sur la dispersion des charges au sein de la matrice. En effet, différentes morphologies à différentes échelles peuvent être obtenues lors de l'introduction de nanocharges dans une matrice. Les charges peuvent être présentes sous forme de particules élémentaires ou peuvent se regrouper pour former des agrégats, au-delà d'une certaine taille (≈ 500 nm) on parle de structure agglomérée. Le choix du procédé d'élaboration et des paramètres associés est donc primordial pour optimiser les propriétés du matériau. Le PLA permet d'utiliser différents procédés pour mettre en œuvre des nanocomposites.

Le procédé le plus couramment utilisé pour l'élaboration de nanocomposite PLA est le mélange par voie fondue. Pour ce procédé qui se base sur l'utilisation d'une extrudeuse ou d'un mélangeur interne, la dispersion des charges est assurée par le cisaillement qui permet aux chaines polymères de diffuser entre les charges. La température, le mode de cisaillement et le temps de résidence sont des paramètres de mise en œuvre déterminant au niveau de la dispersion des charges. Ce procédé est utilisé avec un grand nombre de charges comme le carbonate de calcium [63], la silice [79], les halloysites [18], les montmorillonites [18], [80] et le graphène [81]. Un deuxième procédé, un peu moins courant, est le mélange par voie solvant. Il est principalement utilisé en laboratoire, car c'est la méthode la plus facile à mettre en place. Elle consiste à mélanger une suspension de charges dans un polymère en solution. Le polymère doit être soluble dans le solvant choisi pour la suspension. Les chaines polymères

gonflées par le solvant peuvent alors diffuser entre les charges. Le solvant est ensuite éliminé par évaporation. L'intérêt est de travailler avec une solution peu visqueuse (solvant de faible viscosité, concentration en polymère…) afin de faciliter la dispersion des charges dans la solution. Cependant, l'utilisation de solvants organiques (chloroforme, dichlorométhane, diméthylacétamide) rend cette méthode peu vertueuse pour l'environnement, ce qui limite son adaptation à l'échelle industrielle. La voie solvant est surtout utilisée dans le cas de nanocomposites chargés avec des nanofibrilles ou nanocristaux de cellulose [82], [83], [84], car la cellulose n'est pas très sable thermiquement. Un autre procédé moins utilisé, mais très efficace pour obtenir une très bonne dispersion des charges, est la polymérisation *in situ.* Ce procédé consiste à mélanger les charges avec le monomère fondu ou en solution. Puis la polymérisation est réalisée en présence de charges dans le milieu portée à une température adéquate avec l'ajout ou non de catalyseur ou amorceur de polymérisation. Ainsi les chaines polymères vont croître entre les charges ce qui permet généralement une bonne dispersion des charges voire une délamination des feuillets dans le cas de charges lamellaires. La polymérisation *in situ* de nanocomposites PLA a déjà été réalisée à partir de montmorillonites [56], [85], de nanotubes de carbone [86] et de silice [87] dans des conditions sur lesquelles nous reviendrons de manière détaillée dans le chapitre III.B.

4.2. b) Nanocomposites PLA à charges sphériques

Pour les nanocomposites à base de PLA, les études menées avec de la silice, du carbonate de calcium ou encore de l'argent non modifiés en surface sont regroupées dans le **Tableau 2**. Ces études montrent généralement peu d'efficacité de l'ajout de ces charges en termes de gain de propriétés barrière. En effet, dans le cas de matrice amorphe, la perméabilité relative minimale obtenue dans ces études est de 0.93 avec 6.5 %vol de carbonate de calcium [63]. Cette valeur est en accord avec le modèle de Maxwell [15]. Cependant, il a été remarqué que de plus faibles perméabilités relatives sont obtenues dans le cas d'une matrice PLA semi-cristalline [87], [88], [89], [90]. Dans ce cas les valeurs ne correspondent pas aux valeurs attendues avec les modèles théoriques. Il pourrait être suspecté un effet supplémentaire des charges conduisant à une augmentation de la cristallinité de la matrice.

Tableau 2 - Propriétés barrière de nanocomposites PLA à charges sphériques non modifiées en surface. Φ_v correspond à la fraction volumique de charges et $P/P_{0\,min}$ **:** Φ_v correspond à la perméabilité relative minimum obtenue sur l'ensemble des échantillons et la fraction volumique correspondante (la perméabilité relative correspond au ratio entre la perméabilité de l'échantillon et la perméabilité de référence du PLA donnée dans les études).

Charges	**Gamme de Φv (% vol)**	**Procédé /Matrice** (SC : semi-cristalline, NP : non précisée)	$P/P_{0\,min}$ **:** Φ_v **(perméant*)**	**Ref**
Silice	0,5%	Polymérisation *in situ* / Matrice SC	**0,59** : 0,5 %vol (H_2O)	[87]
			0,63 : 0,5 %vol (O_2)	
	0,5-3,5%	Voie solvant/ Matrice NP	**0,37** : 2 %vol (O_2)	[88]
	0,5%	Voie fondue / Matrice amorphe	**1,30** : 0,5% vol (O_2)	[79]
Carbonate de calcium ($CaCO_3$)	4-6,5%	Voie fondue/ Matrice amophe	**0,93** : 6,5 %vol (O_2)	[63]
Argent	0,1-2%	Voie solvant (ajout d'un plastifiant : tributylacetocitrate) Matrice SC	**0,72** : 0,3 %vol (O_2)	[90]
			0,74 : 0,3 %vol (H_2O)	[90], [89]

(*) Conditions de mesures utilisées : O_2 : 0 %HR/23 °C et H_2O : 90 %HR/ 38 °C

4.2. c) Nanocomposites PLA à charges de formes allongées

On recense parmi ces charges principalement des nanotubes d'halloysites, des nanofibrilles de cellulose et des nanocristaux de cellulose modifiés ou non en surface. Les nanotubes d'halloysitessont constitués de feuillets d'aluminosilicate du type $Al_2O_3.4SiO_2.H_2O$ enroulés sur eux-mêmes, formant des tubes d'un diamètre externe de l'ordre de 50 nm et une longueur comprise entre 100 et 2000 nm [91]. Les nanofibrilles de cellulose ont un diamètre d'environ 50 nm et une longueur de quelques micromètres [92], ce qui leur confère un facteur de forme élevé. Les nanocristaux de cellulose ont un facteur de forme plus faible avec un diamètre d'une dizaine de nanomètres et une longueur que quelques centaines de nanomètres [83]. Les perméabilités relatives minimales obtenues avec des halloysites non modifiées ainsi que des nanofibrilles et des nanocristaux de cellulose non modifiés ont été regroupés dans le **Tableau 3**. Les perméabilités relatives obtenues avec les nanocelluloses sont généralement plus faibles que celles obtenues avec des halloysites. Elles sont également inférieures aux

valeurs attendues à partir des modèles théoriques comme le modèle de Nielsen [9]. De plus, les valeurs de perméabilité relative des nanocomposites à base de nanocelluloses semblent différer significativement entre l'eau et le dioxygène.

Tableau 3 - Propriétés barrière de nanocomposites PLA à charges de formes allongées non modifiées en surface.
Φ_v correspond à la fraction volumique de charges et **$P/P_{0\,min}$: Φ_v** correspond à la perméabilité relative minimum obtenue sur l'ensemble des échantillons et la fraction volumique correspondante (la perméabilité relative correspond au ratio entre la perméabilité de l'échantillon et la perméabilité de référence du PLA donnée dans les études).

Charges	**Gamme de Φ_v (%vol)**	**Procédé /Matrice** (SC : semi-cristalline, NP : non précisée)	**$P/P_{0\,min}$: Φ_v (perméant*)**	**Ref**
Halloysites	0,5-7,5%	Voie fondue/ Matrice amorphe	**0,80** : 3,0 %vol(O_2)	[18], [93]
	0,5-3,5%	Voie solvant/ Matrice SC	**0,82** : 1,5 %vol (O_2)	[94]
Nanocristaux de cellulose (CNC)	0,5-2%	Voie fondue/ Matrice amorphe	**0,25** : 0,8 %vol (O_2) **0,57** : 0,8 %vol (H_2O)	[95]
	1-4%	Voie fondue/ Matrice SC	**0,28** : 4 %vol (O_2) **0,64** : 4 %vol (H_2O)	[96]
	2-5%	Voie solvant/ Matrice amorphe	**0,63** : 5 %vol (O_2) **0,80** : 2 %vol (H_2O)	[82]
	1-13%	Voie solvant/ Matrice SC	**0,57** : 4 %vol (O_2)	[83], [97]
			0,10 : 3 %vol (O_2 ,80 %HR) **0,22** : 3 %vol (H_2O)	[98]
Nanofibrilles de cellulose (CNF)	0,2-0,8 %	Voie fondue	**0,5** : 0,8 %vol (O_2)	[92]
	1-4%	Voie solvant	**0,96** : 4 %vol (O_2, 41 %HR)	[84]
			0,92 : 4 %vol (H_2O)	[84]

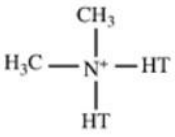
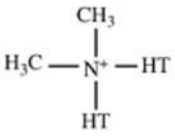
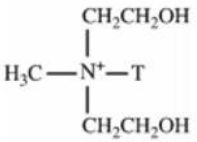
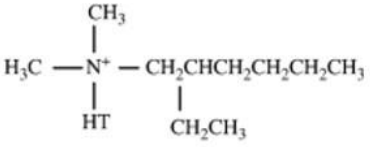
(*) Conditions de mesures utilisées sauf mention contraire : **O_2** : 0 %HR/23 °C et **H_2O** : 90 %HR/ 38 °C

4.2. d) Nanocomposites PLA à charges lamellaires

Concernant les nanocomposites PLA à charges lamellaires, on recense l'utilisation du graphène (ou oxyde de graphène) et des argiles comme la saponite, la kaolinite, les micas de fluorine, les hydroxydes doubles lamellaires et plus couramment les montmorillonites (MMT). Les montmorillonites sont des feuillets d'aluminosilicates hydratés, du type 2 :1. Ces feuillets sont constitués d'un réseau octaédrique d'oxyde d'aluminium (AlO_6) entouré de deux réseaux tétraédriques d'oxyde de silicium (SiO_4). Les feuillets possèdent un très grand facteur de forme, avec une épaisseur de l'ordre de 1 nm et une longueur pouvant aller jusqu'au micromètre. Les montmorillonites sont très utilisées dans l'élaboration de nanocomposites avec l'objectif de les retrouver sous forme de feuillets individuels dans la matrice [17], [99]. Pour ce faire, outre l'optimisation des conditions d'élaboration, il est généralement utilisé des montmorillonites organo-modifiées afin d'améliorer la compatibilité charge/matrice. Ainsi, pour la matrice PLA, le cation Na^+ présent dans la montmorillonite naturelle est échangé par l'un des cations présentés dans le **Tableau 4**.

Tableau 4 - Nomenclature de montmorillonites modifiées commerciales et formule semi-développée du cation alkyl ammonium associé [100].

Cloisite™ series from Southern Clay Co

Name	Modifier structure	Modifier content (wt%)
Cloisite 15A		43
Cloisite 20A		38
Cloisite 30B		30
Cloisite 25A		34

HT: Hydrogenated tallow (~65% C_{18}, ~30% C_{16}, ~5% C_{14})

Les feuillets de graphène, du fait de leur grand facteur de forme, sont également de bons candidats pour augmenter les propriétés barrière. Cependant, peu d'études ont été réalisées avec le PLA, car leur faible affinité avec ce polymère rend leur dispersion souvent mauvaise, ce qui diminue leur efficacité [81], [101].

Le **Tableau 5** présente une liste exhaustive d'études réalisées sur les propriétés barrière de nanocomposites PLA à charges lamellaires modifiées ou non, pour différents taux de charges, procédés et perméants. On peut d'abord remarquer le nombre important d'études réalisées avec des MMT, qui utilisent dans la majorité des cas un procédé par voie fondue. Pour les MMT, de plus faibles perméabilités relatives sont obtenues avec un cation organique et notamment un cation polaire (cas de la Cloisite®30B). De plus, en comparaison des montmorillonites, de plus faibles fractions volumiques de graphène ou d'oxyde de graphène sont nécessaires pour obtenir des niveaux de perméabilité relative équivalents.

Tableau 5 - Propriétés barrière pour des nanocomposites PLA à charges lamellaires.
Φ_v correspond à la fraction volumique de charges et **$P/P_{0\,min}$: Φ_v** correspond à la perméabilité relative minimum obtenue sur l'ensemble des échantillons et la fraction volumique correspondante (la perméabilité relative correspond au ratio entre la perméabilité de l'échantillon et la perméabilité de référence du PLA donnée dans les études).

Charges	**Modification de surface**	**Gamme de Φ_v (% vol)**	**Procédé/ Matrice** (SC : semi-cristalline, NP : non précisé)	**$P/P_{0\,min}$: Φ_v (perméant *)**	**Ref**
Montmorillonites (MMT)	/	3%	Voie solvant/ Matrice SC	**1,16** :3 %vol (H_2O)	[102]
		0,5-3,5%	Voie solvant/ Matrice NP	**0,64** :1,5 %vol (O_2)	[94]
		0,5-7,5%	Voie fondue/ Matrice amorphe	**0,85** : 7,5 %vol (O_2)	[18]
	Cloisite®15A (C15A)	0,25%	Polymérisation *in situ*/ Matrice SC	**0,88** : 0,25 %vol (O_2), **0,59** : 0,25 %vol (H_2O)	[87]
		0,02-0,2%	Voie solvant/ Matrice NP	**0,71** : 0,2 %vol (O_2 ,30 °C)	[103]
	Cloisite®20A (C20A)	3%	Voie solvant/ Matrice SC	**0,64** : 3 %vol (H_2O)	[102]
		0,02-0,2%	Voie solvant/ Matrice NP	**0,87** : 0,3 %vol (O_2, 30 °C),	[103]
	Cloisite®25A (C25A)	1,5-3,5%	Voie solvant/ Matrice NP	**0,44** : 3 %vol (O_2)	[104]
		2,5%	Voie fondue (Extrusion souflage avec ajout de plastifiant : Acetyltriethyl citrate) / Matrice NP	**0,59** : 2,5 %vol (O_2), **0,37** : 2,5 %vol (H_2O)	[105]

Montmorillonites (MMT)	Cloisite®30B (C30B)	0,5-6,5 %	Voie fondue / Matrice amorphe	**0,38** : 10 %vol (O_2)	[80], [106], [18], [107], [108], [109], [110], [111], [112], [113], [114]
				0,3 :10 %vol (H_2O)	[111], [112], [106], [114]
		0,5-6,5%	Voie solvant/ Matrice SC	**0,42** : 6,5 %vol (O_2)	[103], [115],
		0,5-6,5%		**0,53** : 6,5 %vol (H_2O)	[102], [115]
	Octadecylamonium cation	1,5-2%	Voie fondue/ Matrice amorphe	**0,85** : 1,5% (O_2, 90 %HR)	[108], [109]
				0,47 : 2% vol (O_2)	[116]
	Acide 18-animostearique	0,5-2,5%	Voie fondue/ Matrice amorphe	**0,61** : 1,5 %vol (O_2)	[117]
	dimethyl dialkyl amine	0,3-3%	Voie solvant/ Matrice SC	**0,34** : 3 %vol (O_2), **0,21** : 3 %vol (H_2O)	[115]
	Distearyldimethyl ammonium chloride	0,2-2%	Voie solvant/ Matrice SC	**0,45** : 2 %vol (O_2), **0,2** : 2 %vol (H_2O)	[115]
Hydroxydes double lamellaires	Sodium dodecyl sulfate	0,5-3%	Voie solvant/ Matrice NP	**0,95** : 0,5 %vol(O_2)	[118]
Mica de fluorine	N-(coco-alkyl) N-N-bis (2-hydroxyethyl) -N methylammonium	1,6-4,2%	Voie fondue/ Matrice amorphe	**0,19** : 4,2 %vol (O_2)	[108], [119]

	Ocatdecylamonium cation	2%	Voie fondue/ Matrice amorphe	**0,47** : 2 %vol (O_2)	[116]
Saponite	Hexadecyltributy--phosphonium	2%	Voie fondue/ Matrice amorphe	**0,58** : 2 %vol (O_2)	[108]
Kaolinite	Nature non précisé	2%	Voie fondue/ Matrice amorphe	**0,60** : 2 %vol (O_2)	[120], [121]
Oxide de graphène	/	0,2-0,5%	Voie fondue/ Matrice amorphe	**0,80** : 0,5 %vol (O_2)	[81]
	/	0,1-1 %	Voie solvant/ Matrice amorphe	**0,33** : 0,3 %vol (O_2, 50 %HR)	[122], [101]
Graphène	/	0,1-0.4 %	Voie solvant/ Matrice amorphe	**0,32** : 0,3 %vol (O_2, 50 %HR)	[122]

(*) Conditions de mesures utilisées sauf mention contraire : **O_2** : 0 %HR/23 °C et **H_2O** : 90 %HR/ 38 °C

4.2. e) Discussion

Un certain nombre de conclusions peuvent être tirées de cette revue de littérature sur les matrices PLA contenant une ou plusieurs phases imperméables.

Premièrement, une diminution de la perméabilité relative est constatée avec l'augmentation du taux de cristallinité du PLA qui semble davantage marquée au-delà de 35% de cristallinité. De plus, la structure de la phase cristalline, liée aux conditions de cristallisation, est un facteur qui peut jouer sur la perméabilité. Enfin, si la présence de *RAF* a été considérée pour expliquer des augmentations de la diffusion ou de la solubilité, il semble que cette dernière n'a pas entrainé de modification de perméabilité.

Concernant l'influence de nanocharges imperméables sur la perméabilité, la **Figure 28**, construite à l'aide des différentes études citées précédemment, montre l'évolution de la perméabilité relative en fonction du taux volumique de charges. Tout d'abord, la perméabilité relative d'une matrice PLA contenant des charges imperméables est généralement inférieure à 1 ce qui montre que les charges permettent d'améliorer les propriétés barrière du PLA. Les résultats pour les nanocomposites à matrice amorphe, (**Figure 28a**) montrent généralement une plus grande efficacité des graphènes des micas de fluorine sur la diminution de perméabilité. Par ailleurs, les montmorillonites modifiées avec un cation organique, notamment la Cloisite®30B, mènent généralement à une plus grande réduction de la

perméabilité que les montmorillonites Na^+. Les nanocelluloses (cristaux ou fibrilles) semblent également être intéressantes pour diminuer la perméabilité du PLA. Cependant ces charges présentent une faible stabilité thermique [123] ce qui rend difficile leur utilisation pour l'élaboration de nanocomposites en mélangeur interne ou en extrusion. De ce fait, les nanocelluloses ne seront pas utilisées dans les approches expérimentales de cette thèse.

Il est également à noter que les perméabilités relatives des nanocomposites semi-cristallins (**Figure 28b**) couvrent globalement une gamme de valeurs assez similaires à celle des nanocomposites amorphes. On observe toutefois une plus grande dispersion des valeurs pour un type de charges donné, ce qui peut s'expliquer en partie par une grande variabilité des conditions expérimentales et par une possible modification du taux de cristallinité de la matrice en présence de charges.

Enfin, dans tous les cas (matrice PLA amorphe ou semi-cristalline) on relève quelques valeurs de perméabilité relative supérieures ou égales à 1. La **Figure 28** montre clairement, comme attendu que la perméabilité relative ne dépend pas uniquement du taux de charges mais aussi de multiples facteurs dont il conviendra de hiérarchiser les effets dans notre étude expérimentale. La pertinence de l'approche en machine learning sera également intéressante à évaluer dans ce cadre.

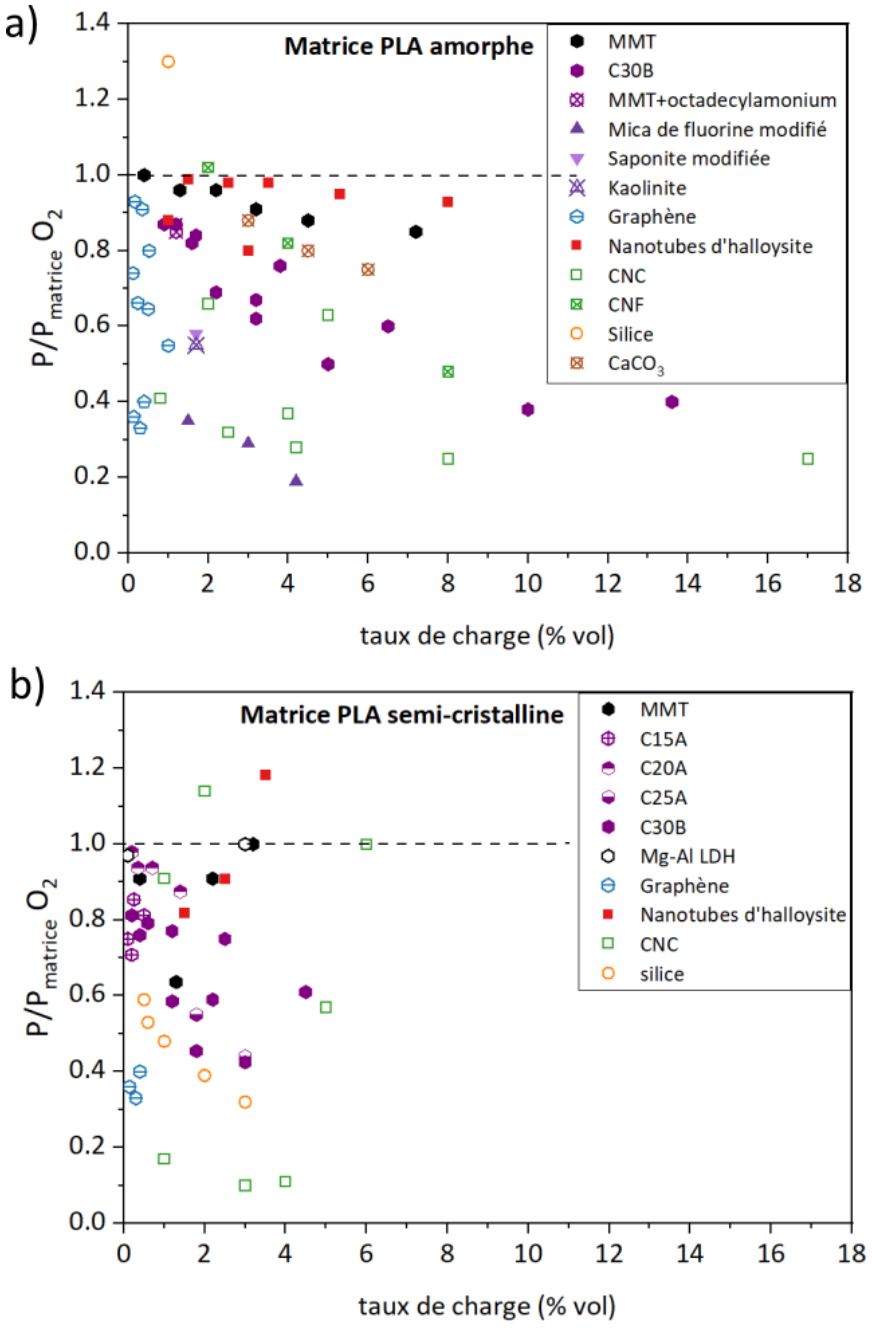


Figure 28 - Evolution de la perméabilité au dioxygène des nanocomposites par rapport à la perméabilité de la matrice (P/P matrice) en fonction du taux volumique de charges (a) dans le cas d'une matrice amorphe et (b) dans le cas d'une matrice semi-cristalline. Les données sont calculées à partir de travaux expérimentaux [18], [28], [79], [80], [81], [82], [83], [87], [88], [93], [94], [95], [96], [97], [98], [92], [101], [103], [104], [106], [108], [110], [115], [118], [120], [122].

5. Conclusion

Ce chapitre bibliographique a permis de rappeler les bases des mécanismes de transport de petites molécules, dans les films polymères denses. L'intérêt d'introduire une phase imperméable dans les matrices polymères pour en améliorer les propriétés barrière, que ce

soit la phase cristalline ou des charges imperméables, a été montré par différents modèles théoriques. Ces modèles prennent en compte un effet de tortuosité au sein du matériau, qui s'exprime le plus souvent pour des systèmes binaires idéaux en fonction de la fraction volumiques de phase imperméable et du facteur de forme des entités dispersées ainsi que de leur orientation.

Néanmoins, les systèmes peuvent être bien plus complexes reposant sur des paramètres plus nombreux et possiblement interreliés. Une nouvelle approche a donc été envisagée pour notre étude en complément de l'approche expérimentale et théorique : le machine learning. L'avantage du machine learning est qu'il repose exclusivement sur l'apprentissage à partir de données (expérimentales ou simulées), contrairement aux modèles théoriques. Cet outil a déjà été utilisé pour la prédiction de perméabilité dans le cas de polymères, mais jamais pour des nanocomposites. Face à la multitude de facteurs pouvant gouverner la perméabilité et la diversité des systèmes envisageables, il a été décidé de se concentrer dans un premier temps sur une seule matrice afin de nous affranchir de paramètres spécifiquement liés à la structure chimique de la phase continue du matériau. Ainsi, une analyse détaillée d'une cinquantaine d'études expérimentales a été réalisée dans le cas d'une matrice en PLA. Le choix de ce polymère a été fait pour permettre de couvrir une gamme étendue de procédés de mise en œuvre et de microstructures. Les études de perméabilité de nanocomposites à base de PLA sont nombreuses, basées sur des charges différentes et permettent ainsi d'avoir accès à un nombre assez important de données expérimentales qu'il convient toutefois de compléter.

Ainsi, à la suite de cette étude bibliographique, nous nous attacherons donc dans un premier temps, à établir des relations procédés/microstructures/perméabilité à travers la caractérisation détaillée de notre propre plateforme de matériaux PLA, que nous allons judicieusement élaborer et caractériser. À travers cette plateforme de matériaux PLA contenant une phase imperméable nous viserons de couvrir un nombre suffisant de procédés de mise en œuvre et de microstructures ainsi que de paramètres pouvant influencer la perméabilité. Les charges incorporées seront uniquement des charges inorganiques pour éviter toute dégradation avec les procédés d'élaboration choisis. Enfin, en ajoutant les données de la littérature à nos propres données expérimentales, il sera possible de mettre en place une approche permettant d'identifier les paramètres gouvernant les propriétés barrière et d'utiliser le machine learning pour prédire la perméabilité relative.

Dans un second temps, nous étudierons de manière expérimentale l'influence de l'introduction de deux phases imperméables dans la matrice PLA afin de voir si des comportements additifs ou des synergies opèrent. Pour cela, l'effet de la combinaison de la phase cristalline du PLA avec une charges, dont le type sera varié, pour différents procédés de mise en œuvre sera analysé. Par ailleurs, l'effet de l'incorporation de deux charges imperméables différentes dans une matrice PLA amorphe sera également discuté.

Enfin sur la base des études de machine learning menées avec le PLA, l'étude de la perméabilité de nanocomposites sera élargie à un grand nombre de matrices polymères. Le but étant de proposer un outil permettant de cibler des compositions/procédés d'élaboration de nanocomposites permettant d'obtenir des valeurs de perméabilité visées.

6. Références

[1] H. Fujita, A. Kishimoto, K. Matsumoto, Concentration and temperature dependence of diffusion coefficients for systems polymethyl acrylate and n-alkyl acetates, Trans. Faraday Soc. 56 (1960) 424. https://doi.org/10.1039/tf9605600424.

[2] A. Kishimoto, H. Fujita, H. Odani, M. Kurata, M. Tamura, SUCCESSIVE DIFFERENTIAL ABSORPTIONS OF VAPORS BY GLASSY POLYMERS, J. Phys. Chem. 64 (1960) 594–598. https://doi.org/10.1021/j100834a020.

[3] M.H. Klopffer, B. Flaconneche, Transport Properties of Gases in Polymers: Bibliographic Review, Oil & Gas Science and Technology - Rev. IFP 56 (2001) 223–244. https://doi.org/10.2516/ogst:2001021.

[4] G.S. Park, Transport Principles—Solution, Diffusion and Permeation in Polymer Membranes, Synthetic Membranes: Science, Engineering and Applications, Springer (1986) 57–107. https://doi.org/10.1007/978-94-009-4712-2_3.

[5] J. Crank, Diffusion in Polymers, Academic Press (1968).

[6] A. Fick, Ueber Diffusion, Annalen Der Physik 170 (1855) 59–86. https://doi.org/10.1002/andp.18551700105.

[7] G.J. Van Amerongen, Influence of structure of elastomers on their permeability to gases, Journal of Polymer Science 5 (1950) 307–332. https://doi.org/10.1002/pol.1950.120050304.

[8] A.S. Michaels, R.B. Parker Jr., Sorption and flow of gases in polyethylene, Journal of Polymer Science 41 (1959) 53–71. https://doi.org/10.1002/pol.1959.1204113805.

[9] L.E. Nielsen, Models for the Permeability of Filled Polymer Systems, Journal of Macromolecular Science—Chemistry (1967). https://doi.org/10.1080/10601326708053745.

[10] G. Choudalakis, A.D. Gotsis, Permeability of polymer/clay nanocomposites: A review, European Polymer Journal 45 (2009) 967–984. https://doi.org/10.1016/j.eurpolymj.2009.01.027.

[11] E.P. Giannelis, Polymer Layered Silicate Nanocomposites, Advanced Materials 8 (1996) 29–35. https://doi.org/10.1002/adma.19960080104.

[12] A.S. Michaels, H.J. Bixler, Solubility of gases in polyethylene, Journal of Polymer Science 50 (1961) 393–412. https://doi.org/10.1002/pol.1961.1205015411.

[13] S. Zid, Finite element modeling and experimental approach of gas transport in polymer-based multimaterials and complex systems, Thèse de doctorat, Université Lyon 1 (2019).

[14] H. Fricke, THE ELECTRIC CONDUCTIVITY AND CAPACITY OF DISPERSE SYSTEMS, Physics 1 (1931) 106–115. https://doi.org/10.1063/1.1744988.

[15] J.C. Maxwell, A Treatise on Electricity and Magnetism, Clarendon Press, 1873.

[16] A. Peterlin, Dependence of diffusive transport on morphology of crystalline polymers, Journal of Macromolecular Science, Part B 11 (1975) 57–87. https://doi.org/10.1080/00222347508217855.

[17] S. Singha, M.S. Hedenqvist, A Review on Barrier Properties of Poly(Lactic Acid)/Clay Nanocomposites, Polymers 12 (2020) 1095. https://doi.org/10.3390/polym12051095.

[18] Y. Guo, K. Yang, X. Zuo, Y. Xue, C. Marmorat, Y. Liu, C.-C. Chang, M.H. Rafailovich, Effects of clay platelets and natural nanotubes on mechanical properties and gas permeability of Poly (lactic acid) nanocomposites, Polymer 83 (2016) 246–259. https://doi.org/10.1016/j.polymer.2015.12.012.

[19] E.L. Cussler, S.E. Hughes, W.J. Ward, R. Aris, Barrier membranes, Journal of Membrane Science 38 (1988) 161–174. https://doi.org/10.1016/S0376-7388(00)80877-7.

[20] W.T. Brydges, S.T. Gulati, G. Baum, Permeability of glass ribbon-reinforced composites, J Mater Sci 10 (1975) 2044–2049. https://doi.org/10.1007/BF00557482.

[21] N.K. Lape, E.E. Nuxoll, E.L. Cussler, Polydisperse flakes in barrier films, Journal of Membrane Science 236 (2004) 29–37. https://doi.org/10.1016/j.memsci.2003.12.026.

[22] E. Picard, A. Vermogen, J.-F. Gérard, E. Espuche, Barrier properties of nylon 6-montmorillonite nanocomposite membranes prepared by melt blending: Influence of the clay content and dispersion state: Consequences on modelling, Journal of Membrane Science 292 (2007) 133–144. https://doi.org/10.1016/j.memsci.2007.01.030.

[23] R.K. Bharadwaj, Modeling the Barrier Properties of Polymer-Layered Silicate Nanocomposites, Macromolecules 34 (2001) 9189–9192. https://doi.org/10.1021/ma010780b.

[24] L. Olivier, M. Sabard, R. Fulchiron, E. Espuche, L. David, A. Guiu, Influence of α-ZrP fillers and process conditions on the morphology and the gas barrier properties of filled polyamide 6 films, Journal of Polymer Science Part B: Polymer Physics 46 (2008) 1734–1746. https://doi.org/10.1002/polb.21515.

[25] E. Picard, J.-F. Gérard, E. Espuche, Reinforcement of the Gas Barrier Properties of Polyethylene and Polyamide Through the Nanocomposite Approach: Key Factors and Limitations, Oil Gas Sci. Technol. – Rev. IFP Energies Nouvelles 70 (2015) 237–249. https://doi.org/10.2516/ogst/2013145.

[26] O. Gain, E. Espuche, E. Pollet, M. Alexandre, Ph. Dubois, Gas barrier properties of poly(ε-caprolactone)/clay nanocomposites: Influence of the morphology and polymer/clay interactions, Journal of Polymer Science Part B: Polymer Physics 43 (2005) 205–214. https://doi.org/10.1002/polb.20316.

[27] K. Dal Pont, Nanocomposites à matrice élastomère à base de charges lamellaires synthétiques alpha-ZrP : influence de la modification des charges sur les propriétés mécaniques et barrière aux gaz, Thèse de doctorat, Université Lyon 1, 2011.

[28] F. Morel, Compréhension des phénomènes interfaciaux dans les composites à base de charges carbonate de calcium précipité: influence du traitement de surface et du procédé de mise en œuvre, Thèse de doctorat, Université de Lyon (2010).

[29] S. Zid, M. Zinet, E. Espuche, Modeling diffusion mass transport in multiphase polymer systems for gas barrier applications: A review, Journal of Polymer Science Part B: Polymer Physics 56 (2018) 621–639. https://doi.org/10.1002/polb.24574.

[30] S. Zid, M. Zinet, E. Espuche, 3D Mass diffusion in ordered nanocomposite systems: Finite element simulation and phenomenological modeling, Journal of Polymer Science Part B: Polymer Physics 57 (2019) 51–61. https://doi.org/10.1002/polb.24758.

[31] T. Htira, S. Zid, M. Zinet, E. Espuche, Finite Element Analysis of Gas Diffusion in Polymer Nanocomposite Systems Containing Rod-like Nanofillers, Polymers 13 (2021) 2615. https://doi.org/10.3390/polym13162615.

[32] C. Wolf, H. Angellier-Coussy, N. Gontard, F. Doghieri, V. Guillard, How the shape of fillers affects the barrier properties of polymer/non-porous particles nanocomposites: A review, Journal of Membrane Science 556 (2018) 393–418. https://doi.org/10.1016/j.memsci.2018.03.085.

[33] D.M. Dutton, G.V. Conroy, A review of machine learning, The Knowledge Engineering Review 12 (1997) 341–367. https://doi.org/10.1017/S026988899700101X.

[34] T. Jiang, J.L. Gradus, A.J. Rosellini, Supervised Machine Learning: A Brief Primer, Behavior Therapy 51 (2020) 675–687. https://doi.org/10.1016/j.beth.2020.05.002.

[35] R. Gentleman, V.J. Carey, F. Hahne, W. Huber, R. Gentleman, S. Falcon Unsupervised Machine Learning, Bioconductor Case Studies, Springer (2008) 137–157. https://doi.org/10.1007/978-0-387-77240-0_10.

[36] Z. Ghahramani, O. Bousquet, U. von Luxburg, G. Rätsch, Unsupervised Learning, Advanced Lectures on Machine Learning , Springer (2004) 72–112. https://doi.org/10.1007/978-3-540-28650-9_5.

[37] V. Nasteski, An overview of the supervised machine learning methods, HORIZONS.B 4 (2017) 51–62. https://doi.org/10.20544/HORIZONS.B.04.1.17.P05.

[38] D. Bzdok, M. Krzywinski, N. Altman, Machine learning: supervised methods, Nature Methods 15 (2018) 5. https://doi.org/10.1038/nmeth.4551.

[39] M. Somvanshi, P. Chavan, S. Tambade, S.V. Shinde, A review of machine learning techniques using decision tree and support vector machine, International Conference on Computing Communication Control and Automation (2016) 1–7. https://doi.org/10.1109/ICCUBEA.2016.7860040.

[40] S. Ray, A Quick Review of Machine Learning Algorithms, International Conference on Machine Learning, Big Data, Cloud and Parallel Computing (2019) 35–39. https://doi.org/10.1109/COMITCon.2019.8862451.

[41] S.J. Rigatti, Random Forest, Journal of Insurance Medicine 47 (2017) 31–39. https://doi.org/10.17849/insm-47-01-31-39.1.

[42] Y. Liu, Y. Wang, J. Zhang, B. Liu, M. Ma, J. Chang, New Machine Learning Algorithm: Random Forest, Information Computing and Applications, Springer (2012). 246–252. https://doi.org/10.1007/978-3-642-34062-8_32.

[43] C.-C. Chang, C.-J. Lin, LIBSVM: A library for support vector machines, ACM Trans. Intell. Syst. Technol. 2 (2011) 1–27. https://doi.org/10.1145/1961189.1961199.

[44] E. Champa-Bujaico, P. García-Díaz, A.M. Díez-Pascual, Machine Learning for Property Prediction and Optimization of Polymeric Nanocomposites: A State-of-the-Art, International Journal of Molecular Sciences 23 (2022) 10712. https://doi.org/10.3390/ijms231810712.

[45] P.N. Khanam, M. AlMaadeed, S. AlMaadeed, S. Kunhoth, M. Ouederni, D. Sun, A. Hamilton, E.H. Jones, B. Mayoral, Optimization and Prediction of Mechanical and Thermal Properties of Graphene/LLDPE Nanocomposites by Using Artificial Neural Networks, International Journal of Polymer Science 2016 (2016) 5340252. https://doi.org/10.1155/2016/5340252.

[46] M. Zakaulla, Y. pasha, S. kesarmadu Siddalingappa, Prediction of mechanical properties for polyetheretherketone composite reinforced with graphene and titanium powder using artificial neural network, Materials Today: Proceedings 49 (2022) 1268–1274. https://doi.org/10.1016/j.matpr.2021.06.365.

[47] G. Zhu, C. Kim, A. Chandrasekarn, J.D. Everett, R. Ramprasad, R.P. Lively, Polymer genome–based prediction of gas permeabilities in polymers, Journal of Polymer Engineering 40 (2020) 451–457. https://doi.org/10.1515/polyeng-2019-0329.

[48] M. Zhou, A. Vassallo, J. Wu, Toward the inverse design of MOF membranes for efficient D2/H2 separation by combination of physics-based and data-driven modeling, Journal of Membrane Science 598 (2020) 117675. https://doi.org/10.1016/j.memsci.2019.117675.

[49] J.W. Barnett, C.R. Bilchak, Y. Wang, B.C. Benicewicz, L.A. Murdock, T. Bereau, S.K. Kumar, Designing exceptional gas-separation polymer membranes using machine learning, Science Advances 6 (2020) 1–7. https://doi.org/10.1126/sciadv.aaz4301.

[50] Bioplastics market development update 2023, European Bioplastics e.V (2023). https://www.european-bioplastics.org/market/ (accessed August 20, 2024).

[51] M. Labonté, C. Dubois, Processing of Impact Modifed PLA in a Continous Process at High Speed: Comparison with PET Molding Conditions – A New Era, Polymer-Plastics Technology and Engineering 54 (2015) 368–374. https://doi.org/10.1080/03602559.2014.958774.

[52] S. Farah, D.G. Anderson, R. Langer, Physical and mechanical properties of PLA, and their functions in widespread applications — A comprehensive review, Advanced Drug Delivery Reviews 107 (2016) 367–392. https://doi.org/10.1016/j.addr.2016.06.012.

[53] M. Drieskens, R. Peeters, J. Mullens, D. Franco, P.J. Lemstra, D.G. Hristova-Bogaerds, Structure versus properties relationship of poly(lactic acid). I. Effect of crystallinity on barrier properties: Structure Vs. Barrier Properties of PLA, J. Polym. Sci. B Polym. Phys. 47 (2009) 2247–2258. https://doi.org/10.1002/polb.21822.

[54] H.J. Lehermeier, J.R. Dorgan, J.D. Way, Gas permeation properties of poly(lactic acid), Journal of Membrane Science 190 (2001) 243–251. https://doi.org/10.1016/S0376-7388(01)00446-X.

[55] C. Jérôme, P. Lecomte, Recent advances in the synthesis of aliphatic polyesters by ring-opening polymerization, Advanced Drug Delivery Reviews 60 (2008) 1056–1076. https://doi.org/10.1016/j.addr.2008.02.008.

[56] M.-A. Paul, C. Delcourt, M. Alexandre, P. Degée, F. Monteverde, A. Rulmont, P. Dubois, (Plasticized) Polylactide/(Organo-)Clay Nanocomposites by in situ Intercalative Polymerization, Macromolecular Chemistry and Physics 206 (2005) 484–498. https://doi.org/10.1002/macp.200400324.

[57] L.-T. Lim, R. Auras, M. Rubino, Processing technologies for poly(lactic acid), Progress in Polymer Science 33 (2008) 820–852. https://doi.org/10.1016/j.progpolymsci.2008.05.004.

[58] D. Wu, L. Wu, L. Wu, B. Xu, Y. Zhang, M. Zhang, Nonisothermal cold crystallization behavior and kinetics of polylactide/clay nanocomposites, Journal of Polymer Science Part B: Polymer Physics 45 (2007) 1100–1113. https://doi.org/10.1002/polb.21154.

[59] S. Fernandes Nassar, A. Guinault, N. Delpouve, V. Divry, V. Ducruet, C. Sollogoub, S. Domenek, Multi-scale analysis of the impact of polylactide morphology on gas barrier properties, Polymer 108 (2017) 163–172. https://doi.org/10.1016/j.polymer.2016.11.047.

[60] N. Delpouve, A. Saiter, J.F. Mano, E. Dargent, Cooperative rearranging region size in semi-crystalline poly(l-lactic acid), Polymer 49 (2008) 3130–3135. https://doi.org/10.1016/j.polymer.2008.04.045.

[61] A. Guinault, C. Sollogoub, V. Ducruet, S. Domenek, Impact of crystallinity of poly(lactide) on helium and oxygen barrier properties, European Polymer Journal 48 (2012) 779–788. https://doi.org/10.1016/j.eurpolymj.2012.01.014.

[62] M. Cocca, M.L.D. Lorenzo, M. Malinconico, V. Frezza, Influence of crystal polymorphism on mechanical and barrier properties of poly(l-lactic acid), European Polymer Journal 47 (2011) 1073–1080. https://doi.org/10.1016/j.eurpolymj.2011.02.009.

[63] F. Morel, E. Espuche, V. Bounor-Legaré, O. Persynn, M. Lacroix, Impact of coated calcium carbonate nanofillers and annealing treatments on the microstructure and gas barrier properties of poly(lactide) based nanocomposite films, Journal of Polymer Science Part B: Polymer Physics 54 (2016) 649–658. https://doi.org/10.1002/polb.23957.

[64] B. Kalb, A.J. Pennings, General crystallization behaviour of poly(l-lactic acid), Polymer 21 (1980) 607–612. https://doi.org/10.1016/0032-3861(80)90315-8.

[65] J. Trifol, D. Plackett, C. Sillard, O. Hassager, A.E. Daugaard, J. Bras, P. Szabo, A comparison of partially acetylated nanocellulose, nanocrystalline cellulose, and nanoclay as fillers for high-performance polylactide nanocomposites, Journal of Applied Polymer Science 133 (2016) 43257. https://doi.org/10.1002/app.43257.

[66] P. Takkalkar, M.J. Tobin, J. Vongsvivut, T. Mukherjee, S. Nizamuddin, G. Griffin, N. Kao, Structural, thermal, rheological and optical properties of poly(lactic acid) films prepared through solvent casting and melt processing techniques, Journal of the Taiwan Institute of Chemical Engineers 104 (2019) 293–300. https://doi.org/10.1016/j.jtice.2019.08.018.

[67] J. Zhang, K. Tashiro, H. Tsuji, A.J. Domb, Disorder-to-Order Phase Transition and Multiple Melting Behavior of Poly(l-lactide) Investigated by Simultaneous Measurements of WAXD and DSC, Macromolecules 41 (2008) 1352–1357. https://doi.org/10.1021/ma0706071.

[68] B. Eling, S. Gogolewski, A.J. Pennings, Biodegradable materials of poly(l-lactic acid): 1. Melt-spun and solution-spun fibres, Polymer 23 (1982) 1587–1593. https://doi.org/10.1016/0032-3861(82)90176-8.

[69] L. Cartier, T. Okihara, Y. Ikada, H. Tsuji, J. Puiggali, B. Lotz, Epitaxial crystallization and crystalline polymorphism of polylactides, Polymer 41 (2000) 8909–8919. https://doi.org/10.1016/S0032-3861(00)00234-2.

[70] S. Saeidlou, M.A. Huneault, H. Li, C.B. Park, Poly(lactic acid) crystallization, Progress in Polymer Science 37 (2012) 1657–1677. https://doi.org/10.1016/j.progpolymsci.2012.07.005.

[71] M. Pluta, A. Galeski, Crystalline and supermolecular structure of polylactide in relation to the crystallization method, Journal of Applied Polymer Science 86 (2002) 1386–1395. https://doi.org/10.1002/app.11280.

[72] J. Menczel, B. Wunderlich, Phase transitions in mesophase macromolecules: The transitions of poly(*p*-acryloyloxybenzoic acid), Polymer 22 (1981) 778–782. https://doi.org/10.1016/0032-3861(81)90014-8.

[73] D. Heidrich, M. Gehde, The 3-Phase Structure of Polyesters (PBT, PET) after Isothermal and Non-Isothermal Crystallization, Polymers 14 (2022) 793. https://doi.org/10.3390/polym14040793.

[74] M.L. Di Lorenzo, M.C. Righetti, Crystallization-induced formation of rigid amorphous fraction, POLYMER CRYSTALLIZATION 1 (2018) e10023. https://doi.org/10.1002/pcr2.10023.

[75] N. Delpouve, A. Saiter, E. Dargent, RIGID AND MOBILE AMORPHOUS FRACTIONS IN TWO POLY(LACTIC ACID), 8th World Congress of Chemical Engineering, Montreal (2009).

[76] F.-D. Kopinke, M. Remmler, K. Mackenzie, M. Möder, O. Wachsen, Thermal decomposition of biodegradable polyesters—II. Poly(lactic acid), Polymer Degradation and Stability 53 (1996) 329–342. https://doi.org/10.1016/0141-3910(96)00102-4.

[77] K. Jamshidi, S.-H. Hyon, Y. Ikada, Thermal characterization of polylactides, Polymer 29 (1988) 2229–2234. https://doi.org/10.1016/0032-3861(88)90116-4.

[78] A. Sangroniz, A. Chaos, M. Iriarte, J. del Río, J.-R. Sarasua, A. Etxeberria, Influence of the Rigid Amorphous Fraction and Crystallinity on Polylactide Transport Properties, Macromolecules 51 (2018) 3923–3931. https://doi.org/10.1021/acs.macromol.8b00833.

[79] J. Sepulveda, C. Villegas, A. Torres, E. Vargas, F. Rodriguez, S. Baltazar, A. Prada, A. Rojas, J. Romero, S. Faba, M.J. Galotto, Effect of functionalized silica nanoparticles on the mass transfer process in active PLA nanocomposite films obtained by supercritical impregnation for sustainable food packaging, The Journal of Supercritical Fluids 161 (2020) 104844. https://doi.org/10.1016/j.supflu.2020.104844.

[80] E. Picard, E. Espuche, R. Fulchiron, Effect of an organo-modified montmorillonite on PLA crystallization and gas barrier properties, Applied Clay Science 53 (2011) 58–65. https://doi.org/10.1016/j.clay.2011.04.023.

[81] F. Li, C. Zhang, Y. Weng, X. Diao, Y. Zhou, X. Song, Enhancement of Gas Barrier Properties of Graphene Oxide/Poly (Lactic Acid) Films Using a Solvent-free Method, Materials 13 (2020) 3024. https://doi.org/10.3390/ma13133024.

[82] E. Espino-Pérez, J. Bras, G. Almeida, C. Plessis, N. Belgacem, P. Perré, S. Domenek, Designed cellulose nanocrystal surface properties for improving barrier properties in polylactide nanocomposites, Carbohydrate Polymers 183 (2018) 267–277. https://doi.org/10.1016/j.carbpol.2017.12.005.

[83] E. Espino-Pérez, J. Bras, V. Ducruet, A. Guinault, A. Dufresne, S. Domenek, Influence of chemical surface modification of cellulose nanowhiskers on thermal, mechanical, and barrier properties of poly(lactide) based bionanocomposites, European Polymer Journal 49 (2013) 3144–3154. https://doi.org/10.1016/j.eurpolymj.2013.07.017.

[84] R. Kumar, S. Kumari, B. Rai, R. Das, G. Kumar, Effect of nano-cellulosic fiber on mechanical and barrier properties of polylactic acid (PLA) green nanocomposite film, Mater. Res. Express 6 (2019) 125108. https://doi.org/10.1088/2053-1591/ab5755.

[85] G.L. Re, S. Benali, Y. Habibi, J.-M. Raquez, P. Dubois, Stereocomplexed PLA nanocomposites: From in situ polymerization to materials properties, European Polymer Journal 54 (2014) 138–150. https://doi.org/10.1016/j.eurpolymj.2014.03.004.

[86] S. Bourbigot, G. Fontaine, A. Gallos, S. Bellayer, Reactive extrusion of PLA and of PLA/carbon nanotubes nanocomposite: processing, characterization and flame retardancy, Polymers for Advanced Technologies 22 (2011) 30–37. https://doi.org/10.1002/pat.1715.

[87] M.A. Ortenzi, L. Basilissi, H. Farina, G. Di Silvestro, L. Piergiovanni, E. Mascheroni, Evaluation of crystallinity and gas barrier properties of films obtained from PLA nanocomposites synthesized via “in situ” polymerization of l-lactide with silane-modified nanosilica and montmorillonite, European Polymer Journal 66 (2015) 478–491. https://doi.org/10.1016/j.eurpolymj.2015.03.006.

[88] A. Mohsen, N. Ali, Mechanical, Color and Barrier, Properties of Biodegradable Nanocomposites Polylactic Acid/Nanoclay, Journal of Bioremediation & Biodegradation 09 (2018) 1000455. https://doi.org/10.4172/2155-6199.1000455.

[89] H. Chi, J. Xue, C. Zhang, H. Chen, L. Li, Y. Qin, High Pressure Treatment for Improving Water Vapour Barrier Properties of Poly(lactic acid)/Ag Nanocomposite Films, Polymers 10 (2018) 1009-1011. https://doi.org/10.3390/polym10091011.

[90] C. Fan, H. Chi, C. Zhang, R. Cui, W. Lu, M. Yuan, Y. Qin, Effect of multiscale structure on the gas barrier properties of poly(lactic acid)/Ag nanocomposite films, Polymers for Advanced Technologies 30 (2019) 1709–1715. https://doi.org/10.1002/pat.4601.

[91] E. Jasinski, V. Bounor-Legaré, A. Taguet, E. Beyou, Influence of halloysite nanotubes onto the fire properties of polymer based composites: A review, Polymer Degradation and Stability 183 (2021) 109407. https://doi.org/10.1016/j.polymdegradstab.2020.109407.

[92] B.N. Jung, H.W. Jung, D.H. Kang, G.H. Kim, M. Lee, J.K. Shim, S.W. Hwang, The fabrication of flexible and oxygen barrier cellulose nanofiber/polylactic acid nanocomposites using cosolvent system, Journal of Applied Polymer Science 137 (2020) 49536. https://doi.org/10.1002/app.49536.

[93] W.L. Tham, B.T. Poh, Z.A. Mohd Ishak, W.S. Chow, Transparent poly(lactic acid)/halloysite nanotube nanocomposites with improved oxygen barrier and antioxidant properties, J Therm Anal Calorim 126 (2016) 1331–1337. https://doi.org/10.1007/s10973-016-5834-7.

[94] S.H. Othman, H.N. Ling, R.A. Talib, M.N. Naim, N.P. Risyon, Md. Saifullah, PLA/MMT and PLA/Halloysite Bio-Nanocomposite Films: Mechanical, Barrier, and Transparency, JNanoR 59 (2019) 77–93. https://doi.org/10.4028/www.scientific.net/JNanoR.59.77.

[95] S.S. Karkhanis, N.M. Stark, R.C. Sabo, L.M. Matuana, Water vapor and oxygen barrier properties of extrusion-blown poly(lactic acid)/cellulose nanocrystals nanocomposite films, Composites Part A: Applied Science and Manufacturing 114 (2018) 204–211. https://doi.org/10.1016/j.compositesa.2018.08.025.

[96] S.H. Sung, Y. Chang, J. Han, Development of polylactic acid nanocomposite films reinforced with cellulose nanocrystals derived from coffee silverskin, Carbohydrate Polymers 169 (2017) 495–503. https://doi.org/10.1016/j.carbpol.2017.04.037.

[97] E. Fortunati, M. Peltzer, I. Armentano, L. Torre, A. Jiménez, J.M. Kenny, Effects of modified cellulose nanocrystals on the barrier and migration properties of PLA nano-biocomposites, Carbohydrate Polymers 90 (2012) 948–956. https://doi.org/10.1016/j.carbpol.2012.06.025.

[98] M.D. Sanchez-Garcia, J.M. Lagaron, On the use of plant cellulose nanowhiskers to enhance the barrier properties of polylactic acid, Cellulose 17 (2010) 987–1004. https://doi.org/10.1007/s10570-010-9430-x.

[99] Y. Cui, S. Kumar, B.R. Kona, D. van Houcke, Gas barrier properties of polymer/clay nanocomposites, RSC Advances 5 (2015) 63669–63690. https://doi.org/10.1039/C5RA10333A.

[100] K. Yoon, H. Sung, Y. Hwang, S. Kyun Noh, D. Lee, Modification of montmorillonite with oligomeric amine derivatives for polymer nanocomposite preparation, Applied Clay Science 38 (2007) 1–8. https://doi.org/10.1016/j.clay.2007.01.003.

[101] H.-D. Huang, P.-G. Ren, J.-Z. Xu, L. Xu, G.-J. Zhong, B.S. Hsiao, Z.-M. Li, Improved barrier properties of poly(lactic acid) with randomly dispersed graphene oxide nanosheets, Journal of Membrane Science 464 (2014) 110–118. https://doi.org/10.1016/j.memsci.2014.04.009.

[102] J.-W. Rhim, S.-I. Hong, C.-S. Ha, Tensile, water vapor barrier and antimicrobial properties of PLA/nanoclay composite films, LWT - Food Science and Technology 42 (2009) 612–617. https://doi.org/10.1016/j.lwt.2008.02.015.

[103] H.C. Koh, J.S. Park, M.A. Jeong, H.Y. Hwang, Y.T. Hong, S.Y. Ha, S.Y. Nam, Preparation and gas permeation properties of biodegradable polymer/layered silicate nanocomposite membranes, Desalination 233 (2008) 201–209. https://doi.org/10.1016/j.desal.2007.09.043.

[104] J.-H. Chang, Y.U. An, G.S. Sur, Poly(lactic acid) nanocomposites with various organoclays. I. Thermomechanical properties, morphology, and gas permeability, Journal of Polymer Science Part B: Polymer Physics 41 (2003) 94–103. https://doi.org/10.1002/polb.10349.

[105] C. Thellen, C. Orroth, D. Froio, D. Ziegler, J. Lucciarini, R. Farrell, N.A. D'Souza, J.A. Ratto, Influence of montmorillonite layered silicate on plasticized poly(l-lactide) blown films, Polymer 46 (2005) 11716–11727. https://doi.org/10.1016/j.polymer.2005.09.057.

[106] N. Tenn, N. Follain, J. Soulestin, R. Crétois, S. Bourbigot, S. Marais, Effect of Nanoclay Hydration on Barrier Properties of PLA/Montmorillonite Based Nanocomposites, J. Phys. Chem. C 117 (2013) 12117–12135. https://doi.org/10.1021/jp401546t.

[107] L. Di Maio, P. Scarfato, M.R. Milana, R. Feliciani, M. Denaro, G. Padula, L. Incarnato, Bionanocomposite Polylactic Acid/Organoclay Films: Functional Properties and Measurement of Total and Lactic Acid Specific Migration, Packaging Technology and Science 27 (2014) 535–547. https://doi.org/10.1002/pts.2054.

[108] S. Sinha Ray, K. Yamada, M. Okamoto, Y. Fujimoto, A. Ogami, K. Ueda, New polylactide/layered silicate nanocomposites. 5. Designing of materials with desired properties, Polymer 44 (2003) 6633–6646. https://doi.org/10.1016/j.polymer.2003.08.021.

[109] S. Sinha Ray, K. Yamada, M. Okamoto, K. Ueda, Polylactide-Layered Silicate Nanocomposite: A Novel Biodegradable Material, Nano Lett. 2 (2002) 1093–1096. https://doi.org/10.1021/nl0202152.

[110] S. Sinha Ray, K. Yamada, M. Okamoto, K. Ueda, New polylactide-layered silicate nanocomposites. 2. Concurrent improvements of material properties, biodegradability and melt rheology, Polymer 44 (2003) 857–866. https://doi.org/10.1016/S0032-3861(02)00818-2.

[111] W. Zheng, M. Beeler, J. Claus, X. Xu, Poly(lactic acid)/montmorillonite blown films: Crystallization, mechanics, and permeation, Journal of Applied Polymer Science 134 (2017) 45260. https://doi.org/10.1002/app.45260.

[112] S. Singh, R.K. Gupta, A.K. Ghosh, S.N. Maiti, S.N. Bhattacharya, Poly (L-lactic acid)/layered Silicate Nanocomposite Blown Film for Packaging Application: Thermal, Mechanical and Barrier Properties, Journal of Polymer Engineering 30 (2010) 361–376. https://doi.org/10.1515/POLYENG.2010.30.5-7.361.

[113] R.N. Darie, E. Pâslaru, A. Sdrobis, G.M. Pricope, G.E. Hitruc, A. Poiată, A. Baklavaridis, C. Vasile, Effect of Nanoclay Hydrophilicity on the Poly(lactic acid)/Clay Nanocomposites Properties, Ind. Eng. Chem. Res. 53 (2014) 7877–7890. https://doi.org/10.1021/ie500577m.

[114] M. Żenkiewicz, J. Richert, A. Różański, Effect of blow moulding ratio on barrier properties of polylactide nanocomposite films, Polymer Testing 29 (2010) 251–257. https://doi.org/10.1016/j.polymertesting.2009.11.008.

[115] B. Şengül, R.M.A. El-abassy, A. Materny, N. Dilsiz, Poly(lactic acid)/Organo-Montmorillonite Nanocomposites: Synthesis, Structures, Permeation Properties and Applications, Polym. Sci. Ser. A 59 (2017) 891–901. https://doi.org/10.1134/S0965545X17060098.

[116] S.R. Chowdhury, Some important aspects in designing high molecular weight poly(L-lactic acid)–clay nanocomposites with desired properties, Polymer International 57 (2008) 1326–1332. https://doi.org/10.1002/pi.2464.

[117] F. Li, C. Zhang, Y. Weng, Improvement of the Gas Barrier Properties of PLA/OMMT Films by Regulating the Interlayer Spacing of OMMT and the Crystallinity of PLA, ACS Omega 5 (2020) 18675–18684. https://doi.org/10.1021/acsomega.0c01405.

[118] Z.D. Demirkaya, B. Sengul, M.S. Eroglu, N. Dilsiz, Comprehensive characterization of polylactide-layered double hydroxides nanocomposites as packaging materials, J Polym Res 22 (2015) 124. https://doi.org/10.1007/s10965-015-0759-6.

[119] S. Sinha Ray, K. Yamada, M. Okamoto, A. Ogami, K. Ueda, New Polylactide/Layered Silicate Nanocomposites. 3. High-Performance Biodegradable Materials, Chem. Mater. 15 (2003) 1456–1465. https://doi.org/10.1021/cm020953r.

[120] J.M. Lagaron, L. Cabedo, D. Cava, J.L. Feijoo, R. Gavara, E. Gimenez, Improving packaged food quality and safety. Part 2: Nanocomposites, Food Additives & Contaminants 22 (2005) 994–998. https://doi.org/10.1080/02652030500239656.

[121] L. Cabedo, J. Luis Feijoo, M. Pilar Villanueva, J.M. Lagarón, E. Giménez, Optimization of Biodegradable Nanocomposites Based on aPLA/PCL Blends for Food Packaging Applications, Macromolecular Symposia 233 (2006) 191–197. https://doi.org/10.1002/masy.200690017.

[122] A.M. Pinto, J. Cabral, D.A.P. Tanaka, A.M. Mendes, F.D. Magalhães, Effect of incorporation of graphene oxide and graphene nanoplatelets on mechanical and gas permeability properties of poly(lactic acid) films, Polymer International 62 (2013) 33–40. https://doi.org/10.1002/pi.4290.

[123] F. D'Acierno, C.A. Michal, M.J. MacLachlan, Thermal Stability of Cellulose Nanomaterials, Chem. Rev. 123 (2023) 7295–7325. https://doi.org/10.1021/acs.chemrev.2c00816.

Chapitre II

Matériel et méthodes

1. Matériel ____ *80*

1.1. La matrice PLA ____ 80

1.2. Les charges ____ 80

1.3. Plateforme des systèmes PLA élaborés ____ 82

2. Caractérisations ____ *83*

Ce chapitre est consacré à la présentation de la matrice PLA et des charges utilisées dans ce travail de thèse ainsi qu'à la présentation succincte des systèmes étudiés dans les différents chapitres expérimentaux.

1. Matériel

1.1. La matrice PLA

Les matériaux étudiés dans les chapitre III et chapitre IV sont tous composés d'une matrice d'acide polylactique (PLA) qui est soit fournie par NatureWorks® (Ingeo™ Bioploymer 2003D) soit obtenue par polymérisation du lactide menée au cours de la thèse, dont les caractéristiques seront données en relation avec les conditions de polymérisation utilisées dans les parties relevant de l'utilisation de ce PLA. Les principales caractéristiques du grade commercial Ingeo Bioploymer 2003D sont reportées dans le **Tableau 1**.

Tableau 1- Principales caractéristiques du PLA Ingeo™ Biopolymer 2003D [1]

Propriétés	***Ingeo Bipolymer™ 2003D***
Isomère D	4 %mol
Densité	1.25
Indice de fluidité	6 g/10 min (210 °C ; 2,16 kg)
Module d'Young	500 GPa
Température de fléchissement sous charge	55 °C

1.2. Les charges

Dans cette thèse différentes nanocharges ont été sélectionnées, de natures et de formes différentes. Elles sont présentées dans le **Tableau 2** avec leurs principales caractéristiques.

Tableau 2 - Caractéristiques des charges utilisées (*d* : diamètre moyen, *L* : longueur moyenne, *w* : épaisseur moyenne de la charge unitaire, *CEC* : capacité d'échange cationique)

	Nomenclature	**Nom commercial/ fournisseur**	**Dimensions /forme**	**Modification de surface**	**Densité**
Silice hydrophile	SiOH	Aerosil® 200 / Evonick Operations GmbH	*d* = 20 ± 5 nm **Sphère**	/	2,2 [2]
Silice hydrophobe	$SiCH_3$	Aerosil® AR974 / Evonick Operations GmbH	*d* =20 ± 5 nm **Sphère**	Diméthyl dichlorosilane (0.7-1.3 %mass carbone)	2,2 [2]
Montmorillonite modifiée	OMMT	Cloisite® 30B /Southern Clay Product	*L* = 200 nm *w* = 1-2 nm **Plaquette**	Méthyl tallow bis-2-hydroxyéthyl, ammonium quaternaire (29 %mass) CEC = 90 meq/100 g	1,98 [3]
Halloysite	HNT	Nanotubes d'halloysite/ Sigma-Aldrich	*L* = 300 -1000 nm *d* ~40 nm **Tube**	/	2,53 [4]
Nanoparticules d'argent	Ag	Nanopoudre d'argent métallique (99.9 % metal basis) / American Element	*d* = 35± 5 nm **Sphère**	/	10,5 [5]
Oxyde de graphène	GNP	KNG-180-3 Nanoplaquettes d'oxyde graphène Knano (Xianen, China)	*L* = 500 - 1000 nm *w* ~1 nm **Plaquette**	/	2,2 [6]

1.3. Plateforme des systèmes PLA élaborés

Une large plateforme de matériaux à base de PLA a été préparée lors de cette thèse. Elle permet d'avoir une approche incrémentale de la complexité des matériaux étudiés et viendra compléter les données de la littérature.

Dans un premier temps, des matériaux ont été préparés avec une seule phase imperméable, qui peut être soit une charge imperméable, soit la phase cristalline du PLA. Concernant l'introduction de charges, deux procédés ont été utilisés : le mélange par voie fondue et la polymérisation *in situ* avec le but de conserver le PLA amorphe. Les nanocomposites amorphes préparés par voie fondue avec une large gamme de charges à l'aide d'un mélangeur interne sont dénommés PLA/charge/X avec X la fraction volumique de charges. Les nanocomposites amorphes obtenus par polymérisation *in situ* sont désignés par PLAis/$SiCH_3$/X pour les échantillons contenant de la silice hydrophobe et PLAis_OMMT pour la montmorillonite. L'échantillon PLAis_OMMT, contenant 15 %vol de OMMT, a été redispersé dans du PLA commercial par voie fondue, pour des raisons qui seront explicitées dans le chapitre III.B, et les matériaux ainsi obtenus sont nommés PLA/PLAis_OMMT/X avec X la fraction volumique finale de montmorillonite. Par ailleurs, pour ces deux procédés, des PLA non chargés ont été préparés dans les mêmes conditions et sont dénommés PLAref pour le PLA préparé en voie fondue et PLAis pour le PLA obtenu par polymérisation. La phase cristalline du PLA a, quant à elle, été obtenue par traitement thermique de films de PLA amorphe à l'état vitreux et les échantillons sont nommés PLA/T_a/X avec T_a la température de recuit et X le taux de cristallinité. La préparation de l'ensemble de ces échantillons sera détaillée dans les différentes parties du chapitre III.

Dans un second temps, l'étude s'est portée sur l'effet de la présence de deux phases imperméables au sein de la matrice PLA. Pour cela des nanocomposites semi-cristallins contenant une charge ont été préparés soit par mélange en voie solvant (PLA_SR/charges/X) soit par mélange voie fondue suivi d'un traitement thermique (PLA_MBA/charges/X). Des PLA semi-cristallins non chargés ont également été préparés avec ces deux procédés selon les mêmes conditions : PLA_SR et PLA_MBA. De plus, des nanocomposites amorphes constitués de deux charges différentes ont également été élaborés par mélange en voie fondue. Pour ces études, des montmorillonites ont été mélangées avec d'une part de la silice (PLA/$SiCH_3$_X/OMMT_Y) et d'autre part avec de l'oxyde de graphène (PLA/GNP_X/OMMT_Y)

avec X la fraction volumique de silice (ou de graphène) et Y la fraction volumique de montmorillonite. La préparation de l'ensemble ces matériaux est décrit dans les différentes parties du chapitre IV.

Le **Tableau 3** regroupe l'ensemble des séries de matériaux de références et de nanocomposites préparés et étudiés expérimentalement.

2. Caractérisations

Les méthodes et protocoles de caractérisation sont détaillés dans les sections « matériel et méthodes » de chaque partie. Afin de donner une vue d'ensemble des caractérisations menées, nous précisons ici que :

- Les caractérisations physico-chimiques ont été réalisées par chromatographie d'exclusion stérique (SEC), par résonance magnétique nucléaire du proton (RMN ^{1}H) et par spectroscopie infrarouge à transformée de fourrier (FTIR).
- Les caractérisations thermiques ont été réalisées par analyse thermogravimétrique (ATG) et par calorimétrie différentielle à balayage (DSC).
- Les morphologiques ont été observées par microcopie électronique en transmission (MET) et en balayage (MEB). Elles ont également analysé par diffusion des rayons X aux petits angles (SAXS) et aux grands angles (WAXS).
- Les propriétés barrière ont été évaluées par mesure de perméabilité à la vapeur d'eau (90 %HR, 23 °C) et au dioxygène (0 %HR, 23 °C).

Tableau 3 - Nomenclature des échantillons utilisés dans le manuscrit.

Nomenclature	Procédé	Phase imperméable 1 (X %vol)	Phase imperméable 2 (Y %vol)	Chapitre
PLAref	Mélange par voie fondue	/	/	Chap. III
PLA/110°C/X	PLAref recuit à 110 °C	Phase cristalline (0 – 50 %vol)	/	Chap. III. A
PLA/120°C/X	PLAref recuit à 120 °C			
PLA/SiOH/X	Mélange par voie fondue	Silice hydrophile (1 – 4 %vol)	/	Chap. III. A et III. B
PLA/$SiCH_3$/X		Silice hydrophobe (1 – 10 %vol)		
PLA/Ag/X		Argent (0,5 – 4 %vol)		
PLA/HNT/X		Halloysite (0,5 – 10 %vol)		
PLA/OMMT/X		Montmorillonite modifiée (2,5 - 15% vol)		
PLA/GNP/X		Oxyde de graphène (0,05 - 1,5% vol)		
PLAis	Polymérisation *in situ*	/	/	Chap. III. B
PLAis/$SiCH_3$/X		Silice hydrophobe (5 – 7 %vol)	/	
PLAis_OMMT		Montmorillonite modifiée (≈ 15 %vol)		
PLA/PLAis_OMMT/X	Polymérisation *in situ* + mélange par voie fondue	Montmorillonite modifiée (1,5 -7 %vol)		

PLA_SR	Mélange par voie solvant	/	Phase cristalline (35 %vol)	Chap. IV. A
PLA_SR/SiOH/X		Silice hydrophile (2 - 5% vol)		
PLA_SR/$SiCH_3$/X		Silice hydrophobe (1,5 – 5,5 %vol)		
PLA_SR /HNT/X		Halloysite (1,5 – 11 %vol)		
PLA_SR /OMMT/X		Montmorillonite modifiée (1,5 – 10 %vol)		
PLA_SR /GNP/X		Oxyde de graphène (0,05 - 1,5% vol)		
PLA_MBA	Mélange par voie fondue suivi d'un recuit à 120 °C	/	Phase cristalline (50 %vol)	Chap. IV. A
PLA_MBA/SiOH/X		Silice hydrophile (1 – 4 %vol)		
PLA_MBA/$SiCH_3$/X		Silice hydrophobe (1 – 10 %vol)		
PLA_MBA/HNT/X		Halloysite (0,5 – 10 %vol)		
PLA_MBA/OMMT/X		Montmorillonite (2,5 – 10 %vol)		
PLA_MBA /GNP/X		Oxyde de graphène (0,05 - 1,5% vol)		
PLA/$SiCH_3$_X/OMMT_Y	Mélange par voie fondue	Silice hydrophobe (2 – 7 % vol)	Montmorillonite modifiée (4 -10 %vol)	Chap. IV. B
PLA/GNP_X/OMMT_Y		Oxyde de graphène (0,1 – 0,5 %vol)		Chap. IV. B

[1] Donnée fabricant, Natureworks.
https://www.natureworksllc.com/~/media/technical_resources/technical_data_sheets/technicaldatasheet_2003d_ffp-fsw_pdf.pdf

[2] Safety data sheet Aerosil®200, Evonik (2019).
https://www.freemansupply.com/MSDS/Combined/Fillers/Aerosil200.pdf

[3] N. Tenn, N. Follain, J. Soulestin, R. Crétois, S. Bourbigot, S. Marais, Effect of Nanoclay Hydration on Barrier Properties of PLA/Montmorillonite Based Nanocomposites, J. Phys. Chem. C 117 (2013) 12117–12135. https://doi.org/10.1021/jp401546t.

[4] Données fabricant, Sigma Aldrich.
https://www.sigmaaldrich.com/FR/fr/product/aldrich/685445?srsltid=AfmBOorv9MaIdomGyD-J0X2EMwB_4lyNXqgYzEvjKkOZpubT9Y5Je-rr

[5] Données fabricant, American element.
https://www.americanelements.com/silver-nanoparticles-7440-22-4

[6] Données fabricant, Nanoshel LCC.
https://pdf.indiamart.com/impdf/8456503491/SELLER-1385392/graphene-nano-powder.pdf

Chapitre III

Design de matériaux à matrice PLA contenant une phase imperméable

Chapitre III - Design de matériaux à matrice PLA contenant une phase imperméable

Introduction _____ **89**

Chapitre III.A : Influence of different type of impermeable phase on the permeability of PLA films : nanofillers versus crystalline phase _____ **91**

Chapitre III.B : PLA nanocomposites based on silica and organo-modified montmorillonite : a comparative investigation of different solvent-free synthesis routes on morphology and water permeability _____ **137**

Chapitre III.C : Data Driven modelling as a new route to design PLA based materials with high barrier properties _____ **173**

Conclusion _____ **197**

Supplementary information _____ **199**

Introduction

L'objectif de ce chapitre est de comprendre et d'établir des relations microstructure/ perméabilité dans le cas de matrice PLA contentant une seule phase imperméable afin d'identifier les paramètres les plus pertinents. Pour cela, une plateforme de matériaux PLA a été préparée en jouant sur différents paramètres.

Tout d'abord, différents types de phases imperméables ont été introduites dans la matrice PLA avec d'une part la phase cristalline du PLA et d'autre part des charges considérées comme imperméables. Concernant ces dernières, une large gamme de formes, de facteurs de forme et de natures chimiques a été utilisée. Puis dans un second temps, deux procédés permettant d'élaborer des nanocomposites amorphes (mélange par voie fondue et polymérisation *in situ*) ont été mis au point et utilisés avec une charge sphérique et une charge lamellaire. Les perméabilités des matériaux ainsi obtenus ont été comparées et mises en relation avec la microstructure de la matrice et l'état de dispersions des charges. Les résultats expérimentaux obtenus ont été comparés à des modèles empiriques présentés dans le chapitre bibliographique, permettant de décrire la perméabilité à partir de paramètres microstructuraux.

L'ensemble des données issues de la caractérisation fine de la plateforme de matériaux que nous avons élaborés ajoutées aux données issues de l'analyse de la littérature présentée dans le chapitre bibliographique a permis de constituer une base de données de 69 échantillons sur laquelle nous nous sommes focalisés pour prédire la perméabilité par des approches de machine learning. Après l'entrainement et la validation de deux modèles, il a été possible de cibler des compositions de matériaux pour des niveaux de perméabilité choisis.

Il est à noter que les annexes des différentes parties sont regroupées en fin de chapitre.

La première partie de ce chapitre présente l'effet de l'ajout d'une phase imperméable, en considérant différentes natures, sur la perméabilité. Les matériaux étudiés sont soit des PLA semi-cristallins obtenus par traitement thermique (cristallisation froide) soit des nanocomposites amorphes élaborés par mélange en voie fondue. Cette étude se présente sous la forme d'un article qui a été soumis au Journal *Polymer Testing* en octobre 2024.

Chapitre III.A - Influence of different type of impermeable phase on the permeability of PLA films: nanofillers versus crystalline phase

1. Abstract ***92***

2. Introduction ***92***

3. Experimental ***94***

3.1. Material **94**

3.2. PLA neat films and nanocomposites preparation **95**

3.3. Characterization methods **96**

3.3. a) Size exclusion chromatography (SEC) 96

3.3. b) Thermal analysis 97

3.3. c) PLA microstructure analysis 98

3.3. d) Nanofillers dispersion analysis 98

3.3. e) Permeability measurements 99

4. Results and discussion ***100***

4.1. Morphological characterization of the reference and nanocomposite films series **100**

4.1. a) Reference amorphous PLA films 100

4.1. b) Nanocomposite films 101

4.1. c) Semi-crystalline PLA films 113

4.2. Gas and water vapor permeability of amorphous nanocomposites and semi-crystalline PLA films **119**

5. Conclusion ***128***

6. References ***130***

1. Abstract

Different amorphous PLA-based nanocomposites series allowing to vary the nanofiller shape from spherical (hydrophobic/hydrophilic silica, silver), to tubular (halloysites) and lamellar (montmorillonite, graphene) have been prepared for filler content up to 15 vol%. In parallel, a semi-crystalline PLA films series has been prepared by annealing amorphous PLA films from the glassy state with the aim to achieve different degree of crystallinity. The mobility of the polymer chains and the impermeable domains (either filler domains or crystalline phase) contained in each membrane have been characterized in detail. Membranes water vapor and oxygen permeability coefficients have been determined with the aim to evidence the governing factors for barrier properties. For nanocomposite membranes, the matrix microstructure and chains mobility were not significantly affected by the addition of fillers, so the barrier properties were mainly governed by the filler domains size and dispersion. For semi- crystalline membranes, the increase in crystallinity led to a decrease of the amorphous chains mobility (*MAF*) which was found to also influence the permeability. Theorical models were used to describe the evolution of the experimental relative permeability and an equivalence diagram was proposed to have a direct comparison of the effect of fillers and crystallinity on the permeability.

2. Introduction

Polymers are attractive materials because of their low cost, ease of processing and low density. However, the significant environmental footprint of petroleum-based polymers, and particularly the large amount of waste produced by packaging, has led to a growing interest in biodegradable polymers. Poly(lactic acid) (PLA) combines the advantages of being both bio-sourced and biodegradable and is therefore a promising alternative to replace petroleum-based polymers for short-term applications such as packaging. Although PLA accounts for 60% of the total quantity of biodegradable polymers produced for packaging in 2023 [1], one of the obstacles to greater market penetration is its low gas and water barrier properties [2], [3], [4]. Faced with this challenge, lot of studies focused on barrier improvement by adding an

impermeable dispersed phase within the permeable continuous polymer phase with the aim to lengthen the diffusion path and decrease the permeable phase content.

In this context, PLA nanocomposites containing impermeable nanofillers have been developed in the last decades. If the efficiency of lamellar type nanofillers as a mean to bring a significant tortuosity effect has been shown by several authors [5], [6], [7], [8], [9] it has to be noticed that only few works focused on the use of spherical or nanotube-type fillers [10], [11], [12], [13]. The performances of the nanocomposite materials are usually discussed as a function of the introduced fillers (aspect ratio, volume fraction, dispersion state), the polymer chain mobility and the filler/matrix interface [10], [14], [15], [16], [17], [18]. It is noteworthy that the comparison between barrier properties obtained from different fillers is rarely performed and it is often limited to two or three filler types, such as montmorillonite versus nanocellulose nanocrystals and nanofibers [19], [20] or montmorillonite versus halloysite nanotubes [21].

Another way of inducing the presence of an impermeable phase within a polymer matrix is to anneal the polymer in order to create a crystalline phase. Due to its significantly higher density than the amorphous phase, the crystalline phase is usually considered as an impermeable phase [10], [22], [23], [24], [25]. Moreover, modification of the chain mobility at the crystalline/amorphous region can also occur and be estimated through the mobile amorphous fraction (*MAF*) with respect to the rigid amorphous fraction (*RAF*) [26], [27]. Although some studies focused on the effect of the crystalline phase on PLA permeability [24], [25], [26], [27] showing a global increase of barrier properties with the increase of the crystallinity, no detailed relations were established neither with the crystalline morphology nor with the *MAF*/*RAF* contents.

The aim of the present work is to prepare and finely characterize a PLA-based material platform in which each material series contains a specific type of dispersed impermeable phase. For that goal, different amorphous PLA-based nanocomposite series containing either lamellar (montmorillonite, graphene), spherical (hydrophobic/hydrophilic silica, silver) or halloysite nanotubes were prepared by melt-blending for filler content up to 15 vol%. Semi-crystalline PLA samples with increasing degree of crystallinity have also been prepared by annealing reference amorphous PLA films. Morphology as well as PLA chain mobility are deeply investigated for each materials series. Oxygen and water vapor permeability

coefficients of the different samples are determined and discussed as a function of the material structural parameters. From this experimental analysis, the governing factors of the transport are identified for each materials series and allow to choose for each PLA-based materials series, the appropriate physical models enabling to predict accurately the permeability data. Finally, a permeability diagram allowing to easily establish equivalence laws between the different investigated impermeable phases is proposed. According to our knowledge, it is the first time that such a large material platform is prepared and investigated, going from experimental to modeling approach, with the aim to compare the effects of different types of impermeable phases on PLA barrier properties.

3. Experimental

3.1. Material

Poly(lactide acid) PLA 2003D, containing 4.1 mol% of D-isomers and with a density of 1.25, was provided by NatureWorks LLC. The average molar mass, M_n, was determined by size exclusion chromatography and is equal to 86,000 g/mol. Different impermeable nanofillers were selected in order to cover a wide range of filler shapes going from spheres to tubes and platelets (**Figure A.1**). Their main characteristics are summarized in **Table A.1.**

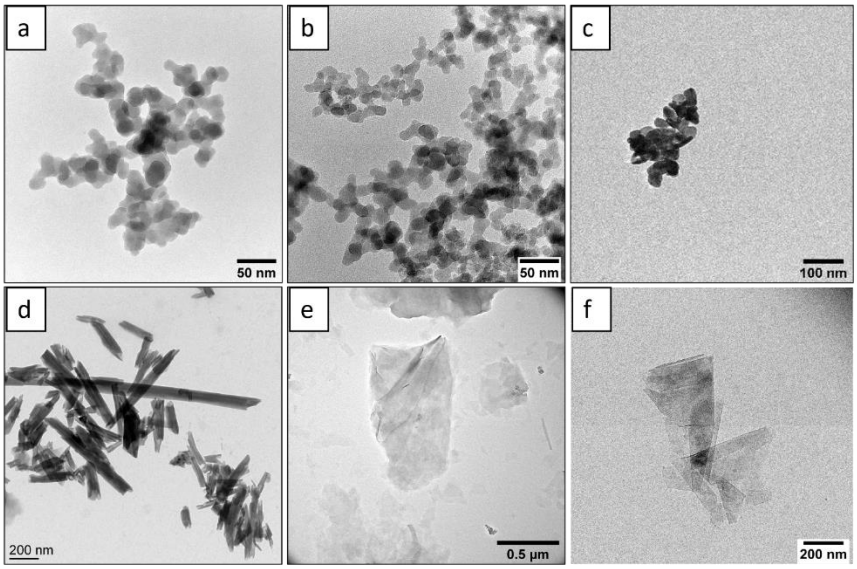


Figure A.1 - TEM micrographs of the selected fillers: a) hydrophilic silica, b) hydrophobic silica; c) silver, d) halloysite nanotubes, e) organo-modified montmorillonite and f) graphene oxide.

Table A.1 - Characteristics of the selected fillers (*d* stands for the mean diameter, *L* for the mean length and *w for* the mean thickness of the elementary fillers, *CEC* for the cationic exchange capacity).

Nanofiller type	Nomenclature	Commercial name / supplier	Dimensions /shape	Surface modification	Density
Hydrophilic silica	SiOH	Aerosil® 200 / Evonick Operations GmbH	*d* = 20 ± 5 nm **Sphere**	/	2.2
Hydrophobic silica	$SiCH_3$	Aerosil® AR974 / Evonick Operations GmbH	*d* = 20 ± 5 nm **Sphere**	Dimethyl dichlorosilane (0.7-1.3 wt% carbon)	2.2
Organo modified montmorillonite	OMMT	Cloisite®30B /Southern Clay Product	*L* = 200 nm *w* = 1-2 nm **Platelet**	Methyl tallow bis-2-hydroxyethyl, quaternary ammonium (29 wt%) CEC = 90 meq/100 g	1.98
Halloysite nanotubes	HNT	Halloysite nanotubes/ Sigma-Aldrich	*L* = 300 - 1000 nm *d* ≈ 40 nm **Tubes**	/	2.53
Silver nanoparticles	Ag	Silver Metal Nanopowder (99.9 % metal basis) / American Element	*d* = 35 ± 5 nm **Sphere**	/	10.5
Graphene oxide	GNP	KNG-180-3 Graphene oxide nanoplatelets Knano (Xianen, China)	*L* = 500 - 1000 nm *w* ≈ 1 nm **Platelet**	/	2.2

3.2. PLA neat films and nanocomposites preparation

PLA nanocomposites were prepared by melt-blending using a Haake internal mixer. Compounding was carried out at a set-point temperature of 185 °C and a rotation speed of 50 rpm. The residence time was fixed at 10 min. The nanofillers content ranged from 0 to 15 vol%. Unfilled PLA was melt-processed in the same conditions to prepare a reference material. Then 130 ± 10 µm films were prepared from each compound by compression molding at 180 °C under 150 bars for 2 min, with 4 min of preheating. To obtain amorphous films, samples were placed between two metal plates at room temperature after thermo-compression and cooled under compressed air for few minutes. As PLA is very sensitive to

hydrolysis during melt processing, all materials (PLA granular, nanofillers as well as the compounds) were dried at least 24 h in a vacuum oven at 85 °C before each processing step (melt compounding and compression molding).

Semi-crystalline PLA films with different degrees of crystallinity were prepared from PLA amorphous films by annealing in an oven at T_a = 110 °C or 120 °C under atmospheric pressure for durations varying between 0 and 24 h.

In this work, reference amorphous PLA film is denoted PLAref, nanocomposites films are referred as PLA/filler type/X where X is the volume content of the filler and semi-crystalline PLA films are named PLA/Ta/χ_c where T_a is the annealing temperature and χ_c is the degree of crystallinity. **Table A.2** summarizes the different films series investigated in this work.

Table A.2 - Name of the different PLA-based films.

Sample name	Type of impermeable phase	Range of impermeable phase content (vol%)
PLAref	/	0
PLA/SiOH/*X*	Hydrophilic silica	0 - 4
PLA/$SiCH_3$/*X*	Hydrophobic silica	0 - 10
PLA/Ag/*X*	Silver metal powder	0 - 4
PLA/OMMT/*X*	Organo modified montmorillonite	0 - 15
PLA/HNT/*X*	Halloysite nanotubes	0 - 10
PLA/GNP/*X*	Graphene oxide platelets	0 - 1.5
PLA/T_a/χ_c	PLA crystalline phase	0 - 50

3.3. Characterization methods

3.3. a) Size exclusion chromatography (SEC)

PLA average molar masses were measured for the different samples by SEC analyses. First, samples were dissolved in chloroform (3 mg/mL) and the solutions were filtered on a PTFE filter plate (pore size = 0.45 µm) before analysis. Then, SEC analyses were carried out with a Polymer Lab type C mixed PLgel column (length = 30 cm, diameter = 7.8 mm, stationary phase 5 PSDVB, temperature = 25 °C, feed rate = 0.5 mL/min, separation performance = 2.10^2 to

2.10^6 g/mol). The refraction index and the light diffusion were measured respectively by Shimadzu RID20 and TREOS Wyatt sensor.

3.3. b) Thermal analysis

Thermogravimetric analyses (TGA) were performed by using a Mettler Toledo TGA/DSC 1 STAR^e System to determine the degradation temperature of the nanocomposites and the nanofillers content. The samples were heated from 25 to 500 °C at 10 °C/min under dry nitrogen flow. The weight loss was recorded as a function of the temperature. The onset degradation temperature was determined by using tangent method. The nanofiller volume content (ϕ_v) was determined from the mass residues at the 500 °C plateau, the density of the PLA and the density of the filler. For nanocomposites filled with OMMT the mass content of the organic cation (30 wt%) was added to the residual mass for volume fraction calculations.

Differential scanning calorimetry (DSC) experiments were performed by using a TA Instrument Q200 calorimeter calibrated with indium standard. Experiments were conducted under nitrogen flow (50 mL/min). Samples (5-10 mg) were placed in an aluminum pan. The melting behavior was investigated through experiments performed with a heating ramp from 25 to 200 °C at 10 °C/min using a standard mode. The degree of crystallinity (χ_c) of the PLA was calculated according to equation (A.1):

$$\chi_c = \frac{\Delta H_m - \Delta H_{cc}}{\Delta \mathrm{H}_{m\infty}(1 - \phi_m)} \qquad (A.1)$$

where ΔH_m is the enthalpy of melting , ΔH_{cc} is the enthalpy of cold crystallization , Φ_m the mass fraction of fillers and $\Delta H_{m\infty}$ is the enthalpy of the infinite crystal with a value of 93 J/g [28]. The analysis of the PLA glass transition was performed by Temperature Modulated Differential Scanning Calorimetry, using a modulated temperature program. The samples were heated from 10 to 90 °C at an average heating rate of 2 °C/min with an oscillation amplitude of 0.318 °C (heat mode only) and a period of 60 s [26]. The glass transition temperature was taken at the onset of the transition. The ΔC_p value was calculated from the onset to the end of the glass transition. The quantity of mobile amorphous fraction (*MAF*) was determined according to equation (A.2):

$$MAF = \frac{\Delta C_p}{\Delta C_{p0}\,(1-\phi_m)} \qquad (A.2)$$

Where Φ_m is the mass fraction of fillers, ΔC_p the heat capacity change of the studied sample and ΔC_{p0} the heat capacity change of the amorphous PLA. The quantity of rigid amorphous fraction *(RAF*) was calculated according to equation (A.3).

$$RAF = 1 - MAF - \chi_c \qquad (A.3)$$

The uncertainties on the degree of crystallinity as well as the *MAF* and the *RAF* have been calculated by uncertainties propagation of the heat capacity and the enthalpy.

3.3. c) PLA microstructure analysis

The crystalline structure of annealed PLA was investigated by small and wide-angle X-ray scattering (SAXS/WAXS). Experiments were performed at the European Synchrotron Radiation Facility (ESRF, Grenoble, France) on the BM02 beamline. The incident photon energy was 15.7 keV (λ = 0.77 Å). The sample-to-detector distance was respectively about 23 cm for the WAXS and 3.15 m for the SAXS, and the chosen beam stop had a diameter of 2.5 mm. The *q*-range of SAXS was calibrated using silver behenate and that of WAXS using LaB_6. The contribution of the empty cell was subtracted from the scattering images of the studied samples, and the intensity was normalized by sample thickness and azimuthally averaged to obtain *I vs. q*, where *I* is the signal intensity and *q* is the diffusion vector.

The morphology of the semi-crystalline PLA has also been characterized by scanning electron microscopy (SEM) observations with a voltage of 5 kV using a Secondary Electron detector. Before observations, the samples surfaces were prepared with a Leica Ultracut B microtome at room temperature using oscillating diamond knife. The samples were then etched with chloroform vapor for 28 minutes to remove the amorphous phase.

3.3. d) Nanofillers dispersion analysis

Nanofiller dispersion in the films cross section was observed by Transmission Electron Microscopy (TEM). The nanocomposite films were ultramicrotomed with oscillating diamond knife (Diatom, 35°) on a Leica Ultracut B microtome at room temperature with a knife speed between 0.8 and 1.2 mm/s to give section thickness of 60 - 70 nm. The sections were then

transferred on a 200-mesh copper grid with a carbon membrane. The TEM bright field observations were performed on a JEOL-1400 flash microscope operating at 120 kV. For nanocomposites based on halloysite nanotubes, the filler dispersion was observed in the cross section and parallel to the film surface.

For nanocomposites films containing spherical or halloysite fillers, ImageJ software as well as Scikit-image processing in Python were used to measure the diameters, the area, the aspect ratio, and the number of impermeable domains per surface unity in the different samples. In the case of Cloisite®30B and graphene, due to lack of contrast and the complexity of the filler domain shapes, the proportion as well as the aspect ratio of different classes of filler domains were measured manually with ImageJ software. The interparticle distance for all the nanocomposites was also measured manually using ImageJ software. For all samples, the mean values of each morphological parameter were determined from the analysis of at least 60 filler domains.

3.3. e) Permeability measurements

Permeability measurements were performed on samples of 5 cm² effective area with a thickness between 100 and 150 µm, Oxygen transmission rate (OTR in cm^3_{STP}.cm/[cm².day]) was measured at 23 °C and 0 % relative humidity with a MOCON OX-TRAN®. The test cell was composed of two chambers separated by the film. Nitrogen containing 2 % of hydrogen (N_2/H_2) was used as the carrier gas and pure oxygen was used as the test gas. Before each measurement, a nitrogen purge (flow of 10 mL/min) during 48 h was realized to remove trace of atmospheric oxygen. Oxygen was then introduced at 20 mL/min and the oxygen flux going through the film was measured by a coulometric sensor.

Water vapor transmission (WVTR in g/[m².day]) was measured at 23 °C and 90 % relative humidity with a MOCON PERMATRAN W3/33 equipped with an infrared sensor. Water transfer though the films was conducted by N_2 gas at 100 sccm to the infrared sensor.

In all cases, the permeability *P* is calculated from the steady state flux *J* according to the equation (A.4):

$$P = \frac{J.e}{p} \qquad (A.4)$$

where *e* is the sample thickness (cm), taken from the average value of five measurements and *p* the difference of pressure between the upstream and the downstream compartments (cmHg). The permeability coefficient *P* is expressed in barrer units (1 barrer = 10^{-10} cm^3_{STP} .cm.cm^{-2}.s^{-1}.$cmHg^{-1}$ = 3.36.10^{-16} mol.m.m^{-2}.s^{-1}.Pa^{-1}).

4. Results and discussion

4.1. Morphological characterization of the reference and nanocomposite films series

4.1. a) Reference amorphous PLA films

PLA films prepared according to the same processing conditions as the nanocomposite films are used as reference and were characterized.

The average molar mass of PLA after the melt blending and compression step was similar to the one of the PLA granular (86,000 g/mol) showing that no significant degradation occurred during the processing step. The TGA thermogram of the reference PLA film is given in **Figure A.2**. The degradation begins at 348 °C and the subsequent mass loss observed corresponds to hydrolysis of the PLA chains and then a decomposition of the oligomers [29]. The residue at 500 °C is equal to 0%.

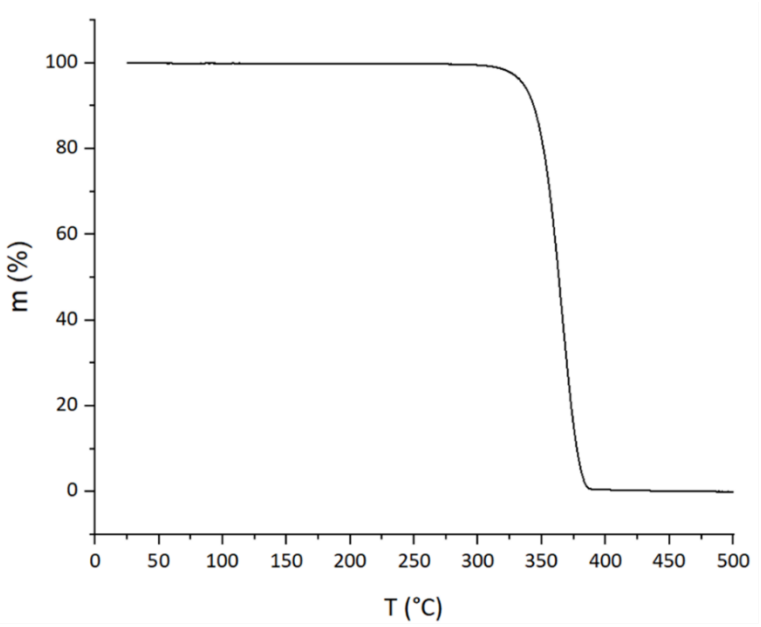


Figure A.2 - TGA thermogram of the reference PLA film at 10 °C/min under nitrogen.

The DSC thermogram (**Figure A.3**) shows the glass transition temperature (T_g) of the reference film at 56 ± 1 °C which is in agreement with values reported in the literature [6], [10]. The small endothermic peak observed at the glass transition, is assigned to physical aging phenomenon [30]. The thermogram exhibits at higher temperature an exotherm associated with the PLA cold crystallization (T_{cc} = 118 ± 2 °C) and a melting peak (T_m = 150 ± 2 °C). The values of the different transitions reported in the present work are similar to those found in the literature for PDLLA processed and characterized under similar conditions [6], [10], [24]. Moreover, the amorphous nature of the reference film is confirmed as the melting enthalpy and the cold crystallization enthalpy have the same value ($\Delta H_{cc} = \Delta H_f$ = 24 ± 2 J/g). The ΔC_{p0} value of the reference amorphous PLA was fond to be 0.52 ± 0.02 $J.g^{-1}.°C^{-1}$ in agreement with the study of Guinault *et al.* on PDLLA [24].

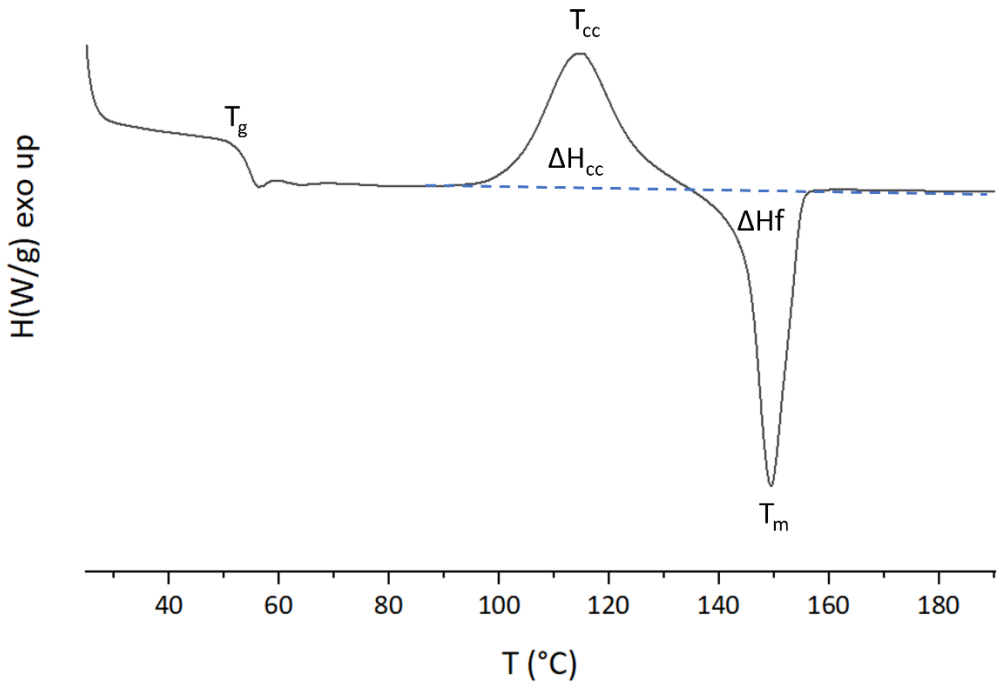


Figure A.3 - DSC thermogram of the reference PLA film corresponding to the first heating performed at 10 °C/min.

4.1. b) Nanocomposite films

Table A.3 summarizes the values of the average molar mass of the reference PLA and of the most highly filled material for each studied nanocomposites series as well as the data (degradation temperature and mass residue at 500 °C) obtained from TGA. The M_n values measured for PLA/$SiCH_3$/10, PLA/Ag/4, PLA/HNT/10 and PLA/GNP/1.5 are in the same range,

close to the value obtained for the reference PLA film. PLA films filled with OMMT exhibit a lower M_n indicating a higher extent of degradation during the process. However, it could be noticed that all materials allowed the preparation of non-brittle self-standing films. The TGA thermograms relative to the nanocomposites (**Supplementary Figure A.1**) exhibit degradation temperatures comparable to the one of PLAref for low filler content. For high content of fillers, a lower T_d value is obtained, with a minimum value of 337 °C for PLA/HNT/10 (**Table A.3**). The values of the residue measured at high temperature are in good agreement with the expected filler contents.

Table A.3 - Matrix number average molar mass, degradation temperature at the onset and mass residue determined for the different nanocomposite series.

Sample	Mn (10^3 g/mol)	T_d (°C)	Mass residue at 500 °C (%)
PLAref	87 ± 3	348 ± 1	0 ± 0.1
PLA/SiOH/1	/	347 ± 1	1.2 ± 0.1
PLA/SiOH/3	/	347 ± 1	5.2 ± 0.1
PLA/SiOH/4	/	347 ± 1	6.5 ± 0.1
PLA/$SiCH_3$/1	/	347 ± 1	1.5 ± 0.1
PLA/$SiCH_3$/4	/	347 ± 1	7.0 ± 0.1
PLA/$SiCH_3$/5	/	347 ± 1	8.0 ± 0.1
PLA/$SiCH_3$/10	77 ± 6	347 ± 1	16.3 ± 0.1
PLA/Ag/0.5	/	348 ± 1	3.9 ± 0.1
PLA/Ag/1	/	346 ± 1	5.2 ± 0.1
PLA/Ag/3	/	342 ± 1	20.8 ± 0.1
PLA/Ag/4	79 ± 5	340 ± 1	26.3 ± 0.1
PLA/HNT/0.5	/	348 ± 1	1.2 ± 0.1
PLA/HNT/2	/	343 ± 1	3.8 ± 0.1
PLA/HNT/4	/	342 ± 1	7.5 ± 0.1
PLA/HNT/10	71 ± 5	337 ± 1	18.3 ± 0.1
PLA/OMMT/2.5	50 ± 3	347 ± 1	3.0 ± 0.1
PLA/OMMT/5	/	345 ± 1	6.3 ± 0.1
PLA/OMMT/10	/	343 ± 1	10.9 ± 0.1
PLA/OMMT/15	58 ± 7	341 ± 1	14.9 ± 0.1
PLA/GNP/0.05	/	347 ± 1	< 0.1 ± 0.05
PLA/GNP/0.1	/	347 ± 1	0.14 ± 0.05
PLA/GNP/0.5	/	346 ± 1	0.87 ± 0.05
PLA/GNP/1.5	85 ± 3	348 ± 1	2.7 ± 0.05

The DSC thermograms of the different nanocomposite series are given in **Supplementary Figure A.2.** The glass transition temperature values are comparable for PLAref and the different nanocomposites except for PLA/OMMT/10 and PLA/OMMT/15 which exhibit a slightly lower T_g, value (around 50 °C) (**Table A.4**). Considering experimental uncertainties, it

can be seen that introducing nanofillers in the PLA matrix does not induce significant modifications of the mobile amorphous fraction (*MAF*) and the rigid amorphous fraction (*RAF*) (**Table A.4**). It appears then that for the nanocomposite's series investigated, the fillers have no effect on the polymer chain mobility. For the nanocomposites prepared with the highest amount of OMMT, the decrease of T_g could be related to the decrease of the PLA molar mass observed by SEC. The introduction of nanofillers has no effect on the cold crystallization temperature and the melting temperature. Furthermore, the degree of crystallinity is less than 4 ± 2 % meaning that all nanocomposites can be considered as mostly amorphous.

To conclude, the matrix microstructure and chain mobility of the nanocomposite films prepared by melt-blending are not significantly affected by the fillers. As a result, the permeability properties of the nanocomposites will depend more specifically on the dispersion state, content and shape of the incorporated fillers.

Table A.4 - Matrix properties of the different nanocomposite films.

Sample	T_g (°C)	T_{cc} (°C)	T_m (°C)	χ_c (%)	ΔCp ($J.g^{-1}.°C^{-1}$)	MAF (%)	RAF (%)
PLAref	57 ± 1	103 ± 1	150 ± 2	0 ± 2	0.52 ± 0.02	100 ± 4	0 ± 6
PLA/SiOH/1	57 ± 1	102 ± 1	149± 1	1 ± 2	0.51 ± 0.01	99 ± 5	0 ± 7
PLA/SiOH/3	57 ± 1	103 ± 1	149± 1	2 ± 2	0.49 ± 0.01	99 ± 5	0 ± 7
PLA/SiOH/4	57 ± 1	102 ± 1	149± 1	3 ± 2	0.43 ± 0.01	88 ± 5	9 ± 7
PLA/$SiCH_3$/1	56 ± 1	101 ± 1	149 ± 1	1 ± 2	0.49 ± 0.01	96 ± 5	3 ± 7
PLA/$SiCH_3$/4	56 ± 1	104 ± 1	149 ± 1	2 ± 2	0.48 ± 0.02	99 ± 5	0 ± 7
PLA/$SiCH_3$/5	56 ± 1	104 ± 1	149 ± 1	2 ± 2	0.48 ± 0.02	100 ± 5	0 ± 7
PLA/$SiCH_3$/10	56 ± 1	110 ± 1	150 ± 1	4 ± 2	0.40 ± 0.02	92 ± 6	4 ± 8
PLA/Ag/0.5	56 ± 1	103 ± 1	149 ± 1	1 ± 2	0.50 ± 0.02	100 ± 4	0 ± 6
PLA/Ag/1	55 ± 1	102 ± 1	149 ± 1	3 ± 2	0.50 ± 0.02	100 ± 5	0 ± 7
PLA/Ag/3	54 ± 1	101 ± 1	148 ± 1	2 ± 2	0.42 ± 0.02	100 ± 6	0 ± 8
PLA/Ag/4	53 ± 1	101 ± 1	148 ± 1	2 ± 2	0.36 ± 0.02	95 ± 6	3 ± 8
PLA/HNT/0.5	55± 1	102 ± 1	149 ± 1	0 ± 2	0.53 ± 0.01	100 ± 4	0 ± 6
PLA/HNT/2	55 ± 1	109 ± 1	151 ± 1	0 ± 2	0.48 ± 0.01	96 ± 5	4 ± 7
PLA/HNT/4	54 ± 1	109± 1	152 ± 1	1 ± 2	0.49 ± 0.01	100 ± 5	0 ± 7
PLA/HNT/10	55 ± 1	108 ± 1	150 ± 1	3 ± 2	0.38 ± 0.01	90 ± 6	7 ± 8
PLA/OMMT/2.5	56 ± 1	104 ± 1	149 ± 1	2 ± 2	0.52 ± 0.01	100 ± 4	0 ± 6
PLA/OMMT/5	55 ± 1	109 ± 1	150 ± 1	4 ± 2	0.48 ± 0.03	99 ± 4	0 ± 6
PLA/OMMT/10	52 ± 1	109 ± 1	151± 1	4 ± 2	0.42 ± 0.02	91 ± 4	5 ± 6
PLA/OMMT/15	50 ± 1	110 ± 1	151 ± 1	3 ± 2	0.38 ± 0.02	93 ± 5	7 ± 7
PLA/GNP/0.05	56 ± 1	102 ± 1	149 ± 1	3 ± 2	0.50 ± 0.02	96 ± 4	1 ± 6
PLA/GNP/0.1	58 ± 1	102 ± 1	149 ± 1	1 ± 2	0.52 ± 0.02	100 ± 4	0 ± 6
PLA/GNP/0.5	57 ± 1	102 ± 1	149 ± 1	1 ± 2	0.55 ± 0.02	100 ± 4	0 ± 6
PLA/GNP/1.5	56 ± 1	104 ± 1	150 ± 1	3 ± 2	0.49 ± 0.02	98 ± 4	0 ± 6

The dispersion state of the fillers for the different nanocomposites films has been investigated by TEM. Moreover, to go deeper in the filler dispersion study, quantitative analysis has been realized through quantitative parameters such as the mean size, mean aspect ratio of the dispersed domains and the average density of the filler domains. As shown in **Figure A.4**, for PLA filled with silica, a good dispersion made of small aggregates is observed whatever the silica type and content up to 10 vol%. In complement of **Figure A.4**, TEM micrographs at low magnification are available in supplementary information (**Supplementary Figure A.3** and

Supplementary Figure A.5). TEM micrograph with the area distribution for the whole range of PLA/silica nanocomposite compositions are also given in supplementary material (**Supplementary Figure A.4** for hydrophilic silica and in **Supplementary Figure A.6** for hydrophobic silica).

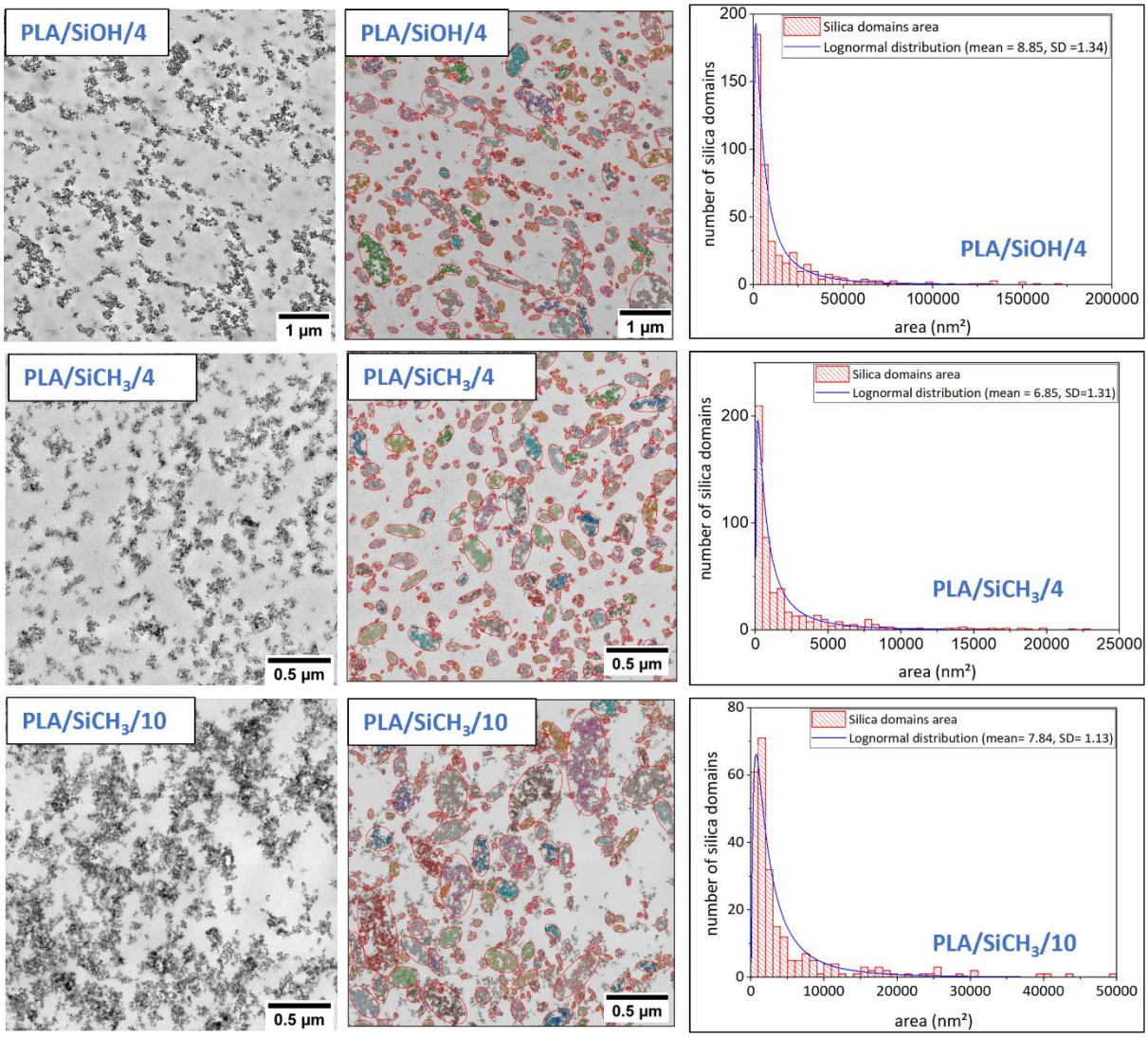


Figure A.4 - TEM micrographs from the cross section of PLA/silica films and the silica domains identifications by Scikit-image processing and their area distribution for PLA/SiOH/4, PLA/$SiCH_3$/4 and PLA/$SiCH_3$/10.

Table A.5 gives the values of the mean area of the silica domains, the mean aspect ratio, the number of domains per unit surface and the distance between the silica domains. It can be remarked that, at similar filler content, the mean size of the aggregates is larger for hydrophilic silica (PLA/SiOH) than for hydrophobic silica (PLA/$SiCH_3$). This trend has also been reported in the literature when comparing surface-modified and non-modified silica in PLA [31], [32] and

explained by a difference in the filler/matrix compatibility which depends on the filler surface properties. The average silica domains area increases with increasing filler content for hydrophilic silica contrary to hydrophobic silica for which the domain area does not vary at filler contents below 10 vol%. However, the mean aspect ratio is the same in all the PLA/silica samples, with a value close to 2. It can be seen that there are more silica domains per surface unity for hydrophobic silica than for hydrophilic silica at similar filler content which shows again a better dispersion of the hydrophobic silica in PLA and logically the distance between the silica domains is smaller in these nanocomposites. At 10 vol%, PLA filled with hydrophobic silica (PLA/$SiCH_3$/10) shows less domains but bigger ones caused by a certain hindrance which prevents a fine dispersion of silica.

Table A.5 – Area, mean aspect ratio, average number of silica domains per unit surface and distance between the impermeable domains for PLA nanocomposites filled with hydrophilic silica (PLA/SiOH) and hydrophobic silica (PLA/$SiCH_3$).

Sample	Area (nm ²)	Mean aspect ratio	Number of domains /µm ²	Inter domains spacing (nm)
PLA/SiOH/1	9 000 ± 7 000	1.7 ± 0.5	5	550 ± 200
PLA/SiOH/3	18 000 ± 30 000	1.8 ± 0.6	7	430 ± 130
PLA/SiOH/4	20 000 ± 30 000	1.8 ± 0.7	16	380 ± 160
PLA/$SiCH_3$/1	3 000 ± 3 000	1.9 ± 0.5	12	290 ± 100
PLA/$SiCH_3$/4	3 000 ± 3 000	1.9 ± 0.6	70	120 ± 40
PLA/$SiCH_3$/5	3 000 ± 5 000	1.9 ± 0.7	60	140 ± 40
PLA/$SiCH_3$/10	8 000 ± 10 000	1.9 ± 0.7	20	150 ± 60

For the nanocomposites based on silver nanoparticles, a heterogeneous filler dispersion is evidenced, with the coexistence of single silver nanoparticles and micrometer size agglomerates (**Figure A.5** and **Supplementary Figure A.7**). Therefore, it has been decided to calculate the area as well as the aspect ratio values by separating the small domains with a diameter below 1 µm and the bigger domains (diameter > 1 µm). Nevertheless, it can be noted that the proportion of micrometer domains is very low (< 10%) for all the silver contents (**Table A.6**).

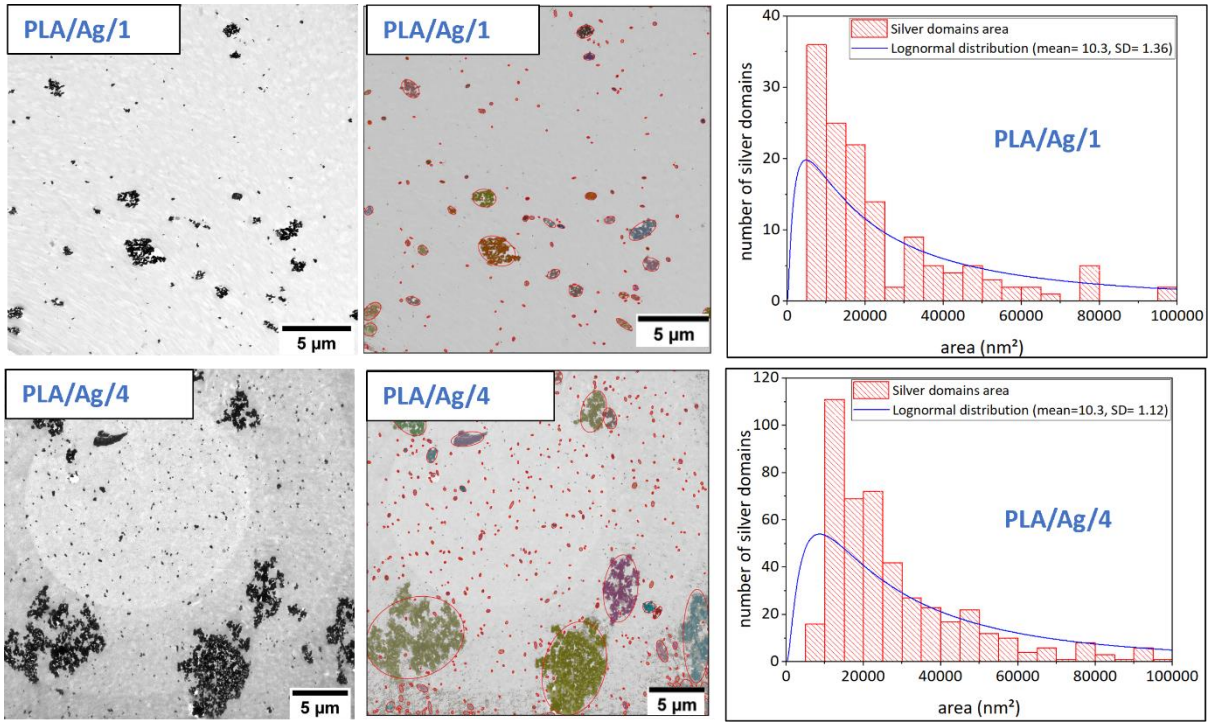


Figure A.5 - TEM micrographs from the cross section of PLA/silver films as well as the silver domains identification by Scikit-image processing and their area distribution for PLA/Ag/1 and PLA/Ag/4.

The average area of the small domains keeps constant for all the samples with a mean value of 5.10^4 nm², whereas the size of the bigger domains increases by one decade between PLA/Ag/0.5 and PLA/Ag/4. Despite these differences of area, the mean aspect ratio is approximately equal to 1.7 in all the samples. Moreover, the mean number of domains is increasing with the silver content from 3 to 16 domains/µm² and the interdomains spacing decreases with the filler content but stays very large (>1,000 nm).

Table A.6 - Area, mean aspect ratio, average number of silver domains per surface unity and distance between the impermeable domains for PLA nanocomposites filled with silver nanoparticles. (*d* corresponds to the diameter of the silver domains).

Sample	*Small domains (d< 1 µm)*			*Big domains (d> 1 µm)*			*All the domains*		
	% by number	Area (10^5 nm²)	Aspect ratio	% by number	Area (10^5 nm²)	Aspect ratio	Mean aspect ratio	Number of domains /µm ²	Inter domains spacing (nm)
PLA/Ag/0.5	97	0.5 ± 0.9	1.7	3	5 ± 2	1.4	1.7	3	4,000 ± 2,000
PLA/Ag/1	92	0.5 ± 0.7	1.7	8	9 ± 7	1.7	1.7	7	2,000 ± 800
PLA/Ag/3	94	0.4 ± 0.5	1.6	6	30 ± 60	2.1	1.6	13	1,200 ± 600
PLA/Ag/4	95	0.4 ± 0.3	1.6	5	50 ± 90	1.9	1.6	16	1,200 ± 600

Halloysite nanotubes are well dispersed within the matrix, which may show a rather good compatibility of the tubes with the PLA matrix. Indeed, the TEM images representative of the film cross section of PLA/HNT/4 show the presence of few small discs, the size of which corresponds to the diameter of the tubes (**Figure A.6a**). This observation is confirmed by additional TEM micrographs in supplementary information (**Supplementary Figure A.8**). Few elongated structures are also evidenced corresponding to the length of unitary tubes. Therefore, it seems that most of the tubes are lying in the plane of the film. The top view of the same sample shown in **Figure A.6b** supports the conclusion drawn from the analysis of the cross sections. Indeed, it shows mostly elongated shapes corresponding to individual tubes lying parallel to the top view. This orientation of the tubes, lying parallel to the surface of the films can be generalized for all the halloysite contents. From these pictures, the length over diameter ratio of the observed individual tubes has been estimated equal to 10 which is in good agreement with the data relative to the individual fillers (**Table A.1**). Increasing the filler amount up to 10 %vol leads to the presence of more numerous small aggregates (**Figure A.6c**), which is in agreement with results reported in other studies on PLA/HNT nanocomposites prepared by melt-blending [12], [13], [21].

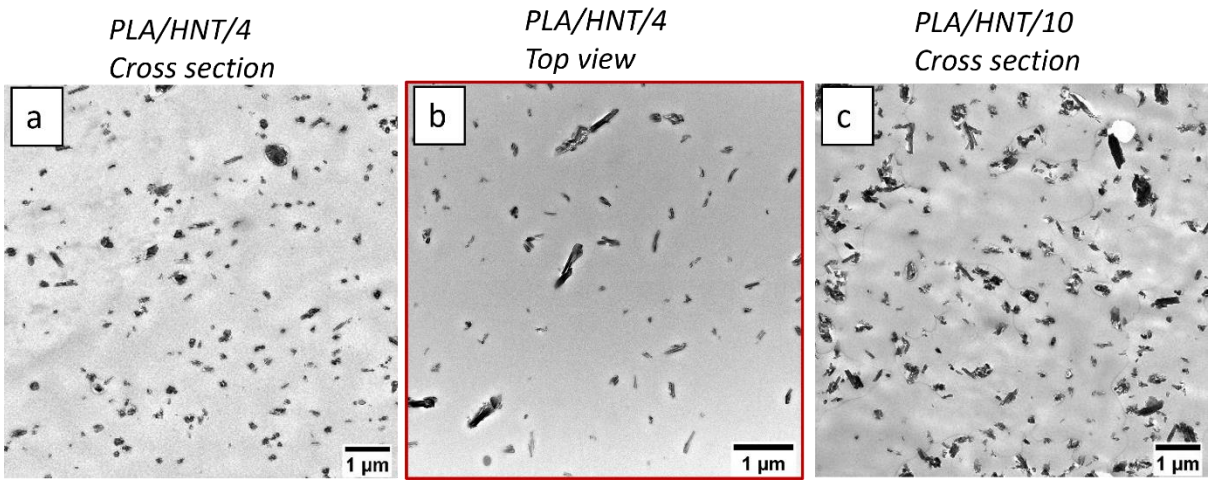


Figure A.6 - TEM micrographs of (a) PLA/HNT/4 from the cross section, (b) PLA/HNT/4 from the top view and (c) PLA/HNT/10.

Although the diameter of these aggregated structures measured on TEM pictures of the cross section is between 200 and 500 nm which is much larger than individual tubes (d ≈ 40 nm) their proportion is low (< 10%) whatever the halloysite content (**Table A.7**). Consequently, the mean L/D ratio of the halloysites domains in all the samples has been considered equal to 10 (reflecting thus the presence of a great majority of individual tubes). From the results in **Table A.7**, it can be seen that the interparticle spacing decreases by a factor of 4 as the filler content increases from PLA/HNT/0.5 to PLA/HNT/10.

Table A.7 - Proportion of aggregated nanotubes domains and their diameter as well as the interdomains spacing values calculated from TEM pictures for halloysites nanocomposites (PLA/HNT).

Sample	% aggregated domains	Aggregates diameter (nm)	Inter domains spacing (nm)
PLA/HNT/0.5	3	450 ± 50	2130 ± 400
PLA/HNT/2	4	490 ± 220	1300 ± 500
PLA/HNT/4	3	250 ± 80	510 ± 170
PLA/HNT/10	10	320 ± 120	540 ± 160

Figure A.7 shows representative TEM micrographs of PLA filled with OMMT. Additional TEM images at higher magnification are presented in supporting material (**Supplementary Figure A.9**). A homogeneous dispersion of the randomly oriented fillers with the co-existence of quasi-individual sheets, small and middle size tactoïds for all filler contents

up to 15 vol% is evidenced as already described in the literature [7], [6], [33]. This homogeneous dispersion is promoted by the presence of hydroxyl functions on the organic cation of the OMMT [21].

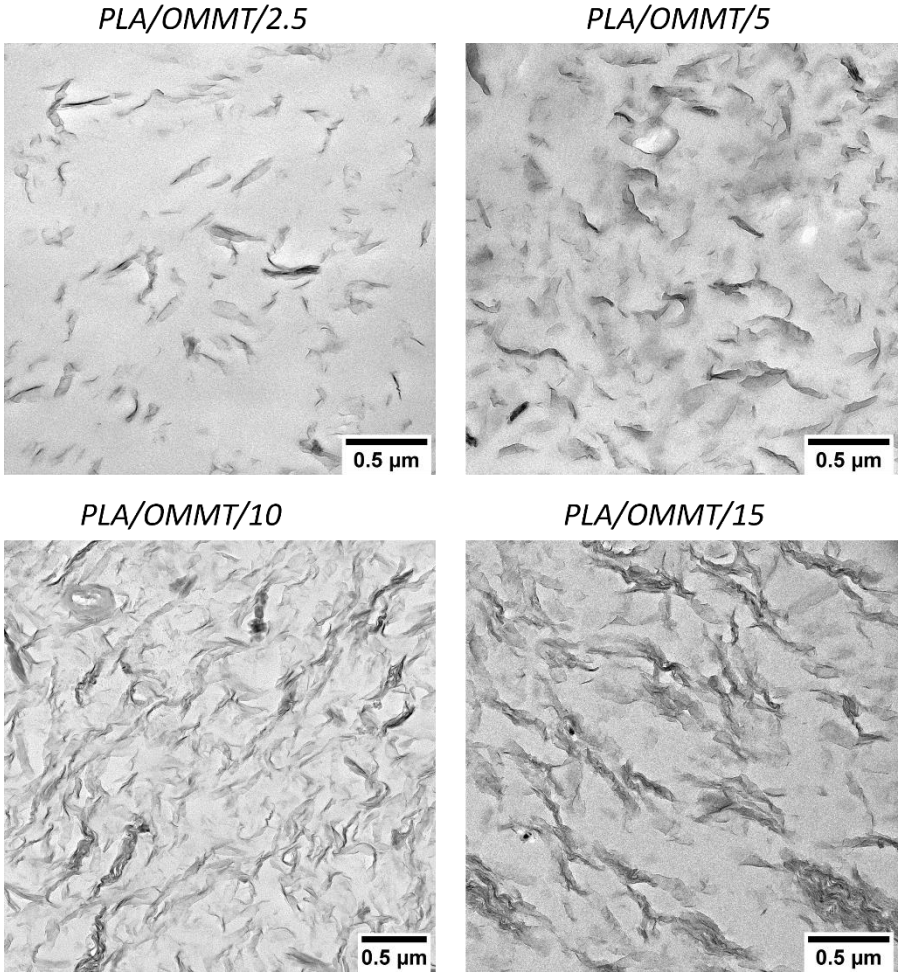


Figure A.7 - TEM micrographs of the cross section of the PLA films filled with an increasing amount of OMMT.

The quantitative analysis of the filler dispersion state (**Table A.8**) shows that the proportion of quasi-individual sheets is slightly decreasing as the filler content increases (from 84% for PLA/OMMT/2.5 to 78% for PLA/OMMT/15) due the hindrance which is not favorable to fine dispersion of the fillers [16]. This leads to an increase of the proportion of middle-size tactoïds with the filler content whereas the proportion of small tactoïds stays constant until 10 %vol of filler. For 15 vol% of OMMT, the proportion of small and middle size tactoïds is higher and the presence of micron size agglomerates has also been observed although present in very small amount. It is worth noting that the mean aspect ratio stays similar whatever the filler

amount, in the range between 79 and 86, which is higher than the mean value of 60 calculated by Tenn *et al.* [7]. Moreover, the lamellar fillers are randomly oriented in all nanocomposite films. However, it should be noted that it is not always the case in films prepared by melt-blending. While, Tenn *et al.* [7] also reported a random orientation of the lamellae, other authors [6], [21] have observed an orientation of the lamellae parallel to the surface of the films. Finally, it can be noted that the interdomains spacing is very small and decreases slightly as the montmorillonite content increases.

Table A.8 - Characteristics of the OMMT dispersion in the PLA/OMMT films (*w* stands for the thickness of the filler domains).

Sample	*quasi-individual sheets*		*Small tactoïds (w< 30 nm)*		*Middle size tactoïds (30 <w< 200 nm)*		*Micron size agglomerates (w> 200 nm)*		*Mean aspect ratio*	*Interdomains spacing (nm)*
	% by number	Aspect ratio	% by number	Aspect ratio	% by number	Aspect ratio	% by number	Aspect ratio		
PLA/OMMT/2.5	84	100	10	12 ± 5	6	7 ± 2	/	/	86	190 ± 100
PLA/OMMT/5	85	100	10	10 ± 2	6	5 ± 2	/	/	86	150 ± 60
PLA/OMMT/10	80	100	10	10 ± 2	10	7 ± 2	/	/	83	60 ± 30
PLA/OMMT/15	78	100	5	7 ± 2	14	7 ± 2	3	2 ± 1	79	100 ± 30

Dispersion of graphene was also investigated and TEM micrographs are shown in **Figure A.8**. At low GNP content (≤0.1 vol%), very good dispersion has been achieved with only few small stacks visible at low magnification. A lot of individual sheets are lying parallel to the surface of the films and it can be observed that the sheets can overlap horizontally and form elongated thin structures (**Figure A.8**). The length of these overlapped structure has been measured and is in a range between 1000 - 1500 nm. Thus, it leads to impermeable domains with higher aspect ratio that the individual graphene sheets. The lack of contrast as well as the few numbers of sheets due to the very low volume content of GNP did not allow to make a statistical analysis of the dispersion as for the other fillers. At higher GNP content (>0.1 vol%), TEM micrographs at low magnification show more numerous and bigger stacked sheets, with a mean aspect ratio of 5; their proportion increases which the GNP content. The TEM micrographs at higher magnification for PLA/GNP/0.5 (**Figure A.8**) also show denser tactoïds. Consequently, it leads to a decrease of the mean filler aspect ratio.

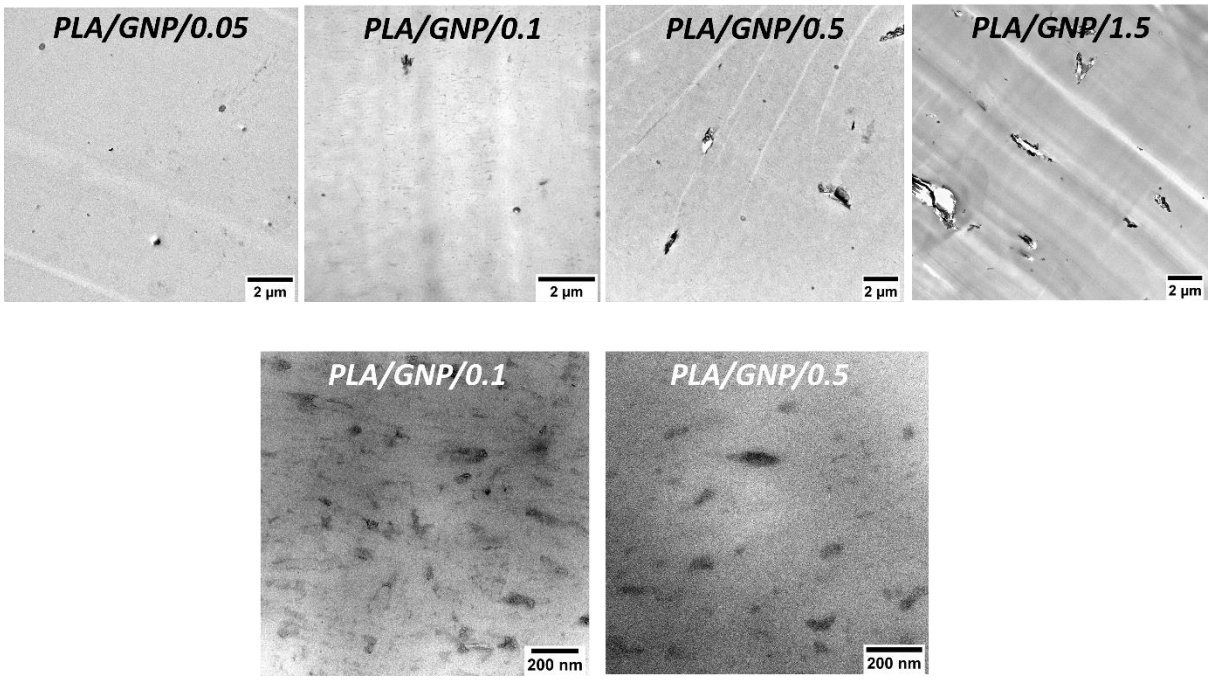


Figure A.8 - TEM micrographs of the cross section of the PLA films filled with graphene at low (up) and high magnification (down).

To sum up, different dispersion states have been evidenced as a function of the type of fillers going from very homogeneous dispersion with silica to more heterogeneous ones with silver. The shape and the mean aspect ratio of the dispersed domains also vary according to the different systems with low elongated impermeable domains for PLA filled with silica (PLA/$SiCH_3$ and PLA/SiOH) in comparison to lamellar domains with high aspect ratio for PLA filled with montmorillonites (PLA/OMMT) or graphene (PLA/GNP). Moreover, the distance between the impermeable domains also varies a lot depending on the samples, with very close domains for PLA/OMMT and PLA/GNP to rather distant ones for PLA/Ag and PLA/HNT. Finally, the wide range of nanocomposites enables to have a wide range of dispersion state, content and shape of incorporated fillers.

4.1. c) Semi-crystalline PLA films

Another type of impermeable phase has been considered in this work: the polymer crystalline phase. To vary the extent of crystallinity, different annealing conditions were applied to the amorphous PLA reference film. The annealing temperatures were fixed at 110 and 120 °C in order to reach the maximum degree of crystallinity of the PLA [6], [10]. This range of

temperatures corresponds to the maximum of the cold crystallization exotherm on the DSC thermograms of the amorphous PLA (**Figure A.3**).

Crystalline morphology

The evolution of the degree of the crystallinity as a function of the annealing time for isothermal crystallization performed at T_a = 110 °C and T_a = 120 °C is reported in **Figure A.9**. A sharp increase of the crystallinity from 0 to 35% is observed for an annealing time between 3 and 10 minutes, and then the degree of crystallinity increases more slowly until 24 h (1440 min) of annealing, to reach a maximum: χ_c = 50%. Similar curve shape has already been described in the literature [25], [26], [27] and the smoother slope after 10 min is attributed to a perfection of the crystalline structure also referred as secondary crystallization.

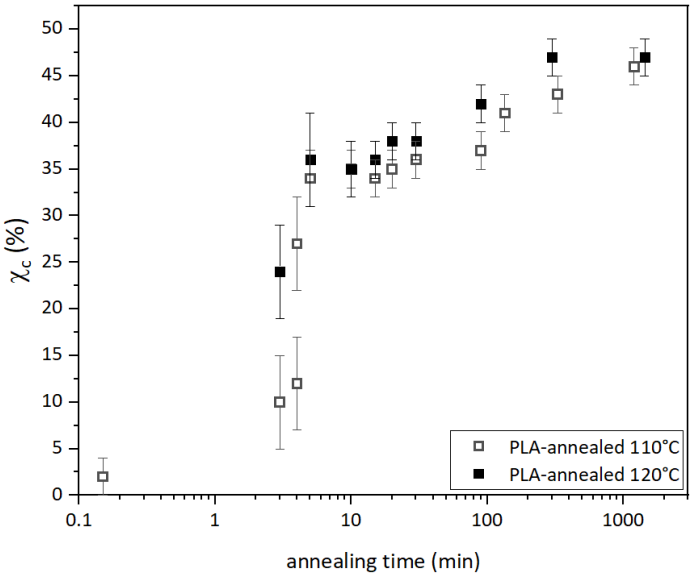


Figure A.9 - Evolution of the crystallinity of the PLA film as a function of the annealing time (log scale) during isothermal crystallization at 110 °C and 120 °C.

Spherolites were evidenced by SEM observations performed on etched semi-crystalline PLA films (**Figure A.10**), which is common for crystallization without any mechanical constraint. Regardless of the degree of crystallinity and the annealing temperature, spherolites were found to be very small, with a diameter in the range of 1 - 2 µm. The spherolite size observed in our samples is slightly smaller than those that have been reported in the literature for similar annealing temperatures (around 5-10 µm) [24], [25], [27]. As the degree of crystallinity increases, the distance between the spherolites decreases until they completely fill the space as it can be seen in **Figure A.10**.

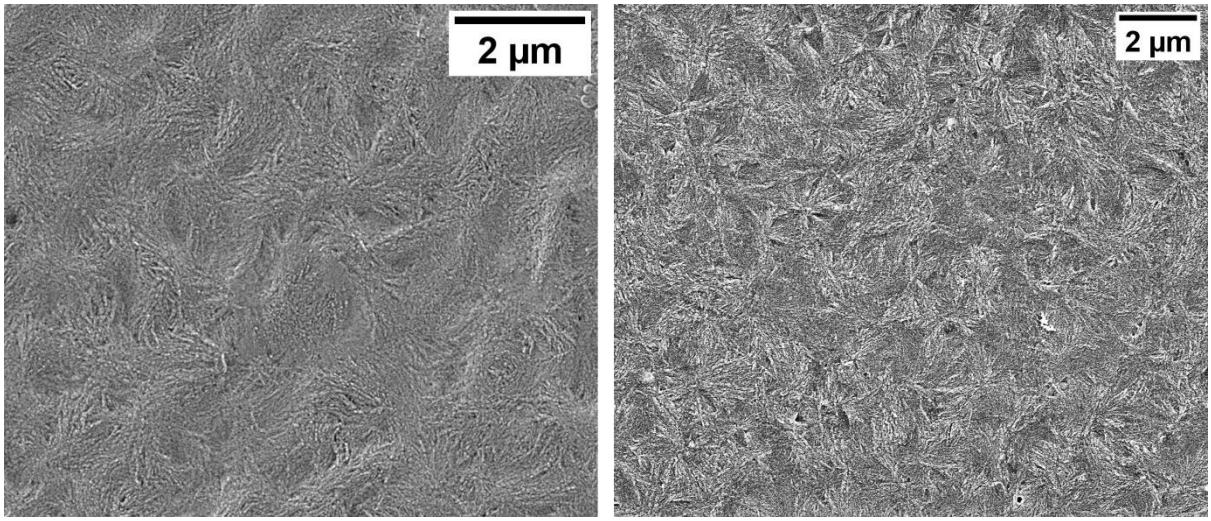


Figure A.10 - SEM images (x 10,000) of annealed PLA respectively for PLA/110°C/11 and PLA/120°C/50.

The DSC thermograms for T_a = 110 °C (**Figure A.11a**) show the presence of two melting peaks for short annealing time until 30 min, while there is only one melting peak for longer annealing time. For samples annealed at 120 °C the presence of two melting peaks becomes less noticeable (**Figure A.11b**). These observations are consistent with previous studies with the same D-isomer content as the PLA and the same annealing temperature used in this study [34], [35]. In the literature, this double peak is attributed the melt-recrystallisation-melt process upon heating of the imperfect or less stable crystals [34]. Moreover, the DSC thermograms obtained for annealing at 110 °C and 120 °C demonstrate a slight shift in the melting temperature from 147 °C to 154 °C with increasing annealing time. This can be related to the increase of the thickness of the crystalline lamellae.

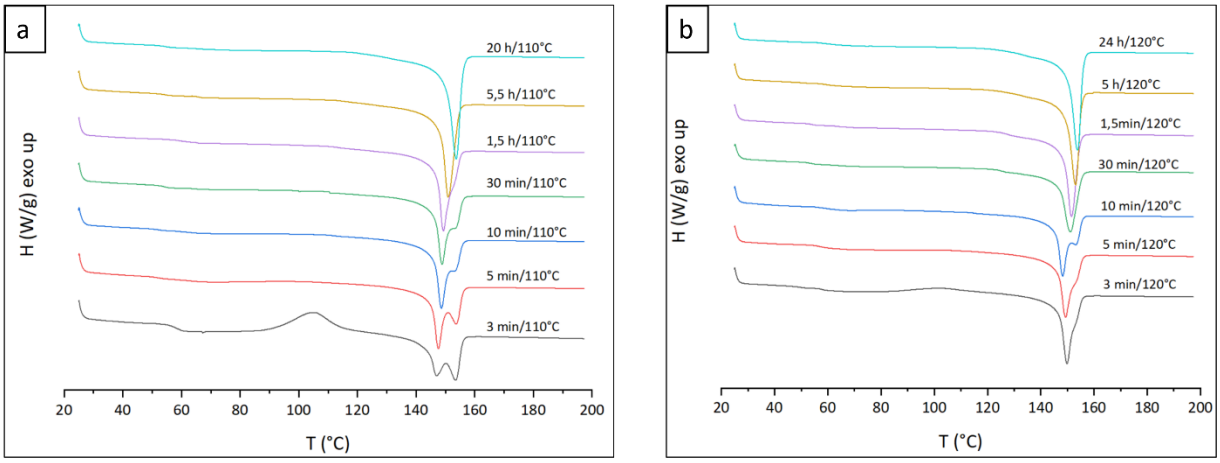


Figure A.11 - DSC thermogram of PLA films annealed at (a) 110 °C and (b) 120 °C. The sample are named: x h/110°C and x h/120°C, where x corresponds to the annealing time.

WAXS measurements were carried out on PLA samples with different degrees of crystallinity. **Figure A.12** exhibits the diffractograms obtained and the assignment of the diffraction peaks. All semi-crystalline samples exhibit reflections peaks associated to the α crystalline form of PLLA which is commonly obtained for the used crystallization conditions [24], [35], [36], (200) and (203) planes at 2θ = 16.8° and 19.0°, with an increase of the peak intensities when the degree of crystallinity increases. It can also be remarked that for χ_c > 35%, small reflection peaks related to (004)/(103), (204) and (015) planes appear at 2θ = 12.5°, 20.6° and 22.3°, respectively; they are also characteristic of the α crystalline form of PLLA [37], [38], [39]. Finally, the α form is confirmed by the presence of small reflection peaks at 2θ = 23.9° and at 2θ = 25°, associated to the (016) and (206) planes [36].

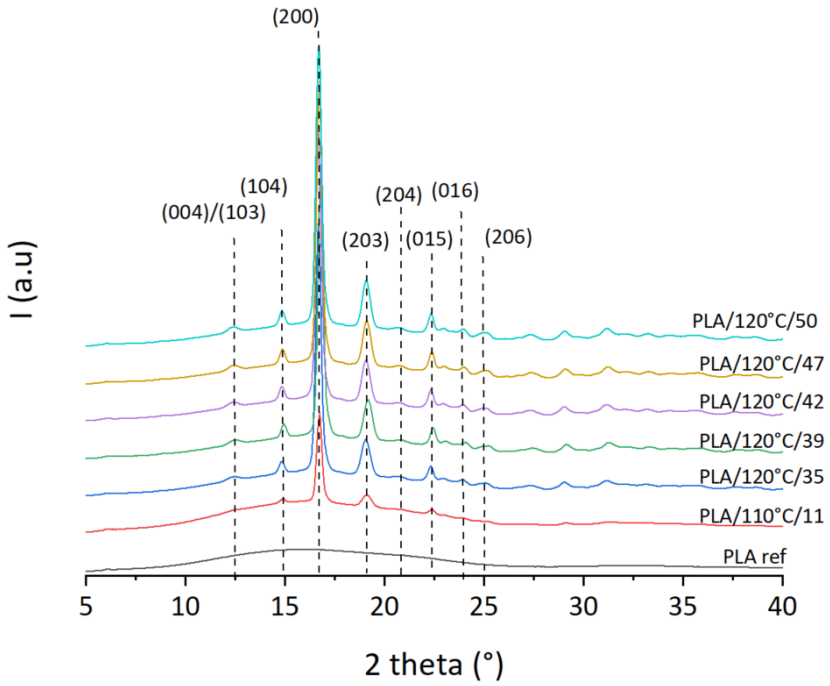


Figure A.12 - WAXS pattern for semi-crystalline PLA with different degree of crystallinity.

SAXS analyses were also performed on annealed PLA with different degree of crystallinity. The Lorentz-corrected scattering diagrams $I(q).q^2 = f(q)$ are represented in **Figure A.13a**. Except for PLA ref, all samples present a scattering intensity with a maximum obtained at a scattering wavevector q_{max}. The values of q_{max} are obtained after fitting with a Lorentz function; they are related to the long period values, L_p, which were calculated according to Bragg's law [27] (equation (A.5)).

$$L_p = \frac{2\pi}{q_{max}} \quad (A.5)$$

From L_p, the crystalline lamellae thickness (L_c) and the thickness of the intercrystallite amorphous region (L_a) were calculated by using equation (A.6) and (A.7).

$$L_c = L_p . \chi_c \quad (A.6)$$

$$L_a = L_p - L_c \quad (A.7)$$

Figure A.13b shows the evolution of the long period (L_p), the crystalline lamellae thickness (L_c) and the distance between the crystalline lamellae (L_a) as a function of χ_c. L_p values decrease from 24 to 20 nm for χ_c between 11% and 35% and then reach a plateau with a value of 20 nm, which is in agreement with literature data reported for PLA [26]. The crystalline lamellae thickness (L_c) increases from 2.5 nm to 10 nm with the increases of χ_c, while the distance between them (L_a) decreases from 20 nm to 10 nm. This increase of the L_c value is related with the shift towards higher temperature of the melting temperature. For χ_c = 50%, L_c value is equal to the L_a value (i.e. 10 nm) which is similar to values reported in the literature [26]. Moreover, similar value of L_p and L_c have been reported at χ_c = 35% independently of the annealing temperature, e.g. 110 or 120 °C [10].

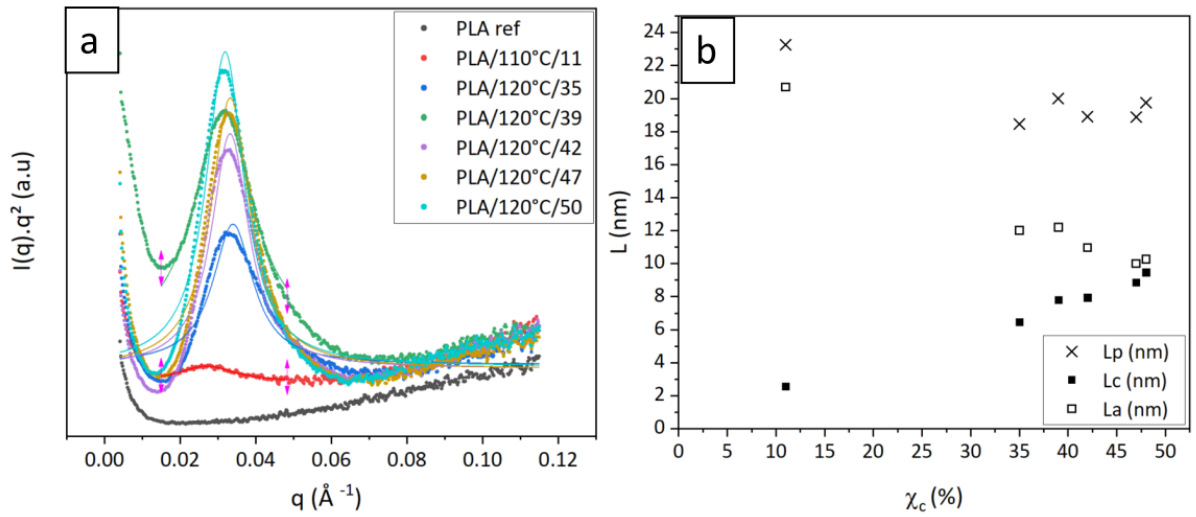


Figure A.13 – (a) SAXS scattering diagrams of semi-crystalline PLA for different degrees of crystallinity and the fitting with a Lorentz correction, (b) evolution of the long period (Lp), the crystalline lamellae thickness (Lc) and the intercrystallite amorphous thickness (La) as a function of the degree of crystallinity.

Structural description of the amorphous phase

The modulated DSC thermogram of the annealed PLA is given in **Supplementary Figure A.10.** For all semi-crystalline PLA samples, the T_g value is 55 °C. No significant T_g shift was observed when comparing the reference amorphous PLA films and the annealed films which is consistent with the study of Guinault *et al.* [24]. Additionally, the amorphous phase contained in our semi-crystalline samples has also been investigated by taking an interest to the mobile amorphous fraction (*MAF*) and rigid amorphous fraction (*RAF*). The presence of a *RAF* in semi-cystalline PLA has been highlighted by several authors in the literature, which is due to the constraints imposed by the crystalline phase on the polymer chains of the amorphous phase [24], [25], [26]. **Figure A14a** shows the evolution of the amount of *RAF* in the amorphous phase for different degrees of crystallinity investigated in this work. The *RAF* increases slowly as the degree of crystallinity increases from 2% to 30%. Above 30% of crytallinity, the *RAF* increase is much more siginficant. Such an increase has also been reported both for PDLLA [40] and for PLLA annealed by a cold crystallization process [26], [41], [42]. In these studies, the strong increase of the *RAF* is explained by a decrease of the free volumes in the amorphous phase caused by annealing process as soon as the maximum of cristallinity is almost reached.

The evolution of the *RAF* is also represented as a function of the distance between crystalline lamallae (L_a) in **Figure 14b**. It can be observed that the proportion of *RAF* increases as L_a decreases, which is expected since the closer the lamellae, the greater the constraint on the chains of the amorphous phase and thus the lower the mobility is. However, the *RAF* content remains globally low (below 25%), explaining the absence of a shift of the T_g [24].

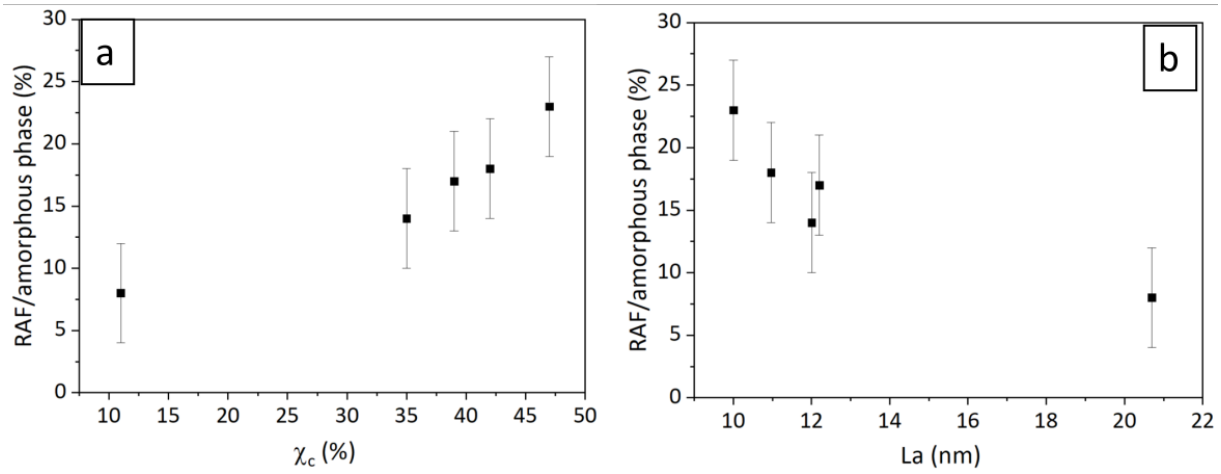


Figure A.14 - (a) Evolution of the *RAF* as a function of crystallinity degree for PLA annealed at 120 °C and (b) as a function of the amorphous interlamellar distance.

All in all, annealing treatment of amorphous PLA at 110 and 120 °C shows the formation of a crystalline phase corresponding to the α-form of the PLA and organized into small (diameter ≈ 1 µm) spherolites. The increase of the degree of crystallinity leads to an increase of the crystalline lamellae thickness L_c as well as a decrease of the amorphous area thickness. Moreover, the increase of crystallinity has also consequences on the amorphous phase, with an increase of the rigid amorphous fraction (*RAF*) above 30% of crystallinity.

4.2. Gas and water vapor permeability of amorphous nanocomposites and semi-crystalline PLA films

Oxygen permeability at anhydrous state and water vapor permeability at 90 %RH were measured at 23 °C on the different film series with two major aims. The first one is to evidence in each nanocomposite film series the factors governing transport properties. The second one is to establish equivalence laws for transport properties between the different series of nanocomposites investigated. The permeability coefficients measured for PLA reference, called P_0, are $P_0(H_2O_{\ 90\ \%RH})$ = 3600 barrer and $P_0(O_{2\ 0\%\ RH})$ = 0.52 barrer. These permeability values are in the range of values reported in the literature for amorphous PLA [6], [10], [25], [43], [44], [45].

The permeability coefficient, *P*, was then measured for the same diffusing molecule and conditions on each nanocomposite film and semi-crystalline film. The relative permeability was calculated for each penetrant and film series according to equation (A.8):

$$Relative\ permeability = \frac{P}{P_0} \qquad (A.8)$$

with P_0 the permeability of the reference PLA and P the permeability of the amorphous nanocomposite or semi-crystalline PLA sample.

First it can be noticed that whatever the nanocomposite samples, the relative permeability is either below or equal to 1 (**Figure A.15**). Inorganic nanofillers such as those used in this work are considered as impermeable fillers [14], [16], [21] thus creating a tortuosity effect. In nanocomposites, the increase of the penetrant diffusion path and the decrease of the volume fraction of permeable phase are considered as the main factors at the origin of the permeability decrease. If the fraction of permeable phase depends on the filler volume fraction, the tortuosity depends on several factors: the initial filler shape, the filler volume amount, the filler dispersion state that is at the origin of the size and aspect ratio of the impermeable dispersed domains [14], [16]. Moreover, in the case of non-spherical domains, their orientation with respect to the gas diffusion path can also play a major role. As different nanofiller shapes were selected in our work, the relative permeability values of the nanocomposites are at first discussed for each filler category. **Table A.9** summarizes the different models that have been used to describe the experimental results.

The relative permeability values for spherical fillers (silica and silver nanoparticles) are shown in **Figure A.15a**. Regardless of the diffusing molecules, i.e. O_2 or H_2O, all samples exhibit better barrier properties than the reference film. Moreover, considering the uncertainty on permeability values, all data define a single curve. The obtained relative permeability values are similar to those obtained by Morel *et al.* for calcium carbonate spherical nanoparticles (relative permeability around 0.95 for 4 vol% for nanofillers) [10]. It is noteworthy that the relative permeability values do not seem to depend on the nanofiller dispersion state as the fine dispersion of silica evidenced for PLA/SiOH/4 and PLA/$SiCH_3$/4 leads, for the same filler content, to similar relative permeability values as the silver aggregates observed for PLA/Ag/3 and PLA/Ag/4. It can then be concluded in the case of spherical fillers, that only the filler content is a discriminative parameter for barrier properties. Considering this conclusion, Maxwell model has been used to describe the evolution of relative permeability coefficients of the nanocomposite series based on spherical fillers. The Maxwell equation reported in

Table A.9 is commonly used for describing the evolution of relative permeability of nanocomposites polymers containing spherical impermeable fillers [10], [46], [47], [48]. The model provides permeability as a function of a single parameter: the content of impermeable phase volume (Φ_v) (**Table A.9**). As shown by the solid line in **Figure A.15** and root mean square deviation value (RMSD) reported in **Table A.9**, and considering experimental uncertainties, Maxwell model gives a good description of the relative permeability for the nanocomposite series based on hydrophilic silica, hydrophobic silica and silver.

Halloysite nanotubes (HNT) also lead to increased barrier properties as demonstrated in **Figure A.15b**. Here again, similar relative permeability decrease is obtained, regardless of the diffusing molecule, e.g. O_2 or H_2O. Compared to the study of Guo *et al.* [21], relative permeability values measured for our systems are slightly lower for a same halloysite content (e.g. 0.87 in our case for a halloysite content of 4 vol% compared to 0.98). Moreover, from the comparison of the data presented in **Figure A.15a and A.15b**, it can be concluded that nanocomposites based on nanotubes exhibit superior barrier properties compared to nanocomposites based on spherical fillers. A previous work coupling experimental analyses and Finite Element Modeling on tubular based nanocomposites has underlined that the diffusion path, in such systems, could be viewed as resulting from both diffusion around the tube diameter and along the tube length, the first contribution being predominant [49]. Due to these two contributions, Maxwell law was inefficient to describe the permeability in such systems. On the other hand and as it was shown that halloysite tubes were mostly lying in the plane of the film, Nielsen model, which is usually used for nanocomposites containing platelets [6], [14], [50], [51] could be appropriate. This model depends on the volume content as well as the mean aspect ratio (α) of the impermeable phase. The experimental relative permeability values obtained on the nanocomposites based on halloysite nanotubes were described with accuracy for an α value of 5 (**Figure A.15**) in agreement with the study of Htira *et al.* [49].

As shown in **Figure A.15c**, the use of organo-modified montmorillonites exhibits a significantly greater decrease in relative permeability as compared to spherical fillers and halloysite nanotubes. Extensive researches in the literature has demonstrated the high efficiency of this type of filler in enhancing barrier properties [2], [8], [9], [52], due to the high mean aspect

ratio achieved when fine filler dispersion state was obtained (e.g. exfoliated or intercalated structures). Our morphological analysis has underlined that in our nanocomposites, the great majority of fillers are dispersed in the form of quasi-individual sheets with random orientation. It has also to be noticed that the relative permeability values measured are similar to those found in the literature for the same kind of systems [6], [7]. Bharadwaj model [5] developed for modelling the barrier properties of nanocomposite with different possible orientation of platelet like fillers nanocomposites was chosen to fit the permeability behavior of PLA/OMMT nanocomposites. The value of the parameter *S* was fixed at 0 which reflects a random orientation of the filler in the matrix as evidenced by microscopic observations. The fitting result is presented in **Figure A.15c** for an aspect ratio value (α) of 80, which corresponds to the mean aspect ratio calculated from our morphological analysis. As shown by the theoretical curve and the RMSD value (**Figure A.15** and **Table A.9**), a good agreement is observed between experimental and calculated values.

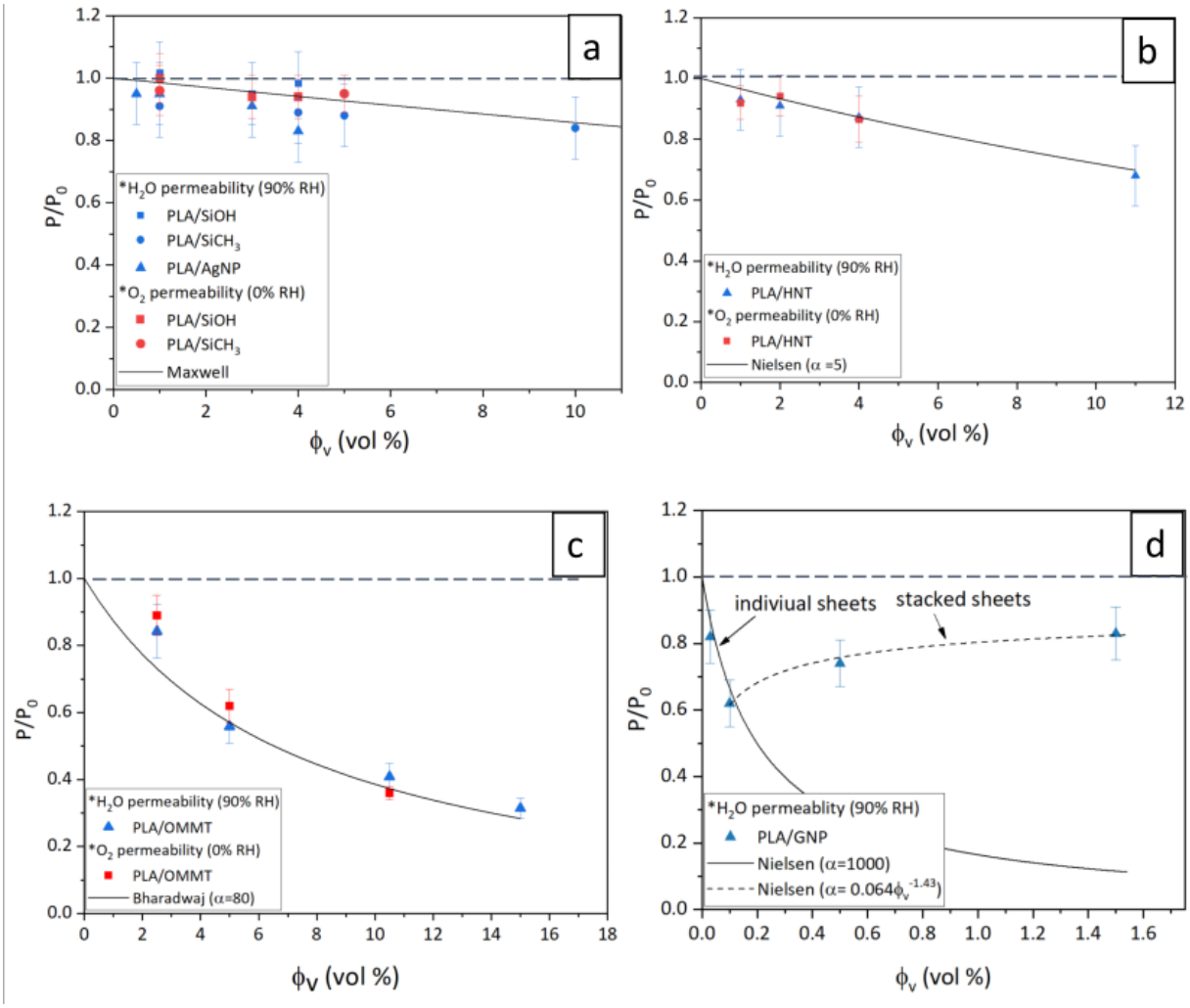


Figure A.15 - Relative permeability as a function of the volume fraction of the different types of impermeable phase (a) spherical fillers, (b) halloysite nanotubes, (c) organo-modified montmorillonites and (d) graphene. Blue symbols stand for water vapor permeability and red symbols stand for dioxygen permeability. The dotted line (---) corresponds to a relative permeability of 1.

The addition of graphene in the PLA matrix leads to a non-monotonous evolution of the relative permeability as a function of the filler amount. Indeed, **Figure A.15d** shows a sharp decrease of the relative permeability below 0.1 vol% GNP leading to a relative permeability value of 0.62 for 0.1 vol% of graphene. For this low GNP content, by taking into account that the GNPs are lying in the film plane, a filler aspect ratio value (α) of 1000 is calculated from Nielsen laws. This aspect ratio value corresponds to that obtained from microscopic observations. However, at higher GNP content (>0.1 vol%), the relative permeability increases with the GNP volume content. This behavior is different from the other filler types but not

very surprising according to our morphological analysis which shows agglomerated sheets with low aspect ratio. This behavior in "V" shape has already been reported in the literature in case of PLA filled with graphene [53], [54]. For these GNP contents the Nielsen model provides aspect ratio values of 140 and 25 for 0.5 vol% GNP and 1.5 vol% GNP, respectively which is in good agreement with microscopy observations. From these calculated aspect ratio values, equation (A.9) was proposed to describe the evolution of the aspect ratio as a function of the GNP volume content for GNP > 0.1 vol% (**Figure A.16**).

$$\alpha = 0.064\Phi_v{}^{-1.43} \qquad (A.9)$$

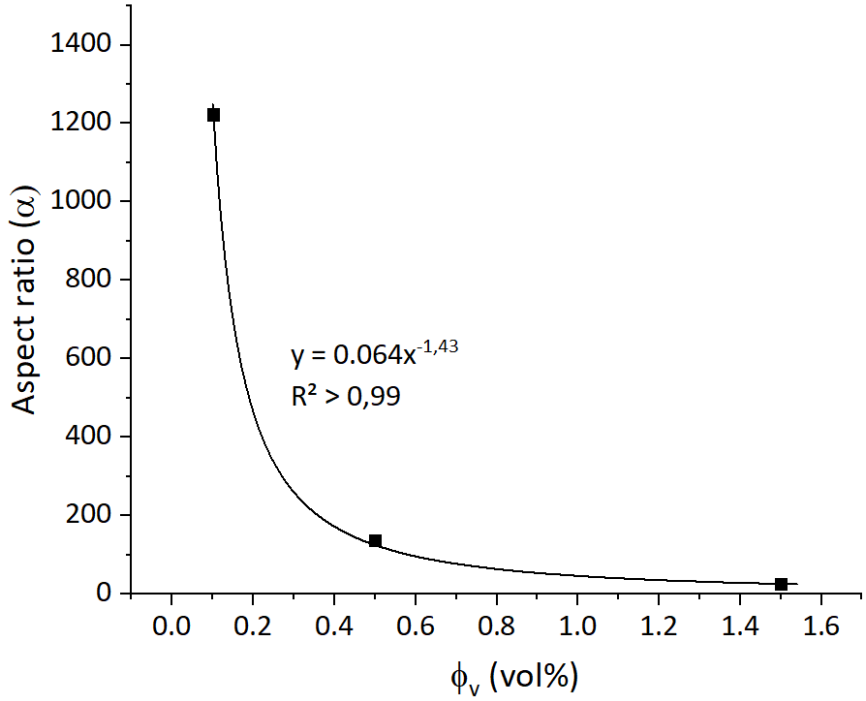


Figure A.16 - Evolution of the theoretical aspect ratio (calculated form the Nielsen equation) with the graphene volume content.

Combination of equation (A.9) and Nielsen model allowed to accurately describe the experimental relative permeability values above 0.1 vol% GNP (**Figure A.15d**).

These experimental results confirm, as expected, that the decrease of the relative permeability observed for nanocomposites highly depends on the amount and aspect ratio of the dispersed impermeable phase.

Table A.9 – Permeability models used in this work for the different types of impermeable phase.

Impermeable phase	Permeability model	Parameters value	RMSD
Spherical	***Maxwell model*** [55] $\frac{P}{P_0} = \frac{1-\Phi_v}{1+\frac{1}{2}\Phi_v}$	$\Phi_v = 0-10\%$	*0.07 (calculated for PLA/$SiCH_3$)*
HNT nanotubes	***Nielsen model*** [50] $\frac{P}{P_0} = \frac{1-\Phi_v}{1+\frac{\alpha}{2}\Phi_v}$	$\Phi_v = 0-10\%$ *α = 5*	0.02
Organo-modified montmorillonite	***Bharadwaj model*** [5] $\frac{P}{P_0} = \frac{1-\phi_v}{1+\frac{\alpha}{2}\Phi_v\frac{2}{3}(S+\frac{1}{2})}$	$\Phi_v = 0-15\%$ *α = 80* *S = 0*	0.06
Graphene	***Nielsen model*** [50] $\frac{P}{P_0} = \frac{1-\Phi_v}{1+\frac{\alpha}{2}\Phi_v}$	$\Phi_v = 0-0.1\%$ *α = 1000*	/
		$\Phi_v = 0.1-1.5\%$ $\alpha = 0.064{\phi_v}^{-1.43}$	/
Spherolites	***Michaels model*** [22] , [23] $\frac{P}{P_0} = \frac{1-\chi_c}{\left(1+\frac{1}{2}\chi_c\right)\beta}$	$\beta = 1$ $\chi_c = 0-50\%$	0.11
		$\beta = 1+\chi_c$ $\chi_c = 0-50\%$	0.06

Φv: filler content, α : aspect ratio, S: orientation parameter , β : chain immobilization factor, χ_c : degree of crystallinity.

Except impermeable fillers, another type of phase which is organic can usually be considered as an impermeable phase. It is the crystalline phase in semi-crystalline polymers [22], [24], [56]. **Figure A.17** confirms the improvement of barrier properties in annealed PLA by showing a significant decrease of the relative permeability as the degree of crystallinity increases. In addition, the permeability results remain unaffected by the annealing temperature due to the similarity in morphology. The results are consistent with previous studies on PDLLA films annealed at the same range of temperatures [6], [24], [25]. One aim of this work was to compare the effects of fillers and crystalline phase on the barrier properties. By comparing the results of **Figure A.15** and **Figure A.17**, it can be observed that for the same amount of

impermeable phase (10 vol%), P/P_0 (PLA/$SiCH_3$/10) > P/P_0 (PLA/110°C/10) > P/P_0 (PLA/HNT/10) > P/P_0 (PLA/OMMT/10).

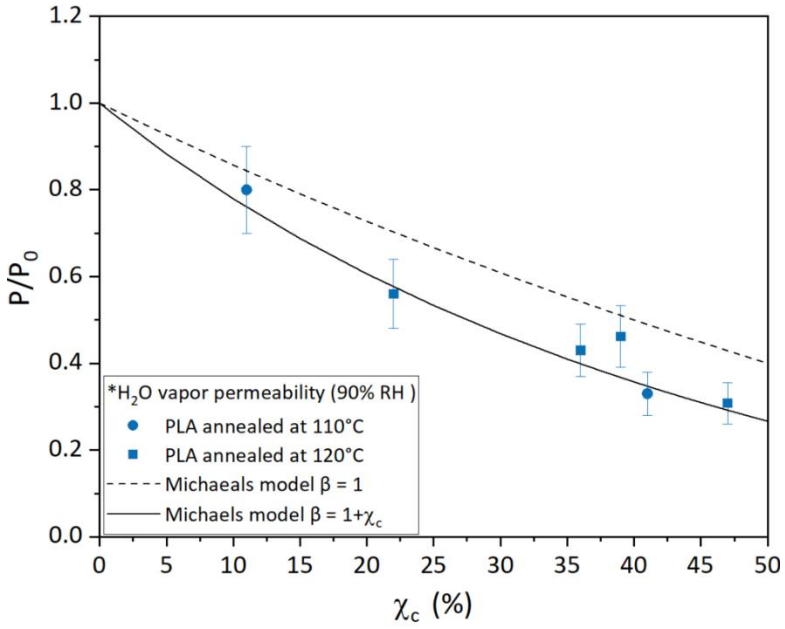


Figure A.17 - Relative permeability as a function of the degree of crystallinity for annealed PLA at 110 °C and 120 °C.

Thus, the crystalline phase leads to a higher permeability decrease than impermeable spheres and much lower than platelet like fillers. In fact, semi-crystalline polymers are complex systems in which coexist the amorphous permeable phase and the crystalline impermeable phase with polymer chains belonging to both phases. The morphology of the crystalline phase consists of crystalline lamellae whose size and aspect ratio can vary depending on the degree of crystallinity and processing conditions [24], [25], [57]. Literature based on modeling shows different trends concerning the effect of the crystallites size on barrier properties. According to Fricke model, the diffusion is more efficiently blocked in the case of wide and thin crystals [23]. However, Nilsson *et al.* [58] showed that in the case of spherolite type morphology, the size of the crystallites had no significant effect on the permeability. For our studied samples, crystallites are organized into spherolites shape with amorphous phase in between the crystallites. Concerning the amorphous phase, a particular attention has to be paid on the role of the interfacial area between crystallite and amorphous phase. As already discussed, polymer chains at the interface could be constrained leading to different chain mobility with respect to chains in the heart of the intercrystallite amorphous region. As already explained,

the *RAF* is representative of the amount of constrained amorphous phase. Different studies have investigated the role of *RAF* on the transport properties of annealed PLA and shows that it has an influence of the permeability [24], [25], [42].

To go further in our analysis on the potential effect of *RAF*, a confrontation of experimental relative permeability values with calculated values from the two phases Michaels model [22], [23] has been made (equation (A.10)).

$$\frac{P}{P_0} = \frac{\Phi_a}{\tau\beta} \qquad (A.10)$$

In this model, Φ_a is the amorphous fraction, τ the tortuosity factor. The authors showed that the β factor, which represents the immobilization of the amorphous chains by the crystallites, is equal to 1 for amorphous polymer and can increase more or less regularly when the fraction of amorphous phase decreases. Concerning the tortuosity factor, by making analogy between electrical conductivity and gas permeability it has been considered that for a spherolitic morphology, the tortuosity factor τ can be written according to equation (A.11) [22]**:**

$$\tau = 1 + \frac{(1 - \Phi_a)}{2} \qquad (A.11)$$

The relative permeability of our semi-crystalline systems has first been fitted with the Micheals model considering that β = 1. A non-negligible error is noted, especially for the higher degree of crystallinity. Thus, to accurately fit the experimental data (RMSD = 0.06) the β factor was gradually increased from 1 for χ_c = 0% to 1.5 for χ_c = 50% to reflect the decrease of the inter-lamellae spacing leading to the increase of the *RAF*.

Finally, thanks to the different models of permeability used to describe the experimental results in the most accurate way, an equivalence diagram has been built (**Figure A.18**) with the aim to make possible to compare the efficiency of the different fillers with respect to crystallinity in terms of barrier properties. The composition domain considered is the domain corresponding to fillers amount less than 15 vol% for which the models could be validated by experimental data. In **Figure A.18**, the full lines represent the evolution of the relative permeability as a function of the volume amount of different filler types (spheres, tubes and platelets). The two Y axes directly show the impact of the crystallinity degree on the relative

permeability. The dotted line represents a theoretical perfect equivalence between the crystalline phase and the fillers. From the proposed representation, it can at first be seen that the curves relative to graphene, montmorillonite and halloysite are above the dotted line, showing a better efficiency of these fillers to reduce the permeability with respect to crystallinity. On the other hand, the curve relative to spherical fillers is below the dotted line. It is also easy to know the volume of each type of phase needed to achieve a given relative permeability value. For example, 8 vol% of crystalline phase would have the same efficiency on permeability than 0.05 vol% of GNP, 2 vol% of OMMT or 7.5 vol% of HNT or 15 vol% of spherical fillers. All these possibilities would lead to a relative permeability of 0.8.

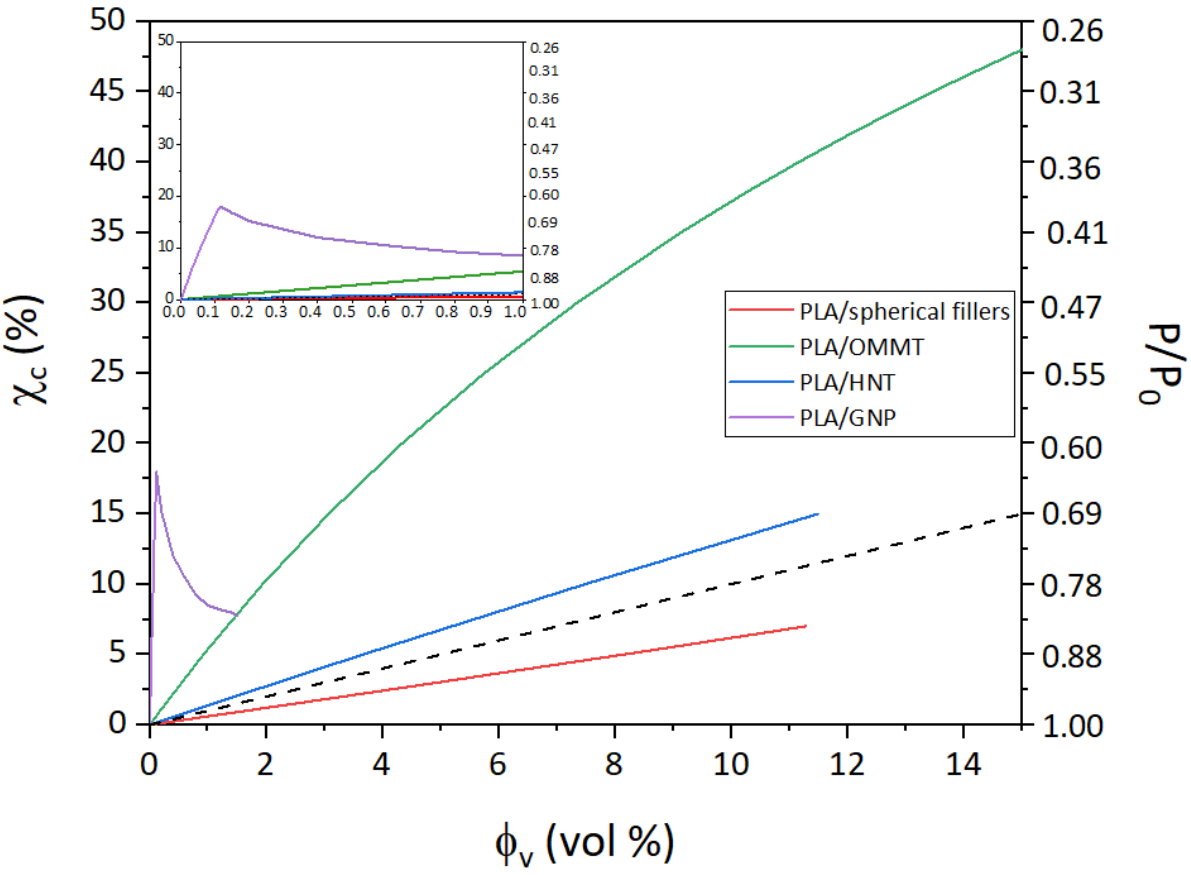


Figure A.18 - Equivalence between the different types of fillers and the crystalline phase content in term of permeability. The dotted line represents theoretical perfect equivalence between the crystallinity and the fillers.

5. Conclusion

In this work, PLA films containing different kinds of impermeable domains were prepared. Amorphous PLA nanocomposite films with different types of fillers (lamellae, spherical and

nanotubes) were made by melt-blending and semi crystalline PLA were obtained by thermal treatments. The filler content ranged from 0 to 15 vol%, and crystallization degree up to 50 %.

Permeability of the films decreases whatever the type of impermeable phase, but different trends were observed. Thanks to in-depth analysis of samples microstructure, microstructure-permeability relations have been established. For the nanocomposite film series, the aspect ratio of the dispersed fillers is the most discriminant factor by increasing tortuosity effect. Consequently, for a same filler content, permeability of PLA filled with lamellar fillers was lower than spherical and tubular filler-based nanocomposites. Among the studied nanofillers, graphene led to the highest barrier properties with a relative permeability of 0.6 for 0.1 vol% but should be used at low amount due to aggregation phenomena observed as soon as 0.1 vol% of graphene. For semi-crystalline PLA, permeability decreased with the increase of crystallinity and the decrease of amorphous chain mobility.

Moreover, the detailed study of the microstructure in relation to permeability allowed to identify for each investigated materials series the governing factors and therefore to identify permeability models and their optimum parameters to accurately fit the experimental data. Finally, and for the first time, an equivalence between crystalline content and fillers content was established. In this way the effect of each type of fillers (up to 15 vol%) on permeability and the equivalent crystallinity degree can be predicted.

6. References

[1] Bioplastics market development update 2023, European Bioplastics e.V (2023). https://www.european-bioplastics.org/market/ (accessed August 20, 2024).

[2] S. Sinha Ray, K. Yamada, M. Okamoto, A. Ogami, K. Ueda, New Polylactide/Layered Silicate Nanocomposites. 3. High-Performance Biodegradable Materials, Chem. Mater. 15 (2003) 1456–1465. https://doi.org/10.1021/cm020953r.

[3] J.-H. Chang, Y.U. An, G.S. Sur, Poly(lactic acid) nanocomposites with various organoclays. I. Thermomechanical properties, morphology, and gas permeability, Journal of Polymer Science Part B: Polymer Physics 41 (2003) 94–103. https://doi.org/10.1002/polb.10349.

[4] A.A. Arman Alim, S.S. Mohammad Shirajuddin, F.H. Anuar, A Review of Nonbiodegradable and Biodegradable Composites for Food Packaging Application, Journal of Chemistry 2022 (2022) 7670819. https://doi.org/10.1155/2022/7670819.

[5] R.K. Bharadwaj, Modeling the Barrier Properties of Polymer-Layered Silicate Nanocomposites, Macromolecules 34 (2001) 9189–9192. https://doi.org/10.1021/ma010780b.

[6] E. Picard, E. Espuche, R. Fulchiron, Effect of an organo-modified montmorillonite on PLA crystallization and gas barrier properties, Applied Clay Science 53 (2011) 58–65. https://doi.org/10.1016/j.clay.2011.04.023.

[7] N. Tenn, N. Follain, J. Soulestin, R. Crétois, S. Bourbigot, S. Marais, Effect of Nanoclay Hydration on Barrier Properties of PLA/Montmorillonite Based Nanocomposites, J. Phys. Chem. C 117 (2013) 12117–12135. https://doi.org/10.1021/jp401546t.

[8] S. Sinha Ray, K. Yamada, M. Okamoto, Y. Fujimoto, A. Ogami, K. Ueda, New polylactide/layered silicate nanocomposites. 5. Designing of materials with desired properties, Polymer 44 (2003) 6633–6646. https://doi.org/10.1016/j.polymer.2003.08.021.

[9] F. Li, C. Zhang, Y. Weng, Improvement of the Gas Barrier Properties of PLA/OMMT Films by Regulating the Interlayer Spacing of OMMT and the Crystallinity of PLA, ACS Omega 5 (2020) 18675–18684. https://doi.org/10.1021/acsomega.0c01405.

[10] F. Morel, E. Espuche, V. Bounor-Legaré, O. Persynn, M. Lacroix, Impact of coated calcium carbonate nanofillers and annealing treatments on the microstructure and gas barrier properties of poly(lactide) based nanocomposite films, Journal of Polymer Science Part B: Polymer Physics 54 (2016) 649–658. https://doi.org/10.1002/polb.23957.

[11] P. Cheviron, F. Gouanvé, E. Espuche, Effect of silver nanoparticles' generation routes on the morphology, oxygen, and water transport properties of starch nanocomposite films, J Nanopart Res 17 (2015) 364. https://doi.org/10.1007/s11051-015-3173-4.

[12] W.L. Tham, B.T. Poh, Z.A. Mohd Ishak, W.S. Chow, Transparent poly(lactic acid)/halloysite nanotube nanocomposites with improved oxygen barrier and antioxidant properties, J Therm Anal Calorim 126 (2016) 1331–1337. https://doi.org/10.1007/s10973-016-5834-7.

[13] G. Gorrasi, R. Pantani, M. Murariu, P. Dubois, PLA/Halloysite Nanocomposite Films: Water Vapor Barrier Properties and Specific Key Characteristics, Macromolecular Materials and Engineering 299 (2014) 104–115. https://doi.org/10.1002/mame.201200424.

[14] S. Singha, M.S. Hedenqvist, A Review on Barrier Properties of Poly(Lactic Acid)/Clay Nanocomposites, Polymers 12 (2020) 1095. https://doi.org/10.3390/polym12051095.
[15] E. Espuche, Nanocomposites for gas barrier applications: Governing factors, single and coupled effects, new routes to optimise the function properties, Polymer Testing 125 (2023) 108124. https://doi.org/10.1016/j.polymertesting.2023.108124.
[16] E. Picard, A. Vermogen, J.-F. Gérard, E. Espuche, Barrier properties of nylon 6-montmorillonite nanocomposite membranes prepared by melt blending: Influence of the clay content and dispersion state: Consequences on modelling, Journal of Membrane Science 292 (2007) 133–144. https://doi.org/10.1016/j.memsci.2007.01.030.
[17] E. Picard, J.-F. Gérard, E. Espuche, Reinforcement of the Gas Barrier Properties of Polyethylene and Polyamide Through the Nanocomposite Approach: Key Factors and Limitations, Oil Gas Sci. Technol. – Rev. IFP Energies Nouvelles 70 (2015) 237–249. https://doi.org/10.2516/ogst/2013145.
[18] O. Gain, E. Espuche, E. Pollet, M. Alexandre, Ph. Dubois, Gas barrier properties of poly(ε-caprolactone)/clay nanocomposites: Influence of the morphology and polymer/clay interactions, Journal of Polymer Science Part B: Polymer Physics 43 (2005) 205–214. https://doi.org/10.1002/polb.20316.
[19] J. Trifol, D. Plackett, C. Sillard, O. Hassager, A.E. Daugaard, J. Bras, P. Szabo, A comparison of partially acetylated nanocellulose, nanocrystalline cellulose, and nanoclay as fillers for high-performance polylactide nanocomposites, Journal of Applied Polymer Science 133 (2016) 43257. https://doi.org/10.1002/app.43257.
[20] L. Petersson, K. Oksman, Biopolymer based nanocomposites: Comparing layered silicates and microcrystalline cellulose as nanoreinforcement, Composites Science and Technology 66 (2006) 2187–2196. https://doi.org/10.1016/j.compscitech.2005.12.010.
[21] Y. Guo, K. Yang, X. Zuo, Y. Xue, C. Marmorat, Y. Liu, C.-C. Chang, M.H. Rafailovich, Effects of clay platelets and natural nanotubes on mechanical properties and gas permeability of Poly (lactic acid) nanocomposites, Polymer 83 (2016) 246–259. https://doi.org/10.1016/j.polymer.2015.12.012.
[22] A.S. Michaels, R.B. Parker Jr., Sorption and flow of gases in polyethylene, Journal of Polymer Science 41 (1959) 53–71. https://doi.org/10.1002/pol.1959.1204113805.
[23] A.S. Michaels, H.J. Bixler, Flow of gases through polyethylene, Journal of Polymer Science 50 (1961) 413–439. https://doi.org/10.1002/pol.1961.1205015412.
[24] A. Guinault, C. Sollogoub, V. Ducruet, S. Domenek, Impact of crystallinity of poly(lactide) on helium and oxygen barrier properties, European Polymer Journal 48 (2012) 779–788. https://doi.org/10.1016/j.eurpolymj.2012.01.014.
[25] M. Drieskens, R. Peeters, J. Mullens, D. Franco, P.J. Lemstra, D.G. Hristova-Bogaerds, Structure versus properties relationship of poly(lactic acid). I. Effect of crystallinity on barrier properties: Structure Vs. Barrier Properties of PLA, J. Polym. Sci. B Polym. Phys. 47 (2009) 2247–2258. https://doi.org/10.1002/polb.21822.
[26] N. Delpouve, A. Saiter, J.F. Mano, E. Dargent, Cooperative rearranging region size in semi-crystalline poly(l-lactic acid), Polymer 49 (2008) 3130–3135. https://doi.org/10.1016/j.polymer.2008.04.045.
[27] S. Fernandes Nassar, A. Guinault, N. Delpouve, V. Divry, V. Ducruet, C. Sollogoub, S. Domenek, Multi-scale analysis of the impact of polylactide morphology on gas barrier properties, Polymer 108 (2017) 163–172. https://doi.org/10.1016/j.polymer.2016.11.047.

[28] B. Kalb, A.J. Pennings, General crystallization behaviour of poly(l-lactic acid), Polymer 21 (1980) 607–612. https://doi.org/10.1016/0032-3861(80)90315-8.
[29] F.-D. Kopinke, M. Remmler, K. Mackenzie, M. Möder, O. Wachsen, Thermal decomposition of biodegradable polyesters—II. Poly(lactic acid), Polymer Degradation and Stability 53 (1996) 329–342. https://doi.org/10.1016/0141-3910(96)00102-4.
[30] X. Monnier, D. Cavallo, M.C. Righetti, M.L. Di Lorenzo, S. Marina, J. Martin, D. Cangialosi, Physical Aging and Glass Transition of the Rigid Amorphous Fraction in Poly(l-lactic acid), Macromolecules 53 (2020) 8741–8750. https://doi.org/10.1021/acs.macromol.0c01182.
[31] S.-M. Lai, Y.-T. Hsieh, Preparation and Properties of Polylactic Acid (PLA)/Silica Nanocomposites, Journal of Macromolecular Science, Part B 55 (2016) 211–228. https://doi.org/10.1080/00222348.2016.1138179.
[32] J. Sepulveda, C. Villegas, A. Torres, E. Vargas, F. Rodriguez, S. Baltazar, A. Prada, A. Rojas, J. Romero, S. Faba, M.J. Galotto, Effect of functionalized silica nanoparticles on the mass transfer process in active PLA nanocomposite films obtained by supercritical impregnation for sustainable food packaging, The Journal of Supercritical Fluids 161 (2020) 104844. https://doi.org/10.1016/j.supflu.2020.104844.
[33] A. Vermogen, K. Masenelli-Varlot, R. Séguéla, J. Duchet-Rumeau, S. Boucard, P. Prele, Evaluation of the Structure and Dispersion in Polymer-Layered Silicate Nanocomposites, Macromolecules 38 (2005) 9661–9669. https://doi.org/10.1021/ma051249+.
[34] P. Song, G. Chen, Z. Wei, W. Zhang, J. Liang, Calorimetric analysis of the multiple melting behavior of melt-crystallized poly(l-lactic acid) with a low optical purity, J Therm Anal Calorim 111 (2013) 1507–1514. https://doi.org/10.1007/s10973-012-2502-4.
[35] Z. Wei, P. Song, C. Zhou, G. Chen, Y. Chang, J. Li, W. Zhang, J. Liang, Insight into the annealing peak and microstructural changes of poly(l-lactic acid) by annealing at elevated temperatures, Polymer 54 (2013) 3377–3384. https://doi.org/10.1016/j.polymer.2013.04.027.
[36] M. Cocca, M.L.D. Lorenzo, M. Malinconico, V. Frezza, Influence of crystal polymorphism on mechanical and barrier properties of poly(l-lactic acid), European Polymer Journal 47 (2011) 1073–1080. https://doi.org/10.1016/j.eurpolymj.2011.02.009.
[37] J. Zhang, K. Tashiro, H. Tsuji, A.J. Domb, Disorder-to-Order Phase Transition and Multiple Melting Behavior of Poly(l-lactide) Investigated by Simultaneous Measurements of WAXD and DSC, Macromolecules 41 (2008) 1352–1357. https://doi.org/10.1021/ma0706071.
[38] P. Pan, W. Kai, B. Zhu, T. Dong, Y. Inoue, Polymorphous Crystallization and Multiple Melting Behavior of Poly(l-lactide): Molecular Weight Dependence, Macromolecules 40 (2007) 6898–6905. https://doi.org/10.1021/ma071258d.
[39] D. Brizzolara, H.-J. Cantow, K. Diederichs, E. Keller, A.J. Domb, Mechanism of the Stereocomplex Formation between Enantiomeric Poly(lactide)s, Macromolecules 29 (1996) 191–197. https://doi.org/10.1021/ma951144e.
[40] N. Delpouve, A. Saiter, E. Dargent, RIGID AND MOBILE AMORPHOUS FRACTIONS IN TWO POLY(LACTIC ACID), 8th World Congress of Chemical Engineering, Montreal (2009).
[41] M. Arnoult, E. Dargent, J.F. Mano, Mobile amorphous phase fragility in semi-crystalline polymers: Comparison of PET and PLLA, Polymer 48 (2007) 1012–1019. https://doi.org/10.1016/j.polymer.2006.12.053.

[42] A. Sangroniz, A. Chaos, M. Iriarte, J. del Río, J.-R. Sarasua, A. Etxeberria, Influence of the Rigid Amorphous Fraction and Crystallinity on Polylactide Transport Properties, Macromolecules 51 (2018) 3923–3931. https://doi.org/10.1021/acs.macromol.8b00833.

[43] H.C. Koh, J.S. Park, M.A. Jeong, H.Y. Hwang, Y.T. Hong, S.Y. Ha, S.Y. Nam, Preparation and gas permeation properties of biodegradable polymer/layered silicate nanocomposite membranes, Desalination 233 (2008) 201–209. https://doi.org/10.1016/j.desal.2007.09.043.

[44] M.A. Ortenzi, L. Basilissi, H. Farina, G. Di Silvestro, L. Piergiovanni, E. Mascheroni, Evaluation of crystallinity and gas barrier properties of films obtained from PLA nanocomposites synthesized via "in situ" polymerization of l-lactide with silane-modified nanosilica and montmorillonite, European Polymer Journal 66 (2015) 478–491. https://doi.org/10.1016/j.eurpolymj.2015.03.006.

[45] J.-W. Rhim, S.-I. Hong, C.-S. Ha, Tensile, water vapor barrier and antimicrobial properties of PLA/nanoclay composite films, LWT - Food Science and Technology 42 (2009) 612–617. https://doi.org/10.1016/j.lwt.2008.02.015.

[46] R.L. Hamilton, Water Vapor Permeability of Polyethylene and Other Plastic Materials, Bell System Technical Journal 46 (1967) 391–415. https://doi.org/10.1002/j.1538-7305.1967.tb01064.x.

[47] M.L. De Haro, J.A.P. Del Río, S. Whitaker, Flow of Maxwell fluids in porous media, Transp Porous Med 25 (1996) 167–192. https://doi.org/10.1007/BF00135854.

[48] S.A. Hashemifard, A.F. Ismail, T. Matsuura, Prediction of gas permeability in mixed matrix membranes using theoretical models, Journal of Membrane Science 347 (2010) 53–61. https://doi.org/10.1016/j.memsci.2009.10.005.

[49] T. Htira, S. Zid, M. Zinet, E. Espuche, Finite Element Analysis of Gas Diffusion in Polymer Nanocomposite Systems Containing Rod-like Nanofillers, Polymers 13 (2021) 2615. https://doi.org/10.3390/polym13162615.

[50] L.E. Nielsen, Models for the Permeability of Filled Polymer Systems, Journal of Macromolecular Science—Chemistry (1967). https://doi.org/10.1080/10601326708053745.

[51] G. Choudalakis, A.D. Gotsis, Permeability of polymer/clay nanocomposites: A review, European Polymer Journal 45 (2009) 967–984. https://doi.org/10.1016/j.eurpolymj.2009.01.027.

[52] C. Thellen, C. Orroth, D. Froio, D. Ziegler, J. Lucciarini, R. Farrell, N.A. D'Souza, J.A. Ratto, Influence of montmorillonite layered silicate on plasticized poly(l-lactide) blown films, Polymer 46 (2005) 11716–11727. https://doi.org/10.1016/j.polymer.2005.09.057.

[53] F. Li, C. Zhang, Y. Weng, X. Diao, Y. Zhou, X. Song, Enhancement of Gas Barrier Properties of Graphene Oxide/Poly (Lactic Acid) Films Using a Solvent-free Method, Materials 13 (2020) 3024. https://doi.org/10.3390/ma13133024.

[54] A.M. Pinto, J. Cabral, D.A.P. Tanaka, A.M. Mendes, F.D. Magalhães, Effect of incorporation of graphene oxide and graphene nanoplatelets on mechanical and gas permeability properties of poly(lactic acid) films, Polymer International 62 (2013) 33–40. https://doi.org/10.1002/pi.4290.

[55] J.C. Maxwell, A Treatise on Electricity and Magnetism, Clarendon Press (1873).

[56] C. Courgneau, S. Domenek, R. Lebossé, A. Guinault, L. Avérous, V. Ducruet, Effect of crystallization on barrier properties of formulated polylactide, Polymer International 61 (2012) 180–189. https://doi.org/10.1002/pi.3167.

[57] H. Tsuji, Y. Tezuka, Stereocomplex Formation between Enantiomeric Poly(lactic acid)s. 12. Spherulite Growth of Low-Molecular-Weight Poly(lactic acid)s from the Melt, Biomacromolecules 5 (2004) 1181–1186. https://doi.org/10.1021/bm049835i.

[58] F. Nilsson, U.W. Gedde, M.S. Hedenqvist, Penetrant diffusion in polyethylene spherulites assessed by a novel off-lattice Monte-Carlo technique, European Polymer Journal 45 (2009) 3409–3417. https://doi.org/10.1016/j.eurpolymj.2009.09.018.

Cette première partie portait sur l'étude de l'influence de la nature de la phase imperméable sur la perméabilité de PLA. Pour cela des PLA avec des taux de cristallinité de 0 à 50 % ont été obtenus par traitement thermique et des nanocomposites ont été préparés par mélange en voie fondue avec un taux de charges de 0 à 15 %vol. Une étude détaillée de la microstructure des matériaux a été effectuée afin d'identifier les facteurs gouvernant la perméabilité. Ainsi, le taux de phase imperméable, la forme initiale des charges, la qualité de la dispersion de la phase imperméable au sein de la matrice (facteur de forme, orientation des domaines dispersés par rapport au flux de diffusion, distance entre les domaines imperméables, fraction d'agrégats) et la fraction amorphe rigide ont été les facteurs les plus discriminants sur la perméabilité. À partir de ces paramètres, des modèles de perméabilité ont été utilisés et ajustés pour décrire au mieux les valeurs expérimentales. Ces modèles théoriques constituent une première approche afin de proposer des paramètres matériaux permettant de satisfaire une certaine perméabilité. Cependant, d'autres facteurs tels que le procédé d'élaboration des nanocomposites pourraient également influencer la perméabilité. Ceci fait donc l'objet de la deuxième partie de ce chapitre. Dans cette étude, deux procédés d'élaboration permettant d'obtenir des nanocomposites PLA amorphes ont été comparés : le mélange par voie fondue et la polymérisation *in situ*. Le caractère amorphe de la matrice est essentiel à préserver afin de s'affranchir de l'influence de la phase cristalline et ne conserver qu'une seule phase imperméable. Deux charges imperméables ont été judicieusement été choisies pour cette étude : une silice hydrophobe et une montmorillonite modifiée avec un cation organique hydrophile. L'intérêt de ce choix et qu'il permet, à travers une gamme réduite de charges est donc d'échantillons, de pouvoir étudier l'influence du procédé avec des charges de natures et de formes différentes. Cette deuxième étude est rédigée sous la forme d'un article à soumettre pour publication.

Chapitre III.B - PLA nanocomposites based on silica and organo-modified montmorillonite: a comparative investigation of different solvent-free synthesis routes on morphology and water permeability

1. Abstract ***138***

2. Introduction ***138***

3. Experimental ***141***

3.1. Materials **141**

3.2. Preparation of the nanocomposites **142**

3.2. a) Melt-blending route 142

3.2. b) *In situ* polymerization route 142

3.3. Film preparation **144**

3.4. Characterization **144**

3.4. a) Size exclusion chromatography (SEC) 144

3.4. b) Nuclear Magnetic Resonance (NMR) 145

3.4. c) Infrared spectroscopy (FTIR) 145

3.4. d) Thermal analysis 145

3.4. e) Nanofiller dispersion analysis 146

3.4. f) Permeability measurements 147

4. Results and discussion ***147***

4.1. Physicochemical and morphological characterization of nanocomposites series as a function of the synthesis route **147**

4.1. a) Silica nanocomposites 148

4.1. b) Montmorillonite nanocomposites 154

4.2. Permeability of nanocomposites: melt blending vs *in situ* polymerization. **163**

5. Conclusion ***166***

6. References ***168***

1. Abstract

Amorphous PLA nanocomposites based on hydrophobic silica or organo-modified montmorillonite (Cloisite®30B) have been prepared according to two different routes: melt-blending for a filler content up to 10 vol% and *in situ* polymerization for a filler content up to 7 vol%. The process and conditions used for *in situ* polymerization have been optimized for each filler type in order to obtain non-brittle self-standing films. While direct reactive processing could be successfully carried out for *in situ* polymerization in the presence of silica, a two-step process had to be used and optimized with montmorillonite. Based on the obtained nanocomposite series, filler dispersion as well as filler/matrix interactions have been investigated and discussed as a function of the synthesis route and filler type. The water vapor barrier properties have been determined leading to conclude that *in situ* polymerization route appears to be particularly efficient to decrease the permeability of highly filled PLA, whatever the filler type.

2. Introduction

Poly(lactic) acid (PLA) is a biobased polyester derived from sugar fermentation and currently represents approximately 60 wt% of the total quantity of biodegradable polymers produced for packaging [1]. Market adoption of PLA could be expanded by improving its barrier properties. The incorporation of nanofillers has been demonstrated to be an effective method for achieving such objective [2], [3], [4], [5]. Indeed, nanofillers are an efficient way to create a tortuosity effect which depends on the filler content, its dispersion state and aspect ratio in the matrix [6], [7]. Usually, the better the dispersion is the greater tortuosity effect is obtained [8].

In most cases the fillers are incorporated into the polymer via melt blending process, which is an efficient and environmentally friendly method (requiring no solvent) to prepare nanocomposites based on thermoplastic polymer matrices [7], [9]. Nevertheless, some studies have reported enhanced filler dispersion for nanocomposites prepared via *in situ* polymerization. This last method consists in creating the polymer chains by the polymerization

of the monomer in presence of the fillers. Most of the time, it has been used to enhance the dispersion state of layered silicate. By this way, an exfoliated structure has been obtained for polypropylene/montmorillonite (3 wt%) prepared by *in situ* polymerization whereas melt-blending resulted in an intercalated structure [10]. Tung *et al* [11] similarly observed a better degree of filler dispersion in the case of *in situ* polymerization for polyamide 6 containing 3 wt% of montmorillonite. The same trend was evidenced by Gain *et al.* in the case of poly-εcaprolactone nanocomposites prepared by *in situ* polymerization with 3 wt% of montmorillonites. This resulted in a further reduction of CO_2 permeability by 20% compared to the melt-blending method [12].

In situ polymerization of lactide in presence of silica has already been reported in the literature. It usually consists in using ring opening polymerization mechanism (ROP) in small reactors. Ortenzi *et al.* achieved the polymerization in bulk using tin octanoate as catalyst with 1 wt% of non-modified silica at 180 °C. A PLA molar mass of 50,000 g/mol was obtained after 2 h of reaction under nitrogen flow [13]. Neranzaki *et al.* reported the polymerization of lactide in bulk using tin octanoate as catalyst, with a non-modified silica content ranging from 2.5 to 20 wt% using a first heating at 160 °C between 70 and 150 min, depending of the silica content, under nitrogen and then a mixing at 200 °C between 5 and 20 min, under high vacuum (~5 Pa) [14]. A decrease of the PLA molar mass was observed from 30,000 g/mol for 5.5 %wt of silica to 5,000 g/mol for 20 wt% silica, attributed to the hindering effect of silica or to interactions between the silanol groups and the lactide. Lastly, Prébé *et al.* investigated the influence of the surface nature of silica on the *in situ* polymerization mechanism and the filler dispersion. Polymerization of the L-lactide was conducted in bulk in a tubular reactor under nitrogen in the presence of 5 wt% of hydrophilic or hydrophobic silica [15] using tin octanoate as catalyst and triphenylphosphine as co-catalyst. The resulting molar mass were 52,000 g/mol for the hydrophilic silica and 87,000 g/mol for hydrophobic silica. Moreover, a nanoscale dispersion state was obtained with hydrophobic silica whereas a percolation network was observed with hydrophilic silica.

In situ polymerization of lactide by ROP has also been reported in the presence of montmorillonites. Ortenzi *et al.* successfully obtained PLA/Cloisite®15A (1 wt% of filler)

nanocomposites with a molar mass of 37,000 g/mol [13]. The polymerization was conducted in bulk at 180 °C for 2 h under nitrogen, using tin octanoate as catalyst. However, Cloisite®30B, which is an organo-modified montmorillonite bearing methyl tallow bis-2-hydroxyethyl quaternary ammonium cation is more commonly used in the case of PLA to achieve good platelet dispersion by melt-blending [2], [8], [16]. The presence of this modified montmorillonite during *in situ* lactide polymerization led to a very low PLA molar mass (10,000 g/mol), as reported by Paul *et al.* [17] in the case of a polymerization in bulk (120° C, 48 h) of lactide with 3 wt% of Cloisite®30B, using tin octanoate as catalyst. To bypass such problem, a two-step process was proposed consisting first in the synthesis in bulk of a PLA-based masterbatch containing 53 wt% of Cloisite®30B with triethyl aluminum as catalyst (120 °C, 16 h). The molar mass of the synthesized PLA was estimated to be 1,200 g/mol. Subsequently, the masterbatch was redispersed in commercial PLA by melt-blending, resulting in a final inorganic content of 3 wt%. Re *et al.*[18] also employed a two-step process but in this case the masterbatch was obtained by *in situ* polymerization in chloroform using 1,8-Diazabicyclo[5.4.0]undec-7-ene as free metal catalyst and 6 wt% of Cloisite®30B. The masterbatch, with a molar mass of 20,000 g/mol, was then melt-blended with commercial PLA in order to obtain nanocomposites containing 3 wt% of inorganic material. Based on our informations, this study is the only one to report the preparation of self-standing PLA/ Cloisite®30B films without the use of any plasticizer. Additionally, the author indicated that the nanoclays exhibited better filler dispersion compared to samples prepared via the conventional melt-blending. They also mentioned some grafting of PLA chains on the clay, which enhanced the filler/matrix interface. Nevertheless, the use of organic solvents is not environmentally sustainable and is not compatible with large scale production.

To the best of our knowledge, only one study reported the synthesis of PLA nanocomposites by reactive extrusion, which represents the more promising ecofriendly route for large-scale production [19]. The ring opening polymerization of lactide was performed in the presence of carbon nanotubes using tin octanoate as catalyst and triphenylphosphine as co-catalyst in a small-scale co-rotating twin-screw extruder. The temperature of the micro extruder was set at 185 °C and the screw speed at 100 rpm. However, it could be noticed that the filler content was very low (1 wt%).

Concerning barrier properties, among the work cited above, only Ortenzi *et al.* [13] and Re *et al*. [18] determined the gas permeability of their nanocomposites, evidencing an increase in barrier properties with respect to neat PLA. However, only very low filler content (less than 3 wt%) has been investigated and no comparison has ever been made between the barrier properties of nanocomposites prepared by the conventional melt-blending route and by a process involving PLA *in situ* polymerization. Thus, it is interesting to know to what extent the use of *in situ* polymerization could modify the barrier properties of the nanocomposites in comparison to the melt-blending route considering an extended range of filler content.

In the present work two fillers are selected to prepare PLA nanocomposites via melt-blending and *in situ* polymerization, respectively: a hydrophobic silica functionalized with dimethyl dichlorosilane and an organo-modified montmorillonite containing methyl tallow bis-2-hydroxyethyl quaternary ammonium cation. The investigated filler range is up to 10 vol%. The goal of the present work is i/to assess the possibility of carrying out lactide *in situ* polymerization by reactive processing in the presence of different amounts of the selected fillers and ii/ to investigate the influence of a process based on *in situ* polymerization with respect to the conventional melt-blending process on the nanocomposite morphology and water vapor permeability.

3. Experimental

3.1. Materials

Polylactide PLA 2003D was kindly provided by NatureWorks LLC (4.1 mol% in D-lactide content, M_n = 85,000 g.mol^{-1}). L-Lactide (purity> 98.0%) and tin(II) 2-ethylhexanoate ($SnOct_2$) were purchased from TCI chemical. Triphenylphosphine (PPh_3) was purchased from Sigma-Aldrich. All components were used as received. Silica functionalized with dimethyl dichlorosilane was supplied by Evonick Operations GmbH under the commercial name Aerosil® AR974. It will be designed as $SiCH_3$ in this work. Cloisite®30B, a montmorillonite modified with methyl tallow bis-2-hydroxyethyl quaternary ammonium cation (as 29 wt% of organic content), was supplied by Southern Clay Product. It is designed as OMMT. $SiCH_3$ fillers

are spherical nanoparticles with a diameter of 20 ± 5 nm and a density of 2.2 while OMMT is a lamellar type filler with a platelet length of 200 – 500 nm and a density of 1.98 [2].

3.2. Preparation of the nanocomposites

3.2. a) Melt-blending route

PLA nanocomposites were prepared from commercial PLA 2003D by melt-blending using a Haake internal mixer. The melt blending step was performed at 185 °C with a rotation speed of 50 rpm for a duration of 10 min. PLA pellets and nanofillers were systematically dried at least 24 h in a vacuum oven at 85 °C prior processing. Unfilled PLA was processed according to the same protocol as the nanocomposites to obtain reference PLA with similar thermomechanical history. Unfilled PLA is referred as PLAref, PLA/hydrophobic silica are referred as PLA/$SiCH_3$/X and PLA/montmorillonite as PLA/OMMT/X where X is the volume content of the filler. X values range from 1 to 10 for PLA/$SiCH_3$/X and from 2.5 to 10 for PLA/OMMT/X.

3.2. b) *In situ* polymerization route

For all systems, the PLA *in situ* polymerization was carried out without any solvent, by ROP of the L-lactide using a coordination-insertion mechanism [20]. $SnOct_2$ was used as catalyst as it has been proven effective for both silica [13], [14], [15] and Cloisite®30B [17], [19]. PPh_3 was utilized as a co-catalyst to enhance polymerization kinetics and achieve high molar mass PLA and minimizing transesterification reactions [15], [19], [21]. The molar ratio $SnOct_2$: lactide was fixed at 1 : 2500 and the molar ratio PPh_3 : lactide at 1 : 3300. The composition of the different systems synthesized in this work is given in **Table B.1**. A step-by-step optimization of the synthesis protocol was realized (**Supplementary Table B.1 and B.2**) as a function of filler used with the aim to obtain the highest PLA average molar mass. The optimized conditions are detailed hereafter.

PLA/silica

For the synthesis of PLA/silica nanocomposites, silica was dried at least 24 h in a vacuum oven at 90 °C before processing. L-lactide, tin(II) 2-ethyl hexanoate, triphenylphosphine and silica

were mixed at room temperature in the proportions given in **Table B.1** before feeding in a Haake internal mixer pre-heated at 175 °C. The synthesis was performed using a rotation speed of 80 rpm for 3 minutes, then decreasing it at 50 rpm for 50 min. Unfilled PLA was prepared in the same conditions and is referred as PLAis.

PLA/montmorillonite

Reactive processing could not be applied to L- lactide/OMMT as it led to brown-colored sticky materials whatever the OMMT content in the range 1-10% vol. As the only change compared to *in situ* polymerized PLA/silica nanocomposites was the filler nature, it was concluded that OMMT had a detrimental effect on lactide polymerization in bulk and under shear and induced predominant degradation phenomena. *In situ* synthesis was then performed in a minireactor to decrease the shear rate and step by step optimization led to use milder polymerization conditions (reaction temperature equal to 120 °C). According to the literature, quite low PLA molar mass could only be obtained with these synthesis conditions, excluding the possibility to directly obtain non brittle self-standing films [17]. It was then decided first to synthesize a masterbatch in the minireactor and then to redisperse this masterbatch in commercial PLA. The theoretical OMMT amount in the masterbatch was fixed at 20 wt%. This choice allowed us to cover the range of OMMT amount in the final film up to 7 vol% while minimizing the amount of PLA of low molar mass in the final films in order to keep non brittle materials. The step-by-step optimization of the *in situ* synthesis is detailed in **Supplementary Table B.2**. Only the optimized conditions are reported hereafter.

Before the synthesis, OMMT was dried 24 h in a vacuum oven at 90 °C.

First, L-Lactide, $SnOct_2$, PPh_3 and OMMT (corresponding to 20 wt%) in the proportions given in **Table B.1** were introduced in a mini glass-reactor and flushed with argon. The temperature was raised to reach 120 °C using an oil bath, and based on step-by-step optimization, the polymerization duration was fixed to 15 h. The reactor was covered with aluminum to maintain a constant temperature all along the reaction duration and avoid the lactide condensation on the upper glass. The synthesized material was removed from the reactor at the molten state. The masterbatch is referred as PLAis_OMMT. Then PLAis_OMMT was grinded and dried in a vacuum oven (24 h, 90 °C). Nanocomposites with different OMMT

contents (1.5, 3, 7 vol%) were obtained by redispersing PLAis_OMMT in a selected amount of commercial PLA (**Table B.1**) using a Haake internal mixer (175 °C, 50 rpm, 10 min). The samples are referred as PLA/PLAis_OMMT/X with X corresponding to the volume amount of OMMT.

Table B.1- Optimized experimental conditions used for the samples prepared by *in situ* polymerization.

	Lactide (g)	*Molar ratio SnOct/ lactide*	*Molar ratio PPh_3/ lactide*	*$SiCH_3$ (g)*	*OMMT (g)*	*PLA 2003D (g)*
PLAis	50	0.0004	0.0003	/	/	/
PLAis/$SiCH_3$/5	50	0.0004	0.0003	4.35	/	/
PLAis/$SiCH_3$/7	50	0.0004	0.0003	8	/	/
PLAis_OMMT	10	0.0004	0.0003	/	2.5	/
PLA/PLAis_OMMT/1.5	4.15	0.0004	0.0003	/	1.1	40
PLA/PLAis_/OMMT/3	8.2	0.0004	0.0003	/	2.2	40
PLA/PLAis_OMMT/7	15.8	0.0004	0.0003	/	4.2	20

3.3. Film preparation

Whatever the preparation route, the nanocomposites were dried in a vacuum oven (24 h, 90 °C) prior to thermocompression. Films with a thickness between 100 and 150 µm were prepared by thermocompression (180 °C, 150 bars, 2 min), placed between two metal plates and rapidly cooled under compressed air for few minutes to obtain amorphous films.

3.4. Characterization

3.4. a) Size exclusion chromatography (SEC)

The PLA average molar mass of the different samples was measured by SEC analysis by dissolving the samples in chloroform (3 mg/mL). The solutions were filtered using a PTFE filter plate (pore size = 0.45 µm). SEC analyses were conducted with a Polymer Lab type C mixed PLgel column (length = 30 cm, diameter = 7.8 mm, stationary phase 5 PSDVB, temperature = 25 °C, solvent feed rate = 0.5 mL/min, separation performance = 2.10^2 to 2.10^6 g/mol). Shimadzu RID20 and TREOS Wyatt sensor were respectively used to measure the refractive index as well as the light diffusion.

3.4. b) Nuclear Magnetic Resonance (NMR)

Liquid state ^{1}H NMR spectroscopy was used to characterize the chemical structure of the synthesized materials. Samples were dissolved in deuterated chloroform (10 mg/mL) and the solutions were filtered on a PTFE filter plate (pore size = 0.45 µm) before analysis. ^{1}H NMR spectra were obtained with a Bruker Avance III equipped with a 5 mm BBFO+ probe with a frequency of 400.1 MHz. The chemical shifts (δ) are given in ppm and were referenced with the deuterated chloroform ($CDCl_3$) signal at 7.26 ppm.

3.4. c) Infrared spectroscopy (FTIR)

Attenuated total reflectance ATR-FTIR has been used to investigate the possible grafting of the PLA chains on OMMT. A Thermoscientific spectrometer with an ATR module equipped with a diamond cold detector was used. IR spectra were recorded in the range 4000-450 cm^{-1}, using the results of 64 scans with a data spacing of 0.4 cm^{-1}. The samples to be analyzed were obtained from the nanocomposites washed and centrifuged three times with chloroform. The insoluble faction was then immersed in chloroform for 2 days and was again washed and centrifuged once to remove any residual soluble fraction. The solid fraction was dried and analyzed.

3.4. d) Thermal analysis

Thermogravimetric analyses (TGA) were carried out on nanocomposite films by using a Mettler Toledo TGA/DSC 1 STAR^{e} System. The samples were heated from 25 to 500 °C at 10 °C/min under dry nitrogen flow (50 mL/min) and the mass evolution was recorded as a function of the temperature. Non-reacted L-lactide content was calculated by the mass loss under 185 °C (see thermogram in supporting information (**Supplementary Figure 1**)) and the nanofiller content was determined from the mass residue at 500 °C. The degradation temperature was determined by the tangent method at the onset of the degradation process.

The matrix microstructure was investigated by differential scanning calorimetry (DSC). The experiments were performed on samples of 5-10 mg by using a TA Instrument Q200 calorimeter under nitrogen flow (50 mL/min) calibrated with indium standard. The heating scan was performed from 25 to 200 °C at 10 °C/min using a standard mode. From these

experiments the glass transition as well as the cold crystallization temperature and the melting temperature were recorded. The degree of crystallinity (χ_c) was calculated according to equation (B.1):

$$\chi_c = \frac{\Delta H_m - \Delta H_{cc}}{\Delta H_{m\infty}(1-\phi_m)} \quad (B.1)$$

where ΔH_m is the enthalpy of melting , ΔH_{cc} is the enthalpy of cold crystallization , Φ_m the weight content of fillers and $\Delta H_{m\infty}$ is the enthalpy of the infinite crystal taken as 93 J/g [22]. The glass transition was more deeply analyzed by Temperature Modulated Differential Scanning Calorimetry, with a modulated temperature program from 10 to 90 °C at an average heating rate of 2 °C/min with an oscillation amplitude of 0.318 °C/min (heat mode only). The glass transition temperature was taken at the onset of the transition. This analysis enables to remove the contribution of the physical aging by keeping only the reversible part of the signal.

3.4. e) Nanofiller dispersion analysis

The dispersion of the fillers in the films cross section was observed by Transmission Electron Microscopy (TEM) with bright field observations at 120 kV. The experiments were performed with a JEOL-1400 flash microscope on 60-70 nm thick slices prepared at room temperature with an oscillating diamond knife (Diatom, 35°) on a Leica Ultracut B microtome. For observation, the sections were transferred on a 200-mesh copper grid with a carbon membrane.

Quantitative measurements of the size, the area, the aspect ratio and the number of filler domains per surface unity have been realized for the different nanocomposites. For silica, the measurements have been done automatically using Scikit-image processing in Python. In the case of OMMT, due to lack of contrast and the complexity of the filler's domain shapes, the proportion as well as the aspect ratio of different classes of filler domains were measured manually with ImageJ software. The interparticle distances for all the nanocomposites were also measured manually using ImageJ software. For all samples, the mean values of each morphological parameter were determined from the analysis of at least 60 fillers' domains.

In complement, the dispersion of OMMT in the film was investigated by small angle X-ray scattering (SAXS) at the European Synchrotron Radiation Facility (ESRF, Grenoble, France) on the BM02 beamline. The *q*-range was calibrated using silver behenate. The incident photon energy was 15.7 keV (λ = 0.77 Å) and the sample-to-detector distance was 3.15 m. The contribution of the empty cell was subtracted from the scattering images of the samples studied, and the intensity was azimuthally averaged and normalized to the sample thickness to obtain I vs. q, where I is the signal intensity and q is the diffusion vector.

3.4. f) Permeability measurements

Water vapor transmission (WVTR in g/[m². day]) experiments were performed at 23 °C and 90 % relative humidity using a MOCON PERMATRAN W3/33 equipped with an infrared sensor. Film samples with a 5 cm² effective area and a constant thickness between 100 ± 5 and 150 ± 5 µm were used. The water transferred through the films was conducted by N_2 as carrier gas at 100 sccm to the infrared sensor. The permeability *P* is calculated from the steady state flux *J* according to equation (B.2):

$$P = \frac{J.e}{p} \qquad (B.2)$$

where *e* is the sample thickness (cm), taken from the average value of five measurements and *p* is the pressure (cm_{Hg}). The permeability coefficient *P* is expressed in barrer units (1 barrer = 10^{-10} cm^3_{STP} .cm.cm^{-2}.s^{-1}.cm_{Hg}^{-1}= 3.36x10^{-16}mol.m.m^{-2}.s^{-1}.Pa^{-1}).

4. Results and discussion

4.1. Physicochemical and morphological characterization of nanocomposites series as a function of the synthesis route

The aim of this part is to compare the microstructure of the nanocomposites prepared either by melt-blending or by *in situ* polymerization for two kinds of filler under investigation, namely $SiCH_3$ and OMMT.

4.1. a) Silica nanocomposites

PLAis and PLAis/$SiCH_3$ were successfully synthesized by *in situ* polymerization via reactive processing. The torque was recorded as the function of the time in the internal mixer (**Figure B.1**). During the synthesis of PLAis, the torque is constant until 15 min (0.5 N.m) and then steadily increases to reach a plateau after 45 min with a final value of 4.5 N.m which reflects the end of the polymerization. The same tendency is observed for PLAis/$SiCH_3$ systems, with a higher value of the torque at the beginning (1.5 N.m) and at the final plateau (6 N.m) due to the presence of silica.

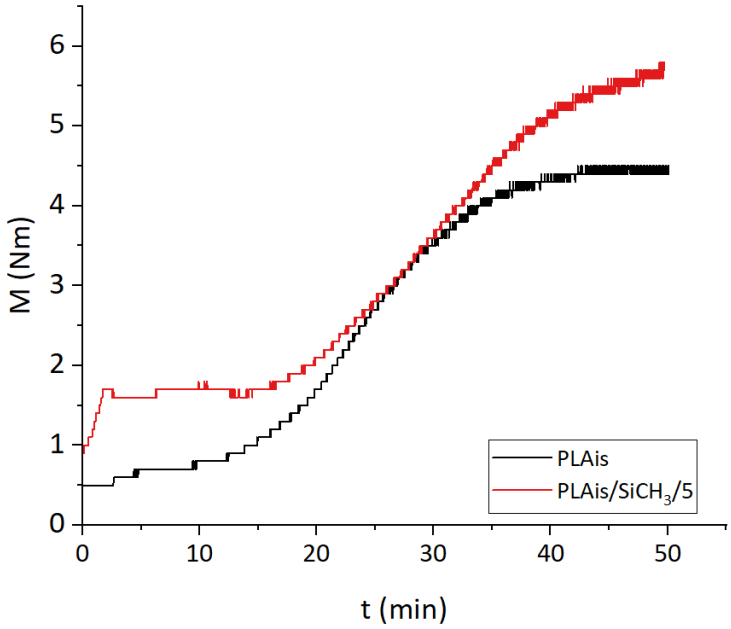


Figure B.1 - Evolution of the torque (M) versus time in the internal mixer during *in situ* polymerization of PLAis/$SiCH_3$/5 at 175 °C.

The structure of the synthesized samples was characterized by ^1H NMR spectroscopy. **Figure B.2** depicts the ^1H NMR spectra of PLAis and PLAis/$SiCH_3$/7. All PLA proton spectra show a quadruplet signal at 5.19-5.12 ppm and a doublet signal at 1.58-1.56 ppm, assigned respectively to the resonance of the proton from the CH and the CH_3 groups of the PLLA repetitive unit [23], [24]. The presence of residual monomer can be identified thanks to the observed quadruplet signal at 5.05-5.00 ppm and the doublet signal at 1.69-1.67 ppm, which are specifically attributed to the proton from the CH and CH_3 groups of the L-lactide [20] . The integration of these signals leads to conclude that a very low content (between 1 and 2 wt%)

of non-reacted L-lactide is present in the *in situ* polymerized samples. Thus, ^{1}H NMR analysis evidences that the polymerization was successful in our experimental conditions, with and without silica. It il also important to precise that no grafting of the PLA chains on the silica is possible as it has dimethyl dichlorosilane groups at the surface.

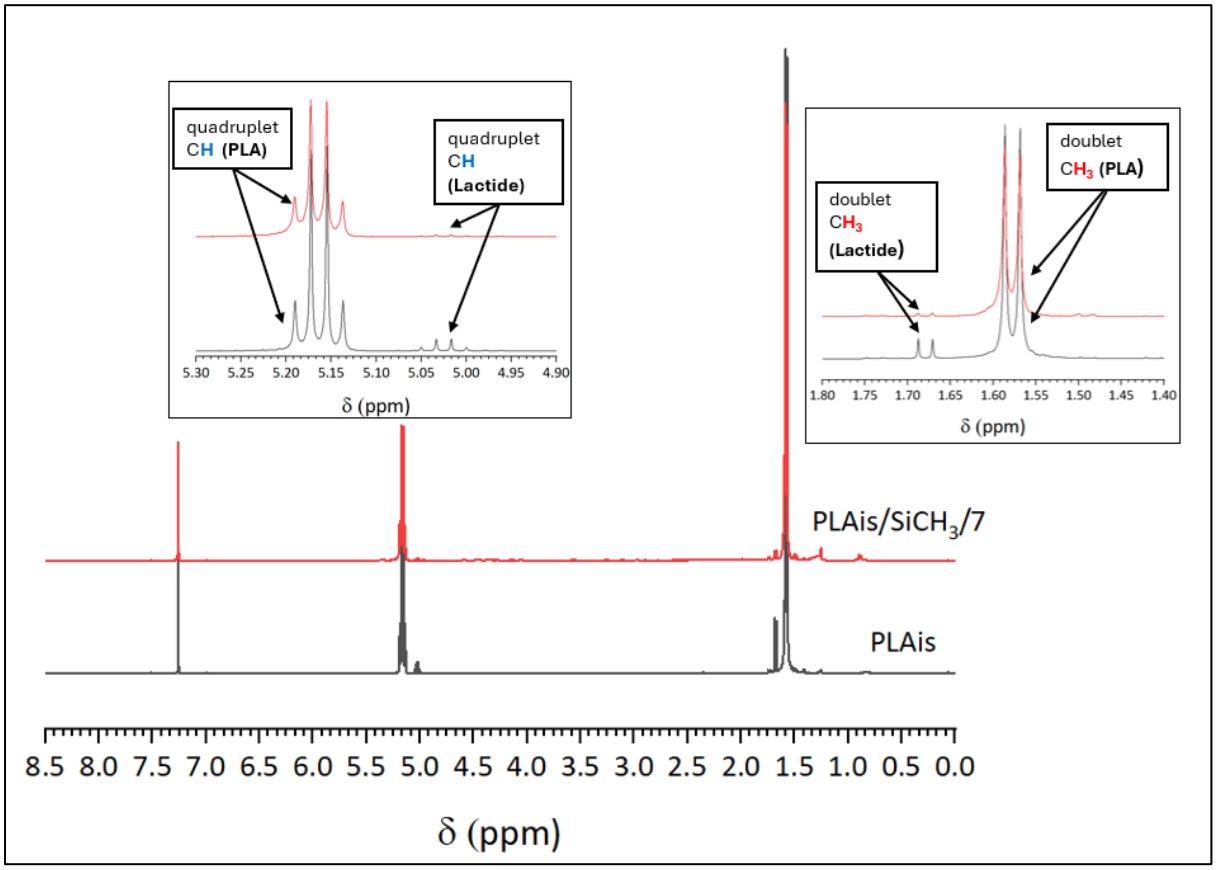


Figure B.2 - ^{1}H NMR spectrum of PLAis and PLAis/$SiCH_3$/7 (after filtration) in $CDCl_3$, 298 K.

SEC analyses were conducted to determine the PLA molar mass for each synthesized sample (either by melt blending or by *in situ* bulk polymerization). **Figure B.3** allows to compare the chromatograms obtained for a highly loaded nanocomposite prepared by melt-blending (PLA/$SiCH_3$/10) and for the nanocomposites prepared by *in situ* polymerization (PLAis/$SiCH_3$/5, PLAis/$SiCH_3$/7). A shift of the signal toward longer elution time is observed between the analysis of the sample prepared by melt-blending and the samples prepared by *in situ* polymerization. This phenomenon is even more pronounced for the highest silica concentration. This reflects higher molar mass for the sample prepared by melt-blending. The molar mass values are gathered for all prepared sample in **Table B.2**. It can be seen that the

average molar mass is not highly influenced by the presence of silica for the melt-blended nanocomposites and stays around 80,000 g/mol. For *in situ* polymerized samples, the molar mass value of the reference matrix is lower (Mn = 58,000 g/mol) and goes from 45,000 g/mol for PLAis/$SiCH_3$/5 to 21,000g/mol for PLAis/$SiCH_3$/7. This trend was also reported in the literature [14], [15] and explained by a hindering effect of silica during polymerization. However, the molar mass for all samples obtained by *in situ* polymerization is over the critical molar mass of PLA, which is about 10,000 g/mol [25], and thus is suitable to obtain non brittle films.

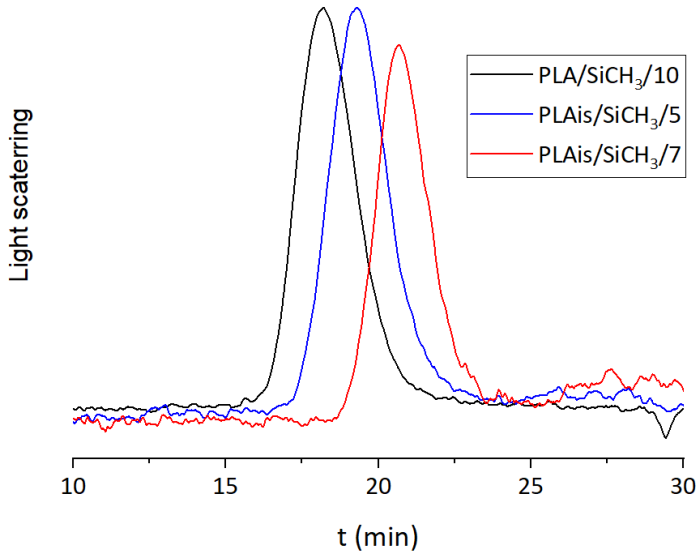


Figure B.3 – SEC chromatographs of PLA/$SiCH_3$/10, PLAis/$SiCH_3$/5 and PLAis/$SiCH_3$/7.

TGA was used to determine the degradation temperature of all samples studied and the amount of unreacted monomer in the case of *in situ* polymerized samples. Indeed, representative TGA curves shown in supporting information (**Supplementary Figure B.2**) exhibit for all samples one major mass loss at high temperature assigned to the degradation temperature of PLA and an additional small mass loss below 150 °C related to the unreacted monomer still present in the samples prepared by reactive processing. The low amount of residual monomers, which was found about 3 wt% for all the samples, is satisfying regarding the short residence time in the internal mixer. All values are summarized in **Table B.2**. T_d is not influenced by the presence of silica for the melt-blended nanocomposites staying around 347 °C. For the *in situ* polymerized samples, T_d is lower due to lower molar mass of the

synthesized PLA. It is also noteworthy that T_d increases with the silica content. It goes from 271 °C for PLAis to 285 °C for PLAis/$SiCH_3$/7. This improvement of the thermal stability by the incorporation of silica has already been reported in the literature for PLA/silica nanocomposites prepared by *in situ* polymerization [14].

DSC thermograms have the same shape for all the samples exhibiting a glass transition temperature (T_g,) a cold crystallization peak (T_{cc}) and a melting peak (T_m). Representative DSC thermograms are given in supplementary information (**Supplementary Figure B.3**). The T_g of the melt-blended samples is about 56 °C for the PLAref and the silica nanocomposites whatever the silica content. The T_g of PLAis is lower (T_g = 48 °C) due to the presence of unreacted monomers which act as plasticizers. The addition of 5 vol% of silica leads to a slight increase of the T_g (T_g = 52 °C), reflecting a lower mobility of the chains, whereas with 7 vol% of silica the T_g value decreases down to 46 °C. As the amount of unreacted monomer is similar for all samples, this decrease of T_g can only be related to the lower value of PLA molar mass for this sample. The cold crystallization temperature is around 102 °C for the two PLA references. The addition of silica below 5 vol% does not significantly change T_{cc} for the melt-blended samples. For higher silica content, T_{cc} increases up to 110 °C for PLA/$SiCH_3$/10. On the contrary, for the *in situ* polymerized sample, the addition of silica decreases the value of T_{cc} up to 89 °C for PLAis/$SiCH_3$/7. This means that the silica promotes nucleation in case of samples prepared by *in situ* polymerization, maybe thanks to shorter chains of the PLA matrix. The melting temperature is equal to 150 °C for the melt-blended PLAref whereas it is equal to 170 °C for the *in situ* polymerized PLAis. This difference is due to the differences of D-isomers content in agreement with the literature [26]. The addition of silica does not lead to a shift of the T_m whatever the process and the filler content. Furthermore, the degree of crystallinity was calculated and confirms that all samples are amorphous.

Table B.2 – Matrix characteristics of silica-based nanocomposites obtained by melt blending and *in situ* polymerization.

	Process	Mn (10^{-3} g/mol)	Mass residue (wt%)	Residual monomer (wt%)	T_d (°C)	T_g (°C)	T_{cc} (°C)	T_m (°C)	χ_c (%)
PLAref	**Melt-blending**	87 ± 4	0	0	348 ± 1	57 ± 1	103 ± 1	150 ± 1	2 ± 2
PLA/SiCH$_3$/1		/	1.5	0	347 ± 1	56 ± 1	101 ± 1	149 ± 1	1 ± 2
PLA/SiCH$_3$/4		/	7.0	0	347 ± 1	56± 1	104 ± 1	149 ± 1	2 ± 2
PLA/SiCH$_3$/5		/	8.0	0	347 ± 1	56 ± 1	104 ± 1	149 ± 1	2 ± 2
PLA/SiCH$_3$/10		77 ± 6	16.3	0	347 ± 1	56 ± 1	110 ± 1	149 ± 1	4 ± 2
PLAis	**Direct *in situ* polymerization**	58 ± 3	0	3.5	271 ± 2	48 ± 1	102 ± 1	172± 1	2 ± 2
PLAis/SiCH$_3$/5		45 ± 3	8.0	2.0	280 ± 2	52 ± 1	93 ± 1	170 ± 1	0 ± 2
PLAis/SiCH$_3$/7		21 ± 3	12.0	3.5	285 ± 2	46 ± 1	89 ± 1	167 ± 1	0 ± 2

Dispersion of silica in the matrix has been investigated by transmission electron microscopy. **Figure B.4** allows to compare the TEM micrographs of samples prepared by melt-blending and *in situ* polymerization for the same filler content (5 vol%). A homogeneous filler dispersion is observed independently of the process with average domain size of 3,000 nm² and mean interdomains spacing in the range 110 - 130 µm. It is noteworthy that PLAis/SiCH$_3$/5 which is prepared by *in situ* polymerization exhibits a better silica dispersion than the nanocomposite prepared by Prébé *et al*. for the same amount of hydrophobic silica using a bulk polymerization in a reactor [15]. This difference could be assigned to a better mixing observed in the internal mixer during the *in situ* polymerization in comparison with the stirring blade used for mixing in the mini reactor. The quality of the silica dispersion stays similar up to 7 vol% for the nanocomposites prepared by *in situ* polymerization whereas the presence of aggregates is noticed in the case of nanocomposites prepared by melt-blending with 10 vol% silica (see additional TEM micrographs given in supporting information (**Supplementary Figure B.4 and B.5**)).

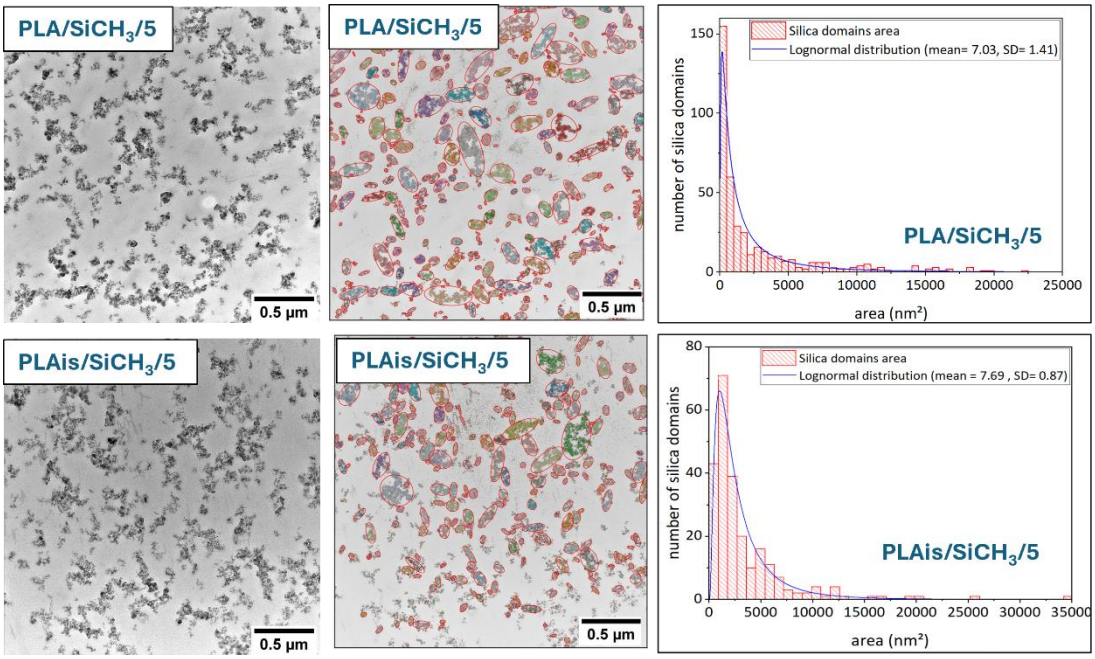


Figure B.4 -TEM micrographs of the cross section of PLA/silica nanocomposite films as well as the silica domains identification by Scikit-image processing and their area distribution for films prepared by melt-blending (PLA/$SiCH_3$/5) and *in situ* polymerization (PLAis/$SiCH_3$/5) with 5 vol% of silica.

Table B.3 - Area, mean aspect ratio, average number of particles per surface unity and distance between the impermeable domains for PLA nanocomposites filled with hydrophilic silica.

Sample	Area (nm ²)	Mean aspect ratio	Number of domains /µm ²	Inter domains spacing (nm)
PLA/$SiCH_3$/1	3,000 ± 3,000	1.9 ± 0.5	12	290 ± 100
PLA/$SiCH_3$/4	3,000 ± 3,000	1.9 ± 0.6	70	120 ± 40
PLA/$SiCH_3$/5	3,000 ± 5,000	1.9 ± 0.7	60	140 ± 40
PLA/$SiCH_3$/10	8,000 ± 10,000	1.9 ± 0.7	20	150 ± 60
PLAis/$SiCH_3$/5	3,000 ± 4,000	1.9 ± 0.6	45	130 ± 50
PLAis/$SiCH_3$/7	4,000 ± 5,000	1.9 ± 0.6	55	110 ± 30

To sum up, self-standing, non-brittle amorphous nanocomposite films have been prepared by melt-blending and by *in situ* polymerization. Due to shorter polymer chains, the nanocomposites prepared by *in situ* polymerization exhibit slightly lower glass transition and degradation temperatures. Concerning the dispersion of silica, no significant differences have been observed as a function of the process for filler content less than 5 vol%. A fine filler

dispersion is kept up to 7 vol% of silica with the *in situ* polymerized samples whereas the quality of the dispersion obtained with the melt-blending becomes poorer for 10 vol% of silica.

4.1. b) Montmorillonite nanocomposites

OMMT-based nanocomposites were prepared either by melt-blending or by the two-step method involving *in situ* polymerization of a highly filled masterbatch and then mixing it with commercial PLA. Prior to the characterization of the final nanocomposite series, characterization of the masterbatch was carried out.

The PLAis_OMMT masterbatch was analyzed by ^{1}H NMR spectroscopy. The spectrum in **Figure B.5** shows a quadruplet signal at 5.19 -5.12 pm and a doublet signal at 1.58-1.56 ppm, which are assigned respectively to the proton resonance of the CH and the CH_3 groups of the PLLA repeating unit [23], [24]. The presence of unreacted monomer can be identified by the quadruplet signal at 5.05-5.00 ppm and the doublet signal at 1.69-1.67 ppm, which are specifically attributed to the proton resonance of the CH and CH_3 groups of the L-lactide [20]. Furthermore, there are also other signals appearing on this spectrum. Among them, a quadruplet signal of low intensity at 4.37-4.32 ppm is characteristic of the proton resonance of CH groups of the polymer's chain ends. The integration ratio between the signal corresponding to the CH of the repeating unit and the one attributed to the CH of the chain ends was used to estimate the molar mass of PLAis_OMMT [20]. It is found to be around 2,000 g/mol which is too low to be determined by SEC in our analytical conditions. This molar mass value agrees with the observations of Paul *et al.* [17] who estimated the molar mass at 1,400 g/mol for a masterbatch containing 53 wt% of Cloisite®30B prepared with a triethylaluminium catalyst. In the literature this low molar mass is explained by the high number of hydroxyl functions present on the alkyl ammonium cation, which promotes also the polymerization and thus leads to increase the number of polymer chains but decrease the degree of polymerization [17], [27]. Furthermore, the NMR spectrum shows a broad signal at 1.26 ppm and a quadruplet signal at 0.90 ppm which can be respectively attributed to the CH_2 and the CH_3 of the alkyl chain of the OMMT cation by comparison with the NMR spectrum of the cation (**Supplementary Figure B.6**).

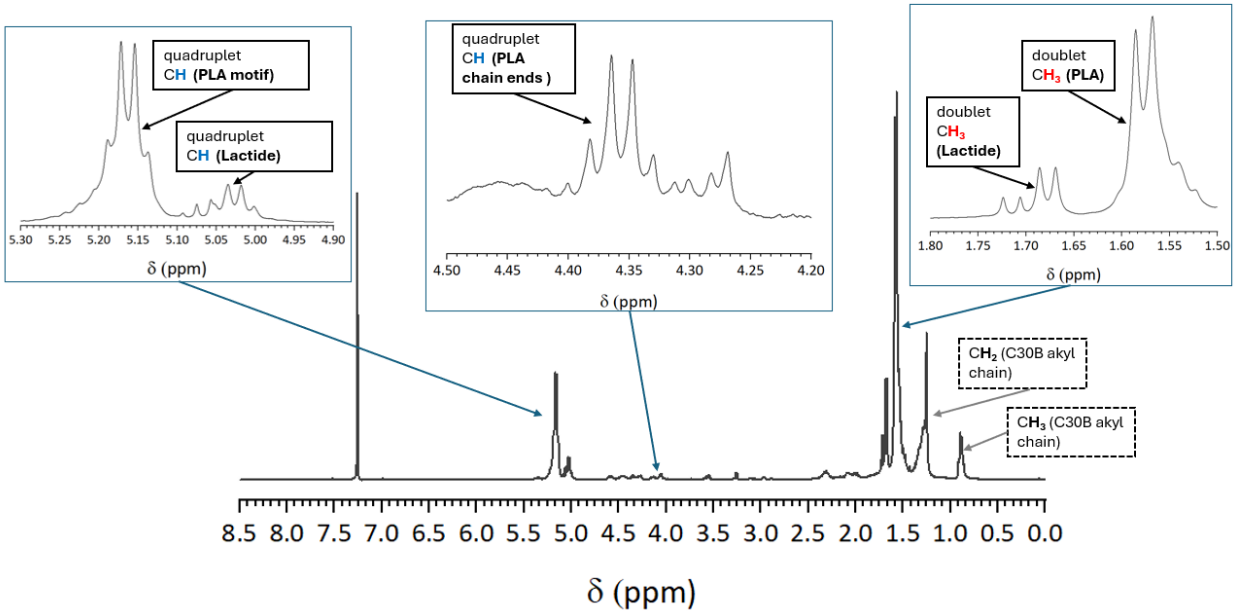


Figure B.5 - ^{1}H NMR spectrum of the PLAis_OMMT (after filtration) in $CDCl_3$, 298K.

The potential grafting of PLA chains on the OMMT during our *in situ* polymerization process performed in bulk has been investigated and compared to the observations of Re *et al.* for *in situ* polymerization in presence of solvent [18]. FTIR analysis has been realized on the insoluble fraction of PLAis_OMMT recovered after washing centrifugation procedure in chloroform. A PLA/OMMT/10 sample prepared by melt blending (thus with no grafting), has also been analyzed, for comparison, after the same washing centrifugation procedure. The FTIR spectra of both samples have been compared to those of OMMT powder and PLA (**Figure B.6**). They exhibit the same peaks as the ones observed with the OMMT alone meaning that both are constituted of OMMT as expected. However, an additional peak at 1750 cm^{-1}, is clearly observed for PLAis_OMMT. This peak assigned to C=O stretching vibration band of PLA [28] is slightly shifted compared to the one observed on the spectrum of PLA (1746 cm^{-1}) (**Figure B.6**). Re *et al.* [18] also reported a shift of 3 cm^{-1} of this same peak and attributed this to the rigidification of the PLA chain grafted on the OMMT surface. Although the grafting cannot be quantified with this methods, it should be noted that the intensity of the peak at 1750 cm^{-1} is very low compared to the signal of the OMMT cation.

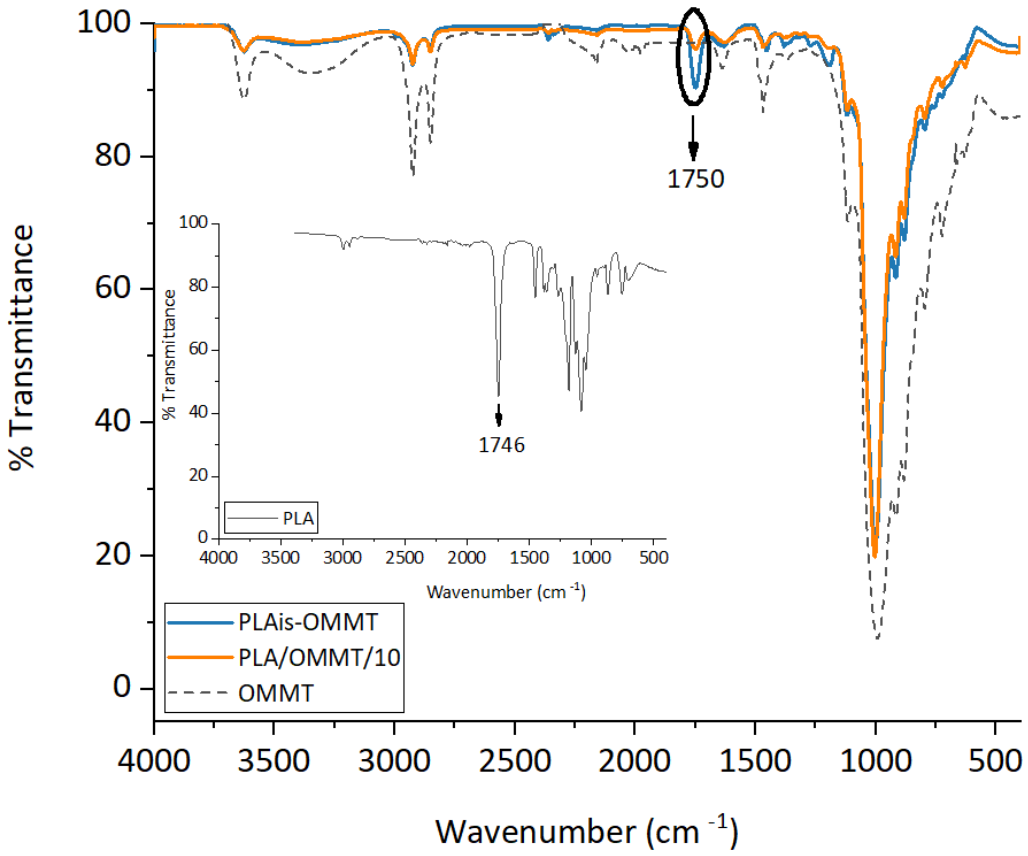


Figure B.6 - ATR-FTIR spectra of PLA, OMMT and the insoluble fraction of PLAis_OMMT and PLA/OMMT/10.

Concerning thermal properties, the TGA thermogram of PLAis_OMMT (**Figure B.7a**) shows a first mass loss of 7 ± 2 % at 145 ± 5 °C corresponding to the unreacted monomer and a second mass loss at 290 ± 10 °C related to the degradation of the PLA. The inorganic mass residue was found equal to 17 ± 3 wt%. The DSC thermogram (**Figure B.7b**) shows only the glass transition with an onset temperature of 28 ± 2 °C. Neither cold crystallization nor melting are observed. These results can be explained by the very small length of the chains contained in the PLAis_OMMT masterbatch.

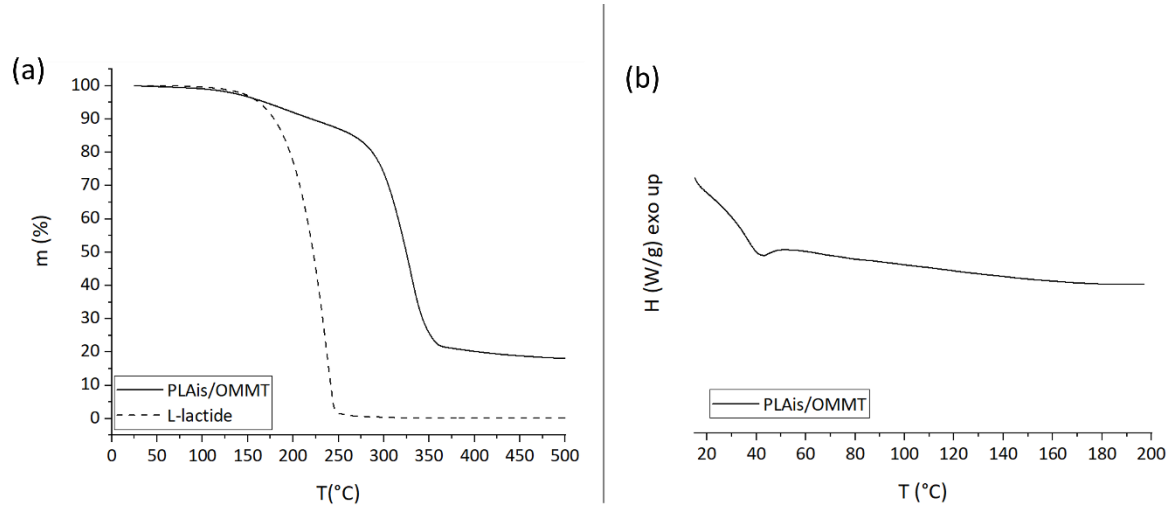


Figure B.7 – (a) TGA thermogram of PLAis_OMMT and L-lactide at 10° C/min under nitrogen and (b) DSC thermogram of PLAis_OMMT corresponding to the first heating at 10 °C/min under nitrogen.

To sum up PLA was successfully polymerized in presence of OMMT but the molar mass of PLAis_OMMT is lower than the PLA critical molar mass of 10,000 g/mol [25]. Consequently, self-standing films could not be prepared from this material alone.

To overcome this problem, PLAis_OMMT was mixed with commercial PLA (PLA 2003D) in an internal mixer according to the proportions given in **Table B.4**. By this way PLA films with OMMT content ranging from 1.5 to 7 vol% have been obtained and are referred to as PLA/PLAis_OMMT/X. To investigate the effect of the synthesis route on the microstructure, the PLA/PLAis_OMMT/X samples were compared with a nanocomposite series prepared from commercial PLA and OMMT by melt-blending and referred as PLA/OMMT/X.

Representative TGA curves are shown in supporting information (**Supplementary Figure B.7**) and the values of the degradation temperature (T_d) are summarized in **Table B.4**. The addition of OMMT by melt-blending leads to a slight decrease of the degradation temperature from 347 °C for PLA/OMMT/2.5 to 343 °C for PLA/OMMT/10. This decrease is attributed to the decrease of the PLA molar mass in presence OMMT during the process [29]. For nanocomposites prepared by the two-step process, it can be first noted that the TGA thermograms show only one mass loss except for PLA/PLAis_OMMT/7. In this case the first mass loss at 160 °C (Δm = 3 wt%) corresponds to the residual monomer whereas the second mass loss at 300 °C corresponds to the degradation of the PLA blend. The incorporation of the

masterbatch in commercial PLA leads to lower T_d values in comparison with the melt-blended samples. Moreover, T_d decreases from 335 °C for PLA/PLAis_OMMT/1.5 to 300 °C for PLA/PLAis_OMMT/3 and PLA/PLAis_OMMT/7 probably due to a higher content of PLAis_OMMT masterbatch in the final material.

DSC heating scans for all the nanocomposite samples show a glass transition T_g, followed by a cold crystallization peak at T_{cc} and a melting peak at T_m (see **Supplementary Figure B.8**). For samples prepared by melt-blending, T_g decreases from 56 to 52 °C when the OMMT amount increases up to 10 vol%, attributed to a slight decrease of the molar mass [29]. For the two-step process, only one T_g is observed which means that the PLA prepared by *in situ* polymerization and the commercial PLA are intimately mixed and behave as one phase. T_g values are lower than the one obtained with the melt-blending process and decrease going from PLA/PLAis_OMMT/1.5 (T_g = 51 °C) to PLA/PLAis_OMMT/7 (T_g = 40 °C) probably due to a higher masterbatch content in the last case. To confirm this hypothesis, experimental T_g *values* have been compared to $T_{g\,Fox}$ calculated with the Fox equation (equation (B.3)).

$$\frac{1}{T_{gFox}} = \frac{w_1}{T_{g1}} + \frac{w_2}{T_{g2}} \qquad (B.3)$$

With T_{g1}, T_{g2} the glass transition temperature of respectively commercial PLA and PLAis_OMMT (T_{g1} = 329 K, T_{g2} = 301 K) and w_1, w_2 the weight fraction of PLA and PLAis in the final blend.

The experimental T_g values are close to the $T_{g\mathrm{Fox}}$ values (**Table B.4**) which confirm that the commercial PLA chains and the polymer chains of PLAis_OMMT form a homogeneous matrix. T_{cc} increases slightly with the addition of OMMT for the melt-blended samples (from 104 °C for 2.5 vol% OMMT to 110 °C for 10 vol% of OMMT) whereas it stays constant for the samples prepared with the two-step process. Furthermore, the addition of OMMT does not change the melting temperature (T_m) whatever the filler content. The lonely observed difference in the melting region is the slightly shifted melting towards lower temperature for the PLA/PLAis_OMMT/X series with respect to PLA/OMMT/X series. More specifically, two melting peaks (T_{m1} ≈ 146 °C and T_{m2} ≈ 155 °C) are observed for PLA/PLAis_OMMT/1.5 and PLA/PLAis_OMMT/3 instead of one melting peak at around 150 °C for the samples prepared

by melt-blending. These two melting peaks are usually attributed to the melt-recrystallisation-melt process upon heating of the imperfect or less stable crystals [30]. For PLA/PLAis_OMMT/7, the thermogram shows a broad melting peak around 145 °C. It may be explained by the presence of the short chains of the synthesized PLA which disturb the crystalline organization of the commercial PLA.

Table B.4- Matrix characteristics of montmorillonite-based nanocomposites obtained by melt blending and *in situ* polymerization.

	Process	PLA 2003D (wt%)	monomer (wt %)	T_d (°C)	T_g (°C) ± 1	T_{gFox} (°C)	T_{cc} (°C) ± 1	T_{m1} (°C) ± 1	T_{m2} (°C) ± 1	χ_c (%) ± 2
PLAref	**Melt-blending**	100	/	348 ± 1	57	/	103	150	/	0
PLA/OMMT/2.5		100	/	347 ± 1	56	/	104	149	/	2
PLA/OMMT/5		100	/	345 ± 1	55	/	109	150	/	4
PLA/OMMT/10		100	/	343 ± 1	52	/	109	151	/	4
PLA/PLAis_OMMT/1.5	**Two-step process**	88	1 ± 0.5	335 ± 3	51	52	115	147	154	0
PLA/PLAis_OMMT/3		80	1 ± 0.5	300 ± 5	47	50	115	144	152	1
PLA/PLAis_OMMT/7		50	3 ± 1	300 ± 5	40	41	116	145	/	3

Concerning the filler dispersion, it can be observed in **Figure B.8** that OMMT is well dispersed in the nanocomposite films, showing the presence of quasi-individual sheets and small to medium-size tactoïds for both processes. TEM micrographs at lower magnification are available in supporting information (**Supplementary Figure B.9**)

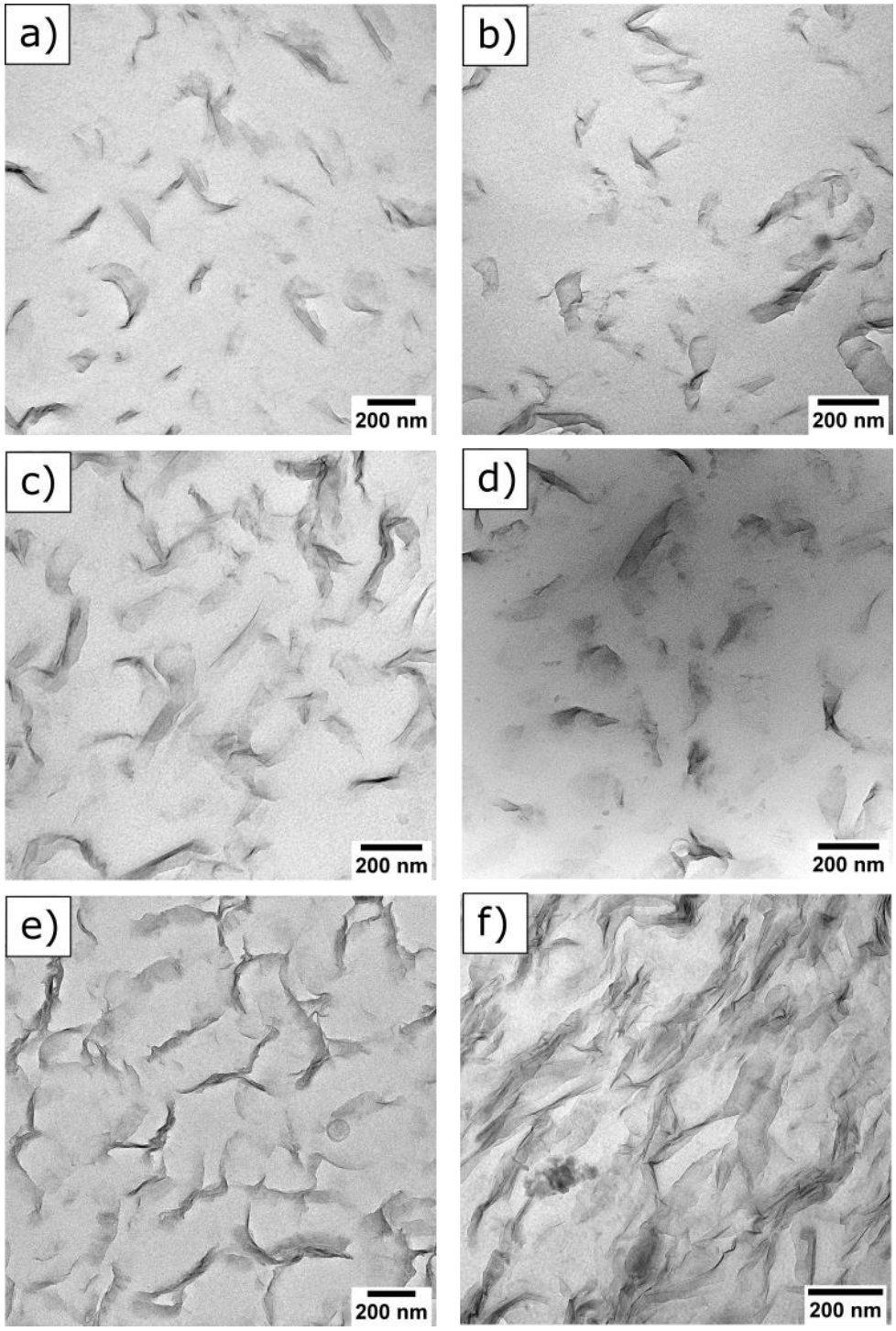


Figure B.8 - TEM micrograph of the cross sections of montmorillonite-based nanocomposites films prepared by the two-step process : (a) PLA/PLAis_OMMT/1.5, (c) PLA/PLAis_OMMT/3, (e) PLA/PLAis_OMMT/7 and by melt-blending : (b) PLA/OMMT/2.5, (d) PLA/OMMT/5, (f) PLA/OMMT/10.

However, the quantitative analysis (**Table B.5**) shows a slightly better filler dispersion for nanocomposites obtained by the two-step method with 90% of quasi-individual sheets for PLA/PLAis_OMMT/3 versus 85% for PLA/OMMT/2.5 prepared by melt-blending. The proportion of small and middle size tactoïds are similar whatever the process. Consequently, the mean aspect ratio is a little bit higher for the nanocomposites prepared by the two-step process with a mean value of 90 for 2.5 vol% of OMMT with respect to 86 for 3 vol% for the melt-blended sample. It is also worth noting that the mean aspect ratio stays almost similar whatever the filler amount for both processes. As expected, the interdomains spacing decreases as the filler content increases. Moreover, the values of the interdomain spacing do not significantly differ as a function of the process. Concerning the orientation, the fillers are randomly oriented for both processes, in agreement with other studies [2], [12], [17], [18].

Table B.5 - Characteristics of the montmorillonite dispersion in the films for the melt-blending process and the two-step process (*w* stands for the thickness of the filler domains).

Sample	*Process*	*quasi-individual sheets*		*Small tactoïds (w< 30 nm)*		*Middle size tactoïds (30 <w< 200 nm)*		*Mean aspect ratio*	*Interdomains spacing (nm)*
		% by number	Aspect ratio	% by number	Aspect ratio	% by number	Aspect ratio		
PLA/OMMT/2.5	Melt-blending	84	100	10	12 ± 5	6	7 ± 2	86	190 ± 100
PLA/OMMT/5		85	100	10	10 ± 2	6	5 ± 2	86	150 ± 60
PLA/OMMT/10		80	100	10	10 ± 2	10	7 ± 2	83	60 ± 30
PLA/PLAis_OMMT/1.5	Two-step process	90	100	3	10 ± 1	7	9 ± 2	91	240 ± 60
PLA/PLAis_OMMT/3		90	100	4	12 ± 4	7	9 ± 3	90	150 ± 50
PLA/PLAis_OMMT/7		85	100	6.5	11 ± 4	8.5	8 ± 2	86	130 ± 30

To go deeper in the filler dispersion analysis, SAXS measurements have been realized on the OMMT powder as well as on PLA/OMMT/2.5 and PLA/PLAis_OMMT/3 films. The SAXS diffractograms of OMMT (**Figure B.9**) show a peak at 2θ = 5.3° corresponding to the OMMT initial basal spacing (d = 16.5 nm). A well-defined peak around 2 θ = 2.6° corresponding to an interlayer distance of 3.4 nm is observed for PLA/OMMT/2.5 supporting the coexistence of intercalated structures. A similar trend is observed for PLA/PLAis_OMMT/3 and in this case, the diffraction peak is slightly shifted to lower angle (from 2.6° to 2.5°) corresponding to a higher interlamellar distance (3.5 nm) and its intensity is higher indicating a higher proportion

of intercalated structures. It can be also noticed for both PLA/OMMT/2.5 and PLA/PLAis_OMMT/3 nanocomposites the presence of a small peak located at the same position as OMMT for PLA/PLAis_OMMT/3 and slightly shifted to higher 2θ value for PLA/OMMT/2.5. This peak can be related to the presence of low amounts of non-intercalated structures. The shift of the peak toward higher 2θ values evidenced for PLA/OMMT/2.5 reflects a slight degradation of the quaternary ammonium cation during the melt blending process [31]. Thus, a slightly better dispersion state of the OMMT is obtained by the two-step process, with more individual sheets and a higher intercalation degree for the small tactoïds.

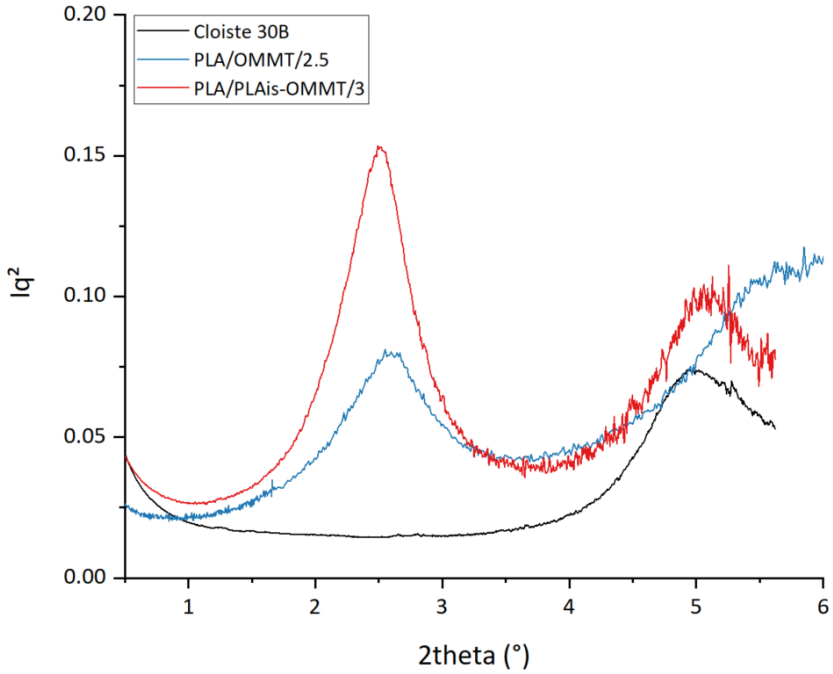


Figure B.9 – SAXS scattering diagrams of OMMT, PLA/OMMT/2.5 and PLA/PLAis_OMMT/3.

To sum up, matrix physico-chemical properties as well as dispersion state of montmorillonite have been compared for amorphous nanocomposites prepared by melt-blending and two-step process based on *in situ* polymerization. The matrix of the nanocomposites prepared by two-step process is composed of synthesized low molar mass PLA and a certain content of commercial PLA, whose respective proportions depend on the montmorillonite content in the final nanocomposite. This blend of short and long PLA chains leads to lower T_d, T_g than for nanocomposites obtained by melt-blending. Concerning the dispersion of montmorillonite,

more individual sheets are observed with the two-step process as well as a higher intercalation degree for the small tactoïds.

4.2. Permeability of nanocomposites: melt blending vs *in situ* polymerization.

Water vapor permeability (23 °C, 90 %RH) has been measured for the different nanocomposite films with the aim to see if differences are observed as a function of the process used to prepare the nanocomposites and if the potential differences can also depend on the filler type.

For silica nanocomposites, the permeability of synthesized PLA (PLAis) was found to be equal to 3650 ± 110 barrer, which is comparable to the permeability of the reference PLA (PLAref) equal to 3600 ± 180 barrer (**Figure B.10**). Thus, despite the difference of molar mass and of D-isomers content, the transport properties of the nanocomposite matrices are similar. Moreover, whatever the process, the permeability of the nanocomposites is always lower than the permeability of the unfilled PLA matrix and it decreases as the silica content increases (**Figure B.10**). This is attributed to the tortuosity effect caused by the presence of the silica which act as impermeable fillers [5], [13]. The experimental permeability values of the nanocomposites have been compared to those calculated from the Maxwell law [32] given by the equation (B.4). This law is commonly used to decribe the permeability of nanocomposites containing spherical impermeable fillers [4], [33], [34]:

$$P = P_0 \frac{1 - \Phi_v}{1 + 0.5\,\Phi_v} \qquad (B.4)$$

With Φ_v the volume fraction of filler and P_0 the permeability of the unfilled PLA matrix.

The Maxwell law gives a rather good description of the experimental values for the nanocomposites prepared by melt-blending as already reported in our previous paper [29]. For the nanocomposites prepared by *in situ* polymerization a good agreement is also observed for silica content up to 5 vol%. However, the nanocomposite prepared by reactive processing *in situ* polymerization with 7 vol% of silica has a lower permeability value than the one predicted by Maxwell law (**Figure B.10**). Two hypotheses can be considered to explain this result. First the samples prepared by *in situ* polymerization show well dispersed fillers up to

7 vol% silica whereas we mentionned the presence of larger aggregates for nanocomposites prepared by melt-blending with 10 vol% of silica. The second hypothesis would be the lower molar mass of the PLAis matrix in PLAis/$SiCH_3$/7 resulting in more chains ends bearing hydroxyl functions, which can create interactions with the water molecules and increase the solubility but slow down in the mean time the diffusion. Indeed, Singh *et al.* [35] showed that the increase of hydroxyl groups leads to increase the water solubiliy for PLA having molar mass below 30,000 g/mol. However, no results about the evolution of the water diffusion coefficient neither the water permeability coefficient as a function of the molar and chain ends have been reported according to our knowledge.

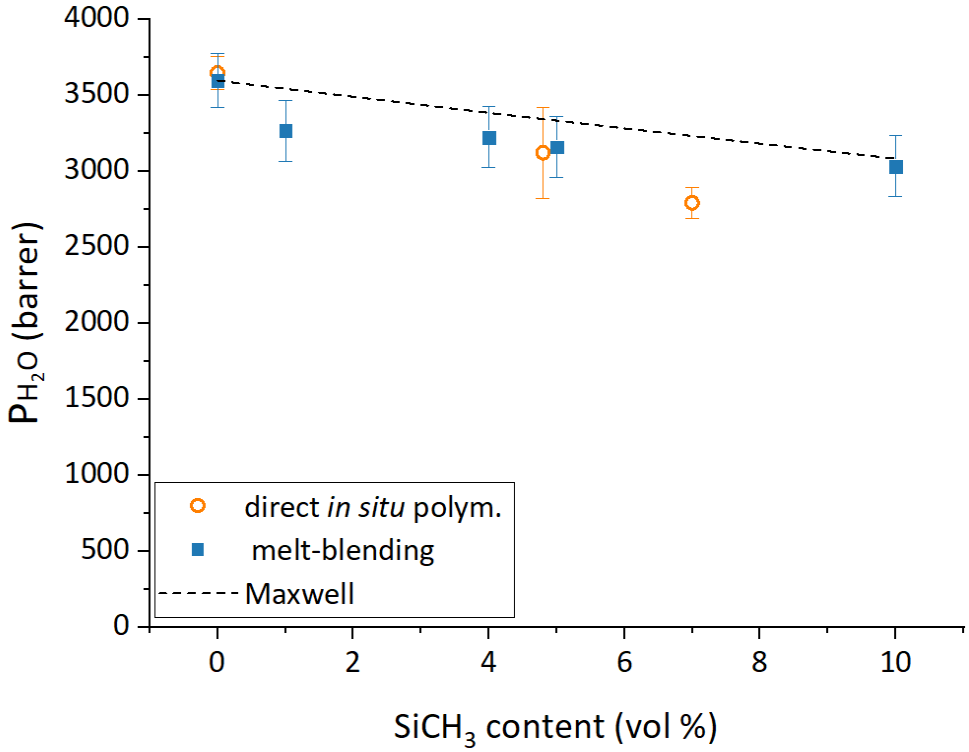


Figure B.10 - Evolution of the water permeability for silica nanocomposites prepared by melt-blending process or *in situ* polymerization. The Maxwell model is plotted in dotted line.

Figure B.11 shows the permeability values measured on the nanocomposites based on OMMT. In this case, only the permeability of the PLAref matrix has been measured and is reported. Whatever the process used to prepare the nanocomposites, the permeability values decrease as the montmorillonite content increases due to the tortuosity effect created by the montmorillonite [7]. The nanocomposite experimental permeability values have been

compared to the theoretical permeability values calculated from Bharadwaj model [36] (equation (B.5)).

$$\frac{P}{P_0} = \frac{1 - \Phi_v}{1 + \frac{\alpha}{2}\Phi_v \frac{2}{3}\left(S + \frac{1}{2}\right)} \qquad (B.5)$$

With P_0 the permeability of the unfilled PLA, Φ_v the volume fraction of filler, α the mean aspect ratio of the filler domains and S the orientation paramter. In this study, S was fixed to 0 which reflects the random orientation of the platelets in the matrix as evidenced by microscopic observations. α was taken equal to 86 and 90 corresponding the mean aspect ratio calculated from the microscopic observation of OMMT-based nanocomposites, respetively obained by the melt-blending and two-step process.

First it can be noted that the slight increase of the aspect ratio from 86 to 90 does not lead to a significative modification of the Bharadwaj model (**Figure B.11**). The model fits well the experimental permeability values for the entire range of nanocomposites prepared by melt-blending. A good agreement between experimental and calculated permeability values is also observed for the nanocomposites prepared by the two step process but only for OMMT content below or equal to 3 vol%. This result shows that introducing a moderate amount of low molar mass PLA (≤ 20 wt%) in the matrix does not induce significant effect on permeability. It also shows that the slightly better dispersion state evidenced by TEM and SAXS analyses does not play a major role here. A sharper decrease in the permeability is observed for the nanocomposites containing 7 vol% of OMMT prepared by the two-step process. This two-step process involves *in situ* polymerization of lactide in the presence of OMMT which leads to grafting of PLA chains on the OMMT, decreasing then probably the possibility of water sorption at the filler/matrix interface [12]. Moreover, the presence of PLA short chains in the commercial PLA in a sufficient amount (50 wt% with respect to commercial PLA) could also lead to an anti-plasticization effect by a decrease of the free volume as already reported in the literature with lactide oligomer [37].

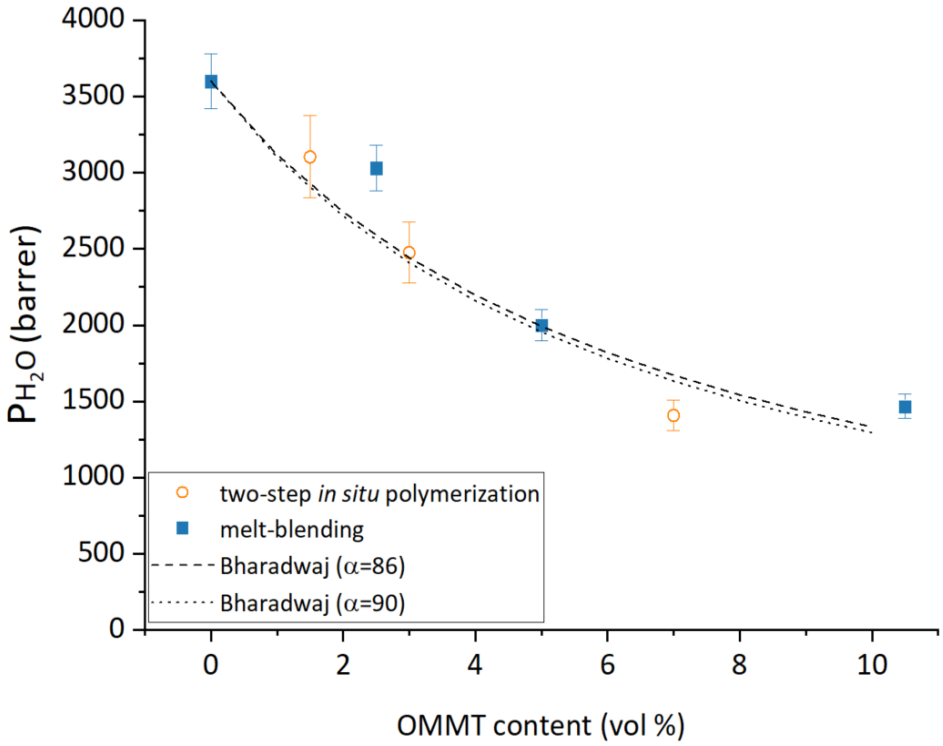


Figure B.11 - Evolution of the relative permeability for OMMT nanocomposites for melt-blending process and the two steps process. The dashed line corresponds to the Bharadwaj model for an aspect ratio value of 86 and the dotted line for an aspect ratio of 90.

5. Conclusion

In this study, PLA films containing either hydrophobic silica or a modified montmorillonite were prepared by melt-blending and *in situ* polymerization.

For the first time a direct and efficient method was reported to prepare silica nanocomposites films via *in situ* polymerization using reactive processing leading to self-standing and non-brittle films containing 5 and 7 vol% of filler. However, reactive processing was unsuccessful with organo-modified montmorillonite and the conditions of *in situ* polymerization had to be adapted to obtain cohesive films. An initial masterbatch containing 20 wt% of OMMT was first prepared via *in situ* polymerization in a reactor (120 °C, inert atmosphere, 15 h), and then dispersed into commercial PLA to reach a nanoclay content from 1.5 to 7 vol%. The nanocomposites microstructures were deeply investigated, and their respective water vapor permeability were measured.

For silica nanocomposites, the dispersion of silica as well as the water vapor permeability are similar up to 5 vol% of silica for samples prepared either from *in situ* polymerization or melt-blending. From 7 vol% of silica, *in situ* polymerization leads to obtain nanocomposites with lower water permeability value which can be attributed either to a better dispersion of the silica and/or to the higher number of hydroxyl groups available (related to the decrease of the molar mass) which could slow down the water diffusion.

In the case of montmorillonite, nanocomposites prepared by two-step *in situ* polymerization are composed of matrix containing high and low molar mass PLA. Nanocomposites prepared by *the* two-step process exhibit a slightly better dispersion of the fillers than the melt-blending ones as well as a lower water vapor permeability for relatively high content of montmorillonite (> 7 vol%). These results corroborate the hypothesis that the differences of permeability between the two processes could be explained by a high number of small chains which could decrease the free volume. Moreover, the grafting of PLA chains on the montmorillonite surface decreases probably the possibility of water sorption at the filler/matrix interface.

Finally, and for the first time the permeability of amorphous PLA nanocomposites prepared by *in situ* polymerization and melt-blending have been compared for two different fillers (eg. hydrophobic silica or Cloisite®30B). This comparison leads to conclude that *in situ* polymerization seems to be more efficient to decrease the permeability in case of highly filled PLA containing either silica or Cloisite®30B.

6. References

[1] Bioplastics market development update 2023, European Bioplastics e.V (2023). https://www.european-bioplastics.org/market/ (accessed August 20, 2024).

[2] N. Tenn, N. Follain, J. Soulestin, R. Crétois, S. Bourbigot, S. Marais, Effect of Nanoclay Hydration on Barrier Properties of PLA/Montmorillonite Based Nanocomposites, J. Phys. Chem. C 117 (2013) 12117–12135. https://doi.org/10.1021/jp401546t.

[3] E. Picard, E. Espuche, R. Fulchiron, Effect of an organo-modified montmorillonite on PLA crystallization and gas barrier properties, Applied Clay Science 53 (2011) 58–65. https://doi.org/10.1016/j.clay.2011.04.023.

[4] F. Morel, E. Espuche, V. Bounor-Legaré, O. Persynn, M. Lacroix, Impact of coated calcium carbonate nanofillers and annealing treatments on the microstructure and gas barrier properties of poly(lactide) based nanocomposite films, Journal of Polymer Science Part B: Polymer Physics 54 (2016) 649–658. https://doi.org/10.1002/polb.23957.

[5] V. Vladimirov, C. Betchev, A. Vassiliou, G. Papageorgiou, D. Bikiaris, Dynamic mechanical and morphological studies of isotactic polypropylene/fumed silica nanocomposites with enhanced gas barrier properties, Composites Science and Technology 66 (2006) 2935–2944. https://doi.org/10.1016/j.compscitech.2006.02.010.

[6] B. Tan, N.L. Thomas, A review of the water barrier properties of polymer/clay and polymer/graphene nanocomposites, Journal of Membrane Science 514 (2016) 595–612. https://doi.org/10.1016/j.memsci.2016.05.026.

[7] S. Singha, M.S. Hedenqvist, A Review on Barrier Properties of Poly(Lactic Acid)/Clay Nanocomposites, Polymers 12 (2020) 1095. https://doi.org/10.3390/polym12051095.

[8] E. Picard, J.-F. Gérard, E. Espuche, Reinforcement of the Gas Barrier Properties of Polyethylene and Polyamide Through the Nanocomposite Approach: Key Factors and Limitations, Oil Gas Sci. Technol. – Rev. IFP Energies Nouvelles 70 (2015) 237–249. https://doi.org/10.2516/ogst/2013145.

[9] M. Tanahashi, Development of Fabrication Methods of Filler/Polymer Nanocomposites: With Focus on Simple Melt-Compounding-Based Approach without Surface Modification of Nanofillers, Materials 3 (2010) 1593–1619. https://doi.org/10.3390/ma3031593.

[10] H. Baniasadi, A. Ramazani S.A., S. Javan Nikkhah, Investigation of in situ prepared polypropylene/clay nanocomposites properties and comparing to melt blending method, Materials & Design 31 (2010) 76–84. https://doi.org/10.1016/j.matdes.2009.07.014.

[11] J. Tung, R.K. Gupta, G.P. Simon, G.H. Edward, S.N. Bhattacharya, Rheological and mechanical comparative study of in situ polymerized and melt-blended nylon 6 nanocomposites, Polymer 46 (2005) 10405–10418. https://doi.org/10.1016/j.polymer.2005.08.043.

[12] O. Gain, E. Espuche, E. Pollet, M. Alexandre, Ph. Dubois, Gas barrier properties of poly(ε-caprolactone)/clay nanocomposites: Influence of the morphology and polymer/clay interactions, Journal of Polymer Science Part B: Polymer Physics 43 (2005) 205–214. https://doi.org/10.1002/polb.20316.

[13] M.A. Ortenzi, L. Basilissi, H. Farina, G. Di Silvestro, L. Piergiovanni, E. Mascheroni, Evaluation of crystallinity and gas barrier properties of films obtained from PLA nanocomposites synthesized via "in situ" polymerization of l-lactide with silane-modified nanosilica and montmorillonite, European Polymer Journal 66 (2015) 478–491. https://doi.org/10.1016/j.eurpolymj.2015.03.006.

[14] M. Nerantzaki, L. Prokopiou, D.N. Bikiaris, D. Patsiaoura, K. Chrissafis, P. Klonos, A. Kyritsis, P. Pissis, In situ prepared poly(DL-lactic acid)/silica nanocomposites: Study of molecular composition, thermal stability, glass transition and molecular dynamics, Thermochimica Acta 669 (2018) 16–29. https://doi.org/10.1016/j.tca.2018.08.025.

[15] A. Prébé, P. Alcouffe, Ph. Cassagnau, J.F. Gérard, *In situ* polymerization of l-Lactide in the presence of fumed silica, Materials Chemistry and Physics 124 (2010) 399–405. https://doi.org/10.1016/j.matchemphys.2010.06.054.

[16] Y. Guo, K. Yang, X. Zuo, Y. Xue, C. Marmorat, Y. Liu, C.-C. Chang, M.H. Rafailovich, Effects of clay platelets and natural nanotubes on mechanical properties and gas permeability of Poly (lactic acid) nanocomposites, Polymer 83 (2016) 246–259. https://doi.org/10.1016/j.polymer.2015.12.012.

[17] M.-A. Paul, C. Delcourt, M. Alexandre, P. Degée, F. Monteverde, A. Rulmont, P. Dubois, (Plasticized) Polylactide/(Organo-)Clay Nanocomposites by in situ Intercalative Polymerization, Macromolecular Chemistry and Physics 206 (2005) 484–498. https://doi.org/10.1002/macp.200400324.

[18] G.L. Re, S. Benali, Y. Habibi, J.-M. Raquez, P. Dubois, Stereocomplexed PLA nanocomposites: From in situ polymerization to materials properties, European Polymer Journal 54 (2014) 138–150. https://doi.org/10.1016/j.eurpolymj.2014.03.004.

[19] S. Bourbigot, G. Fontaine, A. Gallos, S. Bellayer, Reactive extrusion of PLA and of PLA/carbon nanotubes nanocomposite: processing, characterization and flame retardancy, Polymers for Advanced Technologies 22 (2011) 30–37. https://doi.org/10.1002/pat.1715.

[20] J.M. Pérez, C. Ruiz, I. Fernández, Synthesis of a Biodegradable PLA: NMR Signal Deconvolution and End-Group Analysis, J. Chem. Educ. 99 (2022) 1000–1007. https://doi.org/10.1021/acs.jchemed.1c00824.

[21] Ph. Degée, Ph. Dubois, S. Jacobsen, H.-G. Fritz, R. Jérôme, Beneficial effect of triphenylphosphine on the bulk polymerization of L,L-lactide promoted by 2-ethylhexanoic acid tin (II) salt, Journal of Polymer Science Part A: Polymer Chemistry 37 (1999) 2413–2420. https://doi.org/10.1002/(SICI)1099-0518(19990715)37:14<2413::AID-POLA15>3.0.CO;2-#.

[22] B. Kalb, A.J. Pennings, General crystallization behaviour of poly(l-lactic acid), Polymer 21 (1980) 607–612. https://doi.org/10.1016/0032-3861(80)90315-8.

[23] K.A.M. Thakur, R.T. Kean, E.S. Hall, M.A. Doscotch, E.J. Munson, A Quantitative Method for Determination of Lactide Composition in Poly(lactide) Using 1H NMR, Anal. Chem. 69 (1997) 4303–4309. https://doi.org/10.1021/ac970792o.

[24] J.L. Robert, K.B. Aubrecht, Ring-Opening Polymerization of Lactide To Form a Biodegradable Polymer, J. Chem. Educ. 85 (2008) 258. https://doi.org/10.1021/ed085p258.

[25] J.R. Dorgan, J.S. Williams, D.N. Lewis, Melt rheology of poly(lactic acid): Entanglement and chain architecture effects, Journal of Rheology 43 (1999) 1141–1155. https://doi.org/10.1122/1.551041.
[26] L.-T. Lim, R. Auras, M. Rubino, Processing technologies for poly(lactic acid), Progress in Polymer Science 33 (2008) 820–852. https://doi.org/10.1016/j.progpolymsci.2008.05.004.
[27] P.B. Messersmith, E.P. Giannelis, Synthesis and barrier properties of poly(ε-caprolactone)-layered silicate nanocomposites, Journal of Polymer Science Part A: Polymer Chemistry 33 (1995) 1047–1057. https://doi.org/10.1002/pola.1995.080330707.
[28] G. Kister, G. Cassanas, M. Vert, Morphology of poly(glycolic acid) by IR and Raman spectroscopies, Spectrochimica Acta Part A: Molecular and Biomolecular Spectroscopy 53 (1997) 1399–1403. https://doi.org/10.1016/S0584-8539(97)00039-1.
[29] A. Jullin, G. Sudre, N. Hascoët, F. Chinesta, E. Espuche, Influence of different type of impermeable phase on the permeability of PLA films : nanofillers versus crystalline phase, Polymer Testing (Submitted) (2024).
[30] P. Song, G. Chen, Z. Wei, W. Zhang, J. Liang, Calorimetric analysis of the multiple melting behavior of melt-crystallized poly(l-lactic acid) with a low optical purity, J Therm Anal Calorim 111 (2013) 1507–1514. https://doi.org/10.1007/s10973-012-2502-4.
[31] E. Jacquelot, E. Espuche, J.-F. Gérard, J. Duchet, P. Mazabraud, Morphology and gas barrier properties of polyethylene-based nanocomposites, Journal of Polymer Science Part B: Polymer Physics 44 (2006) 431–440. https://doi.org/10.1002/polb.20707.
[32] J.C. Maxwell, A Treatise on Electricity and Magnetism, Clarendon Press, 1873.
[33] M.L. De Haro, J.A.P. Del Río, S. Whitaker, Flow of Maxwell fluids in porous media, Transp Porous Med 25 (1996) 167–192. https://doi.org/10.1007/BF00135854.
[34] S.A. Hashemifard, A.F. Ismail, T. Matsuura, Prediction of gas permeability in mixed matrix membranes using theoretical models, Journal of Membrane Science 347 (2010) 53–61. https://doi.org/10.1016/j.memsci.2009.10.005.
[35] V.M. Singh, D. Koo, G.R. Palmese, R.A. Cairncross, Synthesis of polylactide with varying molecular weight and aliphatic content: Effect on moisture sorption, Journal of Applied Polymer Science 120 (2011) 2543–2549. https://doi.org/10.1002/app.33271.
[36] R.K. Bharadwaj, Modeling the Barrier Properties of Polymer-Layered Silicate Nanocomposites, Macromolecules 34 (2001) 9189–9192. https://doi.org/10.1021/ma010780b.
[37] J. Ambrosio-Martín, M.J. Fabra, A. Lopez-Rubio, J.M. Lagaron, An effect of lactic acid oligomers on the barrier properties of polylactide, J Mater Sci 49 (2014) 2975–2986. https://doi.org/10.1007/s10853-013-7929-x.

Cette deuxième partie traitait de l'influence du procédé de mise en œuvre sur la perméabilité de nanocomposites contenant soit une silice hydrophobe, soit une montmorillonite modifiée par un cation organique hydrophile. Il a été montré que la polymérisation *in situ* permettait de diminuer davantage la perméabilité que le mélange par voie fondue pour des taux de charge relativement élevés (≥ 7 %vol). Cette diminution de perméabilité a été attribuée à la fois à une meilleure dispersion des charges et à des modifications des propriétés de la matrice. Le procédé d'élaboration semble donc être un facteur supplémentaire à prendre en compte pour l'étude de la perméabilité. Devant le nombre conséquent de paramètres pouvant jouer un rôle sur la perméabilité finale, ces paramètres pouvant avoir un effet direct ou indirect sur les propriétés, induisant donc des interrelations, le machine learning a été envisagée comme une nouvelle approche pour prédire la perméabilité d'un matériau. Les des facteurs identifiés dans les deux parties précédentes, c'est-à-dire le taux de phase imperméable, la forme initiale des charges, la dispersion de la phase imperméable au sein de la matrice (facteurs de forme, distance entre les domaines imperméables, fraction d'agrégats), la fraction amorphe rigide et le procédé d'élaboration ont été considérés comme données d'entré dans cette nouvelle approche. L'intérêt du machine learning et qu'il repose uniquement sur les données expérimentales. Il est attendu pour cette approche de pouvoir identifier les paramètres gouvernant la perméabilité. Cette nouvelle approche est l'objet de la dernière étude de ce chapitre. C'est la première fois, à notre connaissance, que le machine learning est utilisé pour prédire la perméabilité de matrice PLA contenant une phase imperméable. Cette dernière étude a été écrite sous forme d'un article et soumise au *Journal Food Packaging and Shelf Life* en octobre 2024.

Chapitre III.C - Data Driven modelling as a new route to design PLA based materials with high barrier properties

1. Abstract ____ *174*

2. Introduction ____ *174*

3. Methods ____ *176*

3.1. Dataset ____ 176

3.2. Modelling ____ 178

3.3. Parameters correlations ____ 179

4. Results and discussion ____ *180*

4.1. Features selection to predict permeability of PLA based materials by machine learning ____ 180

4.2. Machine learning predictions of relative permeability based on an enriched dataset ____ 186

5. Conclusion ____ *193*

6. References ____ *194*

1. Abstract

In this study, two machine learning models (ML), namely Random Forest and Support Vector Machine, have been trained to predict the relative permeability of PLA based materials containing an impermeable phase. A large range of impermeable phases have been investigated, going from spherical, tubular, lamellar fillers to spherolites. Input parameters have been chosen wisely from the material characteristics and statistical correlations have been established to keep only the relevant ones. By this way, additional samples could have been added to the dataset. Good accuracy of the predicted relative permeability has been obtained for both models. The corresponding models were therefore used for proposing the material designs meeting targeted relative permeability values. For the first time, ML models are used to predict the permeability of polymer containing an impermeable phase.

2. Introduction

In recent years, there has been a growing interest in more environmentally friendly polymers for applications requiring high barrier properties. Polylactic acid (PLA) which is a biosourced and biodegradable polymer is a promising alternative to reduce the large amount of waste produced by packaging. However, its low gas and water barrier properties have led to a wide range of studies over the last years which focused on barrier improvement (**Figure C.1**). It has been experimentally shown that the addition of impermeable fillers is an effective method to bring a tortuosity effect leading to decrease the permeability [1], [2], [3]. Another route consists in annealing the amorphous polymer to create a crystalline phase which is also considered as an impermeable phase due to its higher density [4], [5], [6].

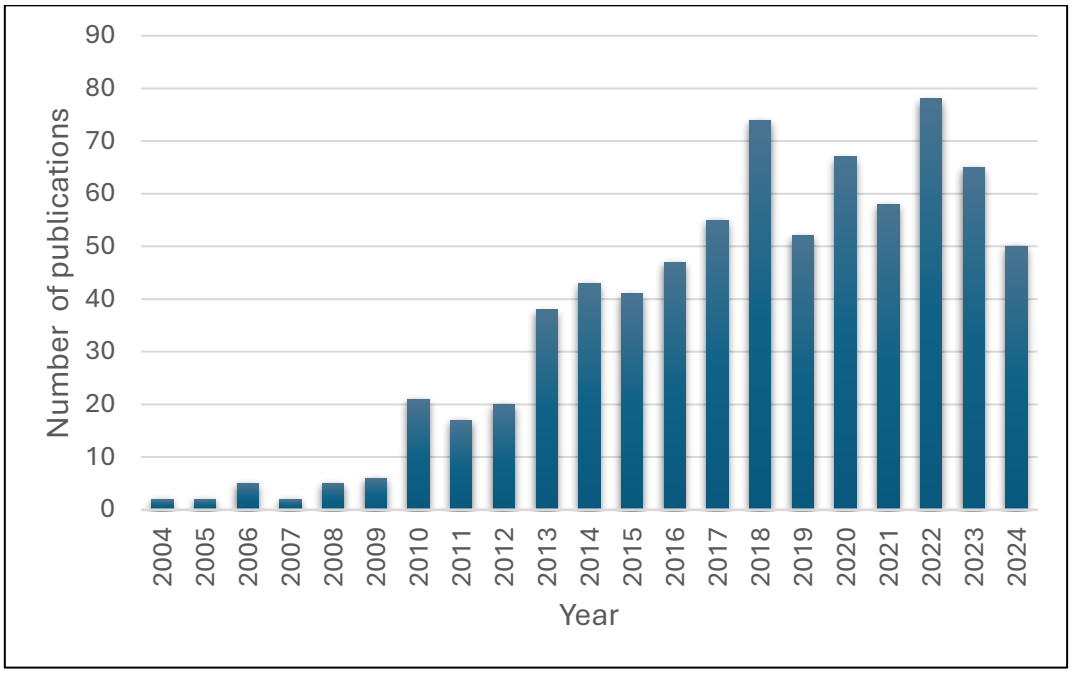


Figure C.1 - Number of publications by year combining the key words: "Polylactic acid" and "barrier properties" (Web of science, October 2024).

However, the barrier properties in these heterogeneous systems are the result of multiple parameters, each of which must be optimized without harming the others and many questions remain unsolved. For example, in most cases, filler dispersion and content tends to be optimized to maximize the tortuosity effect, which is the most effective way of decreasing permeability according to empirical permeability models (Nielsen, Bharadwaj...) [7], [8]. However, from an experimental point of view, the quality of the dispersion usually decreases with the filler content [9], [10], [11], [12], [13], [14]. The question is from which size and proportion, aggregates become unfavorable in terms of barrier properties. Moreover, the addition of an impermeable phase can induce a modification of the mobility of the surrounding polymer chains which may influence the permeability [4], [5], [6]. All this leads to the global question of how these parameters can influence permeability. In other words, which microstructural parameters are predominant for the control of barrier properties? What is the best microstructure to achieve the lowest permeability or which microstructure reflecting the combination of relevant microstructural parameters is appropriate for a targeted permeability value?

Machine learning (ML), which has expanded during these last years, is a powerful tool for such analysis. One of the advantages of this approach is that it is only based on experimental data without

any assumptions. The careful review of the literature on this field shows that so far only few articles based on ML are concerned with polymer barrier properties or gas separation [15], [16], [17] . Moreover, according to our knowledge, no study has been published up to now on analyzing PLA based materials and their related barrier properties by ML approaches, showing the novelty and the originality of our study.

In this work, a data driven modelling approach is proposed to investigate the barrier properties of PLA based materials which contain one impermeable phase. For this purpose, a large dataset including a wide range of nature, shape, size and content of impermeable phase is built and two machine learning regression models: Random Forest and Support Vector Machine, are selected. The first step consists in extracting from the global dataset a reduced one which gives a detailed microstructural description of the materials through a large enough number of parameters. The aim of this first step is *i/* to investigate the effects of this entire set of parameters on the barrier properties *ii/* to evidence potential interrelations between parameters with the aim of identifying the most relevant ones and determining the necessary and sufficient number of parameters required to predict barrier properties. In a second step, the dataset is enlarged with more numerous samples for the previously selected parameters and the ability of Random Forest as well as Support Vector Machine to predict the experimental barrier properties is analyzed. Finally, materials microstructures able to meet different targeted levels of barrier properties are proposed from the developed data driven ML approach.

3. Methods

3.1. Dataset

The data set built for this study is composed of 69 samples which come from our own experimental study [18] and from data collected in the literature [2], [5], [6], [11], [13], [19]. The samples are PLA based materials containing one impermeable phase which is either of nanofiller type or of PLA spherulitic crystalline phase. Concerning the barrier properties, as the permeability experiments were performed by using different experimental conditions for different diffusing molecules (oxygen or water vapor), it has been decided to consider the relative permeability as output. The relative permeability (P/P_0) corresponds to the permeability of the PLA sample containing an impermeable

phase *(P)* over the permeability of the reference PLA (P_0). **Figure C.2** represents the relative permeability values of the samples of the dataset as a function of the impermeable phase volume content. Regarding the values, no simple relation between the relative permeability and the impermeable phase content could be drawn. Thus, additional parameters were considered to give a more detailed description of each sample.

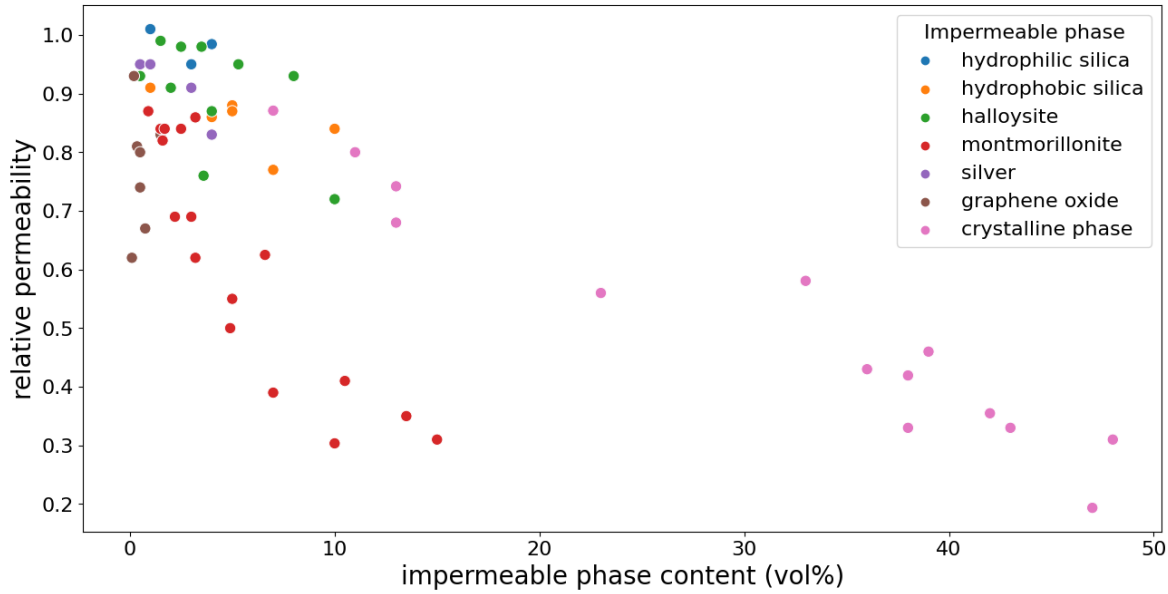


Figure C.2 - Relative permeability as a function of the impermeable phase content for the different impermeable phases of the dataset constituted by 69 samples coming from [2], [5], [6], [11], [13], [18], [19].

The parameters used in this study are listed in **Table C.1**. with their respective range of values. The *shape* corresponds to the initial shape of the fillers. In the case where the impermeable phase is the crystalline PLA phase, this last one is composed of spherolites [5], [20]. The *impermeable_content* corresponds to the volume fraction of the impermeable phase in the material. The *mean_AR* is equal to an average value of ratio of the length over the thickness (or diameter) of the impermeable phase in the material. The *aggregates_content* stands for the fraction of non-unitary fillers and the *inter_domains_spacing* is the mean distance between the impermeable domains. The change of mobility of the polymer chains surrounding the impermeable dispersed domains is taken into account through the rigid amorphous fraction (RAF) [18], [21]. The RAF_a parameter corresponds to the proportion of the rigid amorphous fraction over the global amorphous phase.

Table C.1 - Parameters used and their range values.

PARAMETERS	***Parameter type for ML***	***VALUES***
shape	Input parameters	1: spherolites 2: sphere 3: tubes 4: random platelets 5: oriented platelets
impermeable_content		0 - 50 vol%
mean_AR		1 - 100
aggregates_content		0 - 100%
interdomains_spacing		0 - 4000 nm
RAF_a		0 - 30%
P/P_0	Output parameter	0 - 1

3.2. Modelling

In this study, supervised learning was used to train the models to predict the relative permeability of PLA based samples. As the relative permeability values behave as continuous variable, we choose to work with two regression models: the Random Forest regression and the Support Vector Machine regression. Random Forest (RF) has been chosen because of the limited number of data and the differences of domains between the parameters. Random Forest is a group of several Decision Trees based on binary data sorting. Here, the number of trees has been fixed to 100 and the prediction of the Random Forest is a mean of those 100 Decisions Trees predictions [22], [23]. Support Vector Machine regression (SVM) is an efficient model for nonlinear regression with few data, which uses a kernel and a hyperplane to fit the data. For this model, we used a radial basis functional kernel to recognize the data pattern [22], [23], [24], [25].

Machine learning models have been trained with 80% of the samples from the dataset, chosen randomly in the dataset, using the *train test split* procedure. Then, the 20% remaining samples were used to compare the predicted output with the experimental ones. From this, the mean absolute error (MAE) as well as the coefficient of determination (R^2) have been calculated to evaluate the model accuracy according to equation (C.1) and (C.2), respectively, for the training and the testing results.

$$MAE = \frac{\sum_{i=1}^{n} |yi - \hat{y}i|}{n} \quad (C.1)$$

$$R^2 = 1 - \frac{\sum_{i=1}^{n} (yi - \hat{y}i)^2}{\sum_{i=1}^{n} (yi - \overline{y})^2} \quad (C.2)$$

with n the number of samples, yi the experimental relative permeability, $\hat{y}i$ the predicted relative permeability and $\overline{y}$ the mean of the experimental permeability values.

Cross validation has been used to estimate the robustness of the model by repeating the random splitting procedure 40 times to select different samples used for training the model and for evaluating the accuracy of the model predictions, also called testing or validation data. The cross validation has been done by using *Shuffle Split* strategy. The model is then trained with the training data and evaluated with testing data. The mean absolute error (MAE) and the coefficient of determination (R^2) over the different training and testing have been calculated to estimate the variability of the model performance.

3.3. Parameters correlations

To identify potential correlations between the parameters, correlation coefficients were calculated according to two methods: the Pearson correlation and the Spearman correlation. Pearson correlation coefficient (ρ) [26] measures the linearity between two variables (X, Y) through the ratio of the covariance of the two variables over the product of their standard deviation, according to equation (C.3). A Pearson coefficient with an absolute value of 1 indicates an exact linear relation between the two variables.

$$\rho_{X,Y} = \frac{cov\ (X,Y)}{\sigma_X . \sigma_y} \quad (C.3)$$

Where X and Y are two variables, $cov\ (X,Y)$ is the covariance and σ_X, σ_y are the standard deviation of respectively X and Y.

Spearman correlation measures the monotony of two variables (X, Y) by calculating the Pearsons coefficient between the rank of the variables according to equation (C.4). A Spearman coefficient (r) with an absolute value of 1 indicates a perfect monotony between the two variables [27], [28].

$$r = \rho_{R(X),R(Y)} = \frac{cov\left(R(X),R(Y)\right)}{\sigma_{R(X)} \cdot \sigma_{R(Y)}} \quad (C.4)$$

Where X and Y are two variables, $R(X)$ and $R(Y)$ are the rank of X and Y, $cov\left(R(X),R(Y)\right)$ is the rank covariance and $\sigma_{R(X)}$, $\sigma_{R(Y)}$ are the rank standard deviations.

For both coefficients, a positive value indicates an evolution of the two variables in the same direction whereas a negative coefficient indicates that when a variable increases the other one decreases.

4. Results and discussion

In the first part, the widest data set in terms of input parameters has been selected from available experimental data. The aim is to evidence potential interrelationships between parameters and thus to identify the relevant ones. Then in the second part, RF and SVM models are used with the identified relevant parameters for an extended range of samples to make predictions.

4.1. Features selection to predict permeability of PLA based materials by machine learning

A data set comprising six input parameters as defined below is used:

$$input\ parameters: \begin{bmatrix} shape \\ imperpermeable\ content \\ mean_AR \\ aggrgates_content \\ interdomians_spacing \\ RAFa \end{bmatrix}$$

To have access to all these parameters, only our own experimental data set can be used, which represents 33 samples. Although the number of samples is rather low for machine learning modeling compared to other studies [15], [16], [17], this dataset gathers different natures of fillers with different chemical compositions (hydrophilic and hydrophobic silica, silver metal, halloysite nanotubes, organo-modified montmorillonite, graphene oxide) and different shapes (sphere, tubes, lamellae). For lamellae, a distinction is made between the ones oriented perpendicular to the diffusion flow (oriented lamellae) and the ones with a random orientation (random lamellae). In

addition, unfilled semi-crystalline PLA samples with different degree of crystallinity are part of the dataset, the crystalline phase acting as an impermeable phase [4], [5]. **Figure C.3** shows the relative proportions of each type of impermeable phase and each shape of impermeable phase which are well balanced.

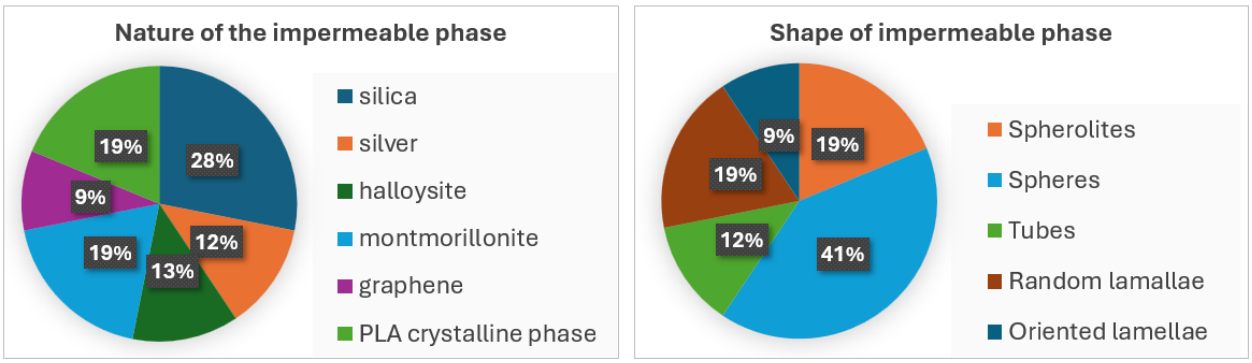


Figure C.3 - Partition of the samples according to the nature and shape of the impermeable phase for the dataset composed of 33 samples.

Random Forest (RF) and Support Vector Machine regressions (SVM) were both applied to this dataset and their ability to predict the relative permeability was compared. Among the 33 samples, 26 were used to train and fit the model and 7 were used for testing the model. The relative permeability predicted by the models (P/P_0 *predicted*) was compared with the experimental values (P/P_0 *experimental*) as shown in **Figure C.4**. Whatever the ML model, training values are close to the bisector which means that the model is well trained to generalize the predictions to new values. The testing values are more dispersed but stay around the bisector meaning that the predicted values are not far from the experimental values. The mean absolute error values of the test are respectively equal to 0.12 and 0.10 for the RF and the SVM models, which is close to the experimental error (around 10%). The R^2 score has also been calculated and is equal to 0.36 for RF and 0.51 for SVM which is not satisfying. In conclusion, these two models have to be enhanced to obtain better predictions.

To improve model predictions, it is relevant to look at the respective influence of the different input parameters over the experimental relative permeability. Indeed, their quantity can influence the precision and the efficiency of the model. This is why one of the major challenges when using machine learning is to find the appropriate parameters, needed and sufficient, to describe the material.

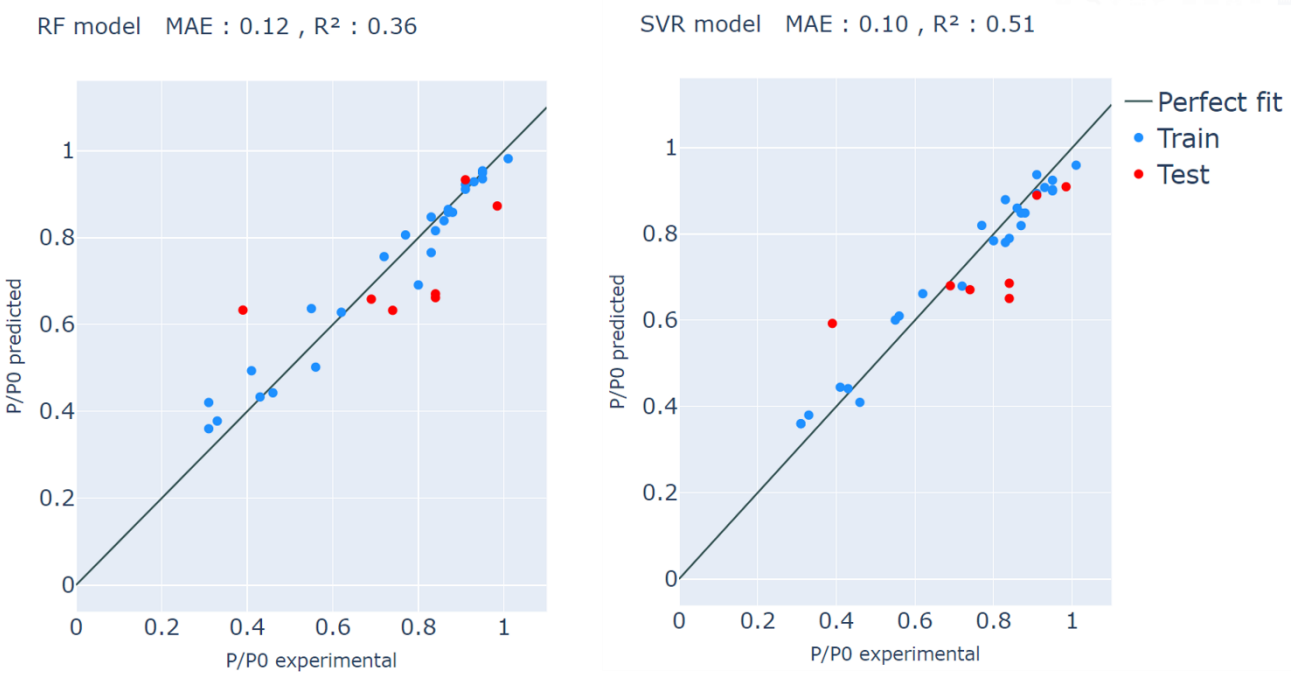


Figure C.4 – Predictions vs Ground-Truths graphs representing the predicted relative permeability versus the experimental permeability for Random Forest regression (left) and Support Vector Machine regression (right). The blue points correspond to the P/P_0 values of the training phase, the red points *the* P/P_0 values of the testing phase and the solid line is the bisector standing for the perfect fit. The dataset counts 33 samples.

For that goal, the Person's and Spearman's correlation coefficients between the different input parameters and the relative permeability have been determined based on the 33 studied samples (**Figure C.5**). For these correlations, the *shape* of impermeable phase has been removed as it is not in a vector space. Pearson's correlation shows that relative permeability mainly depends on the *impermeable_content* (ρ = |0.74|) as well as on the RAF_a (ρ = |0.62|). Moreover, the RAF_a is closely related to the *impermeable_content* (ρ =| 0.87|), which makes the RAF_a a redundant parameter. For Spearman's correlation, relative permeability is closely related to the *impermeable_content* (r = |0.62|) and to the *interparticle_spacing* (r = |0.78|). According to Spearman's correlation the RAF_a and the *interparticle_spacing* are clearly related to the *impermeable_content* (respectively r = |0.60| and |0.64|), which means that these two parameters are redundant with the *impermeable_content*.

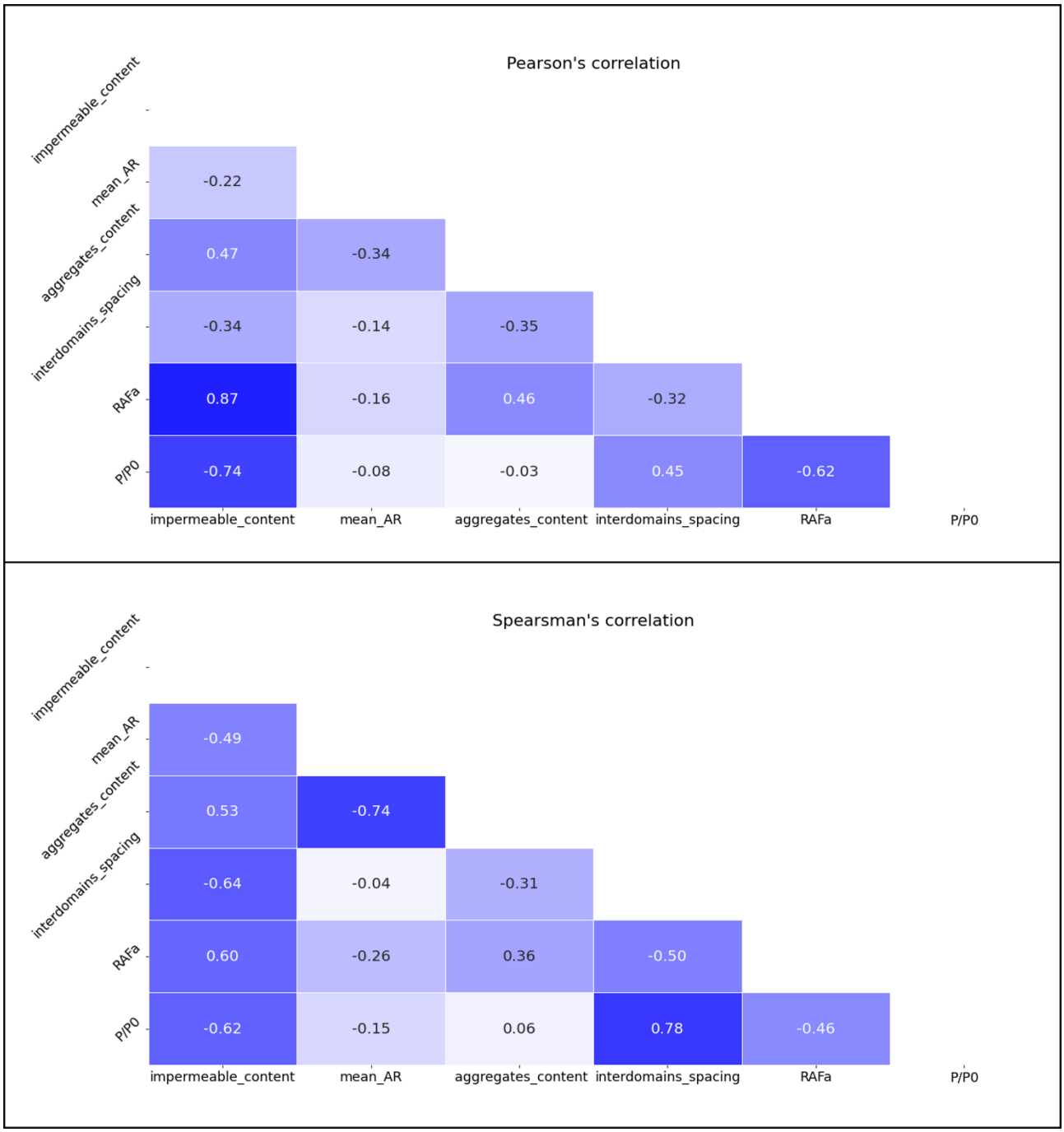


Figure C.5 - Results of the Pearson (up) and Spearman (down) correlation for the different parameters based on the dataset comprising 33 samples.

To go more in detail, the same procedure is done going from systems with low impermeable content (< 15 vol%) and by adding step by step more concentrated systems, to see the effect of the impermeable phase amount on the correlation coefficients. The absolute values of the Pearsons and Spearman's correlation coefficients between the experimental P/P_0 and the different input parameters are presented for different ranges of *impermeable_content* defined as [0-maximum

impermeable_content] in **Figure C.6**. Interestingly, the values of the correlation coefficients obtained for the different input parameters do not show the same trends going from impermeable phase content lower than 15% to content higher than 15%. Indeed, in the first case the *impermeable_content*, the *mean_AR* and the *interdomains_spacing* are the most related to P/P_0 whereas in the second case it is the *impermeable_content*, the RAF_a and the *interdomains_spacing* which have the bigger influence on the relative permeability. However, as the RAF_a and the *interparticle_spacing* are related to the *impermeable_content* as mentioned before, they are not necessary parameters for the study of the relative permeability.

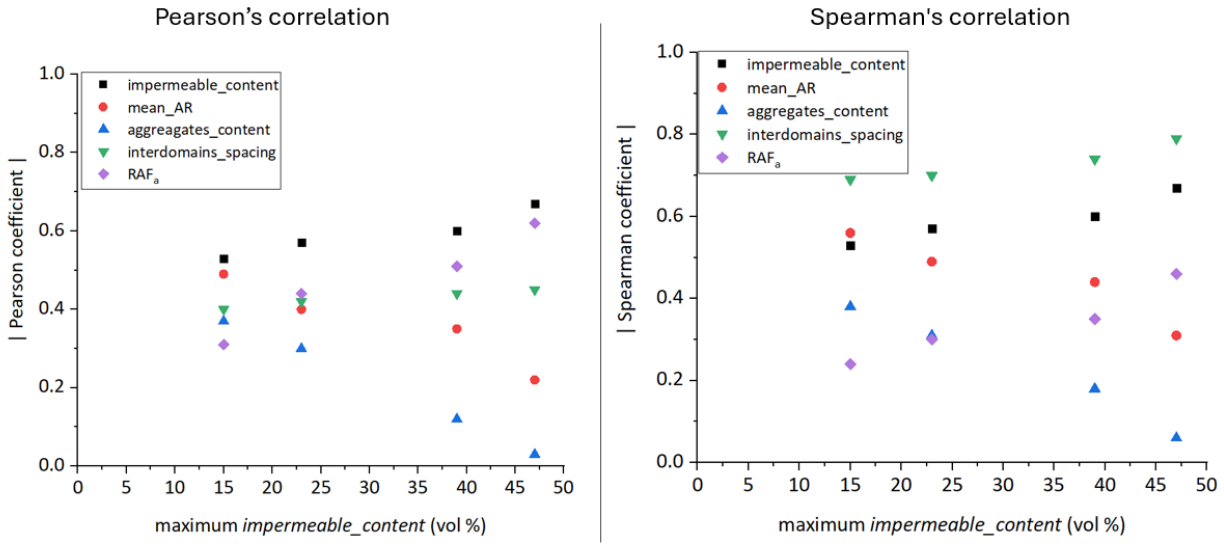


Figure C.6 - Evolution of the absolute value of the Pearson and Spearman correlation coefficients between the experimental relative permeability and the different input features as a function of the [0-maximum impermeable_content] range.

From Pearson and Spearman correlation analysis we can conclude that the most relevant and independent parameters to model relative permeability, with our data, seem to be the *impermeable_content* and the *mean_AR*. These selection of parameters is consistent with the conclusion drawn in the literature from experimental analyses [3], [11], [29], [30].

Thus, the two parameters selected thanks to the correlation (*impermeable_content* and *mean_AR)* as well as the *shape*, which is to our knowledge a key parameter, were considered for performing machine learning with RF and SVM models. The Predictions vs Ground-Truths graphs of the regression models are presented in **Figure C.7**. Both models seem to be well trained as the P/P_0 *predicted* values of training data (blue points) are close to the P/P_0 *experimental* values. Although

the predictions relative to the testing step (represented by the red marks) are less accurate than the training step, the predicted values remain relatively close to the bisector which represents the perfect fit. The mean absolute error (*MAE*), respectively equal to 0.09 with RF and 0.08 with SVM, is comparable to the *MAE* of the previous models (respectively 0.12 for RF and and 0.10 for SVM) which contains a larger number of input parameters. The R^2 score values (respectively 0.53 for RF and 0.69 for SVM) are higher than the ones calculated with the previous models (respectively 0.36 and 0.51). This means that the selection of the parameters does not worsen the accuracy of the predictions and even improves them slightly.

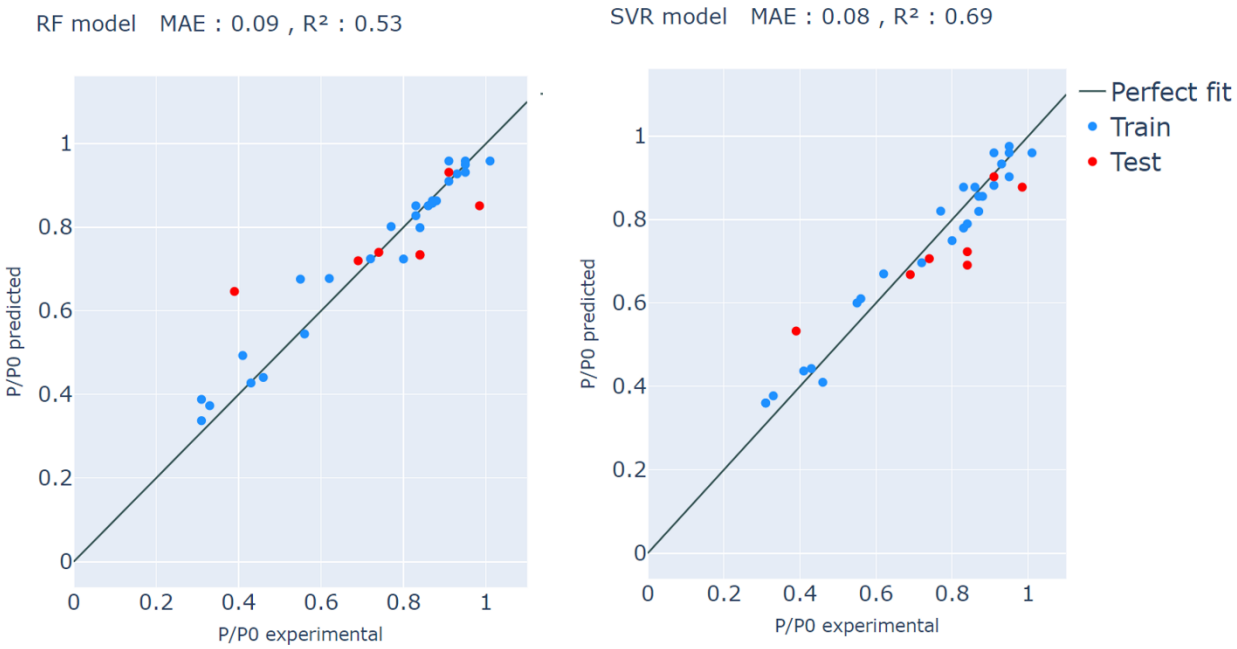


Figure C.7 – Predictions vs Ground-Truths graphs representing the predicted relative permeability versus the experimental relative permeability for Random Forest regression (left) and Support Vector Machine regression (right) with the *shape*, the *impermeable_content* and the *mean_AR* as input parameters. The blue points correspond to the P/P_0 values of the training phase, the red points the P/P_0 values of the testing phase and the solid line is the bisector standing for the perfect fit. The dataset contains 33 samples.

Regarding the limited number of data, we have also checked the results by cross validation with 40 repetitions. The detailed results of the *MAE* and the R^2 score for the testing step and training step are presented as histograms in supplementary information (**Supplementary Figure C.1**). The average value and the standard deviation of the *MAE* and R^2 for the testing step have been calculated and have a respective value of 0.08 ± 0.02 and 0.6 ± 0.3 for both RF and SVM regressions. The mean average values are close to the one obtained in **Figure C.7**. However, the high standard deviation values show that the performance of the model is depending on how the testing and training data

are split in the dataset. This can be explained by the very few numbers of data and especially for low relative relative permeability.

We can conclude from this first part that the relevant selection of the parameters did not worsen the accuracy of the predictions and even allowed a slight improvement, but the small number of samples limit the robustness of the model. This means that the training data must be chosen wisely to have the best predictions, which requires more time.

4.2. Machine learning predictions of relative permeability based on an enriched dataset

To improve and extend the machine learning predictions, the initial dataset composed by 33 samples was enlarged with samples from the literature for which the three previously selected parameters (*shape*, *impermeable_content*, *mean_AR*) used as inputs were known. The new dataset was composed of a total of 69 samples. The partition of the samples considering respectively the impermeable phase nature and shape is given in **Figure C.8**. It can be seen that the proportion of samples in each category is fairly balanced.

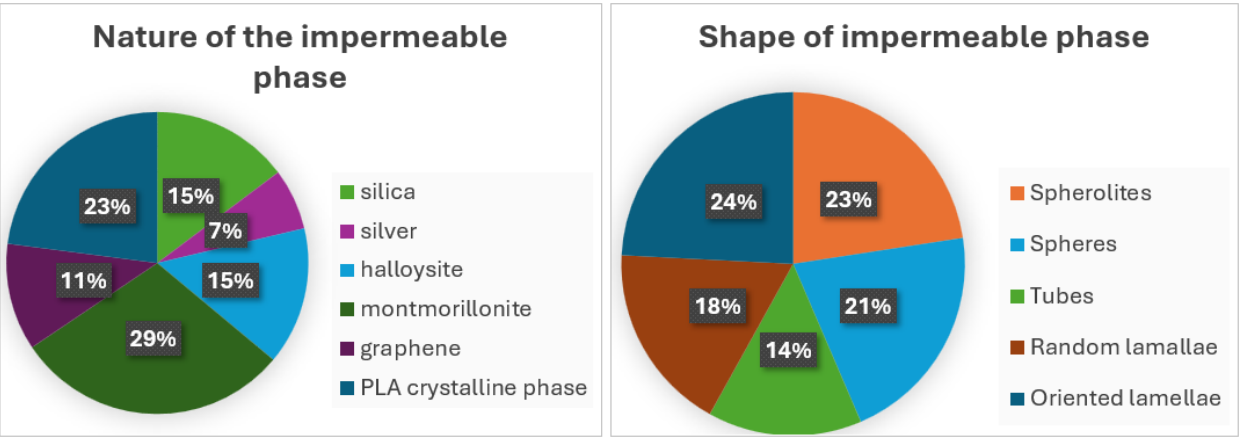


Figure C.8 - Partition of the samples according to the nature and shape of the impermeable phase. The data set is composed of 69 samples.

Random Forest and Support Vector Machine regressions have been used for modeling. 56 samples have been used to train the models and 13 for testing. Predicted P/P_0 values versus experimental P/P_0 values are reported in **Figure 9**. The P/P_0 *predicted* values are close to the P/P_0 *experimental* values for the samples used to train the model (blue points). Concerning the validation of the model, the predicted values obtained from 13 samples used for testing are relatively close to the bisector

for the entire range of relative permeability values which means that the predicted values agree the experimental values. The mean absolute error (*MAE*) is 0.09 for the RF model and 0.08 for the SVM model, which is in the range of the experimental error. These values are similar to the ones obtained in the first part of this study. However, the R^2 score has been greatly improved compared to the previous part with a value of 0.84 with the RF and 0.81 with the SVM versus respective values obtained of 0.53 and 0.69 previously.

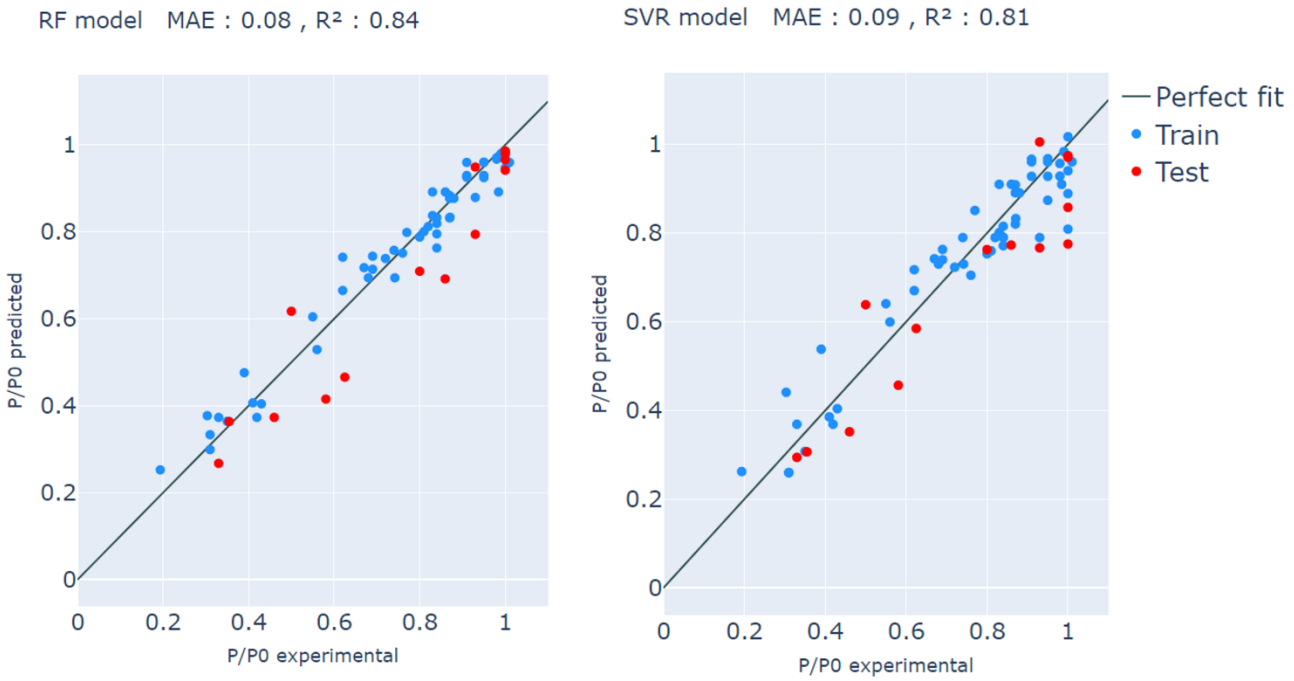


Figure 9- Predictions vs Ground-Truths graph of the predicted P/P_0 over the experimental P/P_0 for Random Forest regression (left) and Support Vector Machine regression (right). The dataset contains 69 samples and 3 parameters as input: the *shape*, the *impermeable_content* and the *mean_AR*.

Cross validation confirms these results for both models with a mean value of the *MAE* equal to 0.08 ± 0.01 and mean value of R^2 of 0.78 ± 0.1. The standard deviations of the *MAE* and R^2 for the testing points are small, which means that the model is more robust than in the first part of the study. This time, the accuracy of the predictions is no longer depending on the choice of the training data. The detailed results of the cross validation presented in histograms are given in supporting information (**Supplementary Figure C.2**). Thus, the addition of samples in the dataset enables us to enhance the accuracy as well as the repeatability of the models' predictions.

To analyze more deeply the accuracy of the models as a function of the shape of the impermeable phase, the relative permeability curves predicted by the RF and SVM models were represented in

Figure C.10 for the five PLA-based series considered in this work, meaning the series containing respectively spherolites, spherical fillers, tubular fillers, randomly dispersed lamellar fillers and lamellar fillers oriented perpendicularly to the diffusion path. For tubes and lamellae, the relative permeability predicted by the models have only been represented for a precise value of *mean_AR* for which a sufficient amount of experimental data could be collected. In parallel, the predicted permeability values of both models were compared to the respective experimental relative permeability values.

Figure C.10 a,b, c exhibit the results obtained for spherolites, spheres and tubes. It can be noticed that the two models show a decrease of relative permeability as the *impermeable_content* increases whatever the shape of impermeable phase as can be expected regarding the literature [5], [19], [31]. For spheres and tubes (**Figure C.10b,c**) both models give similar predictions whereas for spherolites (**Figure C.10a**) models show significant differences in the spherolite range between 10 and 30 vol%. These differences can be explained by the low number of samples in this range of impermeable content for spherolites shapes in the dataset as well as by the different architecture of the two models. Nevertheless, whatever the type of impermeable phase, the predicted relative permeability values of both models are in good agreement with the experimental relative permeability values. Moreover, the mean absolute error has been calculated and is below 0.05 for the different shapes of impermeable phase with both models (**Supplementary Figure C.3**) which confirms the good performance of the models.

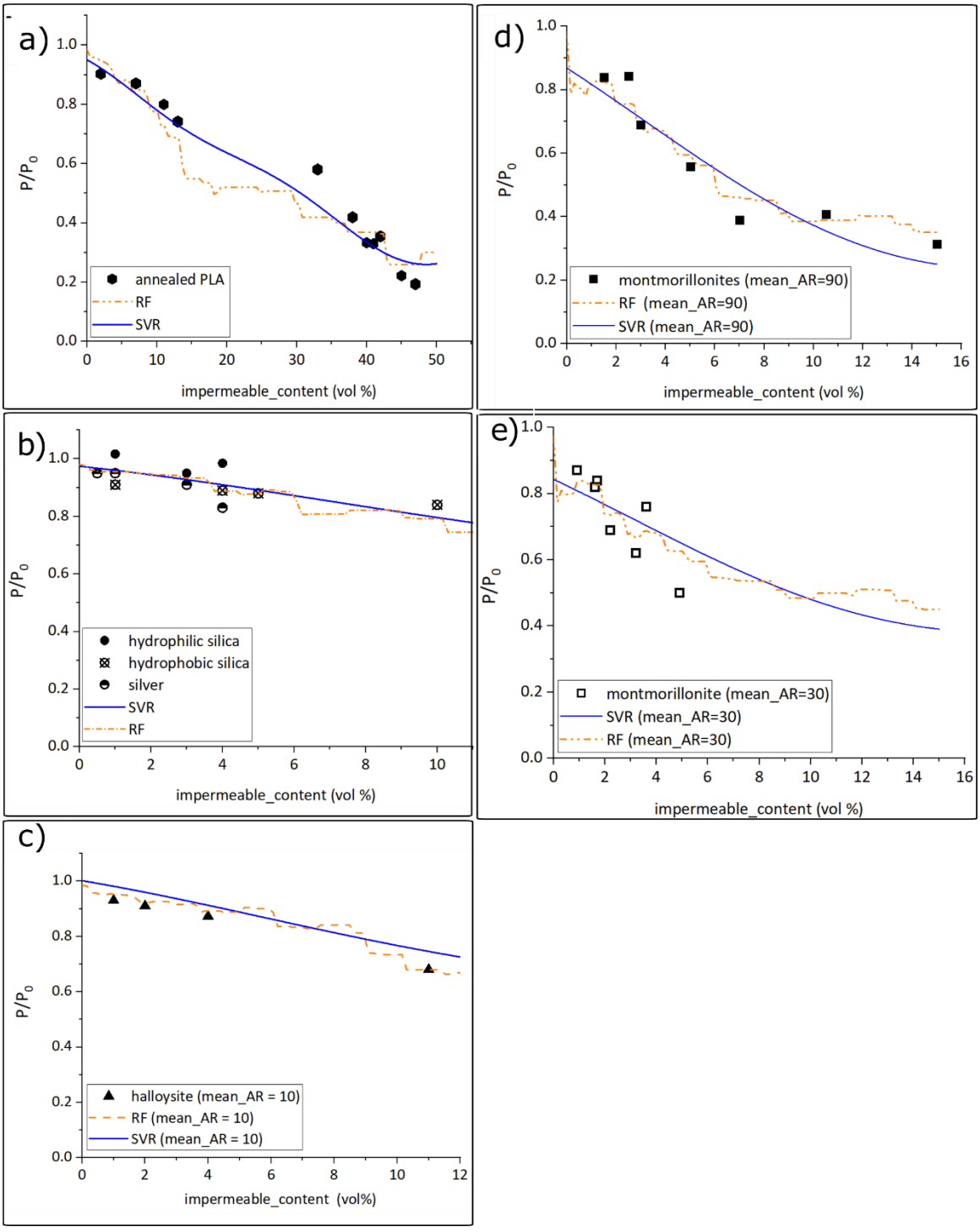


Figure C.10- RF and SVM predicted relative permeability curves as a function of the impermeable phase content and comparison with experimental relative permeability values for PLA containing a) spherolites, b) spherical fillers , c) tubes with a *mean_AR* = 10, d) random lamellae with a *mean_AR* = 90 and e) oriented lamellae with a *mean_AR* = 30.

For impermeable domains with lamellar shape, the comparison between predicted and experimental relative permeability is shown in **Figure C.10d,e.** Both models exhibit the same trend

and show a decrease of the relative permeability as the impermeable phase content increases up to 10 vol%. Above 10 vol% of fillers, the reduction in permeability is more moderate which agrees with both experimental results and empirical theoretical laws (Nielsen, Bharadwaj….) reported in the literature [7], [8]. Here again, the experimental points are located in the immediate vicinity of the curves predicted by the SVM and RF models, showing that the machine learning models are well adapted independently of the lamellae orientation. The mean absolute error is 0.07 for both models in the case of randomly dispersed lamellae which is comparable to the experimental error. For oriented lamellae, the *MAE* value is also equal to 0.07 for the SVM model and even lower for the RF model (MAE_SVR = 0.05) (**Supplementary Figure C.3**)

To conclude, the predicted relative permeability values match well the experimental values for the different shapes of impermeable phase, with mean absolute error values below or equal to 0.07 which corresponds to the experimental error.

In the last part of this work, machine learning models were used to predict the parameters of the impermeable phase dispersed in PLA, (*e.g*. the filler shape, *mean_AR*, and *impermeable_content*) enabling specific levels of P/P_0 with a maximum absolute error of 0.05. The relative permeability values were fixed at 0.8, 0.6 and 0.4, respectively and the parameters selection derived from RF and SVM models were identified. It has to be noted that the selections shown in the **Figure C.11** take into account additional criteria that are presented below and have contributed to reducing the initial selections. These criteria are not included in the models, but they are important as they take into account :

- The impermeable content for fillers (sphere, tubes and lamellae) has been fixed below 15 vol% as beyond this content the materials can become brittle.
- The mean aspect ratio of the impermeable phase for lamellae has been fixed superior to 10 to avoid the presence of big filler aggregates within the PLA matrix.
- For high aspect ratio values (>100) the impermeable phase content has been limited below 1 vol% since the fine dispersion to be obtained in the matrix for this mean aspect ratio is experimentally not achievable at higher content [13], [18]

For a P/P_0 value of 0.8, a high number of selections is proposed by the two models going from *i/*low impermeable content (< 2 vol%) of lamellae with an aspect ratio of the impermeable domains

between 50 and 150 to *ii/*higher impermeable content (2 - 4 vol%) with these same lamellae type fillers but with a lower aspect ratio in the matrix and *iii/* higher content (4 - 10 vol%) of tubes, spheres or spherolites. Moreover, it can be observed that the SVM predictions show also the possibility to work with very low content (0.1 vol%) of lamellae with very high aspect ratio (between 150 and 200) which is not a possibility identified with the RF. For a P/P_0 value of 0.6, the types of impermeable domains do not change in comparison with the previous case. The major difference is a shift of *impermeable_content* towards higher values. Nevertheless, the impermeable phase with the highest aspect ratio (> 100) as well as spherical fillers are no longer among the possibilities. There are also some differences between the two models: tubes are identified as possibilities in the parameters selection with SVM but not with RF and the content of spherolite is higher with SVM than with RF. For a P/P_0 value of 0.4, the number of possibilities is highly reduced. For both models, only lamellar fillers introduced with a content between 10 - 15 vol% with a mean aspect ratio of the impermeable phase between 25 and 100 and spherolites for a content of 30 - 35% are given as possibilities. For SVM, a lower aspect ratio (between 10 and 25) is also suggested with a content between 10 - 15 vol% for lamellae.

To conclude, the possibilities (e.g. *shape*, *mean_AR*, and *impermeable_content*) suggested by the ML models to predict a targeted relative permeability value are similar in most cases. However, it has been noted that SVM suggested more possibilities in some cases which are related to the continuous architecture of the model whereas RF takes more discrete values.

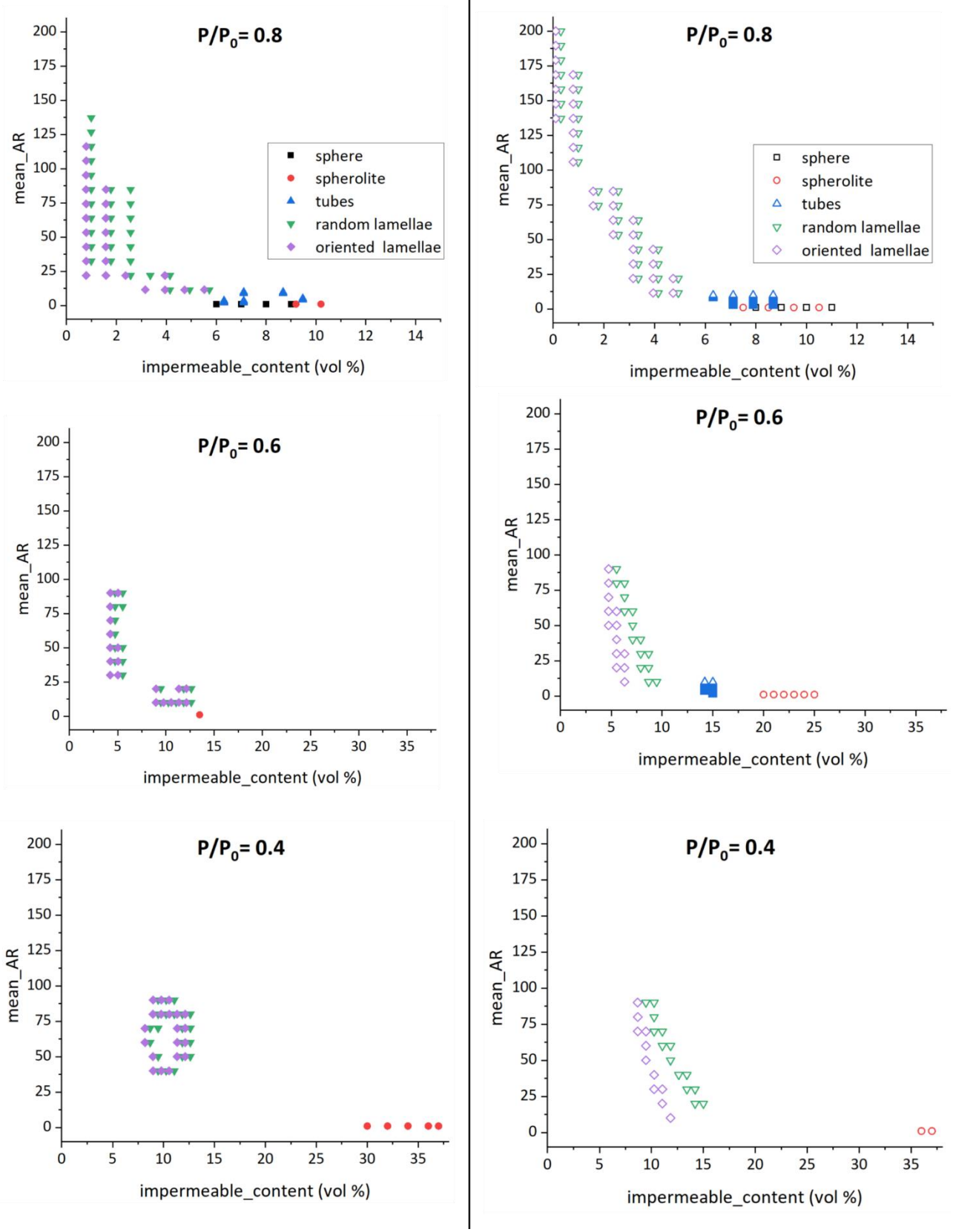


Figure C.11 - RF predictions (left) and SVR predictions (right) for different values of P/P_0 with an absolute error of 0.05: P/P_0 = 0.8, 0.6 and 0.4.

5. Conclusion

In this work, two machine learning models (Random Forest and Support Vector Machine regressions) have been trained to predict the relative permeability of PLA-based materials containing one impermeable phase. A large number of input parameters (filler shape, mean aspect ratio of the impermeable domains, impermeable phase content, aggregates content, interdomains spacing and rigid amorphous fraction) have been studied through a limited amount of data. We first selected the most relevant parameters and removed the interrelated ones to reduce the number on input and improve the accuracy of the predictions. Then additional samples have been added in the dataset and the predictions reached a mean absolute error of 0.08 and a R^2 of 0.78 for both models. Moreover, the accuracy of the predictions has been found equivalent for all the shape of impermeable phase (e.g spherolites, sphere, tubes, random lamellae and oriented lamellae) with mean absolute error values equal or below 0.07. Finally, both SVM and RF models were used to identify the accurate combined selections of shape, mean aspect ratio and volume content of the impermeable phase enabling to reach targeted relative permeability values in the range from 0.8 to 0.4. From these predictions different materials can be prepared for a chosen permeability which gives some liberty on the choice of material composition. Thus, ML seems to be a great tool to assist the design of PLA material requiring to have high barrier properties.

6. References

[1] S. Singha, M.S. Hedenqvist, A Review on Barrier Properties of Poly(Lactic Acid)/Clay Nanocomposites, Polymers 12 (2020) 1095. https://doi.org/10.3390/polym12051095.

[2] E. Picard, E. Espuche, R. Fulchiron, Effect of an organo-modified montmorillonite on PLA crystallization and gas barrier properties, Applied Clay Science 53 (2011) 58–65. https://doi.org/10.1016/j.clay.2011.04.023.

[3] B. Tan, N.L. Thomas, A review of the water barrier properties of polymer/clay and polymer/graphene nanocomposites, Journal of Membrane Science 514 (2016) 595–612. https://doi.org/10.1016/j.memsci.2016.05.026.

[4] A.S. Michaels, H.J. Bixler, Flow of gases through polyethylene, Journal of Polymer Science 50 (1961) 413–439. https://doi.org/10.1002/pol.1961.1205015412.

[5] A. Guinault, C. Sollogoub, V. Ducruet, S. Domenek, Impact of crystallinity of poly(lactide) on helium and oxygen barrier properties, European Polymer Journal 48 (2012) 779–788. https://doi.org/10.1016/j.eurpolymj.2012.01.014.

[6] M. Drieskens, R. Peeters, J. Mullens, D. Franco, P.J. Lemstra, D.G. Hristova-Bogaerds, Structure versus properties relationship of poly(lactic acid). I. Effect of crystallinity on barrier properties: Structure Vs. Barrier Properties of PLA, J. Polym. Sci. B Polym. Phys. 47 (2009) 2247–2258. https://doi.org/10.1002/polb.21822.

[7] L.E. Nielsen, Models for the Permeability of Filled Polymer Systems, Journal of Macromolecular Science—Chemistry (1967). https://doi.org/10.1080/10601326708053745.

[8] R.K. Bharadwaj, Modeling the Barrier Properties of Polymer-Layered Silicate Nanocomposites, Macromolecules 34 (2001) 9189–9192. https://doi.org/10.1021/ma010780b.

[9] E. Picard, J.-F. Gérard, E. Espuche, Reinforcement of the Gas Barrier Properties of Polyethylene and Polyamide Through the Nanocomposite Approach: Key Factors and Limitations, Oil Gas Sci. Technol. – Rev. IFP Energies Nouvelles 70 (2015) 237–249. https://doi.org/10.2516/ogst/2013145.

[10] G. Gorrasi, R. Pantani, M. Murariu, P. Dubois, PLA/Halloysite Nanocomposite Films: Water Vapor Barrier Properties and Specific Key Characteristics, Macromolecular Materials and Engineering 299 (2014) 104–115. https://doi.org/10.1002/mame.201200424.

[11] N. Tenn, N. Follain, J. Soulestin, R. Crétois, S. Bourbigot, S. Marais, Effect of Nanoclay Hydration on Barrier Properties of PLA/Montmorillonite Based Nanocomposites, J. Phys. Chem. C 117 (2013) 12117–12135. https://doi.org/10.1021/jp401546t.

[12] Z. Duan, N.L. Thomas, W. Huang, Water vapour permeability of poly(lactic acid) nanocomposites, Journal of Membrane Science 445 (2013) 112–118. https://doi.org/10.1016/j.memsci.2013.06.008.

[13] F. Li, C. Zhang, Y. Weng, X. Diao, Y. Zhou, X. Song, Enhancement of Gas Barrier Properties of Graphene Oxide/Poly (Lactic Acid) Films Using a Solvent-free Method, Materials 13 (2020) 3024. https://doi.org/10.3390/ma13133024.

[14] S.-M. Lai, Y.-T. Hsieh, Preparation and Properties of Polylactic Acid (PLA)/Silica Nanocomposites, Journal of Macromolecular Science, Part B 55 (2016) 211–228. https://doi.org/10.1080/00222348.2016.1138179.

[15] G. Zhu, C. Kim, A. Chandrasekarn, J.D. Everett, R. Ramprasad, R.P. Lively, Polymer genome–based prediction of gas permeabilities in polymers, Journal of Polymer Engineering 40 (2020) 451–457. https://doi.org/10.1515/polyeng-2019-0329.

[16] J.W. Barnett, C.R. Bilchak, Y. Wang, B.C. Benicewicz, L.A. Murdock, T. Bereau, S.K. Kumar, Designing exceptional gas-separation polymer membranes using machine learning, Science Advances 6 (2020) 1–7. https://doi.org/10.1126/sciadv.aaz4301.

[17] M. Zhou, A. Vassallo, J. Wu, Toward the inverse design of MOF membranes for efficient D2/H2 separation by combination of physics-based and data-driven modeling, Journal of Membrane Science 598 (2020) 117675. https://doi.org/10.1016/j.memsci.2019.117675.

[18] A. Jullin, G. Sudre, N. Hascoët, F. Chinesta, E. Espuche, Influence of different type of impermeable phase on the permeability of PLA films : nanofillers versus crystalline phase, Polymer Testing (Submitted) (2024).

[19] Y. Guo, K. Yang, X. Zuo, Y. Xue, C. Marmorat, Y. Liu, C.-C. Chang, M.H. Rafailovich, Effects of clay platelets and natural nanotubes on mechanical properties and gas permeability of Poly (lactic acid) nanocomposites, Polymer 83 (2016) 246–259. https://doi.org/10.1016/j.polymer.2015.12.012.

[20] H. Tsuji, Y. Tezuka, Stereocomplex Formation between Enantiomeric Poly(lactic acid)s. 12. Spherulite Growth of Low-Molecular-Weight Poly(lactic acid)s from the Melt, Biomacromolecules 5 (2004) 1181–1186. https://doi.org/10.1021/bm049835i.

[21] N. Delpouve, A. Saiter, J.F. Mano, E. Dargent, Cooperative rearranging region size in semi-crystalline poly(l-lactic acid), Polymer 49 (2008) 3130–3135. https://doi.org/10.1016/j.polymer.2008.04.045.

[22] M. Somvanshi, P. Chavan, S. Tambade, S.V. Shinde, A review of machine learning techniques using decision tree and support vector machine, International Conference on Computing Communication Control and Automation (2016) 1–7. https://doi.org/10.1109/ICCUBEA.2016.7860040.

[23] D.M. Dutton, G.V. Conroy, A review of machine learning, The Knowledge Engineering Review 12 (1997) 341–367. https://doi.org/10.1017/S026988899700101X.

[24] C.-C. Chang, C.-J. Lin, LIBSVM: A library for support vector machines, ACM Trans. Intell. Syst. Technol. 2 (2011) 1–27. https://doi.org/10.1145/1961189.1961199.

[25] S. Ray, A Quick Review of Machine Learning Algorithms, International Conference on Machine Learning, Big Data, Cloud and Parallel Computing (2019) 35–39. https://doi.org/10.1109/COMITCon.2019.8862451.

[26] K. Pearson, I. Mathematical contributions to the theory of evolution. —VII. On the correlation of characters not quantitatively measurable, Philosophical Transactions of the Royal Society of London. Series A, Containing Papers of a Mathematical or Physical Character 195 (1997) 1–47. https://doi.org/10.1098/rsta.1900.0022.

[27] C. Spearman, The Proof and Measurement of Association between Two Things, The American Journal of Psychology 15 (1904) 72. https://doi.org/10.2307/1412159.

[28] J. Hauke, T. Kossowski, Comparison of Values of Pearson's and Spearman's Correlation Coefficients on the Same Sets of Data, Quaestiones Geographicae 30 (2011) 87–93. https://doi.org/10.2478/v10117-011-0021-1.

[29] G. Choudalakis, A.D. Gotsis, Permeability of polymer/clay nanocomposites: A review, European Polymer Journal 45 (2009) 967–984. https://doi.org/10.1016/j.eurpolymj.2009.01.027.

[30] L. Cartier, T. Okihara, Y. Ikada, H. Tsuji, J. Puiggali, B. Lotz, Epitaxial crystallization and crystalline polymorphism of polylactides, Polymer 41 (2000) 8909–8919. https://doi.org/10.1016/S0032-3861(00)00234-2.

[31] F. Morel, E. Espuche, V. Bounor-Legaré, O. Persynn, M. Lacroix, Impact of coated calcium carbonate nanofillers and annealing treatments on the microstructure and gas barrier properties of poly(lactide) based nanocomposite films, Journal of Polymer Science Part B: Polymer Physics 54 (2016) 649–658. https://doi.org/10.1002/polb.23957.

Conclusion

Ce chapitre a été consacré à l'étude de la perméabilité dans des matrices PLA contenant une phase imperméable.

Une première étude a permis d'étudier l'influence de la phase cristalline du PLA ainsi que de différentes charges imperméables. Une étude fine de la microstructure des matériaux nous a permis d'identifier les paramètres pouvant jouer un rôle sur la perméabilité. Ainsi, outre la forme initiale de la phase imperméable ainsi que la fraction volumique de phase imperméable qui semble être des paramètres évidents, la dispersion des charges au sein de la matrice a pu être finement décrite et corrélée à la perméabilité. Enfin la mobilité des chaines de la matrice, amoindrie en présence de la phase cristalline du PLA s'est avérée favorable pour les propriétés barrière. À partir de ces observations, différents modèles théoriques de perméabilité ont pu être ajustés pour décrire au mieux les données expérimentales. Ces modèles ont constitué une première approche pour comparer l'effet des différents types de charge sur la perméabilité ainsi que de proposer une équivalence en termes de phase cristalline.

Puis, une deuxième étude a comparé l'influence de deux procédés sur la perméabilité : le mélange par voie fondue et la polymérisation *in situ*. Cette étude qui a été réalisée avec de la silice hydrophobe et une montmorillonite modifiée a montré que le procédé modifie d'une part la dispersion des charges et d'autre part la microstructure de la matrice (masse molaire, bout de chaines, interface charge/matrice). Ces changements ont été mis en relation avec les différences entre les deux procédés qui ont été observées entre les matériaux issus des deux procédés, plutôt pour des taux de charges relativement élevés (> 7 %vol). Le procédé d'élaboration amène donc de multiples modifications de la microstructure du matériau qui ne sont pas prises en compte dans les modèles théoriques de perméabilité. C'est pourquoi il a été choisi d'essayer de modéliser la perméabilité uniquement à partir de données expérimentales en utilisant le machine learning.

Ainsi la dernière partie de ce chapitre a montré la possibilité de prédire la perméabilité en utilisant le machine learning. Deux modèles (*Random Forest* et *Support Vector Machine*) ont été entrainés sur un nombre limité de données relatives à des échantillons de PLA contenant une phase imperméable. Il est en effet à noter que la mise en évidence d'interrelation a permis

de réduire le nombre de paramètres d'entrée. À partir de ces modèles entrainés, de nouvelles valeurs de perméabilité ont pu être prédites avec une erreur proche de l'erreur expérimentale et un coefficient de corrélation supérieur à 0.80. Enfin, ces modèles ont permis de proposer des combinaisons de paramètres matériaux pour l'obtention d'une perméabilité donnée, ce qui permet d'imaginer la conception de nouveaux matériaux avec un certain degré de liberté. Par ailleurs, les prédictions des modèles de machine learning pourraient potentiellement être améliorées avec davantage d'échantillons pour le procédé par polymérisation *in situ*.

Pour poursuivre ce travail, il nous a semblé intéressant d'étudier l'influence de la présence de deux des phases imperméables précédemment étudiées, introduite toutes deux dans la même matrice PLA. La présence de deux phases imperméables soulève les questions suivantes. Cette nouvelle approche permettrait-elle de diminuer davantage la perméabilité ? Avec quels procédés ? Par conséquent, le prochain chapitre s'attachera à discuter de l'ajout simultané de deux phases imperméables dans une matrice PLA et de ses effets sur la perméabilité. L'approche développée se base d'une part, sur la présence de la phase cristalline du PLA et d'une charge imperméable et d'autre part, sur l'ajout de deux charges imperméables différentes dans la matrice PLA amorphe.

Supporting information Chapitre III :

Design de matériaux à matrice PLA contenant une phase imperméable

Supporting information III.A _____ *200*

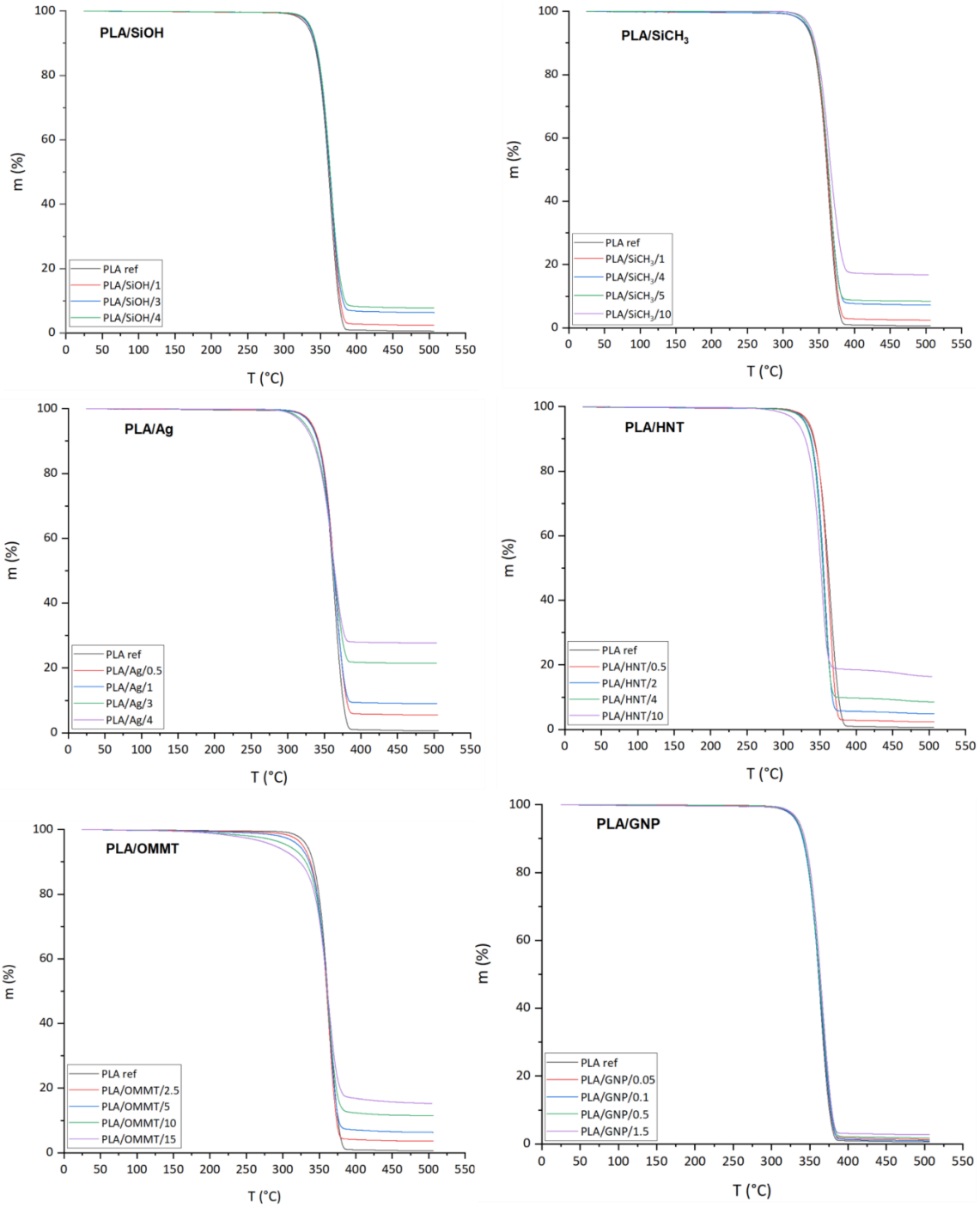
Supporting information III.B _____ *208*

Supporting information III.C _____ *216*

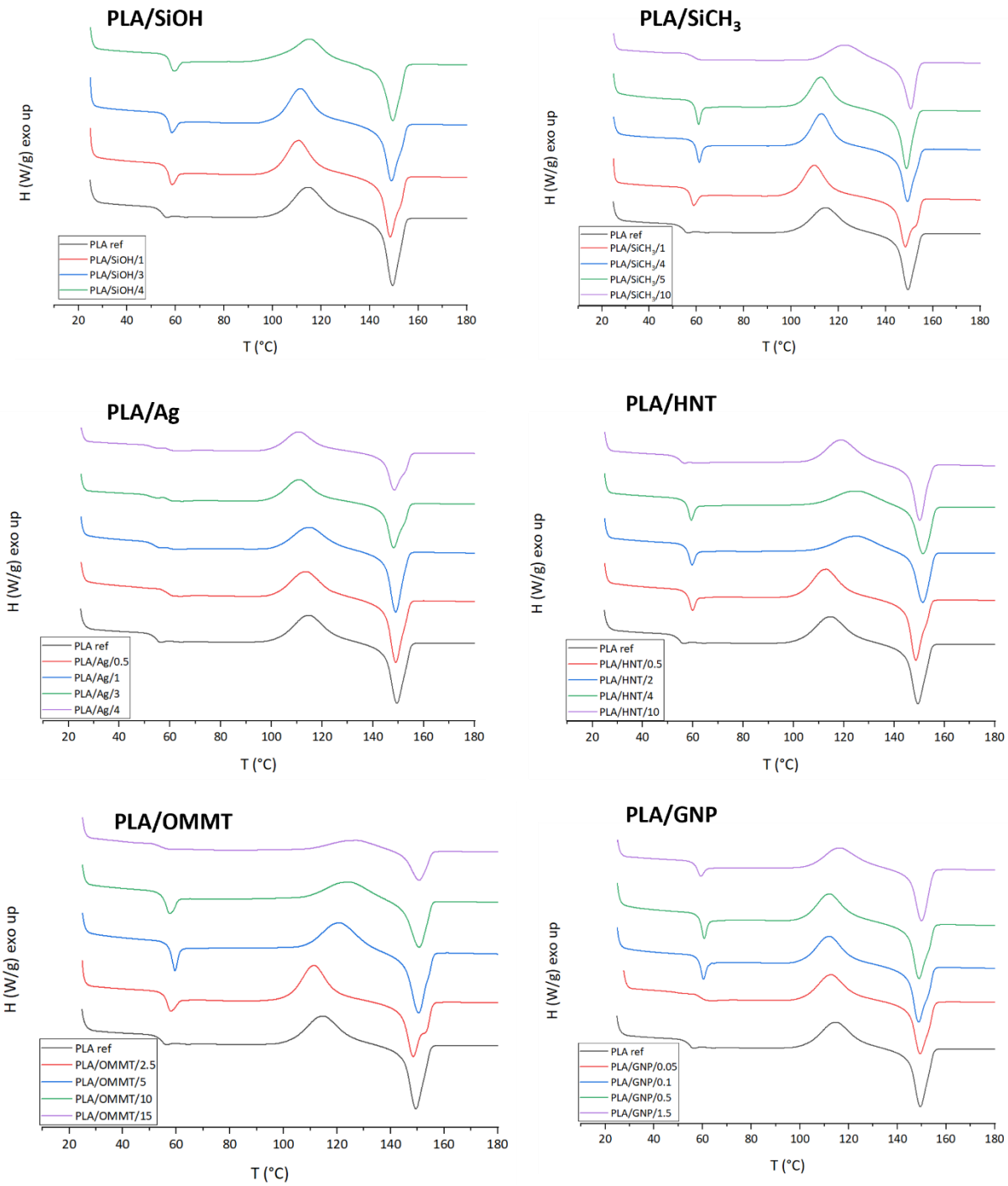
Supporting information III.A:

Influence of different type of impermeable phase on the permeability of PLA films: nanofillers versus crystalline phase

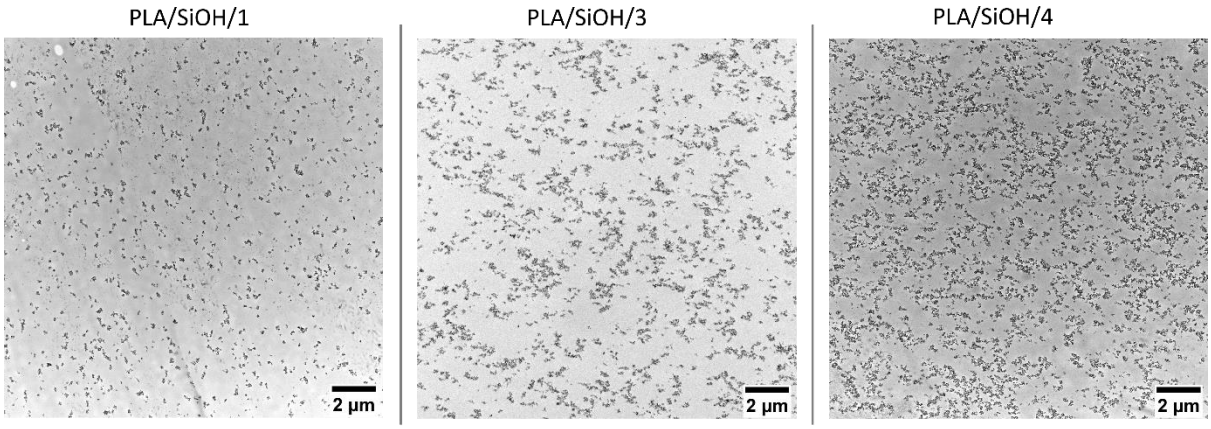
---



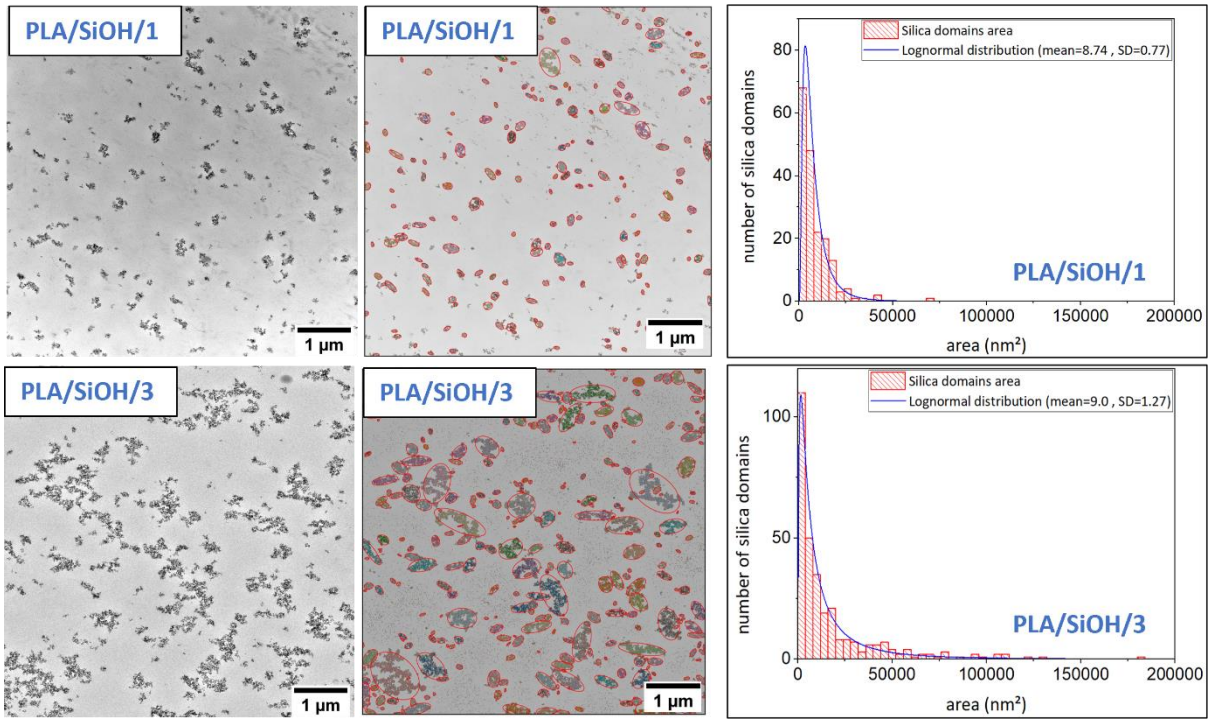
Supplementary Figure A.1 - TGA thermograms of PLA nanocomposites series @10 °C/min under nitrogen.



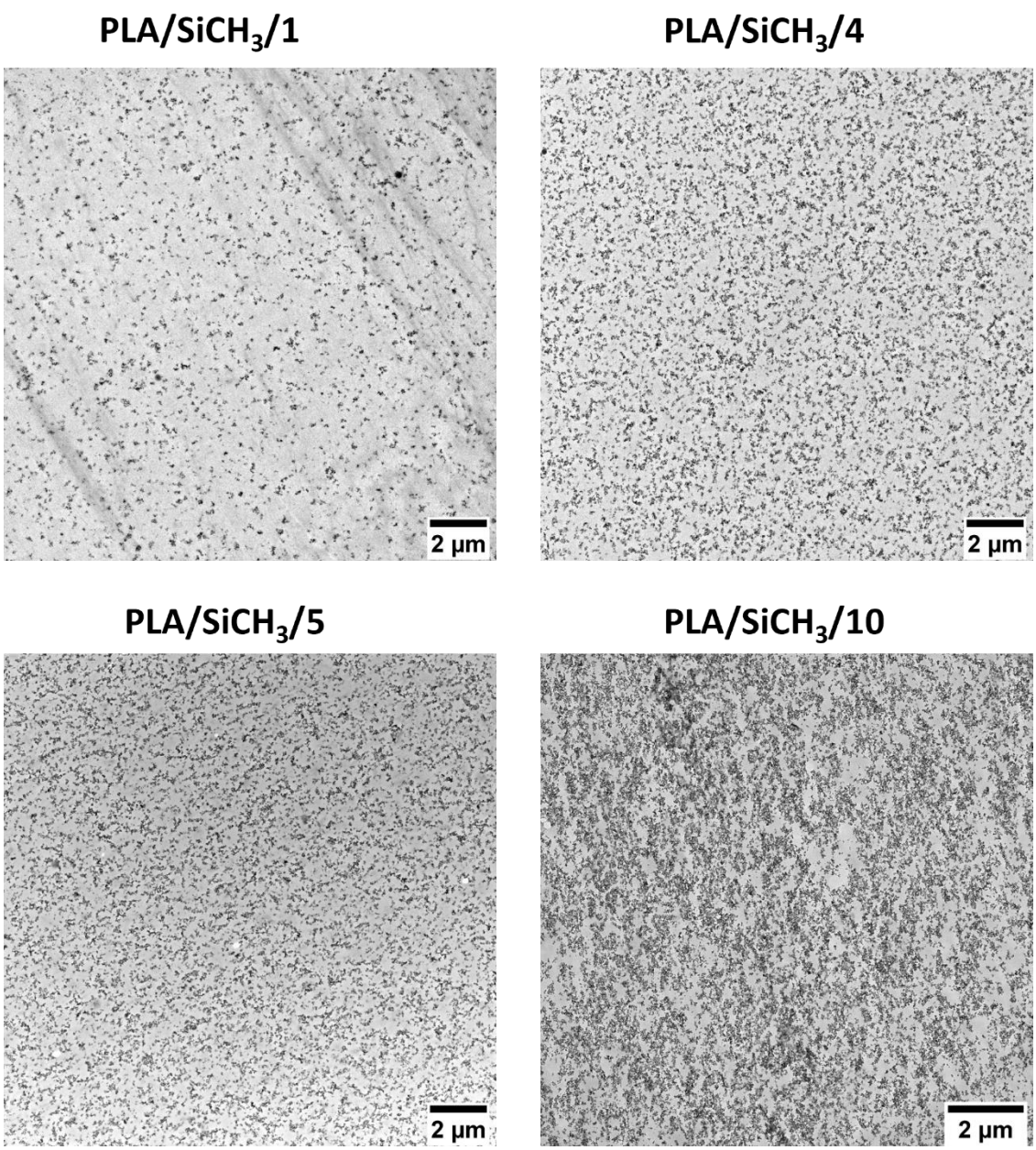
Supplementary Figure A.2 - DSC thermogram of the PLA nanocomposites series @10 °C/min under nitrogen.



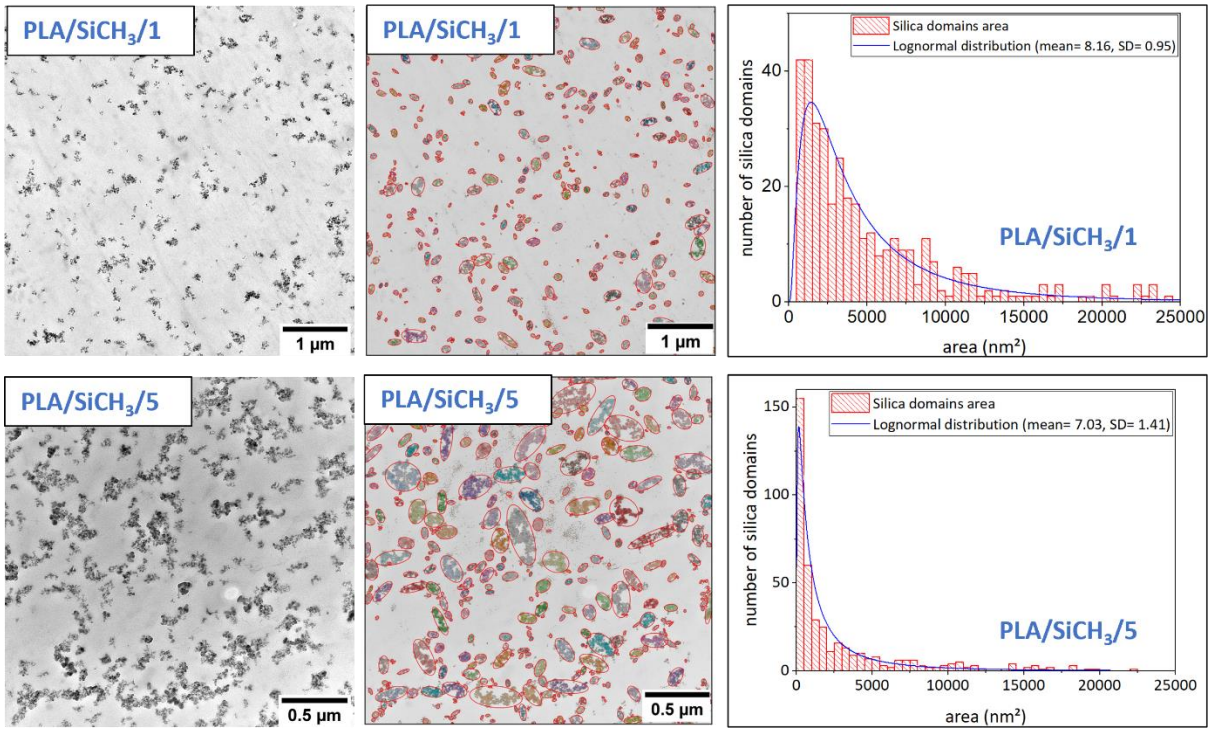
Supplementary Figure A.3 -TEM micrograph at low magnification of PLA/SiOH/1, PLA/SiOH/3 and PLA/SiOH/4



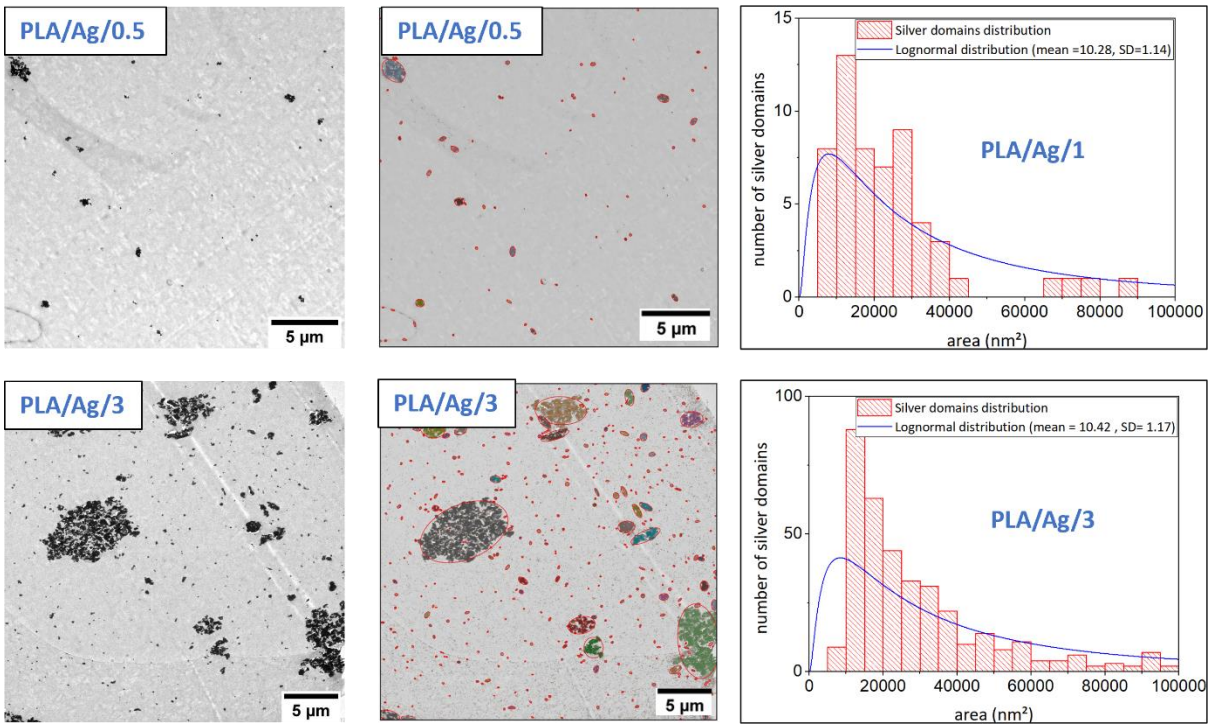
Supplementary Figure A.4 - *TEM micrographs from the cross section of PLA/SiOH films as well as the silica domains identifications by Scikit-image processing and their area distribution for PLA/SiOH /1 and PLA/SiOH/3.*



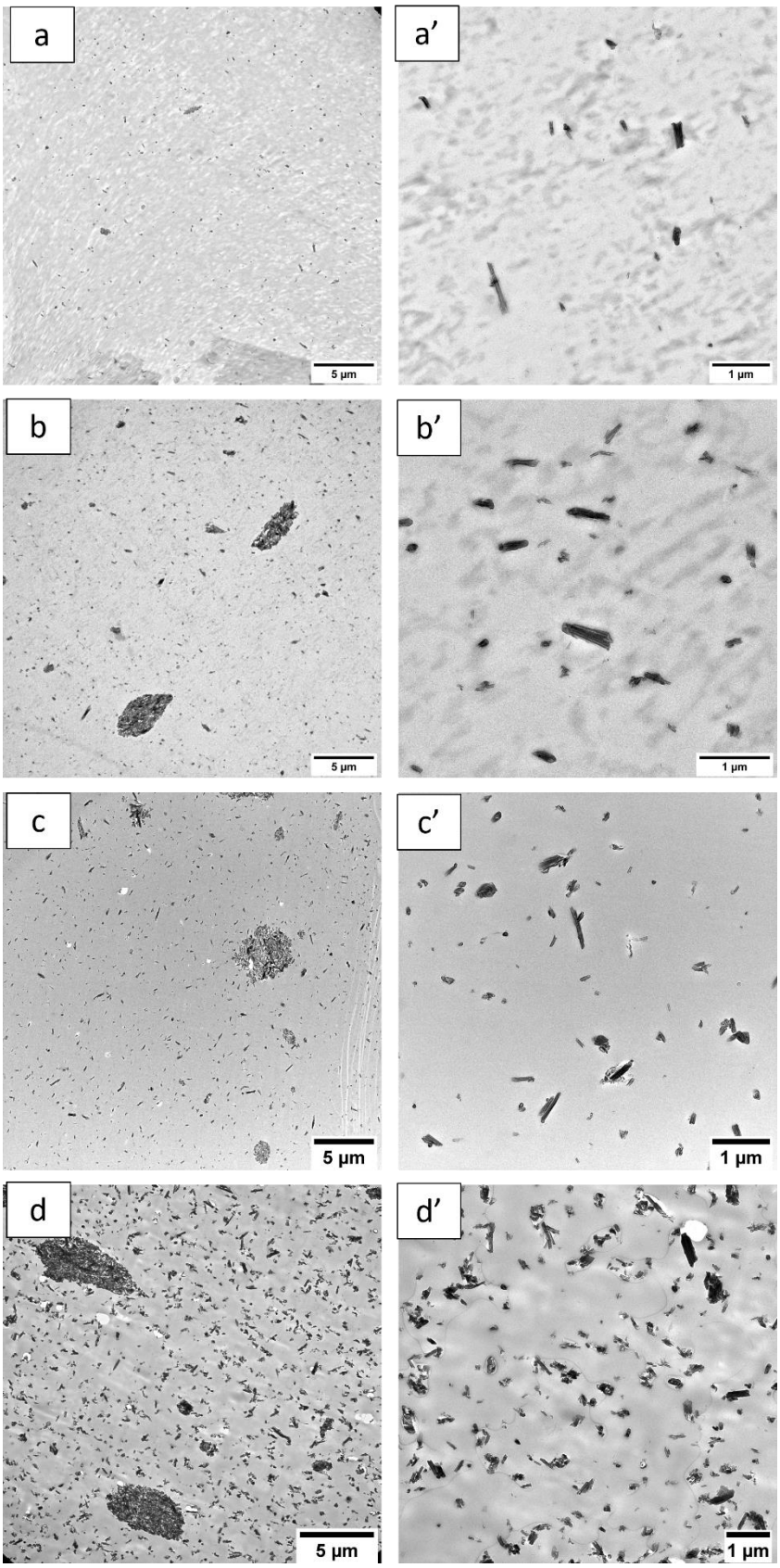
Supplementary Figure A.5 - TEM micrograph at low magnification of PLA/$SiCH_3$/1, PLA/$SiCH_3$/4, PLA/$SiCH_3$/5 and PLA/$SiCH_3$/10.



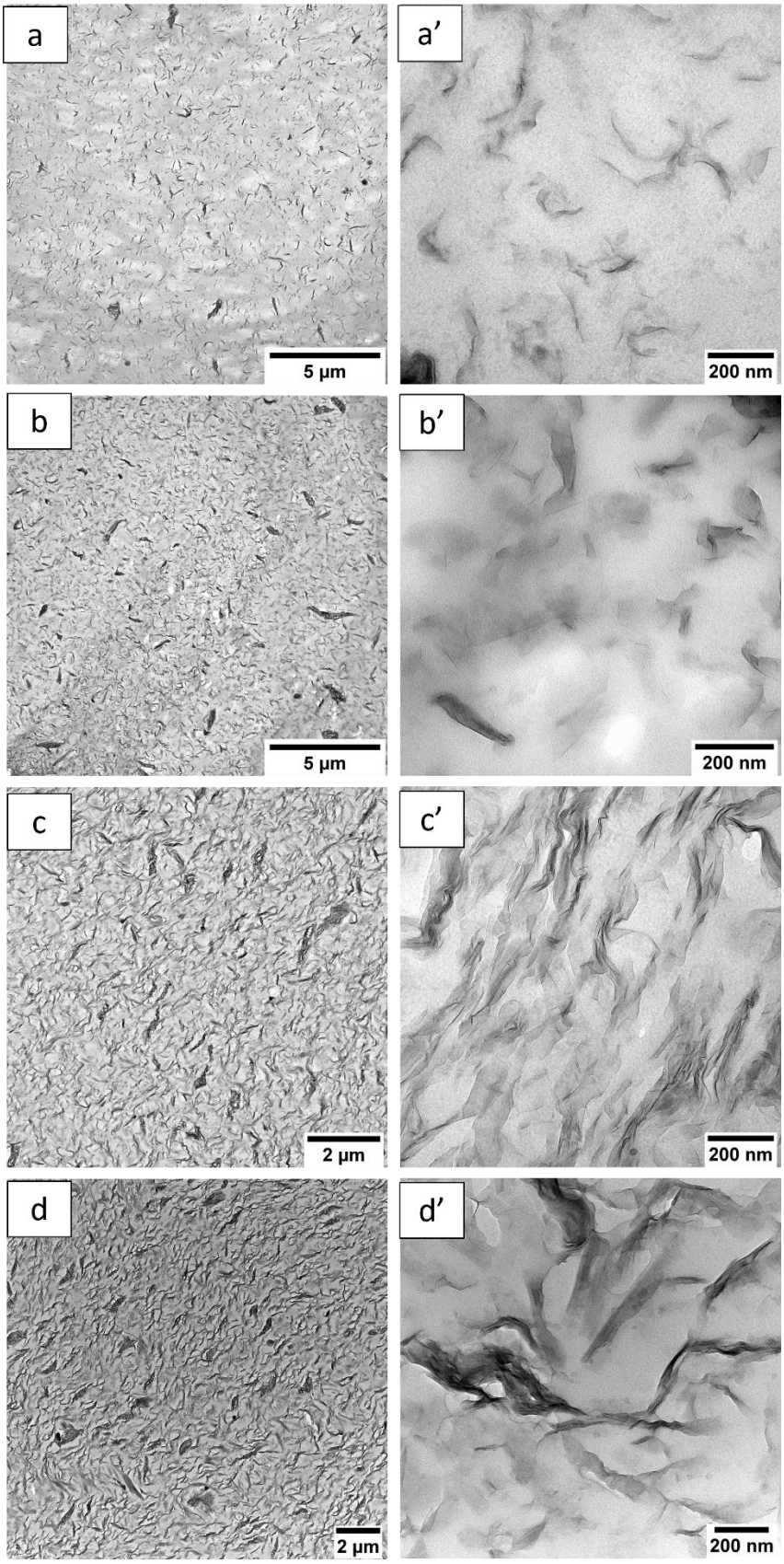
Supplementary Figure A.6 -TEM micrographs from the cross section of PLA/$SiCH_3$ films as well as the silica domains identifications by Scikit-image processing and their area distribution for PLA/$SiCH_3$ /1 and PLA/ $SiCH_3$/5.



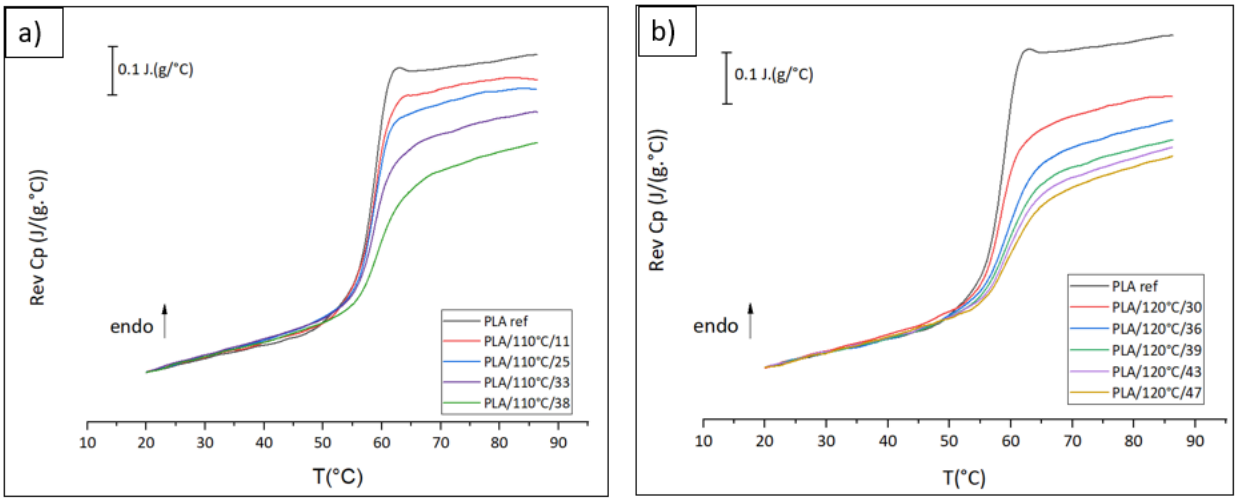
Supplementary Figure A.7 - TEM micrographs from the cross section of PLA/SiOH films as well as the silica domains identifications by Scikit-image processing and their area distribution for PLA/Ag/1 and PLA/Ag/3.



Supplementary Figure A.8 - TEM micrograph of the cross section of PLA/HNT films at low magnification a) PLA/HNT/0.5, b) PLA/HNT/2, c) PLA/HNT/4 and d) PLA/HNT/10 and the same samples at high magnification a', b', c', d'.



Supplementary Figure A.9 - TEM micrograph of the cross section of PLA/OMMT films at low magnification a) PLA/OMMT/2.5, b) PLA/OMMT/5, c) PLA/OMMT/10 and d) PLA/OMMT/15 and the same samples at high magnification a', b', c', d'.



Supplementary Figure A.10 - Modulated DSC thermogram around the glass transition temperature of the annealed PLA films a) PLA/110 °C and b) PLA/120 °C.

Supporting information III.B:

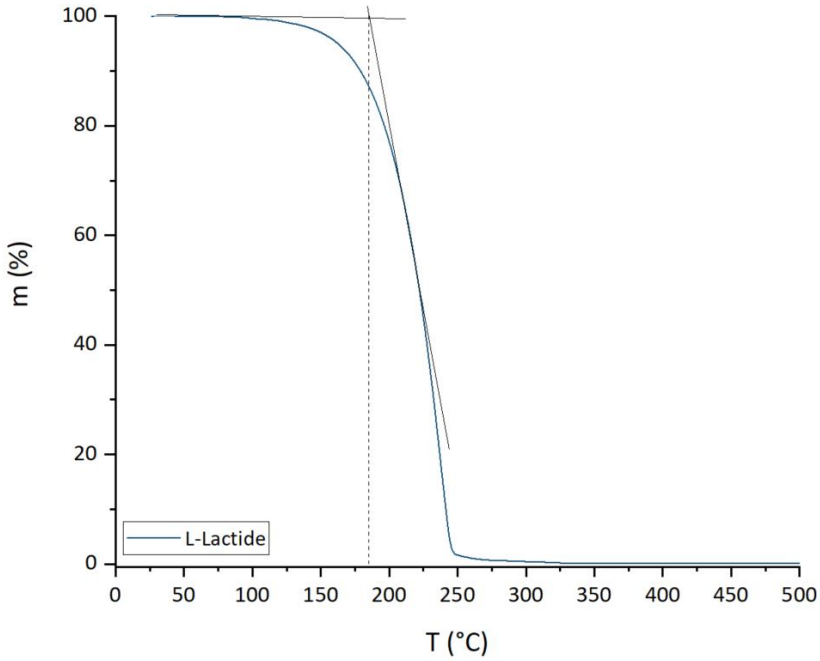
Influence of the process over permeability of amorphous PLA nanocomposites filled with silica or organo-modified montmorillonite: melt-blending vs free solvent *in situ* polymerization.

Supplementary Table B.1 - Mn, Mw/Mn , residual monomer content, degradation temperature and Tg value of polymerized PLA with different molar ratio lactide: $SnOct_2$ and different reaction times in the internal mixer at 185 °C.

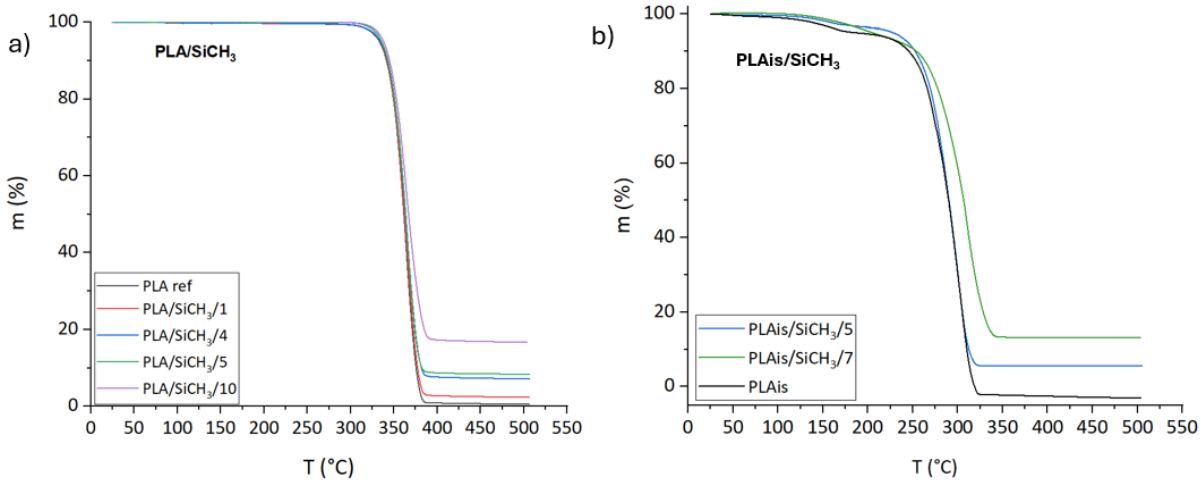
Residence Time	Molar ratio lactide: $SnOct_2$	Mn (g/mol) [(a)]	Mw/Mn [(a)]	Residual monomer (wt %) [(b)]	Td_{onset} (°C) [(b)]	Tg_{onset} (°C)
/	**PLA ref**	87 000 ± 3 000	1.4	0	348 ± 1	57± 1
20 min	2500	33 000 ± 2 000	1.2	3.8 ± 0.5	273 ± 2	46 ± 2
40 min	2500	37 000 ± 1500	1.3	0.9 ± 0.5	276 ± 2	49 ± 2
50 min	2500	45 500 ± 3 000	1.3	0.6 ± 0.5	272 ± 2	50 ± 2
20 min	3700	22 400 ± 1 800	1.1	8.8 ± 0.5	272 ± 2	34 ± 2
40 min	3700	27 500 ± 2 800	1.3	2.2 ± 0.5	270 ± 2	49 ± 2
50 min	3700	32 300 ± 2 500	1.2	0.6 ± 0.5	272 ± 2	49± 2

(a) Calculated from SEC analysis.

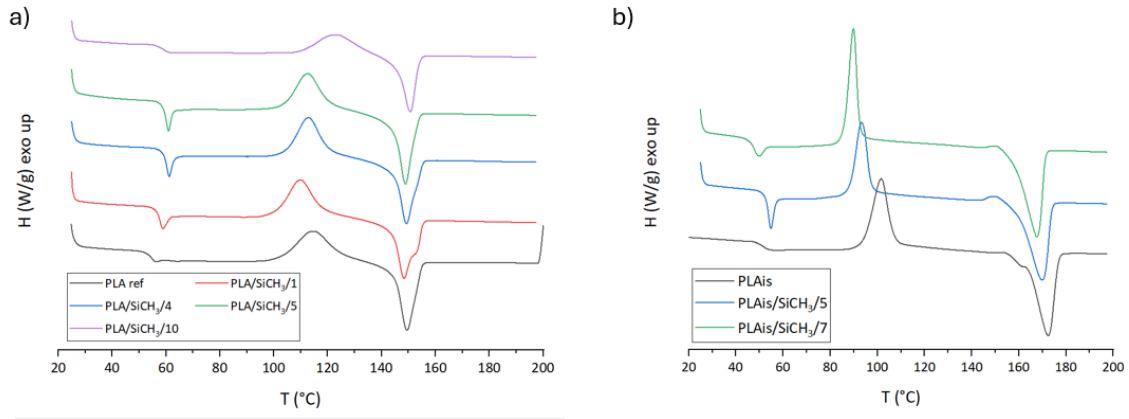
(b) Calculated from TGA analysis.



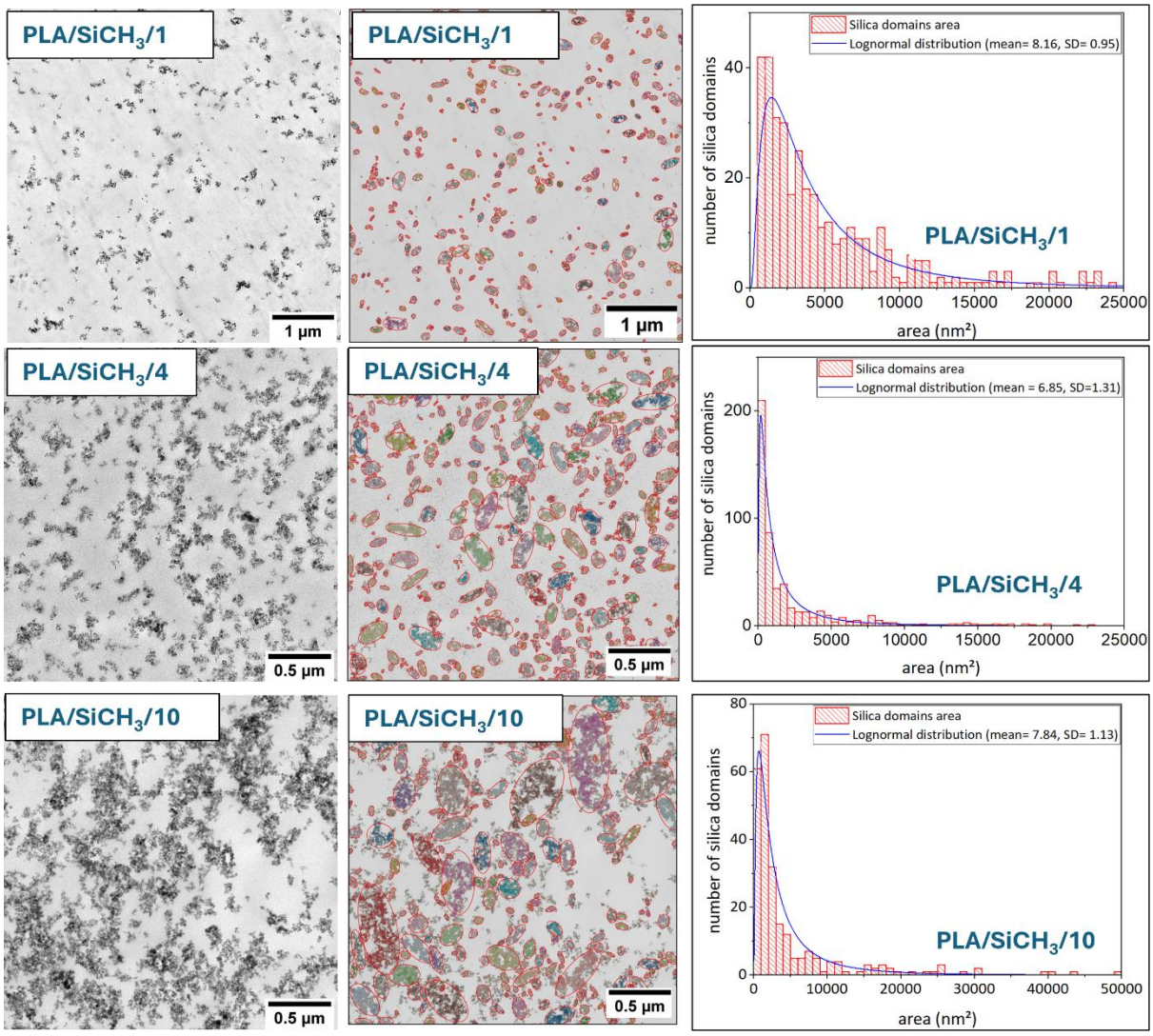
Supplementary Figure B.1- TGA thermograms at 10 °C/min under nitrogen of L-lactide.



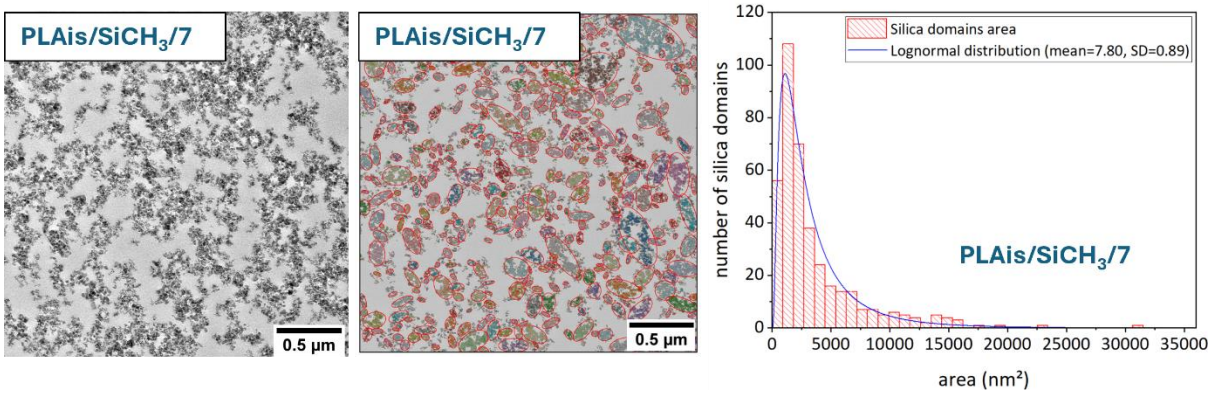
Supplementary Figure B.2- TGA thermograms at 10 °C/min under nitrogen of silica nanocomposites (a) prepared by melt-blending ($PLA/SiCH_3$) and (b) by in situ polymerization ($PLAis/SiCH_3$).



Supplementary Figure B.3 – DSC thermograms at 10 °C/min under nitrogen of silica nanocomposites a) prepared by melt-blending (PLA/SiCH3) and b) by in situ polymerization (PLAis/SiCH3).



Supplementary Figure B.4 – TEM micrographs from the cross sections of PLA/silica films prepared by melt-blending and identifications of the silica domains by Scikit-images processing and their area distribution for PLA/$SiCH_3$/1, PLA/$SiCH_3$/4 and PLA/$SiCH_3$/10.

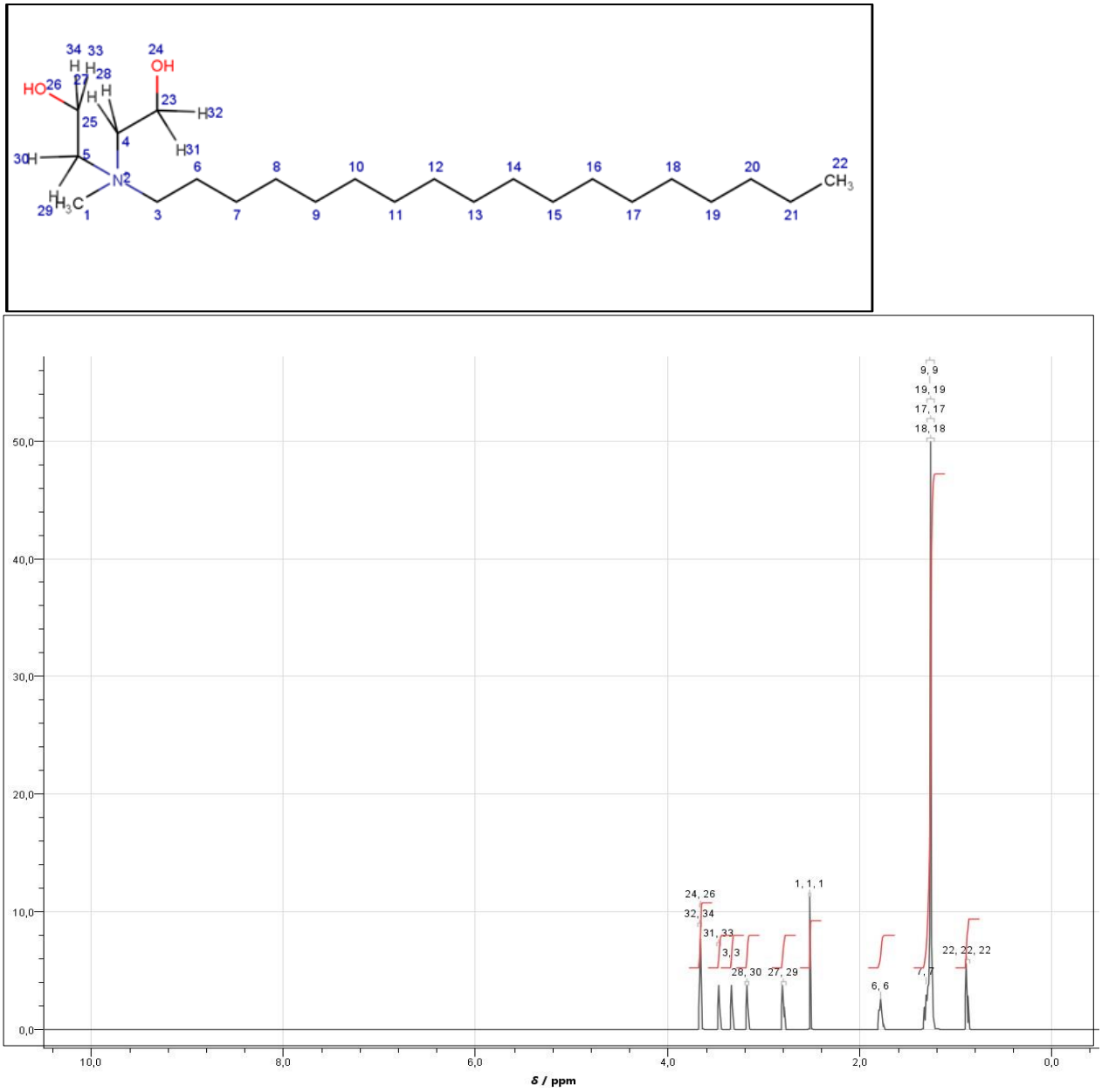


Supplementary Figure B.5 - TEM micrographs from the cross sections of PLA film prepared by in situ polymerization with 7 vol% of silica and identifications of the silica domains by Scikit-images processing and their area distribution.

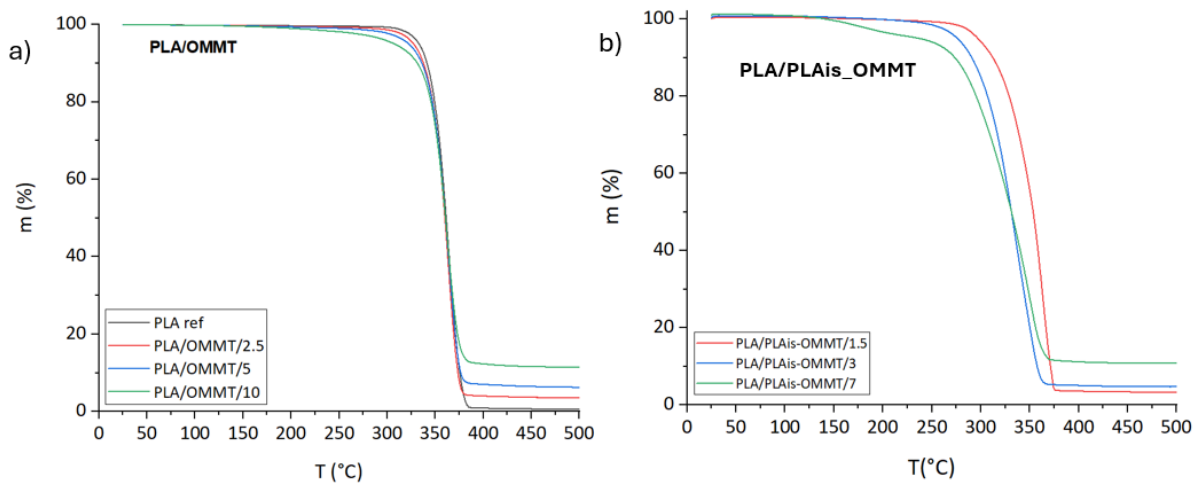
Supplementary Table B.2 – Optimization of the protocol for the in situ polymerization of lactide in presence of OMMT .

$m_{Lactide}$ (g)	catalyst	filler	Filler content	Reactor	Results
50	0.055 g $SnOCt_2$+ 0.026 g PPh_3	Cloisite 30B	8.5 wt%	Internal mixer 185 °C, 50 min	Browned, fluid material and smoke
50	0.055 g $SnOCt_2$+ 0.026 g PPh_3	Cloisite 25A *(no hydroxyl groups on the quaternary ammonium cation)*	8.0 wt%	Internal mixer 175 °C, 50 min	Browned, fluid material and smoke
50	0.026 g PPh_3	Cloisite 30B	8.5 wt%	Internal mixer 175 °C, 30 min	Fluid material, no reactions
50	0.55 g 1,8-Diazabicyclo(5.4.0) undec-7-ene (DBU)	Cloisite 30B	8.5 wt%	Internal mixer 175 °C, 30 min	Browned, fluid material, No smoke
5	0.005 g $SnOCt_2$ +0.5 g PPh_3	Cloisite 30B	3 wt%	Lab reactor under Argon, 180 °C, 1 h	No polymerization (only the melting peak of Lactide detected in DSC)
				Lab reactor under Argon, 180 °C, 3h30	Incomplete polymerization
				Reactor under Argon, 180 °C, 5h30	Almost complete polymerization (<1wt% of Lactide mesured by TGA) Tg = 43°C **BUT** Not self-standing film
10	0.01 g $SnOCt_2$ +0.05 g PPh_3	Cloisite 30B	43	Lab Reactor under Argon, 180 °C, 6h	Poor blending, too much fillers, browned and non-homogeneous material
			20	Lab Reactor under Argon, 160 °C, 4h30	Lightly browned material, incomplete polymerization
				Lab Reactor under Argon, 120 °C, 8h30	Beige material but incomplete polymerization (10 wt% of Lactide measured by TGA) + crystal on the upper glass

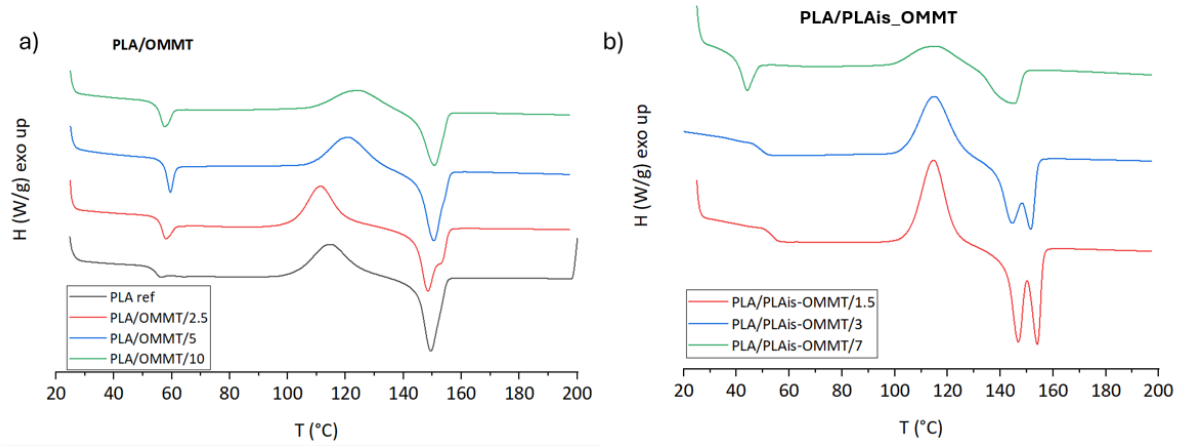
10	0.01 g $SnOCt_2$ +0.05 g PPh_3	Cloisite 30B	20	Lab Reactor under Argon, 120 °C, 16h	Beige material but incomplete polymerization (10 wt% of Lactide measured by TGA) + crystal on the upper glass
				Lab Reactor under Argon, 120 °C, 16h + covered with aluminum to maintain a constant temperature all along the reaction duration and avoid the lactide condensation on the upper glass	Almost complete polymerization (5 wt% of Lactide measured by TGA) less crystals on the upper glass



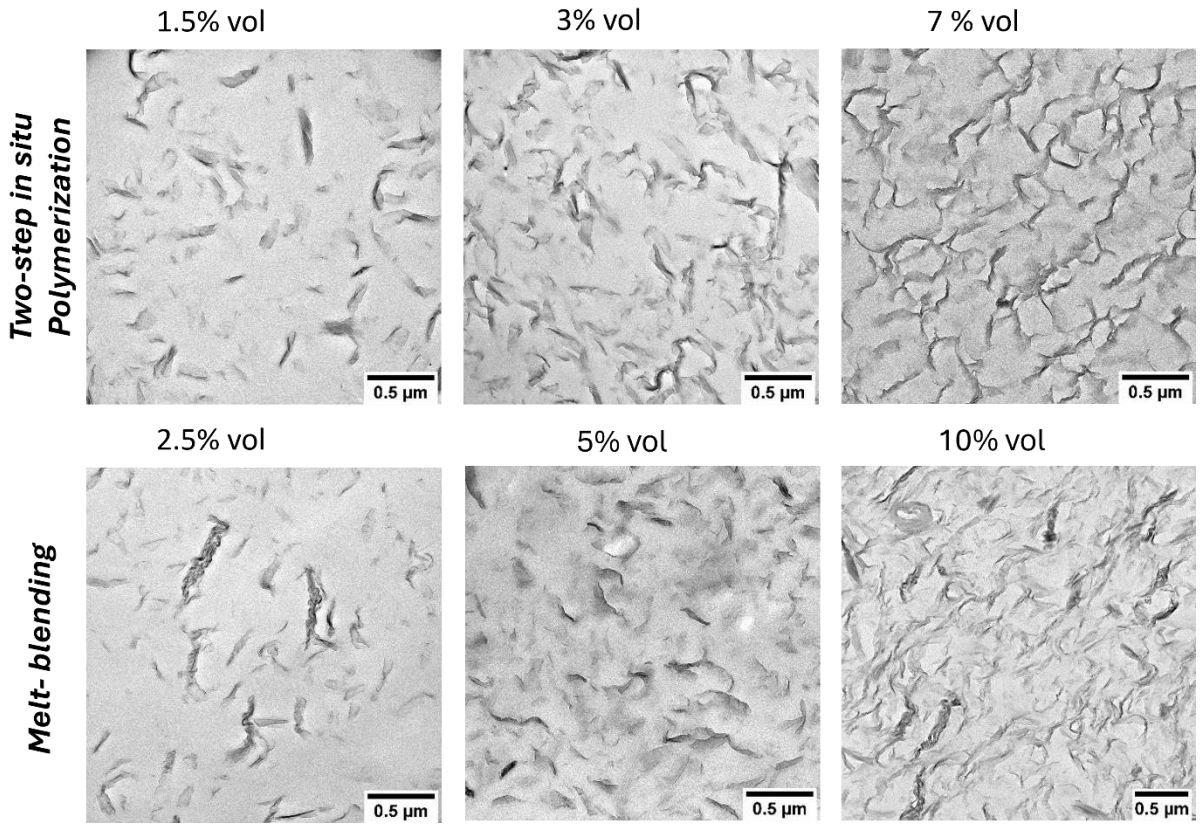
Supplementary Figure B.6 - Skeletal formula of the Cloisite®30B cation and its predicted ^{1}H NMR spectrum by ChemAxon software.



Supplementary Figure B.7- TGA thermograms at 10 °C/min under nitrogen of silica nanocomposites a) prepared by melt-blending (PLA/OMMT) and b) by 2 steps in situ polymerization (PLA/PLAis_OMMT).



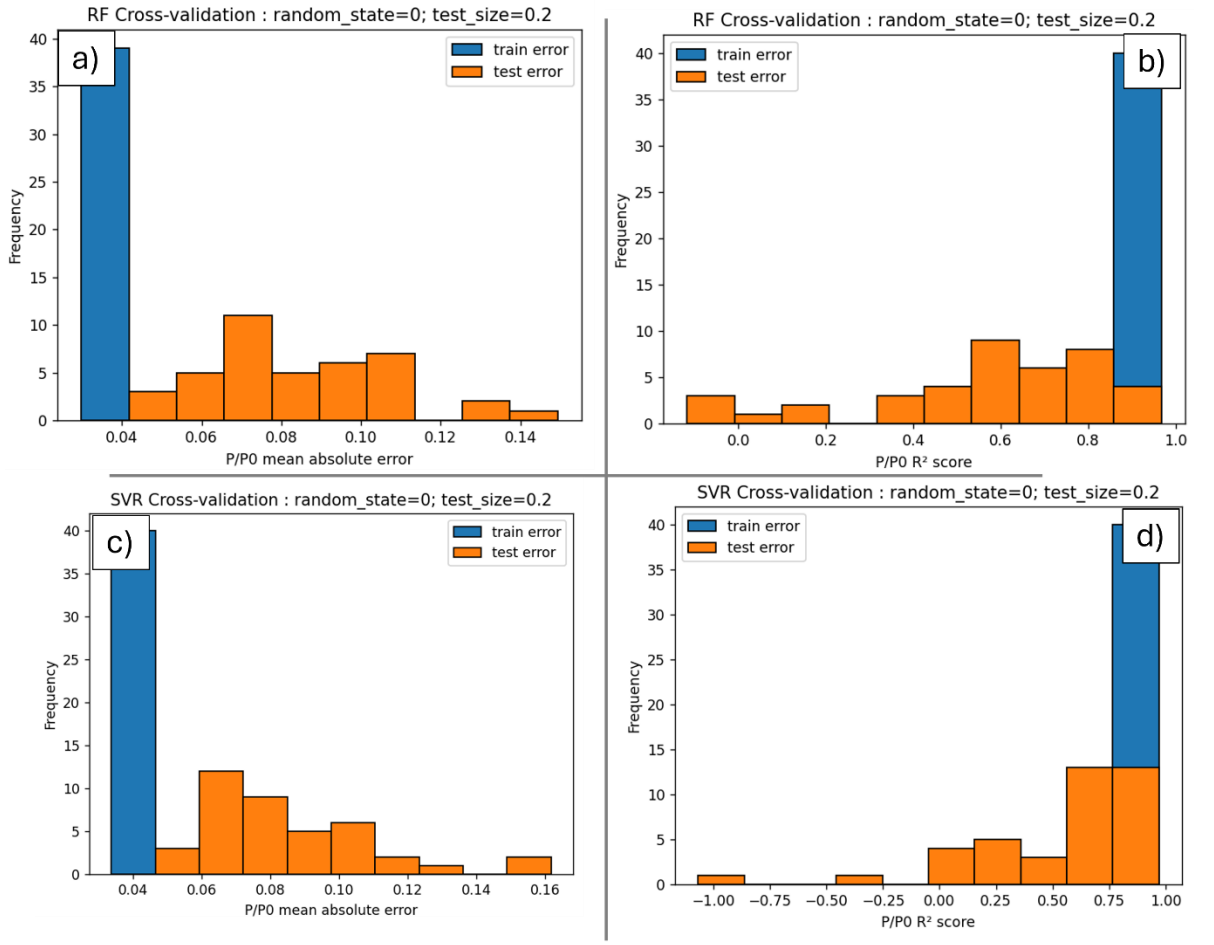
Supplementary Figure B.8 – DSC thermograms at 10 °C/min under nitrogen of silica nanocomposites a) prepared by melt-blending (PLA/OMMT) and b) by 2 steps in situ polymerization (PLA/PLAis_OMMT).



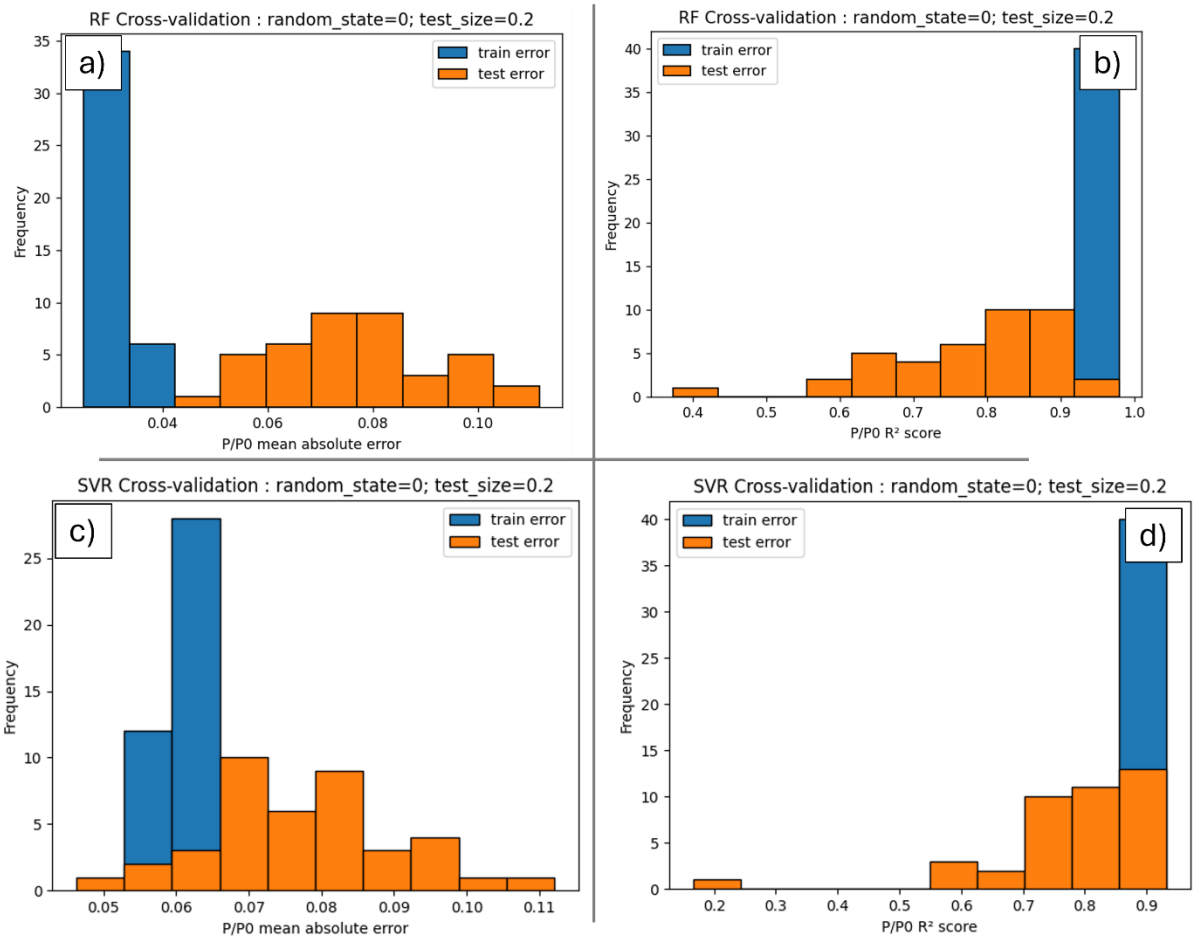
Supplementary Figure B.9 – TEM micrographs of montmorillonite nanocomposites prepared by two-step in situ polymerization and by melt-blending.

Supporting information III.C:

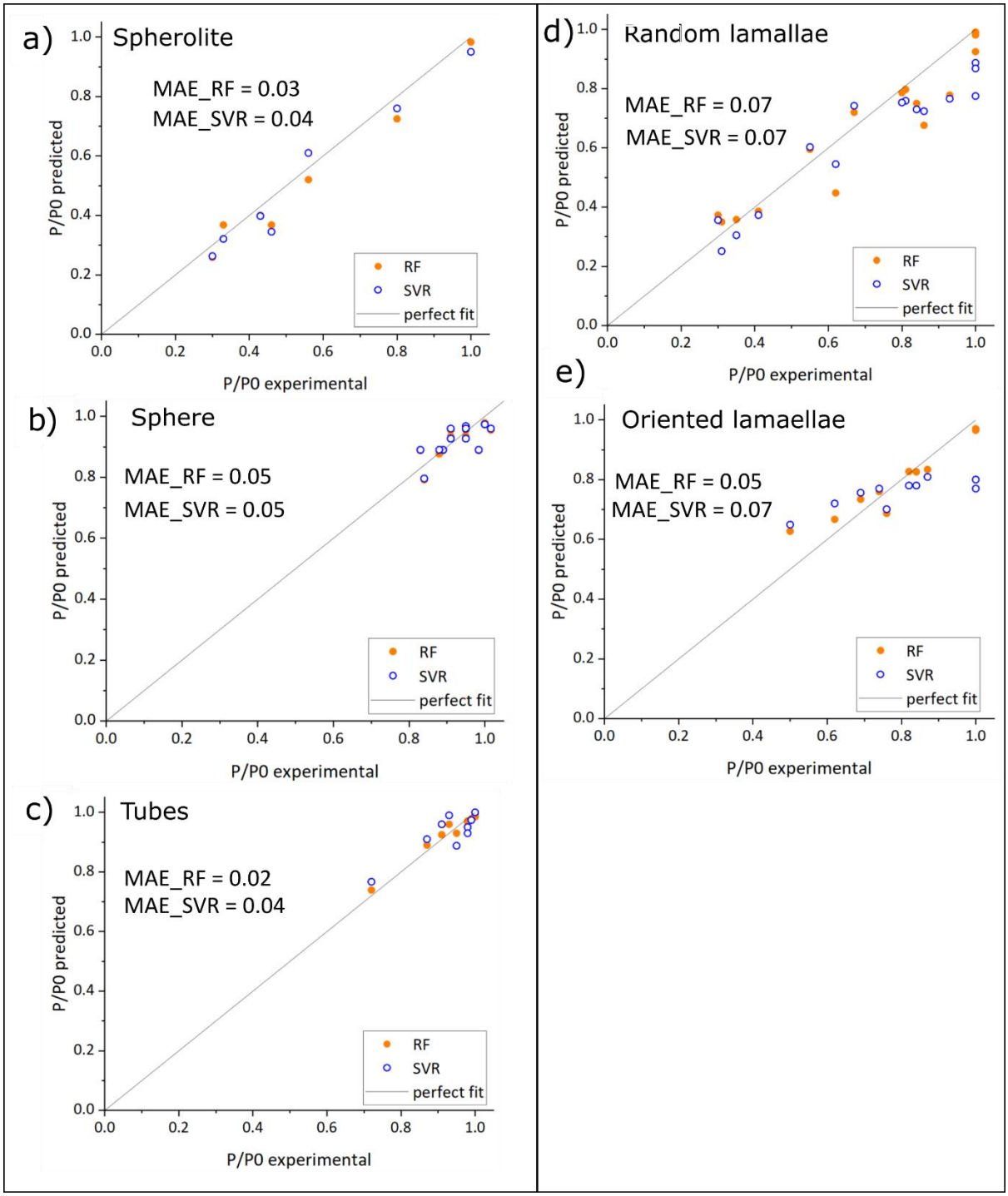
Data Driven modelling as a new route to design PLA based materials with high barrier properties.



Supplementary Figure C.1- Cross validation results with the shape, mean_AR and impermeable_content as input parameters for the first dataset of 33 samples. Distribution of (a) the Random Forest *MAE*, (b) the Random Forest R^2, (c) the SVM *MAE* and (d) the SVM R^2 for the 40 repetitions of the cross validation. The blue bar stands for the training step and the orange bar for the testing step.



Supplementary Figure C.2 - Cross validation results with the shape, mean_AR and impermeable_content as input parameters for the second dataset with 69 samples**.** Distribution of (a) the Random Forest *MAE*, (b) the Random Forest R^2, (c) the SVM *MAE* and (d) the SVM R^2 for the 40 repetitions of the cross validation. The blue bar stands for the training step and the orange bar for the testing step.



Supplementary Figure C.3 - Comparison of the predicted P/P_0 value with the experiment P/P0 for each type of filler. Confusion graph for (a) spherolites, (b) spheres, (c) tubes, (d) random lamellae and (e) oriented lamellae

Chapitre IV

Design de nanocomposites PLA à deux phases imperméables

Chapitre IV - Design de nanocomposites PLA à deux phases imperméables

Introduction _____ **221**

Chapitre IV.A : Influence of the process on the permeability of semi-crystalline PLA nanocomposites : solvent casting versus annealing of melt-blended films _____ **223**

Chapitre IV.B : PLA nanocomposites based on silica and organo-modified montmorillonite: a comparative investigation of different solvent-free synthesis routes on morphology and water permeability _____ **259**

Conclusion _____ **283**

Supplementary information _____ **285**

Introduction

L'objectif de ce chapitre est de comprendre et d'établir des relations microstructures/perméabilité dans le cas de matrice PLA contenant deux phases imperméables et d'identifier de potentiels effets de synergie de ces deux phases sur la perméabilité. Le premier système concerne les nanocomposites semi-cristallins et le second porte sur l'introduction simultanée de deux charges imperméables dans le PLA amorphe.

Plus précisément, la première plateforme de nanocomposites PLA semi-cristallins a été préparée en jouant sur le procédé d'élaboration et le type de charges. Les charges utilisées identiques à celles utilisées pour la préparation des nanocomposites amorphes dans le chapitre précédent. Deux procédés d'élaboration permettant d'obtenir une phase PLA cristalline ont été utilisés et comparés : la voie solvant d'une part et d'autre part un post traitement thermique des nanocomposites amorphes étudiés dans le chapitre précédent. Les perméabilités des matériaux ainsi obtenus ont été comparées et mises en relation avec la mobilité des chaines de la matrice, son taux de cristallinité et la qualité de la dispersion des charges. Enfin, les perméabilités ont été comparées à celles des nanocomposites amorphes du chapitre III.

Une seconde plateforme de nanocomposites a été préparée en incorporant deux charges différentes dans une matrice PLA amorphe. Une montmorillonite organiquement modifiée a été associée d'une part à de la silice et d'autre part à du graphène. Les perméabilités ont été comparées à celles des nanocomposites contenant uniquement une seule de ces charges, à fraction volumique similaire de la charge concernée. Le potentiel effet d'additivité des charges sur la perméabilité a également été étudié.

Il est à noter que les annexes des différentes parties sont regroupées en fin de chapitre.

La première partie de ce chapitre présente l'effet du procédé sur la perméabilité de nanocomposites semi-cristallins préparés avec différents types de charges. Les matériaux étudiés sont soit obtenus par voie solvant soit par traitement thermique de nanocomposites amorphes.

Chapitre IV.A - Influence of the process on the permeability of semi-crystalline PLA nanocomposites: solvent casting versus annealing of melt-blended films

1. Abstract ***224***

2. Introduction ***224***

3. Experimental ***226***

3.1. Materials **226**

3.2. Preparation routes used to obtain semi-crystalline nanocomposites **227**

3.3. Characterization methods **229**

3.3. a) Thermal analysis 229

3.3. b) Microstructure analysis 230

3.3. c) Nanofillers dispersion analysis 231

3.3. d) Permeability measurements 231

4. Results and discussion ***232***

4.1. Influence of the process on the matrix properties of semi-crystalline and nanocomposites films **232**

4.2. Effect of the process on the filler dispersion in nanocomposites films **238**

4.3. Water vapor permeability of semi-crystalline nanocomposites and semi-crystalline PLA **245**

5. Conclusion ***250***

6. References ***251***

1. Abstract

Semi-crystalline polylactic acid (PLA) nanocomposites containing fillers of different type have been prepared by melt-blending followed by annealing treatment or by solvent casting. Silica, halloysite and montmorillonite have been used in the range between 0 and 11 vol%, while graphene was incorporated up to 1.5 vol%. The microstructure and chain mobility of the PLA matrix has been characterized as a function of the process and filler used and a specific attention has been paid to the PLA/filler interfacial behavior. The filler dispersion, investigated by transmission electron microscopy, has been found to be better with the melt-mixing/annealing process than with the solvent casting. The permeability of nanocomposites prepared by solvent casting globally shows a decrease of the permeability with the addition of fillers whereas it is not the case for annealed nanocomposites for which the permeability is often higher than the one of the unfilled annealed PLA. The permeability cannot be only related to the filler dispersion state but results also from the the filler/matrix interfacial properties that depend on the filler type with respect to the matrix but also on the process used to obtain semi-crystalline nanocomposites. It has been shown that, for silica, halloysite nanotubes and graphene, the melt blending/annealing process had a detrimental impact on the filler/matrix interfacial properties and the barrier properties which is not the case for montmorillonite.

2. Introduction

Polylactic acid (PLA) is regarded as one of the most promising polymer for reducing the environmental foodprint by minimizing waste generated by short-term applications [1], [2]. Its ease of processing, transparency, and relatively low cost make it a promising candidate for packaging applications [3]. Moreover, the incorporation of impermeable fillers has been found to be an efficient way to improve its barrier properties [4], [5], [6], [7], [8] . In a previous study, we showed that the permeability of amorphous PLA could be decreased by 25% with the addition of 0.05 vol% of graphene or 2 vol% of organo-modified montmorillonites or 15 vol% of silica [9]. Another way for enhancing the barrier properties is to form a crystalline phase within the polymer matrix. Indeed, this highly dense polymer phase is considered as

impermeable [10] and it was found to decrease significantly the permeability [9], [11], [12]. Regarding these results, combining addition of fillers with the formation of PLA crystalline phase seems to be an interesting route to significantly decrease the permeability of PLA.

A commonly used method to prepare semi-crystalline PLA nanocomposites is the solvent route, which consists in mixing the fillers and the PLA in a suited solvent. Films are obtained following solvent evaporation, which results in the formation of the PLA crystalline phase. The solvent route associated with the use of fillers such as nanocellulose [13], montmorillonite [14], [15], [16], halloysite [17] and graphene [18] has been demonstrated to be an effective method for decreasing PLA permeability. Concerning PLA samples prepared by melt-blending approach, it is known that unlike most polymers, PLA has a low crystallization kinetics from the melt and preferentially crystallizes from the glassy state [12], [19]. Hence, semi-crystalline PLA nanocomposites can be obtained by annealing amorphous samples from the glassy state. Picard *et al.* [20] showed an additive contribution of montmorillonite and the crystalline phase formed by cold annealing on the barrier properties.

Filler dispersion plays a key role in nanocomposite barrier properties. The characteristics of the dispersion of fillers in a given polymer/filler system can be significantly influenced by the process employed to mix the compounds. For melt-mixing, the dispersion of fillers is achieved thanks to shearing forces whereas for solvent mixing, the filler dispersion is obtained through the diffusion of the polymer chains between the swollen fillers. Only few studies have compared the dispersion state obtained by these two methods for PLA-based nanocomposites. Marras *et al.* [21] observed that the montmorillonite sheets in the PLA exhibits higher delamination when using solvent mixing in comparison to melt mixing for montmorillonite content up to 9 wt%. On the contrary, De Silva *et al.* [22] observed a poorer dispersion of halloysite nanotubes, up to 10 wt%, with solvent casting compared to melt-blending. Moreover, the elaboration method has also an influence on the formation of the crystalline phase. While solvent evaporation enables to keep a great mobility in the material during crystallization process, the mobility is more restricted during thermal treatment at the rubbery state. The influence of thermal treatment versus solvent evaporation on the crystalline morphology of PLA nanocomposites has been reported by Trifol *et al.* [23] with cellulose nanocrystals and montmorillonite. The solvent used was N,N-dimethylformamide.

The authors showed that (i) thermal treatment leads to a higher degree of crystallinity than solvent evaporation and (ii) thermal treatment induces the formation of α-crystalline phase whereas α'-crystalline phase is obtained with solvent evaporation. On the contrary, Krikorian *et al.* [24] reported the formation of α-crystalline phase by solvent casting in presence of montmorillonite. Finally, to the best of our knowledge, no comparison has been made on the influence of the process (e.g. solvent casting versus annealing of amorphous samples obtained by melt blending) over the barrier properties of semi-crystalline PLA nanocomposites.

In this study, a wide range of PLA-based semi-crystalline materials containing either lamellar fillers (montmorillonite or graphene) or spherical fillers (hydrophilic/hydrophobic silica) or halloysite nanotubes up to 11 vol% are investigated. Two processes for obtaining semi-crystalline PLA are used and compared: the solvent casting method and the annealing of samples prepared by melt-blending. The differences in the PLA crystalline phase and chain mobility as well as in the filler dispersion are investigated. The water vapor permeability coefficient of the semi crystalline nanocomposites is determined and discussed as a function of the matrix microstructure and filler dispersion states and finally related to the process used to prepare the nanocomposites.

3. Experimental

3.1. Materials

Polylactic acid PLA 2003D was purchased from NatureWorks LLC. The polymer has a density of 1.25 and the molar content of D-isomer is 4.1% mol according to the producer. The average molar mass was determined by size exclusion chromatography and is equal to Mn = 86,000 $g.mol^{-1}$. Different impermeable nanofillers varying by their composition and shape were used and are presented in **Table A.1.**

Table A.1- Characteristics of the different fillers (*d* stands for the mean diameter, *L* for the mean length, and *w* for the mean thickness of the elementary fillers).

Nanofiller type	Nomenclature	Commercial name / supplier	Dimensions /shape	Surface modification	Density
Hydrophilic silica	SiOH	Aerosil® 200 / Evonick Operations GmbH	*d* = 20 ± 5 nm **Sphere**	/	2.2
Hydrophobic silica	$SiCH_3$	Aerosil® AR974 / Evonick Operations GmbH	*d* = 20± 5 nm **Sphere**	Dimethyl dichlorosilane (0,7-1,3 wt% carbon)	2.2
Organo-modified montmorillonite	OMMT	Cloisite® 30B/ Southern Clay Product	*L* = 200 nm *w* = 1-2 nm **Platelet**	Methyl tallow bis-2-hydroxyethyl, quaternary ammonium (29 wt %) CEC =90 meq/100 g	1.98
Halloysite nanotubes	HNT	Halloysite nanotubes/ Sigma-Aldrich	*L* = 300 -1000 nm *d* ~40 nm **Tubes**	/	2.53
Graphene oxide	GNP	KNG-180-3 Graphene oxide nanoplatelets Knano (Xianen, China)	*L* = 500- 1000 nm *w* ~1 nm **Platelet**	/	2.2

3.2. Preparation routes used to obtain semi-crystalline nanocomposites

Two routes were investigated to prepare semi-crystalline PLA nanocomposites films.

The first approach, called annealing method, is a two-step method based for the first step on the preparation of neat PLA and nanocomposites films by melt-blending using a Haake internal mixer. Compounding was carried out at 185 °C with a rotation speed of 50 rpm and the residence time was fixed at 10 min. The nanofillers content ranged from 0 to 11 vol%. Unfilled PLA was also melt-processed in the same conditions to prepare a reference material. Then 130 ± 10 µm amorphous PLA films were prepared from each compound by compression molding at 180 °C under 150 bars for 2 min. Samples were placed between two metal plates at room temperature after thermo-compression and cooled under compressed air for few minutes. As PLA is very sensitive to hydrolysis during melt processing, all materials (PLA granular, nanofillers as well as the compounds) were dried (at least 24 h in a vacuum oven at

85 °C) before each processing step (melt compounding and compression molding). In a second step, to obtain semi-crystalline samples with the maximum degree of crystallinity, neat PLA films and nanocomposites films were annealed from the glassy state in an oven at 120 °C for 24 h [9], [20], [25].

The second approach consists in obtaining semi-crystalline neat PLA and nanocomposite films by the solvent casting method. For each film, 1 g of PLA pellets was dissolved into chloroform and stirred at 400 rpm at room temperature for 3 h. Filler suspensions in chloroform at different concentration of fillers were prepared and sonicated for four periods of 5 min at 20% amplitude (Fisherbrand Model 505 Sonic Dismembrator). Filler suspension was added into the PLA/chloroform solution in a sealed vial and magnetically stirred at 400 rpm during 30 min. The vial was then opened and placed in an ultrasonics bath in “degas” mode for 30 min. The solution was finally cast into Teflon® dishes. After solvent evaporation at room temperature for 3 days, the films were delicately peeled off, dried at 75 °C under vacuum for 2 h and then air-dried at 75 °C for 3 days to remove any residual solvent.

The unfilled PLA films prepared by the melt-blending/annealing methods are referred as PLA_MBA and those prepared by the solvent cast route as PLA_SR. The nanocomposites are named as PLA_MBA/filler/X for the annealing method and as PLA_SR/filler/X for the solvent casting method. X refers to the volume content of fillers. All the film series under study in this work are presented in **Table A.2**.

Table A.2 - PLA and PLA nanocomposites films series: name, composition and process

Sample name	Process	Type of impermeable phase	Range of impermeable phase content (vol%)
PLA_MBA	Melt-blending + annealing	/	0
PLA_MBA/SiOH/X		Hydrophilic silica	0 - 4
PLA_MBA/$SiCH_3$/X		Hydrophobic silica	0 - 10
PLA_MBA/OMMT/X		Organo modified montmorillonite	0 - 15
PLA_MBA/HNT/X		Halloysite nanotubes	0 - 10
PLA_MBA/GNP/X		Graphene oxide platelets	0 - 1.5
PLA_SR	Solvent mixing	/	0
PLA_SR/SiOH/X		Hydrophilic silica	0 - 4
PLA_SR/$SiCH_3$ /X		Hydrophobic silica	0 - 5.5
PLA_SR/OMMT /X		Organo modified montmorillonite	0 - 10
PLA_SR/HNT/X		Halloysite nanotubes	0 - 11
PLA_SR/GNP/X		Graphene oxide platelets	0 - 1.5

3.3. Characterization methods

3.3. a) Thermal analysis

Thermogravimetric analyses (TGA) were realized to investigate the eventual presence of residual solvent, the degradation temperature of the nanocomposites and their nanofillers content. A Mettler Toledo TGA/DSC 1 STAR^e System was used, and the weight loss was recorded as a function of temperature from 25 to 500 °C with a ramp of 10 °C/min under dry nitrogen flow. The degradation temperature was measured according to tangent methods. The nanofiller volume content was calculated from the mass residue at the 500 °C plateau, the density of the PLA and the density of the fillers. It is important to note that in the case of nanocomposites filled with Cloisite®30B, the weight content of the organic cation (30 wt%) was added to the residual mass for filler volume fraction calculations.

A TA Instrument Q200 calorimeter calibrated with indium standard was used for differential scanning calorimetry (DSC) experiments. Samples of about 10 mg were taken from each film and sealed in aluminum pans. The melting temperature as well as the melting enthalpy (ΔH_m) were measured on the heating ramp performed from 25 to 200 °C at 10 °C/min. The degree of crystallinity (χ_c) was calculated according to equation (A.1):

$$\chi_c = \frac{\Delta H_m}{\Delta \mathrm{H}_{m\infty}(1-\phi_m)} \qquad (A.1)$$

where ΔH_m is the melting enthalpy, Φ_m the filler weight content and $\Delta H_{m\infty}$ is the melting enthalpy of the infinite crystal taken equal to of 93 J/g [26]. Temperature Modulated Differential Scanning Calorimetry experiments were carried out to investigate more deeply the glass transition. The sample were heated from 10 to 90 °C at an average heating rate of 2 °C/min with an oscillation of 0.318 °C/min. The glass transition temperature was taken at the onset of the transition. The ΔC_p value was calculated from the onset to the end of the glass transition and the mobile amorphous fraction (*MAF*) was obtained according to equation (A.2):

$$MAF = \frac{\Delta C_p}{\Delta C_{p0}(1-\phi_m)} \qquad (A.2)$$

Where ΔC_p is the heat capacity change of the studied sample and ΔC_{p0} the heat capacity change of the amorphous PLA.

The quantity of rigid amorphous fraction (*RAF*) was calculated according to equation (A.3).

$$RAF = 1 - MAF - \chi_c \qquad (A.3)$$

3.3. b) Microstructure analysis

WAXS experiments were conducted at the European Synchrotron Radiation Facility (ESRF, Grenoble, France) on the BM02 beamline with an incident photon energy of 15.7 keV (λ = 0.77 Å). The aim is to examine the crystalline structure of both the semi-crystalline PLA and semi-crystalline PLA based-nanocomposites. The WAXS was calibrated using lanthanum hexaboride powder standard. The contribution of the empty cell was subtracted from the scattering images of the studied sample, the intensity was normalized by sample thickness

and azimuthally averaged to obtain *I vs. q*, where *I* is the signal intensity and *q* is the diffusion vector.

3.3. c) Nanofillers dispersion analysis

Nanofiller dispersion was investigated by Transmission Electron Microscopy (TEM) on a JEOL-1400 flash microscope operating at 120 kV. Sections with a thickness of 60 - 70 nm were prepared at room temperature by ultramicrotomy (Leica Ultracut B microtome) with an oscillating diamond knife (Diatom, 35°). The sections were then transferred on a 200-mesh copper grid with a carbon membrane.

Quantitative analyses have been performed from the analysis of at least 60 fillers domains using different TEM micrographs. The diameters, the area as well as the aspect ratio and the number of filler domains per surface unity have been calculated by Scikit-images processing in Python for silica and halloysite dispersions. For montmorillonite and graphene, the parameters were determined manually on ImageJ software because of a lack of contrast and the complexity of the shape of the filler domains. Moreover, for all nanocomposites, the distance between each filler domains have been measured manually using ImageJ.

3.3. d) Permeability measurements

Water vapor transmission (WVTR in g/[m². day]) experiments were performed at 23 °C and 90 % relative humidity using a MOCON PERMATRAN W3/33 equipped with an infrared sensor. Film samples with a 5 cm² effective area and a constant thickness between 100 ± 5 and 150 ± 5 µm were used. The water transferred through the films was conducted by N_2 as carrier gas at 100 sccm to the infrared sensor. The permeability *P* is calculated from the steady state flux *J* according to equation (A.4):

$$P = \frac{J.e}{p} \qquad (A.4)$$

where *e* is the sample thickness (cm), taken from the average value of five measurements and *p* is the pressure (cm_{Hg}). The permeability coefficient *P* is expressed in barrer units (1 barrer = 10^{-10} cm^3_{STP} .cm.cm^{-2}.s^{-1}.cm_{Hg}^{-1}= 3.36x10^{-16} mol.m.m^{-2}.s^{-1}.Pa^{-1}).

4. Results and discussion

4.1. Influence of the process on the matrix properties of semi-crystalline and nanocomposites films

For this study it is important to precise that non-brittle and self-standing reference and nanocomposites films were obtained whatever the process. Moreover, as residual solvent can highly impact transport properties, it was checked by TGA analysis that the thermal treatment used to evaporate the solvent in the solvent casting method was efficient and allowed to fully eliminate the solvent (**Supplementary Figure A.1**). The glass transition temperature of the nanocomposite films measured by modulated DSC is similar for the two processes, independently of the filler type used, with a value around 56 °C which is comparable to the value obtained for the two reference semi-crystalline PLA films (**Table A.3** and **Table A.4**). All T_g values are comparable with the values reported In the literature for the MBA process [12], [20], [25] and the SR process [27], [28], [29].

In semi-crystalline nanocomposites, two phases are considered as impermeable: the crystalline phase and the fillers. The crystalline phase of the samples has thus been deeply studied and compared as a function of the process.

First, the PLA crystalline structure has been analysed by WAXS and compared between the nanocomposites and the unfilled PLA films. **Figure A.1a** shows the diffractograms of the unfilled PLA films obtained by MBA and by SR and the assignment of the diffraction peaks. Both diffractograms exhibit two main reflection peaks associated to the α-form of PLLA, already reported in the literature both for solvent casting [23] and for thermal treatment [12]: (200) and (203) planes at q = 0.181 nm and q = 0.134 nm, respectively. Small reflection peaks at q = 0.088 nm, q = 0.146 nm, q = 0.158 nm and q = 0.177 nm related respectively to (004)/(103), (204), (015) and (206) planes are also associated to the α-form of PLLA [30], [31], [32]. Thus, both processes lead to semi-crystalline PLA with a crystalline α-form. WAXS diffractograms of the nanocomposites films filled with silica and montmorillonite are compared to the one of the respective unfilled PLA for the MBA process (**Figure A.1b**) and the SR process (**Figure A.1c**). No differences have been observed between the unfilled PLA and

the nanocomposites whatever the process and the filler content which means that the presence of filler did not affect the structure of the PLA crystalline phase, as already reported in the literature for PLA filled with organo-modified montmorillonites prepared by solvent route [23], [24].

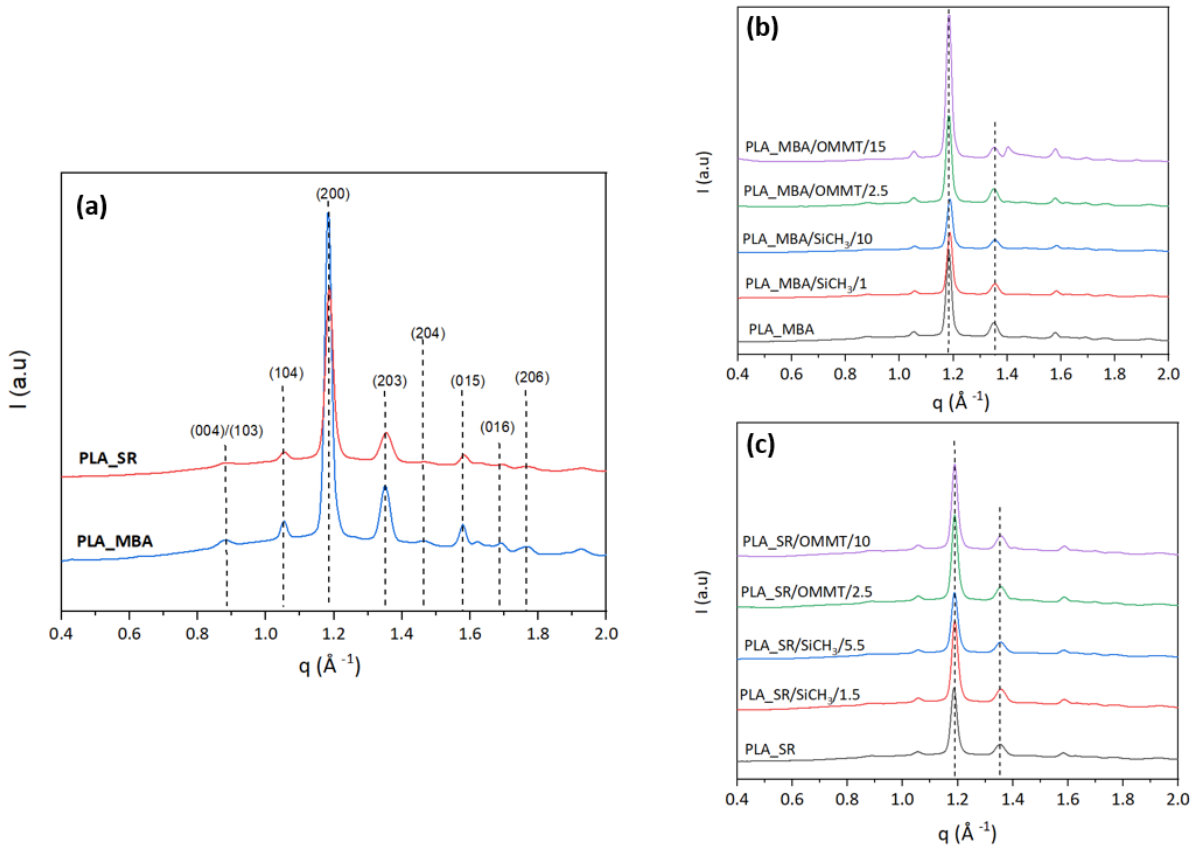


Figure A.1 - WAXS diffractogram of (a) unfilled PLA, (b) nanocomposite films prepared with the MBA process and (c) nanocomposites films with the SC process.

Then, the crystallinity degrees have been investigated by DSC analysis and the values are gathered in **Table A.3** for the MBA samples and in **Table A.4** for the SR samples. The thermograms of unfilled PLA and $SiCH_3$ nanocomposites are presented in **Figure A.2**. For the MBA samples the thermograms show one melting pic at T_m = 154 °C for the unfilled PLA and the $SiCH_3$ nanocomposites (**Figure A.2a**) whereas the thermograms of SR samples show two melting peaks (T_{m1} = 147 °C, T_{m2} = 152 °C) for unfilled PLA and low filled $SiCH_3$ samples (**Figure A.2b**). This double peak can be attributed to the melt-recrystallisation-melt process of unstable crystals [33]. The intensity of the second peak decreases as the filler content increases. For both processes, the same tendency is observed for all the fillers as evidenced by additional thermograms available in supporting information (**Supplementary Figure A.2**

and **Supplementary Figure A.3**). The degree of crystallinity is higher for the MBA samples (χ_c = 47%) than for the SR samples (χ_c = 36%) which is the same whatever the filler content.

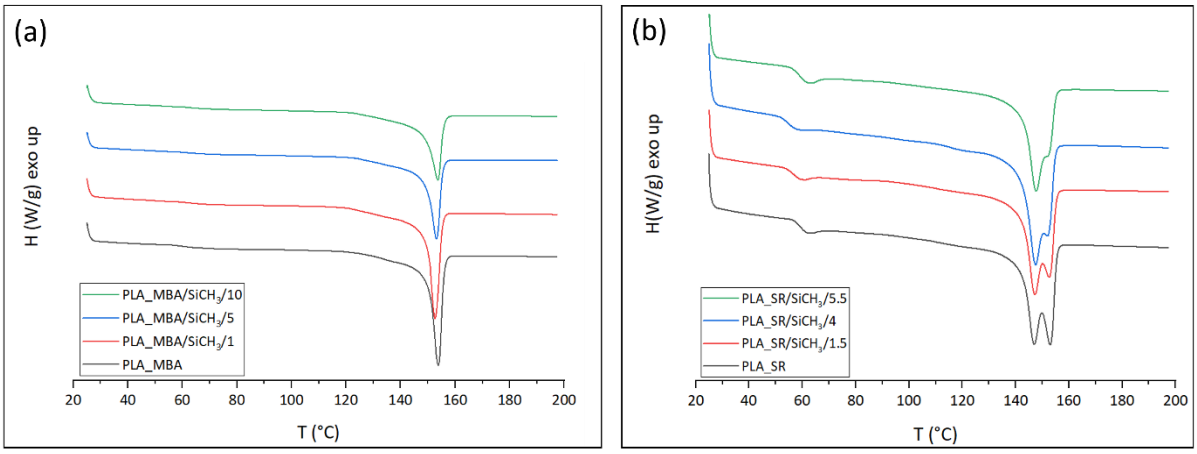


Figure A.2 - DSC thermograms with a heating ramp at 10 °C/min of unfilled PLA and $SiCH_3$ nanocomposites for (a) MBA process and (b) SR process.

Table A.3 - Matrix properties of the different nanocomposite films prepared by melt-blending/annealing (MBA).

Sample	T_g (°C)	T_m (°C)	χ_c (%)	*RAF* (%)
PLA_MBA	56 ± 1	150 ± 2	47 ± 2	13 ± 6
PLA_MBA/SiOH/1	57 ± 1	152± 1	46 ± 2	12 ± 7
PLA_MBA/SiOH/3	57 ± 1	154 ± 1	49 ± 2	6 ± 7
PLA_MBA/SiOH/4	57 ± 1	154 ± 1	47 ± 2	10 ± 6
PLA_MBA/$SiCH_3$/1	56± 1	153 ± 1	49 ± 2	11 ± 7
PLA_MBA/$SiCH_3$/4	56 ± 1	154 ± 1	46 ± 2	16 ± 7
PLA_MBA/$SiCH_3$/5	56 ± 1	153 ± 1	44 ± 2	15 ± 7
PLA_MBA/$SiCH_3$/10	56 ± 1	153 ± 1	44 ± 2	16 ± 8
PLA_MBA/HNT/0.5	55 ± 1	153 ± 1	46 ± 2	9 ± 7
PLA_MBA/HNT/2	56 ± 1	154 ± 1	48 ± 2	11 ± 6
PLA_MBA/HNT/4	56 ± 1	153 ± 1	48 ± 2	13 ± 6
PLA_MBA/HNT/10	55 ± 1	154 ± 1	51 ± 2	8 ± 6
PLA_MBA/OMMT/2.5	55 ± 1	154 ± 1	50 ± 2	11 ± 6
PLA_MBA/OMMT/5	53 ± 1	154 ± 1	50 ± 2	17 ± 6
PLA_MBA/OMMT/10	51 ± 1	154 ± 1	49 ± 2	19 ± 6
PLA_MBA/GNP/0.05	56 ± 1	152 ± 1	46 ± 2	4 ± 6
PLA_MBA/GNP/0.1	58 ± 1	153 ± 1	47 ± 2	6 ± 6
PLA_MBA/GNP/0.5	57 ± 1	152 ± 1	48 ± 2	7 ± 6
PLA_MBA/GNP/1.5	55 ± 1	152 ± 1	45 ± 2	8 ± 6

Table A.4 - Matrix properties of the different nanocomposite films prepared by the solvent route (SR)

Sample	T_g (°C)	T_{m1} (°C)	T_{m2} (°C)	χ_c (%)	*RAF* (%)
PLA_SR	56 ± 1	147± 1	153 ± 1	36 ± 2	14 ± 6
PLA_SR/SiOH/2	56 ± 1	147 ± 1	152± 1	37 ± 2	18 ± 7
PLA_SR/SiOH/3.5	56 ± 1	148 ± 1	/	37 ± 2	16 ± 7
PLA_SR/SiOH/5	56 ± 1	148 ± 1	/	38 ± 2	22 ± 6
PLA_SR/ $SiCH_3$/1.5	57 ± 1	148 ± 1	152 ± 1	36 ± 2	21 ± 7
PLA_SR/$SiCH_3$ /4	55 ± 1	148 ± 1	152 ± 1	41 ± 2	14 ± 7
PLA_SR/$SiCH_3$/5.5	58 ± 1	148 ± 1	/	35 ± 2	16 ± 7
PLA_SR/HNT/1.5	56 ± 1	148 ± 1	152 ± 1	36 ± 2	18 ± 7
PLA_SR/HNT/3	57 ± 1	148 ± 1	152 ± 1	36 ± 2	22 ± 6
PLA_SR/HNT/6.5	57 ± 1	149 ± 1	/	35 ± 2	25 ± 6
PLA_SR/HNT/11	56 ± 1	147 ± 1	/	36 ± 2	15 ± 6
PLA_SR/OMMT/1.5	56 ± 1	147 ± 1	153 ± 1	35 ± 2	17 ± 6
PLA_SR/OMMT/2.5	57 ± 1	147 ± 1	152 ± 1	36 ± 2	19 ± 6
PLA_SR/OMMT/6	58 ± 1	149 ± 1	/	36 ± 2	25 ± 6
PLA_SR/OMMT/8.5	57 ± 1	148 ± 1	/	36 ± 2	23 ± 6
PLA_SR/OMMT/10	55 ± 1	148 ± 1	/	37 ± 2	20 ± 6
PLA_SR/GNP/0.05	56 ± 1	148 ± 1	153 ± 1	40 ± 2	10 ± 6
PLA_SR/GNP/0.1	54 ± 1	148 ± 1	152 ± 1	37 ± 2	17 ± 6
PLA_SR/GNP/0.5	50 ± 1	147 ± 1	153 ± 1	38 ± 2	15 ± 6
PLA_SR/GNP/1.5	56 ± 1	147 ± 1	153 ± 1	39 ± 2	12 ± 6

Finally, the mobility of the amorphous phase of the nanocomposites was investigated thanks to the rigid amorphous phase (*RAF*), whose values are reported in **Table A.3** and **Table A.4**. Literature data are not numerous for the nanocomposites considered in this study. We can only mention that similar values of *RAF* as ours have been reported in the literature for PLA/OMMT nanocomposites prepared by solvent route [23]. As the crystalline amount and then the amorphous amount depends on the process, the proportion of RAF in the amorphous phase (*RAFa*) has been calculated for all the nanocomposites according to equation (A.5) and is represented in **Figure A.3**.

$$RAFa = \frac{RAF}{(1 - \chi_c)} \qquad (A.5)$$

For the MBA nanocomposites (**Figure A.3a**), the *RAFa* is globally lower than the *RAFa* of the MBA unfilled PLA (*RAFa* PLA_MBA = 25%). This results is quite surprising as it is expected that the introduction of fillers increases the *RAF* content [34], [35]. Only PLA_MBA/OMMT has a slightly higher *RAFa* than the unfilled PLA from 5 vol% of filler, which increases with the filler content. On the contrary, SR nanocomposites have globally a higher value of *RAFa* than the SR unfilled PLA (*RAFa* PLA_MBA = 22%). Moreover, the *RAFa* value increases for filler content up to 7 vol% of HNT and OMMT and then decreases and tends towards the value of the PLA_SR. For PLA_SR/GNP nanocomposites, the *RAFa* is globally close to the *RAFa* of the unfilled PLA, with a slight increase for 0.05 vol% and 0.1 vol% GNP and then a decrease at 1.5 vol% of GNP.

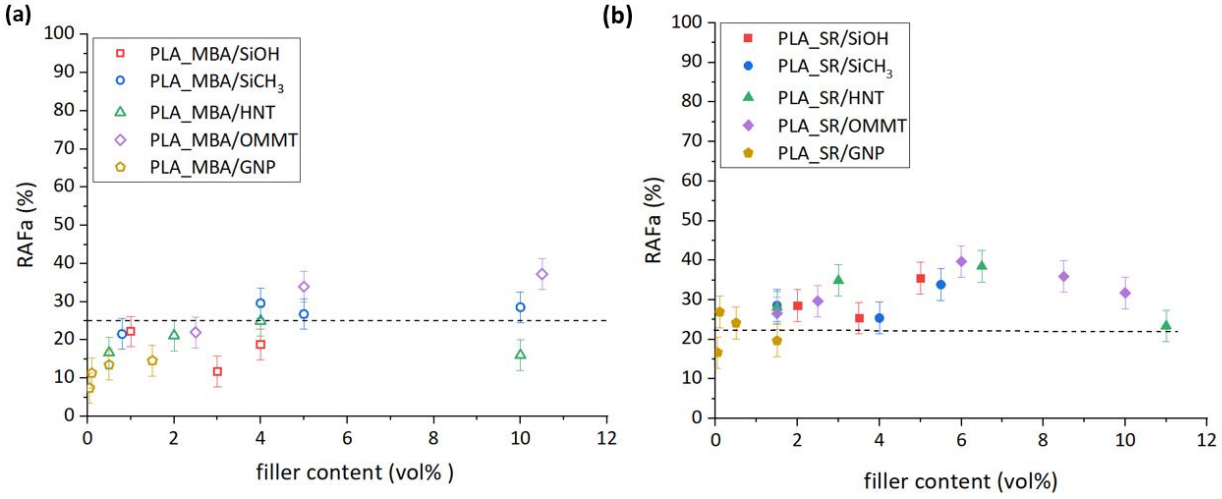


Figure A.3 - Evolution of the RAFa (RAF/amorphous phase amount) as a function of the filler content for a) MBA nanocomposites and (b) SR nanocomposites. The dotted line stands for the RAFa of the respective unfilled PLA.

To sum up, the main difference between the two processes is the degree of crystallinity which is higher for the MBA than SR samples. Nevertheless, the degree of crystallinity is similar in each nanocomposite series whatever the filler content and the crystalline structure of the nanocomposite films prepared by MBA and SR is not affected by the fillers. The T_g values do not evidence significant modification of the global chain mobility as a function of the introduction of fillers. On the other hand, some differences are observed thanks to the RAF concerning the chain mobility at the interfaces in the materials. The *RAFa* values show that the mobility is almost similar for the two unfilled PLA, but the addition of fillers leads to some modifications. The MBA nanocomposites exhibit a lower *RAF* content than the unfilled PLA,

reflecting a higher interfacial mobility, except for the case of montmorillonite. On the contrary, the amorphous phase of the SR nanocomposites has a lower mobility than the unfilled PLA (related to the higher *RAF* values), reaching a minimum at around 6 vol% fillers, then increasing again towards the value of unfilled PLA. The same trend is observed with graphene but shifted towards lower filler amount. In addition to these matrix differences, the process could also play a role on the dispersion of the fillers.

4.2. Effect of the process on the filler dispersion in nanocomposites films

The dispersion of the different fillers in the PLA matrix has been analyzed by TEM observations and compared as a function of the process used to prepare the films. Quantitative parameters such as the mean size of the filler domains, the mean aspect ratio as well as the average density of domains per surface unity and the mean distance between the domains have also been determined.

Figure A.4 allows to compare TEM micrographs of PLA filled with 4 vol% of silica as a function of the processing route. It can be observed that the nanocomposites prepared by MBA exhibit better filler dispersion than those prepared by SR with both hydrophilic and hydrophobic silica. The same results are observed in the entire range of filler content, the TEM micrographs of all the silica nanocomposites are available in supporting information (**Supplementary Figure A.4**)

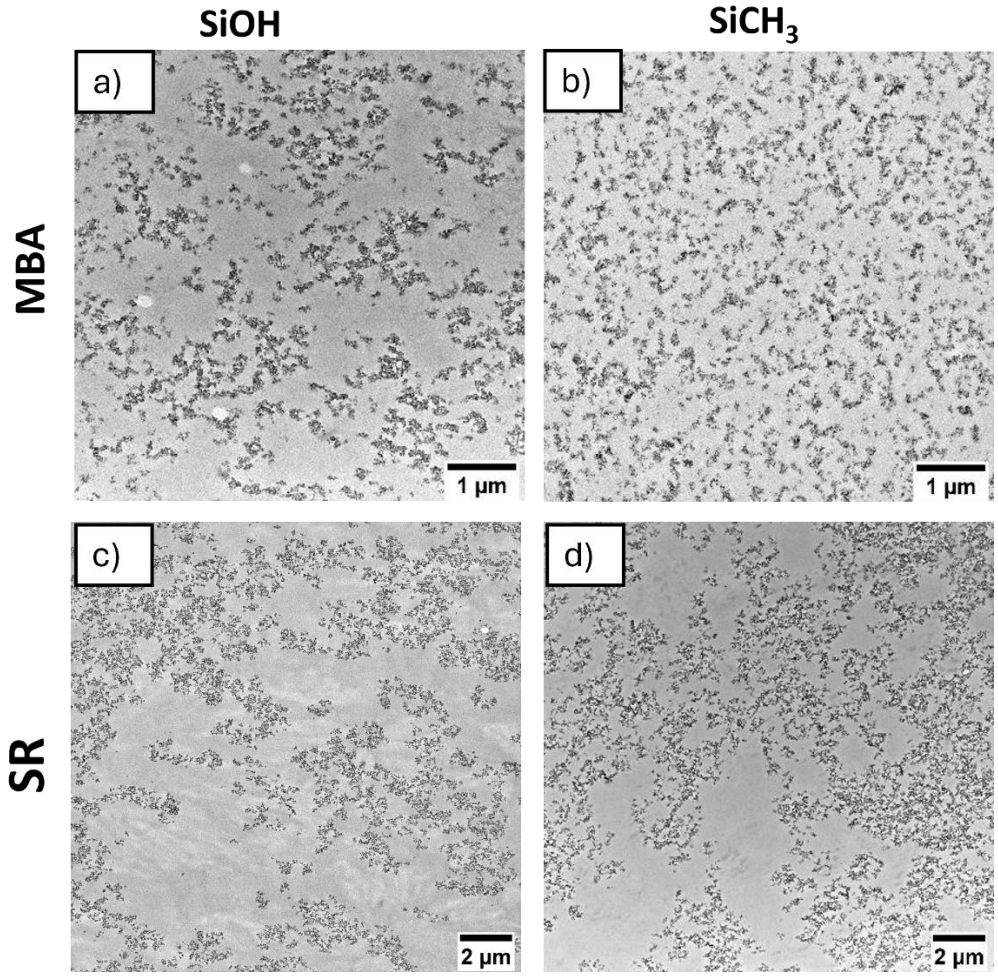


Figure A.4 - TEM micrographs of PLA filled with 4 vol% of silica with MBA process (a) PLA_MBA/SiOH/4, (b) PLA_MBA/$SiCH_3$/4 and with the SR process (c) PLA_SR/SiOH/3.5, (d) PLA_SR/$SiCH_3$/4.

The parameters resulting from the quantitative analysis of the TEM images are summarized in **Table A.5** and confirm the qualitative analysis. In the case of hydrophilic silica (SiOH), the average area of the silica domains goes from 9,000 nm² to 20,000 nm² for nanocomposites prepared by MBA whereas the values are above 30,000 nm² for all nanocomposites prepared by SR. Moreover, the standard deviation on the area values is important for the nanocomposites prepared by SR meaning a more heterogeneous dispersion. The number of domains per surface unity is also higher with the melting route and increases with the silica content up to 16 domains/µm² for PLA_MBA/SiOH/4 whereas it stays at 2.5 domains/µm² for PLA_SR/SiOH/3.5 and PLA_SR/ SiOH/5. In the case of hydrophobic silica ($SiCH_3$), the area of the silica domains for the MBA samples is globally 10 times smaller for the SR samples leading to more than 10 times more silica domains in the MBA samples. Moreover, the silica domains are much further in SR samples with a mean distance of 10 times superior to the MBA

samples. All these results show that a finer and more homogeneous dispersion of the silica is obtained with the MBA process. Furthermore, hydrophilic silica leads to smaller and more numerous domains than hydrophobic silica in case of MBA whereas no significant differences is observed with the SR.

Table A.5- Area, average number of particles per surface unity and distance between the impermeable domains for MBA and SR nanocomposites filled with hydrophilic silica (SiOH) or hydrophobic silica ($SiCH_3$).

Sample	Area (nm^2)	Density (domains/μm^2)	Interdomains spacing (nm)
PLA_MBA/SiOH/1	9,000 ± 7,000	5	550 ± 200
PLA_MBA/SiOH/3	18,000 ± 30,000	7	430 ± 130
PLA_MBA/SiOH/4	20,000 ± 30,000	16	380 ± 160
PLA_SR/SiOH/2	30,000 ± 25 000	< 1	1,880 ± 900
PLA_SR/SiOH/3.5	45,000 ± 41 000	2.5	980 ± 230
PLA_SR/SiOH/4	80,000 ± 100 000	2.5	780 ± 250
PLA_MBA/$SiCH_3$/1	3,000 ± 3,000	12	290 ± 100
PLA_MBA/$SiCH_3$/4	3,000 ± 3,000	70	120 ± 40
PLA_MBA/$SiCH_3$/5	3,000 ± 5,000	60	140 ± 40
PLA_MBA/$SiCH_3$/10	8,000 ± 5,000	20	150 ± 60
PLA_SR/$SiCH_3$/1.5	30,000 ± 40,000	1.9	1,600 ± 600
PLA_SR/$SiCH_3$/4	70,000 ± 100,000	2.5	1,100 ± 400
PLA_SR/$SiCH_3$/5	70,000 ± 100 000	3	900 ± 250

The halloysite dispersion in the nanocomposite film cross sections is shown in **Figure A.5** for both processes. It can be seen that the halloysite nanotubes are well dispersed in the MBA samples, with small discs (40 nm diameter) corresponding to the diameter of the tubes and few elongated structures corresponding to the length of the tubes (**Figure A.5 a,b,c)**, which means that the nanotubes are rather lying in the plane of the films. Few agglomerated structures (diameters between 200 and 500 nm) can be observed, and although their number tends to increase with the filler content, their proportion remains very low (< 10 %) for all filler contents (**Table A.6**).

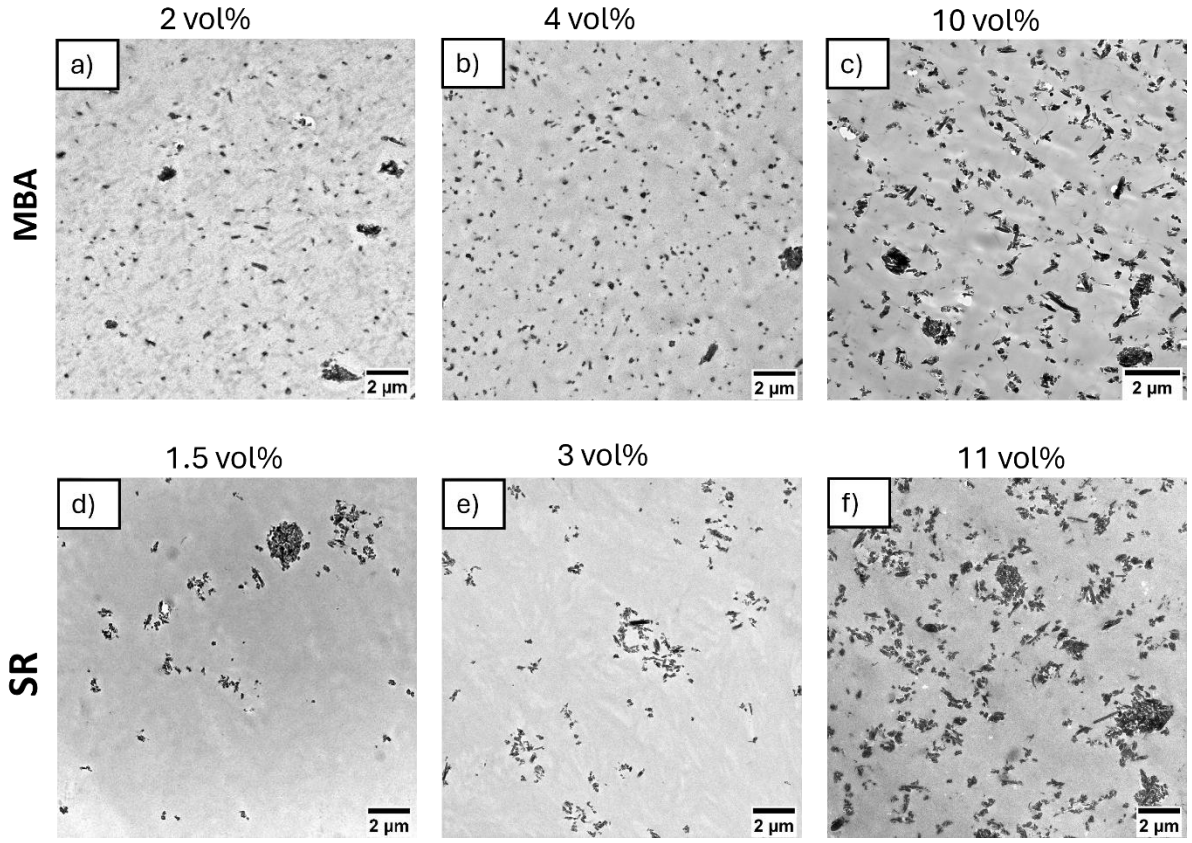


Figure A.5 - TEM micrographs of PLA filled with halloysite prepared by melt-blending annealing a) PLA_MBA/HNT/2, b) PLA_MBA/HNT/4, c) PLA_MBA/HNT/10 and solvent casting d) PLA_SR/HNT/1.5, e) PLA_SR /HNT/3 , f) PLA_SR/HNT/11.

The halloysite dispersion obtained from SR is more heterogenous involving some individual tubes and mainly widely spaced aggregates (**Figure A.5 d,e,f**). The percentage of aggregates increases as the filler content increases and reaches 90 % for 11 vol% of HNT. It is noteworthy that the mean aggregate size is comparable with those observed for the nanocomposites obtained by MBA (between 400 and 600 nm) but their amount is approximately 10 times more important than in the nanocomposites prepared by the MBA, whatever the filler content (**Table A.6**). Lastly, the distance between the filler domains is two times higher with the solvent route. This differences in halloysite dispersion has already been reported in the literature [22] and explained by filler reaggregation during the solvent evaporation.

Table A.6 – Proportion of aggregated nanotube domains and their diameters as well as the interdomains spacing values calculated from TEM micrograph for MBA and SR halloysite nanocomposites

Sample	% aggregated domains	Aggregates diameters (nm)	Interdomains spacing (nm)
PLA_MBA/HNT/0.5	3	450 ± 50	2,100 ± 400
PLA_MBA/HNT/2	4	480 ± 220	1,300 ± 500
PLA_MBA/HNT/4	3	250 ± 80	500 ± 200
PLA_MBA/HNT/10	10	320 ± 118	550 ± 200
PLA_SR/HNT/1.5	33	420 ± 150	2,300 ± 850
PLA_SR/HNT/3	45	470 ± 250	2,000 ± 500
PLA_SR/HNT/6.5	70	500 ± 350	1,200 ± 400
PLA_SR/HNT/11	90	600 ± 400	1,000 ± 400

The dispersion of OMMT has also been compared as a function of the processing route. TEM micrographs (**Figure A.6**) show that in all cases the fillers are rather randomly oriented in the films. A better filler dispersion is observed for the nanocomposites prepared with the melting route independently of the filler content, contrary to the observations reported by Marras *et al.* [21]. Indeed, the filler dispersion is homogenous with the co-existence of quasi-individual lamellae and middle size tactoïds up to 10 vol% of filler. The solvent route leads to bigger and sparser filler domains. Some studies in the literature seem to show better dispersion of OMMT filler by the solvent casting process but no TEM micrographs at low magnification are shown [14], [24], [36]. To go deeper in the comparison, the filler domains have been separated in several categories according to the study of Vermogen *et al.* [37]. The proportion of each category of filler domains (i.e: quasi-individual sheets, small tactoïds, middle size tactoïds and micron size agglomerates) has been calculated as well as their respective mean aspect ratio (α) and the obtained values are reported in **Table A.7**.

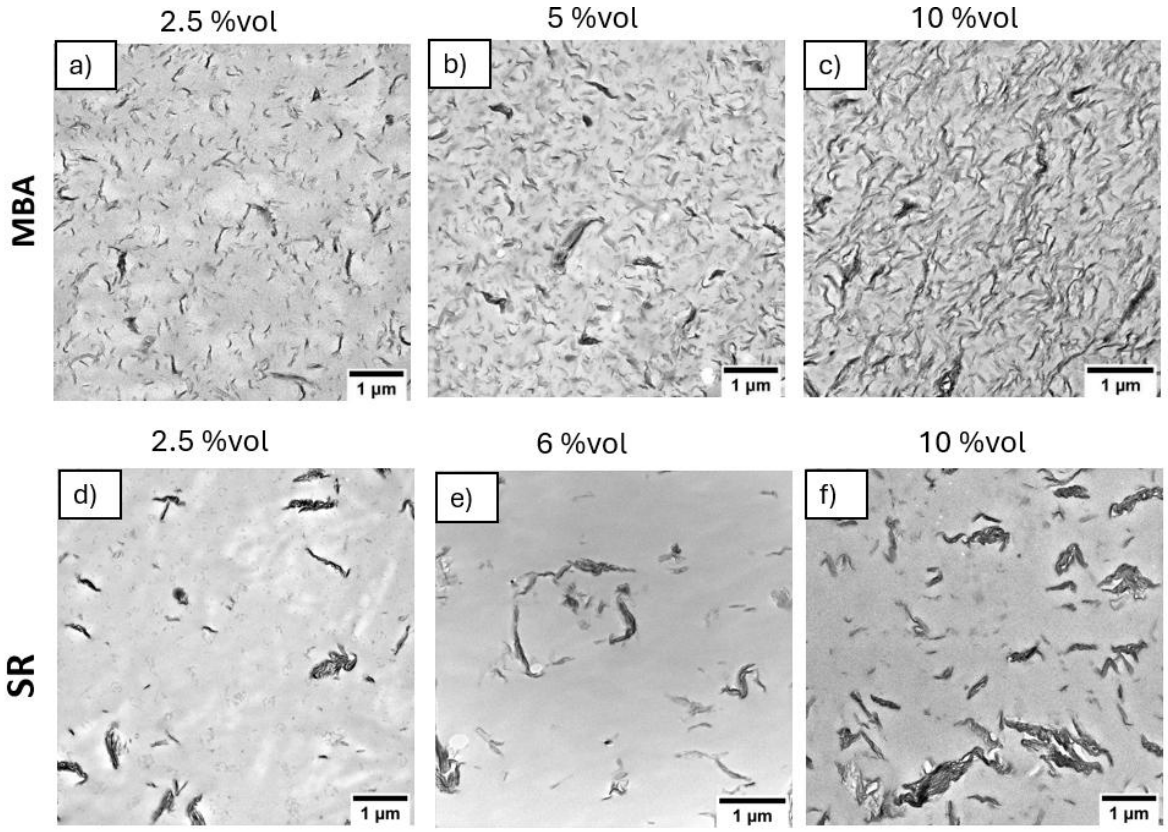


Figure A.6 - TEM micrographs of PLA filled with montmorillonite prepared by melt-blending/annealing a) PLA_MBA/OMMT/2.5, b) PLA_MBA/OMMT/5, c) PLA_MBA/OMMT/10 and solvent casting d) PLA_SR/OMMT/2.5, e) PLA_SR/OMMT/6, f) PLA_SR/OMMT/10.

The quantitative description of the different categories of filler domains reveals that the number of quasi-individual sheets is systematically more important in the case of the MBA with a mean aspect ratio of 100 versus 50 for the SR. Small tactoïds ($e < 30$ nm) with a mean aspect ratio between 10 and 12 have only been evidenced with the MBA process and represent 10% of all the domains whatever the filler content. The proportion of middle size tactoïds ($30 < e < 200$ nm) is greater with the SR with a mean aspect ratio similar for both processes, with values between 5 and 7. Micron size agglomerates ($e > 200$ nm) have only been observed in the case of the SR samples whatever the filler content, with a proportion between 10 and 19 % and a very low aspect ratio. This quantitative analysis confirms the fact that the OMMT is better dispersed with the MBA process than with the SR. Moreover, it also enables to calculate the value of an average aspect ratio which gathered all the categories of filler domains. This mean aspect ratio is between 83 and 86 for the PLA_MBA/OMMT nanocomposites prepared by the melting route whereas the values for PLA_SR/OMMT samples are much lower, between 32 and 39. Finally, the mean distance between the filler

domains decreases as the filler content increases and is smaller for the samples prepared from the MBA samples.

Table A.7 – Characteristics of OMMT dispersion for samples prepared with the melt blending/annealing process (PLA_MBA/OMMT) and the solvent casting process (PLA_SR/OMMT), (*w* stands for the thickness of the filler domains)

Sample	quasi-individual sheets		Small tactoïds (w< 30 nm)		Middle size tactoïds (30 <w< 200 nm)		Micron size agglomerates (w> 200 nm)		Mean aspect ratio	Interdomains spacing (nm)
	% by number	Aspect ratio	% by number	Aspect ratio	% by number	Aspect ratio	% by number	Aspect ratio		
PLA_MBA/OMMT/2.5	84	100	10	12 ± 5	6	7 ± 2	/	/	86	190 ± 100
PLA_MBA/OMMT/5	85	100	10	10 ± 2	6	5 ± 2	/	/	86	150 ± 60
PLA_MBA/OMMT/10	80	100	10	10 ± 2	10	7 ± 2	/	/	83	60 ± 30
PLA_SR/OMMT/1.5	75	50	/	/	15	5 ± 3	10	4 ± 1	39	1,900 ± 600
PLA_SR/OMMT/2.5	70	50	/	/	13	7 ± 3	17	4 ± 1	37	1,300 ± 500
PLA_SR/OMMT/6	63	50	/	/	22	5 ± 2	24	4 ± 1	34	500 ± 150
PLA_SR /OMMT/8.5	65	50	/	/	20	6 ± 3	15	4 ± 1	34	400 ± 150
PLA_SR/OMMT/10	59	50	/	/	22	7 ± 4	19	4 ± 1	32	500 ± 200

Finally, the cross sections of the nanocomposite films filled with graphene were observed by TEM (**Figure A.7**). No significant differences in the filler dispersion state have been observed as a function of the process. For both processes, it was too difficult to observe any graphene sheets in the samples by TEM microscopy under 0.1 vol% of GNP due to the very low amount of fillers. At 0.1 vol% filler, there are almost no stacks visible which means that most of graphene is present as individual sheets (**Figure A.7a,d**). At 0.5 vol% there is the coexistence of quasi individual sheets and small stacks (**Figure A.7b,e**) and the proportion and size of the stacks seem to increase for 1.5 vol% GNP (**Figure A.7c,f**). No quantitative analysis could have been made due to the lack of contrast and the few number of dispersed graphene domains. Indeed, it is important to keep in mind that for this nanocomposite series, the filler content

remains very low (less than 1.5 vol%). Nevertheless, the mean aspect ratio of the unitary filler is between 500 and 1000.

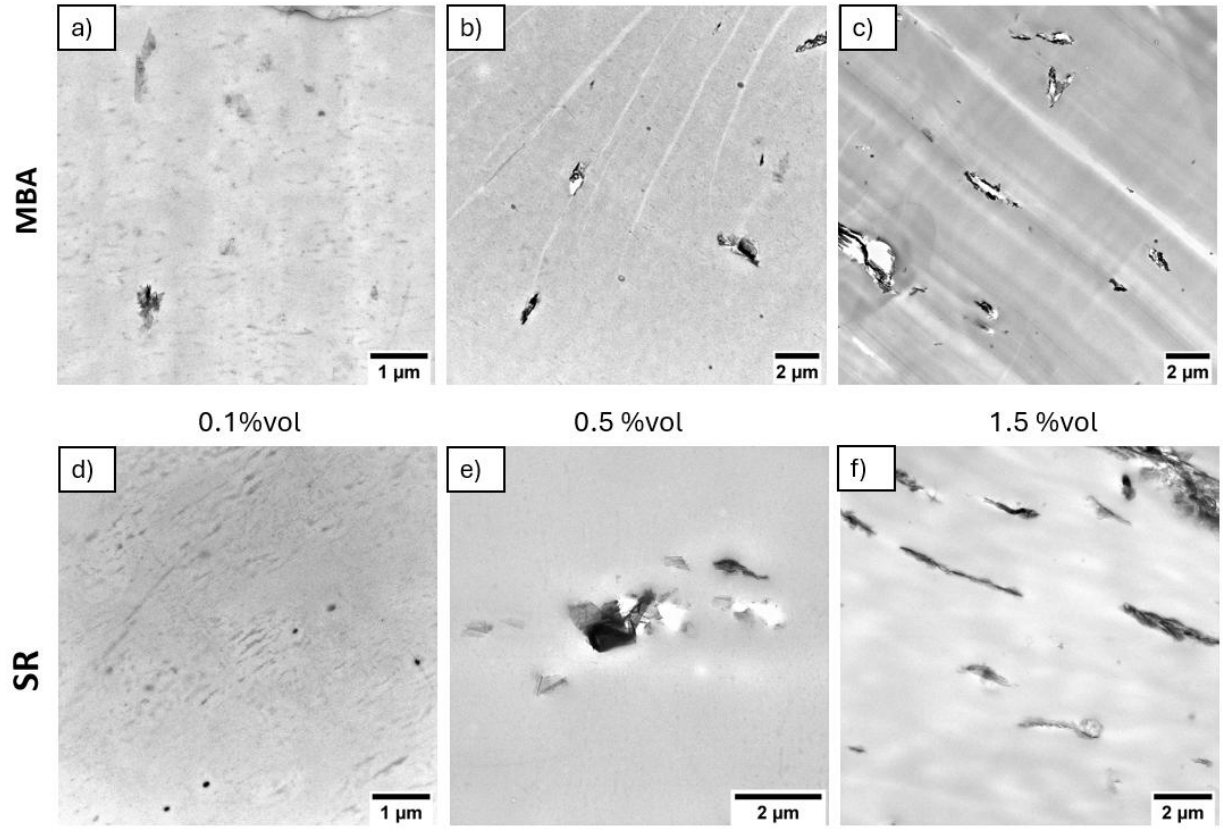


Figure A.7 - TEM micrographs of of PLA filled with graphene prepared by melt-blending annealing: a) PLA_MBA/GNP/0.1, b)PLA_MBA/GNP/0.5, c) PLA_MBA/GNP/1.5 and by solvent casting : d) PLA_SR/GNP/0.1, e) PLA_SR/GNP/0.5, f) PLA_SR/GNP/1.5.

To conclude, the melt-blending/annealing process leads to better filler dispersion states whatever the fille type and content except for graphene.

4.3. Water vapor permeability of semi-crystalline nanocomposites and semi-crystalline PLA

Water vapor permeability coefficients were measured at 23 °C and 90 % RH on the different semi-crystalline nanocomposite films series. The permeability of the semi-crystalline nanocomposites is compared to the permeability of the reference semi-crystalline PLA films prepared with the same process (e.g: PLA_MBA or PLA_SR) by calculating for each sample the relative permeability according to equation (A.6) :

$$Relative\ permeability = \frac{P}{P_{matrix}} \qquad (A.6)$$

Where P is the permeability of the nanocomposites and P_{matrix} is the permeability of the neat semi-crystalline PLA.

As the nanocomposites have the same degree of crystallinity and the same crystalline structure as the respective reference semi-crystalline PLA, it is expected that the evolution of the relative permeability is governed by the fillers. Indeed, the inorganic fillers chosen for this study are known to be impermeable to gas and water vapor, they should create obstacles to the diffusing molecules leading then to tortuosity effects [4], [7], [20], [38]. Moreover, we will also examine if the low differences observed as a function of the process in the *RAFa* values, that are related with the amorphous chain mobility at the interfaces, can play a role on the permeability.

The permeability coefficient measured for the neat semi-crystalline PLA, are respectively P_{matrix}(PLA_MBA) = 1,180 ± 110 barrer and P_{matrix}(PLA_SR) = 1,890 ± 100 barrer. These values are in agreement with the degree of crystallinity and are comparable to values reported respectively for annealed PLA [11] and PLA prepared by solvent casting methods [36].

Figure A.8 presents the relative permeability values obtained for the different nanocomposite series investigated in this work. It can be observed that the relative permeability of the nanocomposites prepared by SR is always below or equal to 1 which is not the case for all the nanocomposites obtained by MBA. It was interesting to look more specifically at each nanocomposite series and to compare the influence of the process. The relative permeability values obtained for silica (hydrophilic and hydrophobic silica) based nanocomposites are shown in **Figure A.8a**. The relative permeability evolution does not depend on the hydrophobic or hydrophilic nature of silica. Indeed, for the nanocomposites prepared by SR, independently of the silica type, the relative permeability value stays around 1 for filler content less than 4 vol% and then slightly decreases. On the contrary, all relative permeability values obtained for the nanocomposites prepared by MBA are slightly higher than 1. For the nanocomposites based on halloysites (**Figure A.8b**), the relative permeability of the SR nanocomposites decreases to 0.76 for 3 vol%. However, an increase of the relative permeability is observed for 11 vol%. Such results have already been observed by Othman *et*

al. [17] beyond 2 vol% HNT. For HNT nanocomposites prepared by MBA, all the permeability values are slightly higher than 1, although the dispersion state is better than in the SR samples. Concerning the nanocomposites filled with montmorillonite all the relative permeability values are below 1. A decrease of the relative permeability is observed with the filler content for both processes, reaching a minimum value of 0.59 for PLA_SR/OMMT/10 and 0.38 for PLA_MBA/OMMT/10 (**Figure A.8c**). The differences can be explained by a better dispersion of the montmorillonites sheets with the melting process leading to a higher value of the average aspect ratio. The relative permeability values obtained with the solvent process are comparable to those reported by Şengül *et al.* [39], [40] with an exfoliated-intercalated-flocculated dispersion and better than those of Koh *et al.* [14] with an intercalated structure. For MBA process, higher values of relative permeability have been obtained by Picard *et al.* [20] who described a less good filler dispersion. Finally, the relative permeability of the nanocomposites containing graphene are completely different between the two processes (**Figure A.8d**). Indeed, for the solvent process all the graphene nanocomposites show a relative permeability below or equal to 1. The addition of graphene leads to a sharp decrease of the relative permeability up to 0.58 for 0.1 vol% GNP and then an increase until 0.82 for 1.5 vol%. This tendency with a V shape has already been reported in a previous study on amorphous graphene nanocomposites as well as in the literature with the solvent casting process [18] and can be attributed to an increase of the GNP agglomerates content at higher filler amount. On the contrary, the MBA leads to relative permeability value well much higher than 1 whereas the GNP dispersion is comparable than in the SR samples.

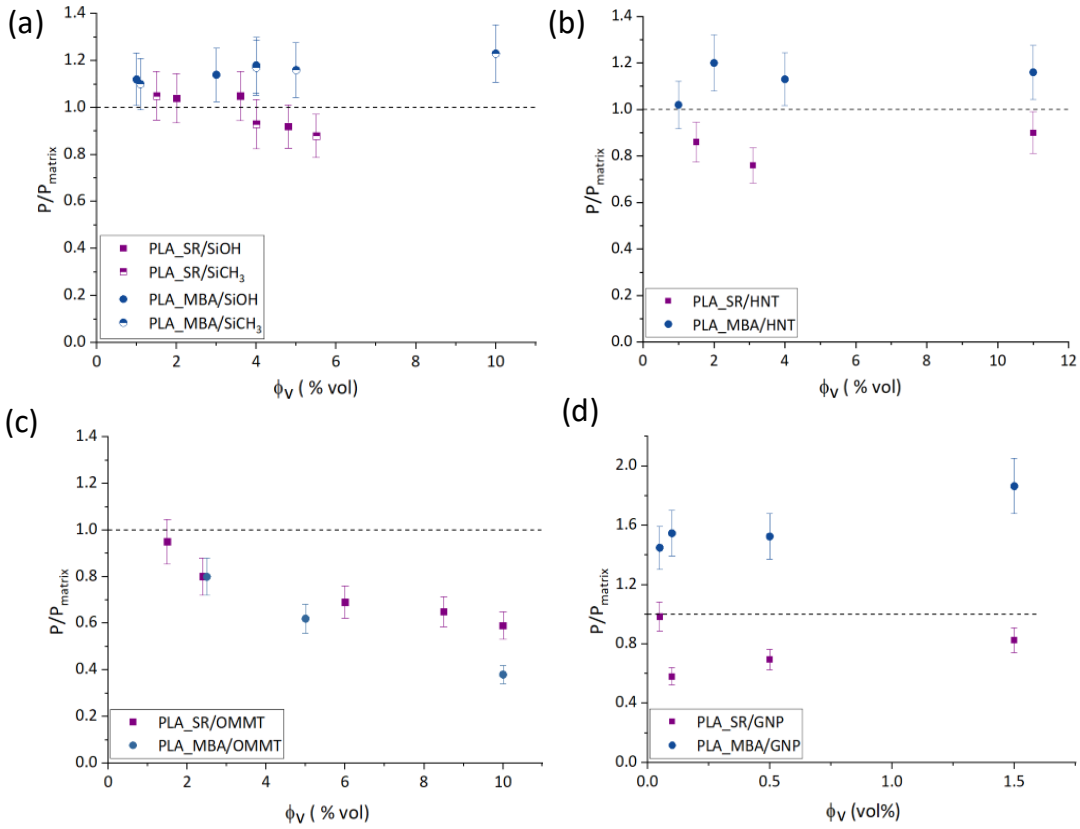


Figure A.8 - Relative permeability as a function of the volume fraction of the different fillers (a) silica, (b) halloysites nanotubes, (c) organo-modified montmorillonites and (d) graphene. The dotted line stands for a relative permeability of 1.

To sum up, the addition of fillers leads to a decrease in permeability for the SR samples, as long as the dispersion is not degraded, whereas it is not the case for most MBA nanocomposites. However, there is no direct relation explaining the differences in permeability between these two processes from the dispersion state of the fillers. As underlined by our investigation, in addition to the dispersion state, the process seems to have a non-negligible influence on matrix chain mobility at the filler/matrix interfaces which seems to also play a role on the permeability. Indeed, in the case of SR, we noted an increase of the *RAF* with the addition of fillers for filler content up to 6 vol% filler and then a decrease to tend to the *RAF* value of the unfilled matrix. Thus, for SR process, it can be proposed that permeability results from both the filler dispersion state and the filler/matrix interactions that are related to the *RAF* values. At low filler content, a good filler dispersion is usually observed, the *RAF* value increases with the amount of developed interfacial area and the trend is a decrease of the permeability. Above 5 - 6 vol% of fillers, both the quality of filler dispersion

and RAF decrease leading to a decrease of the barrier properties. The same trend is observed for graphene, but a shift is observed towards lower filler content due to the high aspect ratio of the individual platelet and a strong filler reaggregation phenomenon at 1.5 vol% of GNP. However, for the nanocomposites based on montmorillonite, the permeability behavior is not in total agreement with the general trend we have described. Indeed, the permeability still decreases above 5 vol% of OMMT. However, it can be noticed that the extent of decrease is less important. We have underlined that although the filler dispersion is less good at high OMMT content, the difference is not as marked as for other fillers. Moreover, the *RAFa* value stays above the value of the reference matrix. These both trends can then explain the permeability behavior in the case of the nanocomposites based on OMMT.

Concerning now the MBA process, it has been shown that the addition of filler leads to *RAF* values lower or equal to that one of the reference PLA matrix, except for OMMT at high content. It can also be observed that the lowest *RAFa* values are observed for the nanocomposites made with SiOH and GNP nanofillers. These low *RAFa* values can appear surprising when compared with the results obtained for the nanocomposites prepared by SR, as the same fillers are supposed to give the same interaction with the matrix. Clearly here, the different behavior is related to the process used to obtain the semi-crystalline nanocomposites. It can be suspected that the rather low values of the *RAFa* are related to low interactions created at the filler/matrix interface, most probably induced by stress concentration occurring during the crystallization process at the rubbery state weakening the filler/matrix interface. In that case, antagonistic effects between tortuosity and diffusion rate at the filler/matrix interface take place leading for nanocomposites based on silica, halloysite or graphene to similar or higher permeability than the reference matrix. Such antagonistic effects have been reported and modelled in the literature as a function of filler surface modification [41], [42], [43]. However, to the best of our knowledge, no such deep analysis was reported in the literature concerning the potential effects of the process. It has to be noticed that the trend evidenced for nanocomposites based on silica, halloysite nanotubes and graphene is not observed for the nanocomposites based on OMMT. Indeed, for these materials, the permeability is lower than for the PLA semi-crystalline matrix, which can be explained by keeping rather high filler/matrix interactions (*RAF* value higher than for the matrix) and a good filler dispersion state.

5. Conclusion

Two distinct processes were used to prepare semi-crystalline PLA films containing various types of fillers: solvent casting and cold crystallization of melt-blended samples. Silica, halloysite and montmorillonite were used in a range between 0 and 11 vol%, while graphene was incorporated up to 1.5 vol%. First it has been noted that annealing treatment leads to a higher degree of crystallinity than solvent route but the crystallinity of the samples does not appear to be affected by the presence of fillers, regardless of the process employed. The filler dispersion state is globally better for the nanocomposites obtained from melt-blending/annealing than with the samples obtained from the solvent route probably due, in the last case, to filler reaggregation in some extent during the solvent evaporation step. The mobility of the PLA chains at the filler/matrix interface has been shown to decrease for the nanocomposites obtained from the solvent route. For the nanocomposites prepared by melt-blending/annealing, the interfacial behavior depends on the filler type: silica, halloysite and graphene lead to increase the polymer chain mobility at the filler/PLA interface in the semi crystalline nanocomposites while organo-modified montmorillonite allows to keep rather strong interactions after the cold crystallization step. This difference in behavior has been assigned to the probable development of stress concentration around silica, halloysite and graphene in the annealed nanocomposites.

The permeability of all the nanocomposites prepared by solvent route tends to decrease with increasing filler amount as long as the filler dispersion is not degraded and the rather strong filler/matrix interactions are kept. For the nanocomposites prepared by melt-blending and annealing, the permeability is slightly higher than the reference matrix except for montmorillonite. The permeability values are then not only related to the filler dispersion state but also to the chain mobility at the filler/matrix interface. The low filler/matrix interactions observed in the semi-crystalline nanocomposites based on silica and graphene play a detrimental role on the barrier properties. Thus, depending on the filler and the process used to prepare the semi-crystalline nanocomposites, either additive effects of filler/matrix interactions and filler dispersion or antagonist effects contribute to the transport properties, leading to enhance or on the contrary decrease the barrier properties.

6. References

[1] M. Labonté, C. Dubois, Processing of Impact Modifed PLA in a Continous Process at High Speed: Comparison with PET Molding Conditions – A New Era, Polymer-Plastics Technology and Engineering 54 (2015) 368–374. https://doi.org/10.1080/03602559.2014.958774.

[2] S. Farah, D.G. Anderson, R. Langer, Physical and mechanical properties of PLA, and their functions in widespread applications — A comprehensive review, Advanced Drug Delivery Reviews 107 (2016) 367–392. https://doi.org/10.1016/j.addr.2016.06.012.

[3] Bioplastics market development update 2023, European Bioplastics e.V (2023). https://www.european-bioplastics.org/market/ (accessed November 26, 2024).

[4] S. Singha, M.S. Hedenqvist, A Review on Barrier Properties of Poly(Lactic Acid)/Clay Nanocomposites, Polymers 12 (2020) 1095. https://doi.org/10.3390/polym12051095.

[5] N. Tenn, N. Follain, J. Soulestin, R. Crétois, S. Bourbigot, S. Marais, Effect of Nanoclay Hydration on Barrier Properties of PLA/Montmorillonite Based Nanocomposites, J. Phys. Chem. C 117 (2013) 12117–12135. https://doi.org/10.1021/jp401546t.

[6] S. Sinha Ray, K. Yamada, M. Okamoto, Y. Fujimoto, A. Ogami, K. Ueda, New polylactide/layered silicate nanocomposites. 5. Designing of materials with desired properties, Polymer 44 (2003) 6633–6646. https://doi.org/10.1016/j.polymer.2003.08.021.

[7] Y. Guo, K. Yang, X. Zuo, Y. Xue, C. Marmorat, Y. Liu, C.-C. Chang, M.H. Rafailovich, Effects of clay platelets and natural nanotubes on mechanical properties and gas permeability of Poly (lactic acid) nanocomposites, Polymer 83 (2016) 246–259. https://doi.org/10.1016/j.polymer.2015.12.012.

[8] F. Li, C. Zhang, Y. Weng, X. Diao, Y. Zhou, X. Song, Enhancement of Gas Barrier Properties of Graphene Oxide/Poly (Lactic Acid) Films Using a Solvent-free Method, Materials 13 (2020) 3024. https://doi.org/10.3390/ma13133024.

[9] A. Jullin, G. Sudre, N. Hascoët, F. Chinesta, E. Espuche, Influence of different type of impermeable phase on the permeability of PLA films : nanofillers versus crystalline phase, Polymer Testing (Submitted) (2024).

[10] A.S. Michaels, H.J. Bixler, Solubility of gases in polyethylene, Journal of Polymer Science 50 (1961) 393–412. https://doi.org/10.1002/pol.1961.1205015411.

[11] M. Drieskens, R. Peeters, J. Mullens, D. Franco, P.J. Lemstra, D.G. Hristova-Bogaerds, Structure versus properties relationship of poly(lactic acid). I. Effect of crystallinity on barrier properties: Structure Vs. Barrier Properties of PLA, J. Polym. Sci. B Polym. Phys. 47 (2009) 2247–2258. https://doi.org/10.1002/polb.21822.

[12] A. Guinault, C. Sollogoub, V. Ducruet, S. Domenek, Impact of crystallinity of poly(lactide) on helium and oxygen barrier properties, European Polymer Journal 48 (2012) 779–788. https://doi.org/10.1016/j.eurpolymj.2012.01.014.

[13] E. Espino-Pérez, J. Bras, V. Ducruet, A. Guinault, A. Dufresne, S. Domenek, Influence of chemical surface modification of cellulose nanowhiskers on thermal, mechanical, and barrier properties of poly(lactide) based bionanocomposites, European Polymer Journal 49 (2013) 3144–3154. https://doi.org/10.1016/j.eurpolymj.2013.07.017.

[14] H.C. Koh, J.S. Park, M.A. Jeong, H.Y. Hwang, Y.T. Hong, S.Y. Ha, S.Y. Nam, Preparation and gas permeation properties of biodegradable polymer/layered silicate nanocomposite membranes, Desalination 233 (2008) 201–209. https://doi.org/10.1016/j.desal.2007.09.043.

[15] J.-W. Rhim, S.-I. Hong, C.-S. Ha, Tensile, water vapor barrier and antimicrobial properties of PLA/nanoclay composite films, LWT - Food Science and Technology 42 (2009) 612–617. https://doi.org/10.1016/j.lwt.2008.02.015.

[16] J.-H. Chang, Y.U. An, G.S. Sur, Poly(lactic acid) nanocomposites with various organoclays. I. Thermomechanical properties, morphology, and gas permeability, Journal of Polymer Science Part B: Polymer Physics 41 (2003) 94–103. https://doi.org/10.1002/polb.10349.

[17] S.H. Othman, H.N. Ling, R.A. Talib, M.N. Naim, N.P. Risyon, Md. Saifullah, PLA/MMT and PLA/Halloysite Bio-Nanocomposite Films: Mechanical, Barrier, and Transparency, JNanoR 59 (2019) 77–93. https://doi.org/10.4028/www.scientific.net/JNanoR.59.77.

[18] A.M. Pinto, J. Cabral, D.A.P. Tanaka, A.M. Mendes, F.D. Magalhães, Effect of incorporation of graphene oxide and graphene nanoplatelets on mechanical and gas permeability properties of poly(lactic acid) films, Polymer International 62 (2013) 33–40. https://doi.org/10.1002/pi.4290.

[19] S. Fernandes Nassar, A. Guinault, N. Delpouve, V. Divry, V. Ducruet, C. Sollogoub, S. Domenek, Multi-scale analysis of the impact of polylactide morphology on gas barrier properties, Polymer 108 (2017) 163–172. https://doi.org/10.1016/j.polymer.2016.11.047.

[20] E. Picard, E. Espuche, R. Fulchiron, Effect of an organo-modified montmorillonite on PLA crystallization and gas barrier properties, Applied Clay Science 53 (2011) 58–65. https://doi.org/10.1016/j.clay.2011.04.023.

[21] S.I. Marras, I. Zuburtikudis, C. Panayiotou, Solution casting versus melt compounding: effect of fabrication route on the structure and thermal behavior of poly(l-lactic acid) clay nanocomposites, J Mater Sci 45 (2010) 6474–6480. https://doi.org/10.1007/s10853-010-4735-6.

[22] R.T. De Silva, M. Soheilmoghaddam, K.L. Goh, M.U. Wahit, S.A.H. Bee, S.-P. Chai, P. Pasbakhsh, Influence of the processing methods on the properties of poly(lactic acid)/halloysite nanocomposites, Polymer Composites 37 (2016) 861–869. https://doi.org/10.1002/pc.23244.

[23] J. Trifol, M. van Drongelen, F. Clegg, D. Plackett, P. Szabo, A.E. Daugaard, Impact of thermal processing or solvent casting upon crystallization of PLA nanocellulose and/or nanoclay composites, Journal of Applied Polymer Science 136 (2019) 47486. https://doi.org/10.1002/app.47486.

[24] V. Krikorian, D.J. Pochan, Poly (L -Lactic Acid)/Layered Silicate Nanocomposite: Fabrication, Characterization, and Properties, Chem. Mater. 15 (2003) 4317–4324. https://doi.org/10.1021/cm034369+.

[25] F. Morel, E. Espuche, V. Bounor-Legaré, O. Persynn, M. Lacroix, Impact of coated calcium carbonate nanofillers and annealing treatments on the microstructure and gas barrier properties of poly(lactide) based nanocomposite films, Journal of Polymer Science Part B: Polymer Physics 54 (2016) 649–658. https://doi.org/10.1002/polb.23957.

[26] B. Kalb, A.J. Pennings, General crystallization behaviour of poly(l-lactic acid), Polymer 21 (1980) 607–612. https://doi.org/10.1016/0032-3861(80)90315-8.

[27] A. Abdulkhani, J. Hoseinzadeh, S. Dadashi, M. Mousavi, A study of morphological, thermal, mechanical and barrier properties of PLA based biocomposites prepared by micro and nano sized cellulosic fibers, Cellulose Chemistry and Technology 49 (2015) 597–605.

[28] E. Espino-Pérez, J. Bras, V. Ducruet, A. Guinault, A. Dufresne, S. Domenek, Influence of chemical surface modification of cellulose nanowhiskers on thermal, mechanical, and barrier properties of poly(lactide) based bionanocomposites, European Polymer Journal 49 (2013) 3144–3154. https://doi.org/10.1016/j.eurpolymj.2013.07.017.

[29] F. Morel, Compréhension des phénomènes interfaciaux dans les composites à base de charges carbonate de calcium précipité: influence du traitement de surface et du procédé de mise en œuvre, Thèse de doctorat, Université Lyon 1 (2010).

[30] M. Cocca, M.L.D. Lorenzo, M. Malinconico, V. Frezza, Influence of crystal polymorphism on mechanical and barrier properties of poly(l-lactic acid), European Polymer Journal 47 (2011) 1073–1080. https://doi.org/10.1016/j.eurpolymj.2011.02.009.

[31] J. Zhang, K. Tashiro, H. Tsuji, A.J. Domb, Disorder-to-Order Phase Transition and Multiple Melting Behavior of Poly(l-lactide) Investigated by Simultaneous Measurements of WAXD and DSC, Macromolecules 41 (2008) 1352–1357. https://doi.org/10.1021/ma0706071.

[32] M.L. Di Lorenzo, M.C. Righetti, Crystallization-induced formation of rigid amorphous fraction, POLYMER CRYSTALLIZATION 1 (2018). https://doi.org/10.1002/pcr2.10023.

[33] P. Song, G. Chen, Z. Wei, W. Zhang, J. Liang, Calorimetric analysis of the multiple melting behavior of melt-crystallized poly(l-lactic acid) with a low optical purity, J Therm Anal Calorim 111 (2013) 1507–1514. https://doi.org/10.1007/s10973-012-2502-4.

[34] J. Leng, N. Kang, D.-Y. Wang, A. Wurm, C. Schick, A. Schönhals, Crystallization behavior of nanocomposites based on poly(l-lactide) and MgAl layered double hydroxides – Unbiased determination of the rigid amorphous phases due to the crystals and the nanofiller, Polymer 108 (2017) 257–264. https://doi.org/10.1016/j.polymer.2016.11.065.

[35] P. Klonos, P. Pissis, Effects of interfacial interactions and of crystallization on rigid amorphous fraction and molecular dynamics in polylactide/silica nanocomposites: A methodological approach, Polymer 112 (2017) 228–243. https://doi.org/10.1016/j.polymer.2017.02.003.

[36] J. Trifol, D. Plackett, C. Sillard, O. Hassager, A.E. Daugaard, J. Bras, P. Szabo, A comparison of partially acetylated nanocellulose, nanocrystalline cellulose, and nanoclay as fillers for high-performance polylactide nanocomposites, Journal of Applied Polymer Science 133 (2016). https://doi.org/10.1002/app.43257.

[37] A. Vermogen, K. Masenelli-Varlot, R. Séguéla, J. Duchet-Rumeau, S. Boucard, P. Prele, Evaluation of the Structure and Dispersion in Polymer-Layered Silicate Nanocomposites, Macromolecules 38 (2005) 9661–9669. https://doi.org/10.1021/ma051249+.

[38] G. Choudalakis, A.D. Gotsis, Permeability of polymer/clay nanocomposites: A review, European Polymer Journal 45 (2009) 967–984. https://doi.org/10.1016/j.eurpolymj.2009.01.027.

[39] B. Şengül, N. Dilsiz, Barrier properties of polylactic acid/layered silicate nanocomposites for food contact applications, Polym. Sci. Ser. A 56 (2014) 896–906. https://doi.org/10.1134/S0965545X14060194.

[40] B. Şengül, R.M.A. El-abassy, A. Materny, N. Dilsiz, Poly(lactic acid)/Organo-Montmorillonite Nanocomposites: Synthesis, Structures, Permeation Properties and Applications, Polym. Sci. Ser. A 59 (2017) 891–901. https://doi.org/10.1134/S0965545X17060098.

[41] K. Dal Pont, Nanocomposites à matrice élastomère à base de charges lamellaires synthétiques alpha-ZrP : influence de la modification des charges sur les propriétés mécaniques et barrière aux gaz, Thèse de doctorat, Université Lyon 1 (2011).

[42] E. Picard, J.-F. Gérard, E. Espuche, Reinforcement of the Gas Barrier Properties of Polyethylene and Polyamide Through the Nanocomposite Approach: Key Factors and Limitations, Oil Gas Sci. Technol. – Rev. IFP Energies Nouvelles 70 (2015) 237–249. https://doi.org/10.2516/ogst/2013145.

[43] T. Htira, S. Zid, M. Zinet, E. Espuche, Finite Element Analysis of Gas Diffusion in Polymer Nanocomposite Systems Containing Rod-like Nanofillers, Polymers 13 (2021) 2615. https://doi.org/10.3390/polym13162615.

Cette première partie concernait l'influence du procédé d'élaboration sur la perméabilité de nanocomposites PLA semi-cristallins. Pour cela des PLA semi-cristallins avec des taux de charges de 0 à 11 %vol ont été obtenus soit par voie solvant soit par traitement thermique de films préparés en voie fondue. Une étude détaillée de la microstructure des matériaux a été effectuée, allant des propriétés de la phase cristalline à la mobilité de la phase amorphe. La dispersion des charges a également été finement étudiée pour chacun des procédés ; une meilleure dispersion a été observée pour les échantillons mélangés par voie fondue, peu importe le type de charges. Les échantillons préparés par voie solvant ont montré une diminution de la perméabilité par rapport à la matrice semi-cristalline non chargée. Au contraire, les échantillons obtenus après traitement thermique ont une perméabilité égale, voire supérieure à celle de la matrice semi-cristalline non chargée, excepté pour les montmorillonites. Ces résultats surprenants ont été attribués à une potentielle fragilisation des interfaces charge/matrice au cours du traitement appliqué pour induire une cristallisation.

Par ailleurs, il est intéressant de comparer les perméabilités relatives des nanocomposites semi-cristallins obtenus par ces deux procédés avec celles des nanocomposites amorphes étudiés dans le chapitre III. Ainsi la **Figure A.9** représente les perméabilités relatives des nanocomposites amorphes et semi-cristallins par rapport à la perméabilité du PLA amorphe.

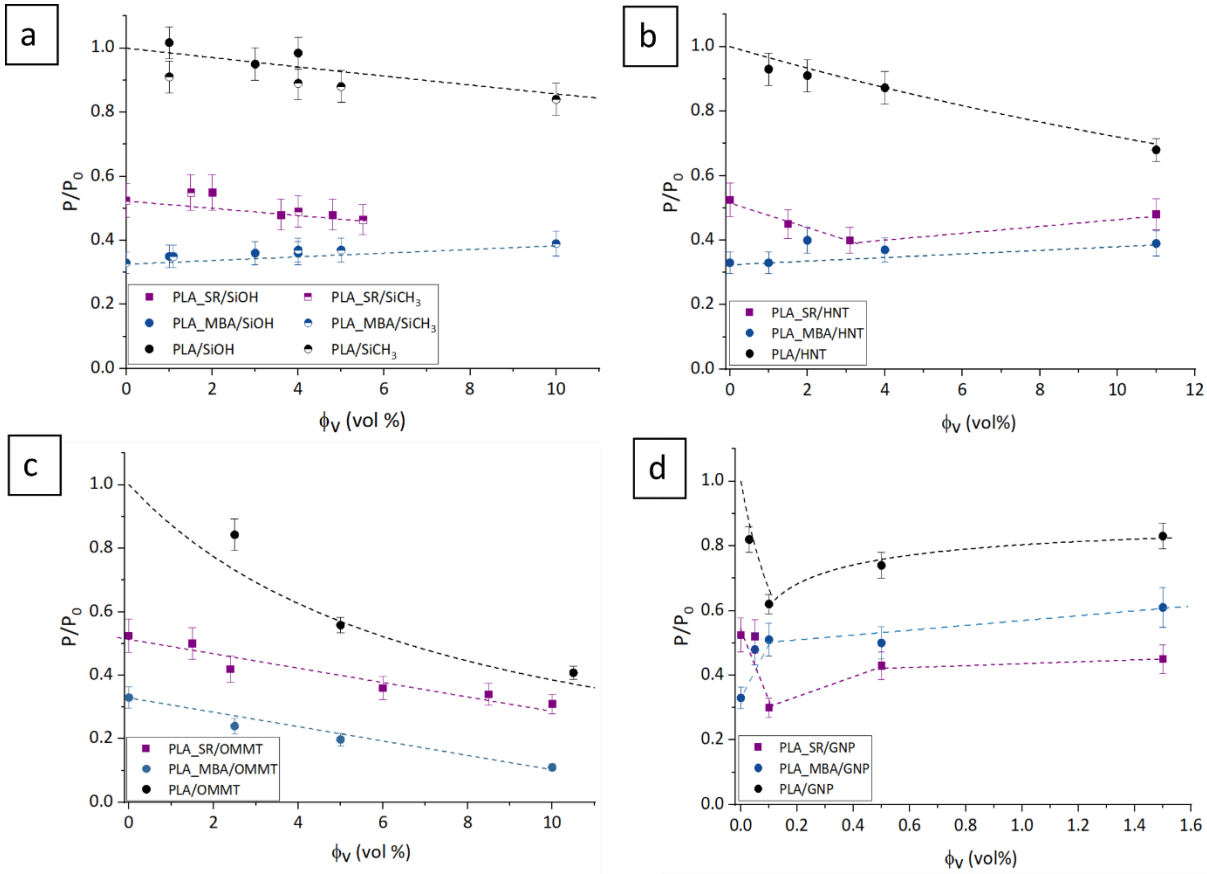


Figure A.9 - Perméabilité relative des nanocomposites amorphes et semi-cristallins (MBA et SR), par rapport à la matrice PLA amorphe, contenant (a) de la silice, (b) des halloysites, (c) des montmorillonites et (d) du graphène. Les lignes en pointillé sont des guides visuels.

Pour les nanocomposites à base de silice (**Figure A.9a**), les échantillons amorphes ont une perméabilité relative plus élevée que ceux préparés par voie solvant (SR), qui ont eux-mêmes une perméabilité plus élevée que les échantillons recuits (MBA), quel que soit le taux de charges et la nature de la silice. La même tendance est observée pour les échantillons chargés avec des halloysites et les montmorillonites (**Figure A.9b,c**). Dans ce cas les différences de perméabilité entre les échantillons sont principalement dues à l'effet de la cristallinité, bien que les écarts semblent plus importants pour de faibles taux de charges. Enfin, dans le cas du graphène, on observe une forme en V pour les nanocomposites amorphes et les nanocomposites MBA avec un minium atteint pour 0,1 %vol dans les deux cas, respectivement P/P_0 = 0,62 et P/P_0 = 0,30. Pour les nanocomposites semi-cristallins SR la perméabilité relative augmente avec le taux de charges et devient supérieure à celles des nanocomposites SR au-delà de 0,1 %vol malgré un plus haut degré de cristallinité de la matrice (**Figure A.9d**). Ce

comportement est du a été attribué une faible interface charges/matrices comme discuté précédemment.

Par ailleurs, à partir de ces résultats, les perméabilités relatives minimum atteintes pour les différentes charges utilisées dans cette thèse ont été regroupées dans le **Tableau A.8.** Ainsi pour la silice hydrophile (SiOH), la silice hydrophobe ($SiCH_3$) et les nanotubes d'halloysite (HNT) la perméabilité minium est atteinte par recuit de films amorphes préparés par mélange en voie fondue (MBA) avec un taux de charges de 1 %vol. Ces échantillons permettent de diminuer par 3 la perméabilité du PLA. La même diminution de perméabilité est obtenue par avec le graphène par voie solvant (SR) avec un taux de charges de 0.1 %vol. Enfin la perméabilité minimum de la plateforme de nanocomposites contenant une charge imperméable est atteinte pour 10 %vol de OMMT préparé par le procédé MBA permettant une réduction de perméabilité par 10 de la matrice PLA amorphe.

Tableau A.8 - Perméabilité relative minimum obtenue pour chaque charge, avec la fraction volumique et le procédé correspondants.

Charge	***Procédé***	***Fraction vol.***	***P/P_0 min***
$SiOH$ /$SiCH_3$	MBA	1 %vol	0,35
HNT	MBA	1 %vol	0,33
OMMT	MBA	10 %vol	0,11
GNP	SR	0,1 %vol	0,3

La présence de deux phases imperméables consistant en une phase cristalline et une charge imperméable permet ainsi de diminuer significativement la perméabilité du PLA. Cependant, l'ajout de charges peut parfois desservir les propriétés barrières dans le cas de PLA semi-cristallins chargés obtenus par traitement thermique.

Par ailleurs, on peut également avoir l'effet deux phases imperméables en associant deux charges dans une matrice PLA amorphe. Cela permet de s'affranchir de la phase cristalline qui peut fragiliser le PLA. Cette approche est l'objet de la deuxième partie de ce chapitre. La montmorillonite, qui a montré être une charge particulièrement efficace pour diminuer la

perméabilité, a été associée à deux autres charges. Pour cela, deux charges ont été judicieusement choisies : l'une sphérique (silice) et l'autre lamellaire (graphène) qui conduisent dans les deux cas à de faibles diminutions de perméabilité. Ainsi cette étude évaluera la potentielle synergie apportée par les montmorillonites pour chacun de ces systèmes. Cette deuxième étude est rédigée sous la forme d'un article.

Chapitre IV.B - Adding montmorillonite in PLA/silica and PLA/graphene nanocomposites: influence on nanocomposite's morphology and barrier properties

1. Abstract ***260***

2. Introduction ***260***

3. Experimental ***262***

3.1. Materials **262**

3.2. PLA nanocomposites preparation **262**

3.3. Characterization methods **263**

3.3.a) Thermal analysis 263

3.3.b) Nanofillers dispersion analysis 265

3.3.c) Permeability measurements 265

4. Results ***266***

4.1. Silica/montmorillonite nanocomposite films **266**

4.1.a) Characterization of silica/montmorillonite nanocomposite films 266

4.1.b) Water vapor permeability of silica/montmorillonite nanocomposites 269

4.2. Graphene/montmorillonite nanocomposites **271**

4.2.a) Characterization of graphene/montmorillonite nanocomposite films 271

4.2.b) Water vapor permeability of graphene/montmorillonite nanocomposites 274

5. Discussion ***275***

6. Conclusion ***278***

7. References ***280***

1. Abstract

Amorphous polylactic acid (PLA) nanocomposites filled with two filler types, e.g. silica and montmorillonite or graphene and montmorillonite, were prepared by melt-blending for a global filler content around 10 vol%. Respective reference silica-based, graphene-based and montmorillonite-based nanocomposites were prepared under the same conditions. The aim of this study was to investigate the potential synergetic effect of the addition of montmorillonites to i/a spherical filler having a slight influence on the permeability and to ii/a lamellar filler having a high aspect ratio and a high influence on the permeability but which is subjected to aggregation in PLA. The effect of the presence of two-fillers on the PLA matrix microstructure as well as on the chain mobility has been investigated. The dispersion of the fillers has been observed by transmission electron microcopy to identify the fillers organization in relation to each other and the potential differences with the nanocomposites containing only one filler. The water vapor permeability has been measured and was found to significantly decrease with the addition of montmorillonite both for silica and graphene nanocomposites. However, no additive effect has been observed whatever the systems.

2. Introduction

Thanks to its biodegradability, its transparency and its ease of processing, polylactic acid (PLA) is a polymer of interest for short term application such as packaging , with the expectation of reducing the environmental food print [1], [2]. Furthermore, the addition of nanofillers in PLA has been widely studied with the aim to lengthen the penetrant diffusion path and decrease the permeable phase content [3], these two phenomena being expected to lead to an increase in barrier properties. Most of studies show the efficiency of adding a unique filler on PLA barrier properties such as calcium carbonate [4], silica [5], silver [6], halloysite [7], [8], montmorillonite [7], [9], [10], graphene [11], [12] and nanocellulose [13], [14].

A few studies have focused on the introduction of two different fillers considering different polymer matrices with the objective to evidence potential synergetic effect of the fillers. Bendahou *et al.* reported synergetic effect between montmorillonite and cellulose nanowiskers in a natural rubber matrix for a global filler content of 5 wt% [15]. Indeed, with

the association of 2.5 %wt of montmorillonite with 2.5 wt% of cellulose nanowiskers the permeability was reduced by 6 compared to 5 wt% of cellulose and by 8 compared to 5 wt% of montmorillonites. However, this improvement in barrier properties seems to depend on the filler content as reported by Oleyaei *et al*. Indeed a synergetic effect was observed between montmorillonite and titanium dioxide dispersed in a starch matrix using a solvent mixing process for 3 wt% of montmorillonite while no significant improvement was observed for higher content (5 wt%) [16]. Cheviron *et al.* showed that the nanocomposite elaboration method could also play a major role in the case of montmorillonite/silver starch [17]. If synergetic effect was reported for the introduction of pre-formed silver nanoparticles with montmorillonite in a starch matrix, no such effect was evidenced when the silver particles were generated in the matrix. Concerning PLA matrix, Trifol *et al.* showed a synergetic effect of montmorillonite with cellulose nanowiskers or cellulose nanofibrils [18] while Bouazack *et al.* evidenced a similar trend with 3 wt% of montmorillonite and at least 2 wt% of epoxyzed graphene [19]. However, these two studies concern semi-crystalline PLA for which the degree of crystallinity is modified with the addition of fillers. Thus, the decrease of permeability cannot be attributed only to the presence of two fillers.

It appears then interesting to investigate the effects of the combination of two fillers in an amorphous PLA matrix. Regarding the previously mentioned studies, the addition of montmorillonite to another filler seems to be an efficient way to improve the barrier properties. Therefore, the current work focuses on the study of the effect of adding montmorillonite in a PLA amorphous matrix in two different cases. On the one hand, montmorillonite will be added to a spherical filler, silica, which is expected to bring a limited decrease of permeability due to its shape and low aspect ratio (equal to 1). On the other hand, montmorillonites will be added to a lamellar filler, graphene oxide, which has already been shown to lead to significant improvement of PLA barrier properties thanks to its high aspect ratio. However, the improvement in that case is limited to low graphene content due to a tendency of graphene oxide to agglomerate above 0.5 vol% [11], [20]. From the comparison of the two filler-based nanocomposites with the reference one filler based-nanocomposites, the main objectives are i/to study the morphology of the two filler-based nanocomposites to see if the addition of a second filler modifies the dispersion state of the initial systems, ii/to

investigate potential modification of the polymer chains mobility and iii/to compare the permeability between the systems containing one and two fillers, at the same volume content, enabling us to study the additive behavior of the two fillers on permeability or to evaluate the possible deviations. In this study the global volume content of fillers is always fixed close to 10 vol%, which will also allow a comparison of the permeability of the different nanocomposites whatever the type of filler.

3. Experimental

3.1. Materials

PLA 2003D was provided by NatureWorks LLC with a D-isomers content of 4.1 mol% and a density of 1.25. The molar mass measured by size exclusion chromatography is equal to 86,000 g/mol. Three different nanofillers were used in this study: i/hydrophobic fumed silica surface treated with dimethyldichlorosilane (Aerosil®AR974, Evonick Operation GmbH) with a density of 2.2 and an average diameter of 20 ± 5 nm, ii/ montmorillonite modified with methyl tallow bis 2-hydroxyethyl quaternary ammonium cation (Cloisite®30B, Southern Clay Product) having a density of 1.98 and a mean length of 200 nm with a one nanometer platelet thickness and iii/ graphene oxide nanoplatelets (KNG-180-3 Graphen Nanoplatetes, Knano) having a density of 2.2, a platelet length between 500 and 1000 nm and thickness of one nanometer.

3.2. PLA nanocomposites preparation

As PLA is very sensitive to hydrolysis during melt processing, the PLA pellets and the fillers were dried at 85 °C under vacuum during one night before processing. Unfilled PLA (PLAref) and four series of PLA nanocomposites were prepared by melt-blending using a Haake internal mixer. The melt blending was performed at 185 °C with a rotation speed of 50 rpm for a residence time of 10 min. The fillers were added after 3 min of mixing. For samples containing two fillers, the fillers have been manually mixed before being introduced into the Haake. After being dried at 85 °C under vacuum for 1 night, the compounds were compressed at 180 °C under 150 bars for 2 min, with 4 min of preheating to obtain films with a thickness between 100 and 150 µm. The films were rapidly cooled at room temperature to obtain amorphous

samples. The different films series and their respective composition are summarized in **Table B.1**.

Table B.1 – Name and composition of the PLA-based samples.

Sample name	***OMMT content (vol% /(% wt))***	***$SiCH_3$ content (vol% /(% wt))***	***GNP content (vol% /(% wt))***
PLAref	0	0	0
PLA/OMMT/5	5.2 (7.8)	0	0
PLA/OMMT/10	10 (15.2)	0	0
PLA/$SiCH_3$/5	0	5 (8.0)	0
PLA/$SiCH_3$/10	0	10 (16.3)	0
PLA/GNP/0.1	0	0	0.1(0.14)
PLA/GNP/0.5	0	0	0.5 (0.9)
PLA/ $SiCH_3$_7/OMMT_4	4.3 (6.4)	7.1(11.5)	0
PLA/$SiCH_3$_5.5/OMMT_5.5	5.5 (8)	5.5 (8.9)	0
PLA/ $SiCH_3$_2/OMMT_9	9.3 (13.8)	2.3 (3.8)	0
PLA/ GNP_0.1/OMMT_10	9.5 (14)	0	0.1 (0.1)
PLA/ GNP_0.5/OMMT_10	9.7 (14.5)	0	0.5 (0.8)

3.3. Characterization methods

3.3.a) Thermal analysis

Thermogravimetric analyses (TGA) were conducted by using a Mettler Toledo TGA/DSC 1 STAR^e System to determine the degradation temperature of the nanocomposites and the nanofillers content. The samples were heated from 25 to 500 °C at a rate of 10 °C/min under dry nitrogen flow. The weight loss was recorded as a function of the temperature and the onset degradation temperature was determined by using the tangent methods. The nanofiller volume content was determined from the mass residues at the 500 °C plateau, the density of the PLA and the density of the filler. For the nanocomposites containing two fillers, the volume fraction of each filler (Φv_i) has been calculated according to equation (B.1)

$$\Phi_{vi} = \frac{x_i \frac{w_{tot}}{\mu_i}}{x_i \frac{w_{tot}}{\mu_i} + \frac{(1 - w_{tot})}{\mu_{PLA}}} \quad (B.1)$$

With x_i the mass proportion of the filler introduced in the internal mixer, w_{tot} the mass residue at 500°C measured by TGA, μ_i the density of the filler and μ_{PLA} the density of PLA.

Furthermore, for nanocomposites filled with Cloisite®30B, the weight content of the organic cation (30 wt%) was added to the residual mass for volume fraction calculations.

Thermal properties of the samples have been investigated through differential scanning calorimetry (DSC) using a TA Instrument Q200 calorimeter calibrated with indium standard. Experiments on samples between 5 and 10 mg placed in an aluminum pan were conducted under nitrogen flow (50 mL/min) with a heating ramp from 25 to 200 °C at 10 °C/min using a standard mode. The cold crystallization temperature (T_{cc}) is taken at the onset whereas the melting temperature (T_m) was taken at the maximum of the endothermic peak. The degree of crystallinity (χ_c) of the PLA was calculated according to equation (B.2):

$$\chi_c = \frac{\Delta H_m - \Delta H_{cc}}{\Delta H_{m\infty}(1 - \phi_m)} \quad (B.2)$$

where ΔH_m is the enthalpy of melting , ΔH_{cc} is the enthalpy of cold crystallization , Φ_m the weight content of fillers and $\Delta H_{m\infty}$ is the enthalpy of the infinite crystal with a value of 93 J/g [21].

The analysis of the glass transition was performed by Temperature Modulated Differential Scanning Calorimetry, using a modulated temperature program with a heating ramp from 10 to 90 °C at an average heating rate of 2 °C/min with an oscillation amplitude of 0.318 °C/min. The glass transition temperature was taken at the onset of the transition. The heat capacity (ΔCp) value was calculated from the onset to the end of the glass transition and the quantity of mobile amorphous fraction (*MAF*) was determined according to equation (B.3):

$$MAF = \frac{\Delta Cp}{\Delta Cp_0 \, (1 - \phi_m)} \quad (B.3)$$

Where Φ_m is the weight content of fillers, ΔC_p the heat capacity change of the studied sample and ΔC_{p0} the heat capacity change of the amorphous PLA. The quantity of rigid amorphous fraction (*RAF*) was calculated according to equation (B.4).

$$RAF = 1 - MAF - \chi_c \qquad (B.4)$$

The uncertainties on the degree of crystallinity as well as the *MAF* and the RAF values have been calculated by the propagation uncertainties of the heat capacity and the enthalpy.

3.3.b) Nanofillers dispersion analysis

The dispersion of nanofillers in the matrix was observed in the films cross section using Transmission Electron Microscopy (TEM). Sections of samples, with a thickness of 60 - 70 nm, were prepared by ultramicrotomy with an oscillating diamond knife (Diatom, 35°) on a Leica Ultracut B microtome at room temperature. For observations, the sections were placed on 200-mesh copper grid with a carbon membrane. A JEOL-1400 flash microscope operating at 120 kV was used in bright field for the observations.

3.3.c) Permeability measurements

Water vapor transmission (WVTR in g/[m². day]) was measured at 23 °C and 90 % relative humidity with a MOCON PERMATRAN W3/33. Water transfered though the films was conducted by N_2 gas at 100 SCCM to the infrared sensor.

The permeability *P* values are calculated according to equation (B.5):

$$P = \frac{J.e}{p} \qquad (B.5)$$

where *J* is the flux at the steady state, *e* is the sample thickness (cm), taken from the average value of five measurements and *p* pressure (cm_{Hg}). The permeability coefficient *P* is expressed in barrer units (1 barrer = 10^{-10} cm^3_{STP} .cm.cm^{-2}.s^{-1}.cm_{Hg}^{-1} = 3.36.10^{-16} mol.m.m^{-2}.s^{-1}.Pa^{-1}).

4. Results

4.1. Silica/montmorillonite nanocomposite films

All the silica/montmorillonite nanocomposites were prepared with a global volume fraction of fillers between 10 and 11 vol%, with different proportion of each filler.

4.1.a) Characterization of silica/montmorillonite nanocomposite films

Whatever the PLA/$SiCH_3$/OMMT nanocomposite composition, the degradation temperature (T_d) is close to the one of neat PLA (in the range between 343 and 347 °C as shown in **Table B.2**). The DSC thermograms (**Figure B.1**) of the silica/montmorillonite nanocomposites show a glass transition, an exothermic peak associated to the cold crystallization and a melting peak, similarly to PLA/$SiCH_3$/10 and PLA/OMMT/10. The thermal properties of the two filler-based nanocomposites are summarized in **Table B.2** and compared with those of the one filler-based nanocomposites prepared with 10 vol% filler (eg. PLA/$SiCH_3$/10, PLA/OMMT/10). The glass transition temperature (T_g) values of PLA/OMMT/$SiCH_3$ are in the range between those of the one filler-based nanocomposite, decreasing from the T_g value of PLA/$SiCH_3$/10 to the T_g value of PLA/OMMT/10 as the montmorillonite content increases. Kontou *et al.* reported a different trend with a higher T_g value for montmorillonite/silica nanocomposites than for one filler-based nanocomposites [22]. The cold crystallization peak is shifted to higher temperatures for the two filler-based nanocomposites ($T_{cc} \approx 126$ °C) with respect to the one filler-based nanocomposites which means that the presence of two fillers is less favorable to the cold crystallization. The melting temperature ($T_m \approx 50$ °C) is not affected by the presence of two fillers nor the degree of crystallinity which stays close to 0. The content of rigid amorphous fraction (*RAF*) is higher in the presence of the two fillers (**Table B.2**) and increases with the content of OMMT up to 15%. Thus, it can be concluded that the introduction of two fillers leads to slightly decrease the mobility of the polymer chains at the filler/matrix interface.

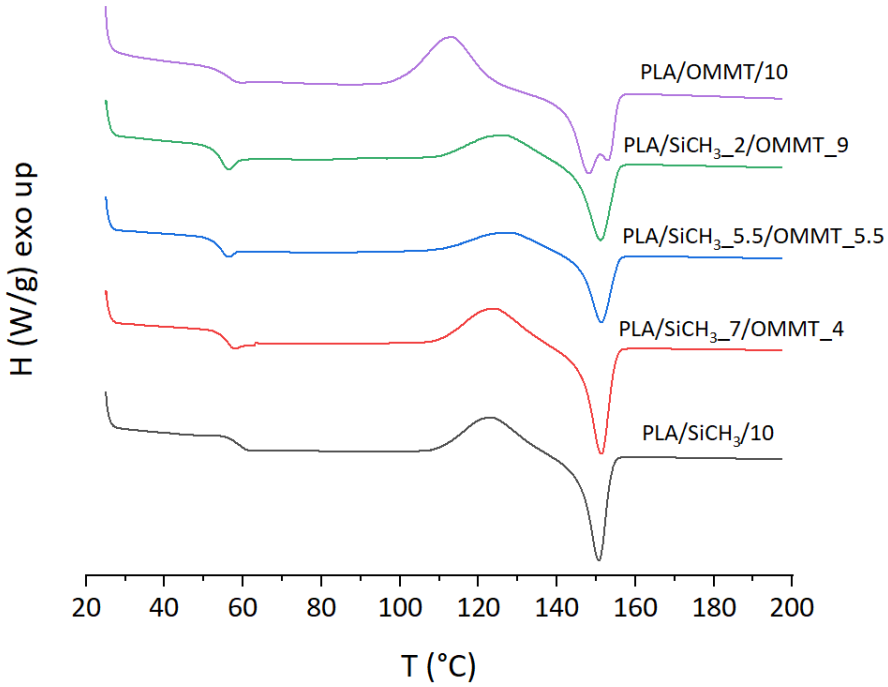


Figure B.1 - DSC thermograms of PLA/$SiCH_3$/OMMT nanocomposites series as well as PLA/$SiCH_3$/10 and PLA/OMMT/10.

To conclude, the presence of both silica and montmorillonite leads to higher cold crystallization temperature as well as an increase of the *RAF,* compared to silica or montmorillonite nanocomposites. These two parameters indicate a reduction of the chain mobility which can have an influence on permeability.

Table B.2 – Matrix properties of the PLA/$SiCH_3$/OMMT nanocomposites as well as PLA/OMMT/10, PLA/$SiCH_3$/10 and PLAref.

Sample	T_d (°C)	T_g (°C)	T_{cc} (°C)	T_m (°C)	χ_c (%)	RAF (%)
PLAref	348 ± 1	57± 1	103 ± 1	150 ± 2	0 ± 2	0 ± 6
PLA/$SiCH_3$/10	347 ± 1	56 ± 1	110 ± 1	150± 1	4 ± 2	4 ± 6
PLA/ $SiCH_3$_7/OMMT_4	347 ± 1	55± 1	124 ± 1	150± 1	5 ± 2	10 ± 6
PLA/ $SiCH_3$_5.5/OMMT_5.5	345 ± 1	54± 1	128 ± 1	151± 1	1 ± 2	14 ± 6
PLA/ $SiCH_3$_2/OMMT_9	343 ± 1	52± 1	127 ± 1	151 ± 1	5 ± 2	15 ± 6
PLA/OMMT/10	343 ± 1	52± 1	110 ± 1	151 ± 1	4 ± 2	5 ± 6

The dispersion of the fillers has been observed by transmission electronic microscopy (TEM). As evidenced by the TEM images presented in **Supplementary Figure B.1**, the PLA/$SiCH_3$

samples show a good dispersion of small silica aggregates (< 0.1 µm²) in the matrix up to 10 vol%. Concerning PLA/OMMT samples, there is the coexistence of quasi-individual sheets, small and middle size tactoïds (**Supplementary Figure B.2**) up to 10 vol%. The montmorillonite domains are thus homogeneously dispersed and randomly oriented in the matrix with a mean domain aspect ratio value around 85. For montmorillonite/silica nanocomposites, **Figure B.2** shows a homogenous dispersion of both fillers as observed for silica nanocomposites and montmorillonite nanocomposites, respectively. Nevertheless, it can be seen at higher magnification that montmorillonites seem to be embedded in silica domains and there are only a few separated silica or montmorillonite domains (**Figure B.2c**). This tendency has been observed in all the PLA/$SiCH_3$/OMMT samples as shown by additional TEM micrographs available in supporting information (**Supplementary Figure B.3**)

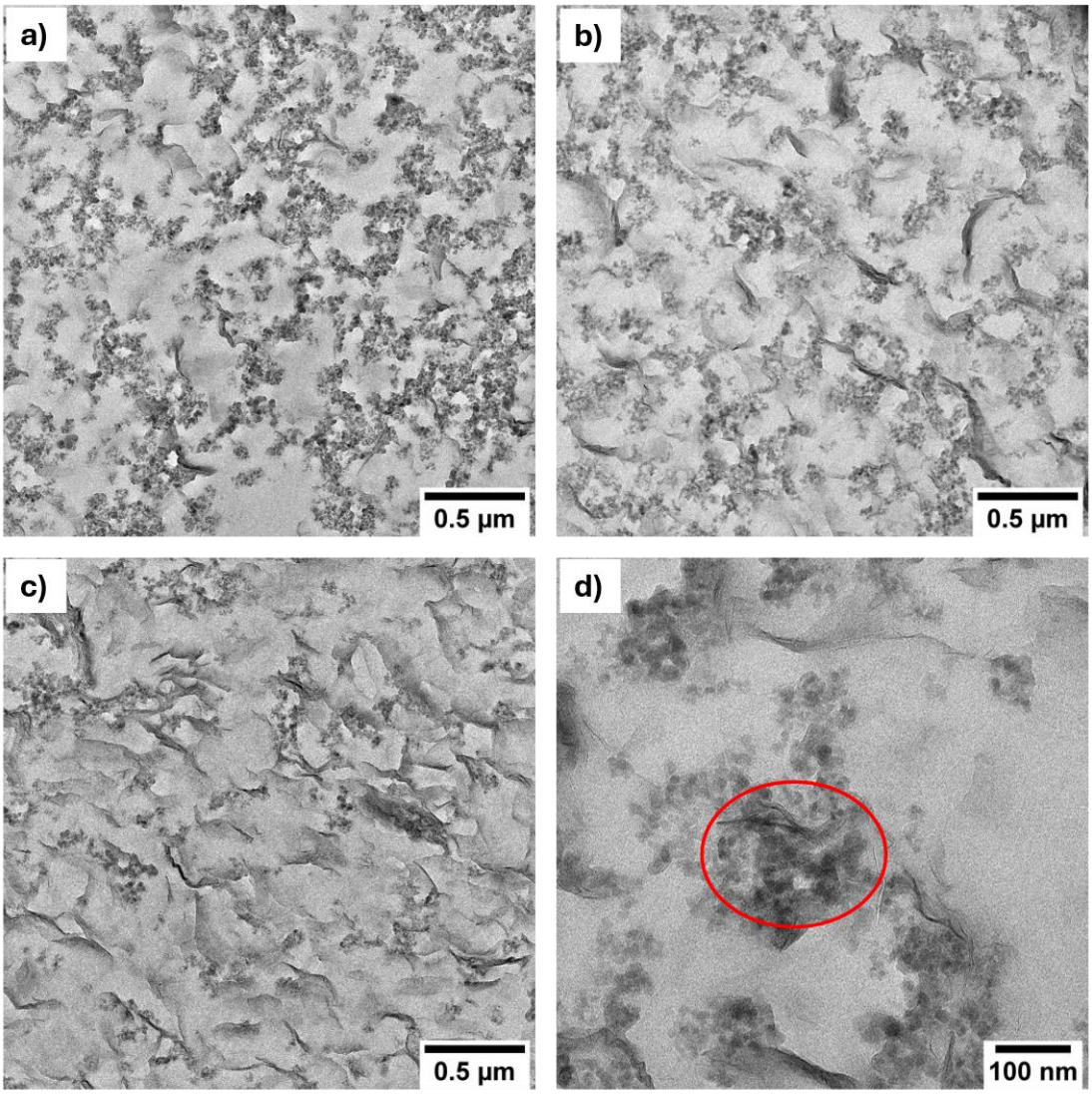


Figure B.2 - TEM micrographs from the cross section of PLA/SiCH3/OMMT nanocomposites at low magnification a) PLA/$SiCH_3$_7/OMMT_4, b) PLA/$SiCH_3$_5.5/OMMT_5.5, c) PLA/$SiCH_3$_2/OMMT_9 and at high magnification d) PLA/$SiCH_3$_5.5/OMMT_5.5.

4.1.b) Water vapor permeability of silica/montmorillonite nanocomposites

Silica and montmorillonite are known to behave as an impermeable phase over the small molecules such as water [3], [10], [23]. Thus, the water vapor permeability coefficients have been measured at 23 °C and 90 %RH on the different nanocomposites as well as on the unfilled PLA (PLAref) to analyze the effect of adding two fillers with respect to only one on the barrier properties. The water permeability values of the different samples are reported in **Figure B.3**. First it can be noticed that all nanocomposites have a permeability lower than the reference PLA (P_{PLAref} = 3,600 ± 150 barrer).

Silica enables to slightly improve the barrier properties of PLA (**Figure B.3**) with permeability going from 3,600 to 3,040 barrer for 10 vol% of silica. Such low decrease of the permeability has already been reported for spherical calcium carbonate nanoparticles in PLA [4] in case of oxygen permeability. On the contrary montmorillonite leads to a significant decrease of water permeability reaching 1,500 barrer for 10 vol% filler (**Figure B.3**). The high efficiency of montmorillonite on the barrier properties is often reported in the literature [9], [10], [24] and it is explained by a high mean aspect ratio of the impermeable dispersed domains when the montmorillonite sheets are well dispersed in the matrix.

The combination of silica and montmorillonite leads to a decrease of the permeability compared to the nanocomposite containing only silica with the same filler content (PLA/$SiCH_3$/10). Moreover, the permeability decreases further when the proportion of montmorillonite increases, reaching 1,450 barrer for PLA/$SiCH_3$_2/OMMT_9 (**Figure B.3**). These results can be attributed to the high aspect ratio of montmorillonite which increases further the tortuosity. Nevertheless, the permeability of the silica/montmorillonite nanocomposites is equal or higher than the permeability of PLA/OMMT/10. Moreover PLA/$SiCH_3$_5/OMMT_5 has a slightly higher permeability than PLA/OMMT/5. The evolution of permeability and the structure/properties relation will be discussed in a later part which will also enable to compare the results with another system, graphene/montmorillonite nanocomposites, which is the object of the next part.

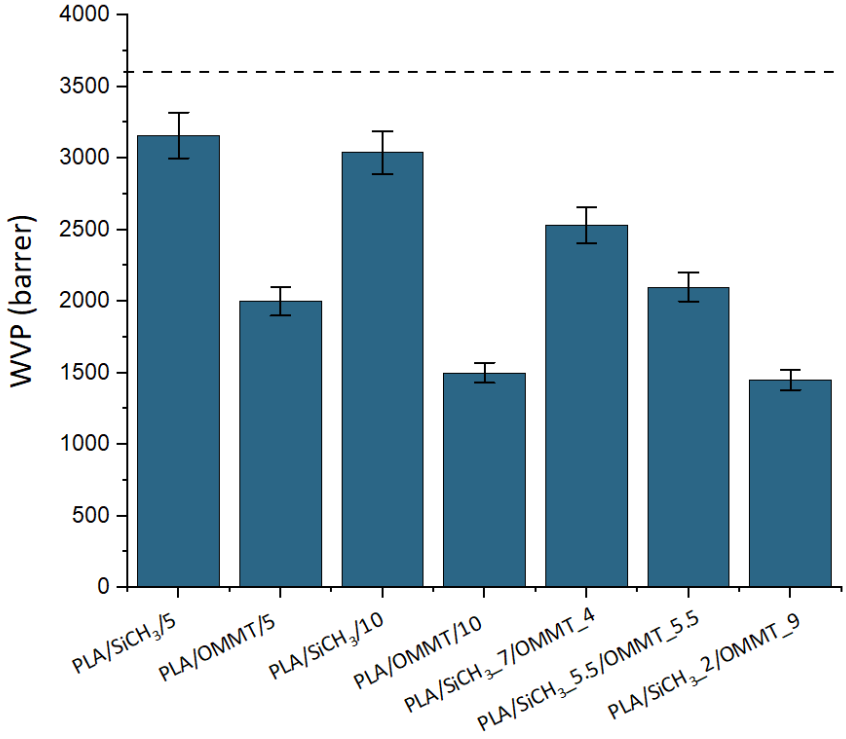


Figure B.3 - Water vapor permeability coefficients (WVP) at 23 °C, 90 %RH of the PLAref, PLA/$SiCH_3$/10, PLA/OMMT/10 and the PLA/$SiCH_3$/OMMT nanocomposites. The dotted line stands for the permeability of the unfilled PLA.

4.2. Graphene/montmorillonite nanocomposites

Graphene/montmorillonite nanocomposites were prepared with a global volume fraction of fillers between 10 and 11 vol% including 10 vol% of montmorillonites. The graphene content is very low (≤ 0.5 vol%) to avoid the formation of graphene agglomerates [20].

4.2.a) Characterization of graphene/montmorillonite nanocomposite films

The addition of montmorillonite with a low amount of graphene in PLA is not detrimental to thermal stability, as T_d is 344 ± 1 °C which is close to the T_d value of the neat PLA (348 ± 1 °C). The DSC thermograms (**Figure B.4**) of the graphene/montmorillonite systems show a glass transition, an exothermic peak associated to the cold crystallization and a melting peak similarly to the PLA/GNP nanocomposites and PLA/OMMT/10. The thermal properties of the samples are summarized in **Table B.3** and can be compared with those relative to the most highly filled nanocomposites of each type of filler (e.g: PLA/GNP/0.1, PLA/GNP/0.5 and PLA/OMMT/10).

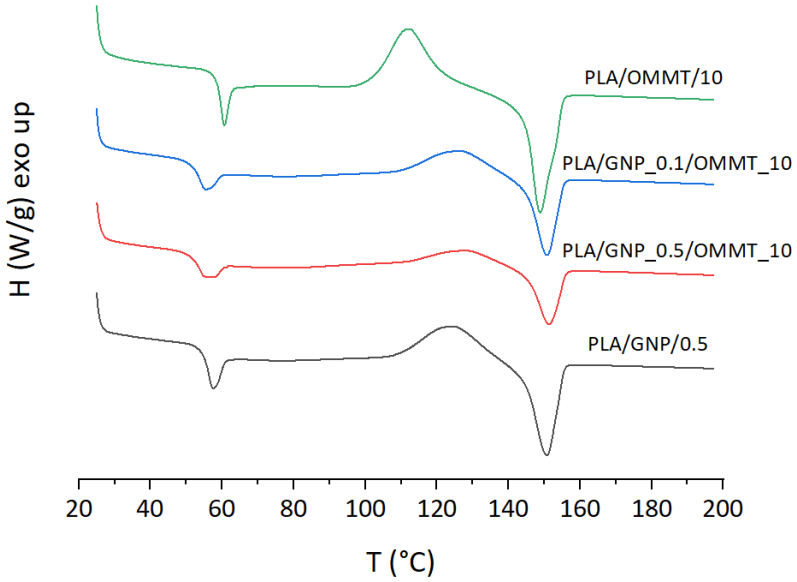


Figure B.4 - DSC thermograms of PLA/GNP/OMMT nanocomposites series as well as PLA/GNP/0.5 and PLA/OMMT/10.

The glass transition temperature (T_g) values of PLA/GNP/OMMT samples are governed by OMMT which is present in high amount with respect to GNP. Indeed, T_g values of the two fillers nanocomposites investigated here are equal to 52°C which is the value recorded for PLA/OMMT/10 (**Table B.3**). The cold crystallization temperature is higher for the PLA/GNP/OMMT samples than for PLA/GNP and PLA/OMMT. The melting temperature (T_m) is almost similar between the PLA/GNP, PLA/OMMT/10 and PLA/GNP/OMMT samples as reported by Bouakaz *et al.* [19]. Furthermore, it was checked that all the samples are amorphous. Finally, the *RAF* content is higher in presence of the two fillers, which reflect that the amorphous phase is more constrained when introducing montmorillonite with graphene, than with only one these fillers. Thus, as for silica/montmorillonite systems, the mobility of the PLA chains seems to be lower at the filler/matrix interface with the combination of montmorillonite and graphene, which can potentially influence permeability.

Table B.3 - Matrix properties of the PLA/GNP/OMMT nanocomposites as well as PLA/OMMT/10, PLA/GNP/0.1, PLA/GNP/0.5 and PLAref.

Sample	T_d (°C)	T_g (°C)	T_{cc} (°C)	T_m (°C)	χ_c (%)	RAF (%)
PLAref	348 ± 1	57± 1	103 ± 1	150 ± 2	0 ± 2	0 ± 6
PLA/GNP/0.1	346 ± 1	58 ± 1	102 ± 1	149 ± 1	1 ± 2	0 ± 6
PLA/GNP/0.5	346 ± 1	57 ± 1	102 ± 1	149 ± 1	1 ± 2	0 ± 6
PLA/GNP_0.1/OMMT_10	344 ± 1	52 ± 1	128 ± 1	151 ± 1	2 ± 2	9 ± 7
PLA/GNP_0.5/OMMT_10	344 ± 1	52 ± 1	126 ± 1	151 ± 1	3 ± 2	15 ± 8
PLA/OMMT/10	343 ± 1	52 ± 1	110 ± 1	151 ± 1	4 ± 2	5 ± 6

The dispersion state of graphene and montmorillonite fillers has been investigated by TEM. TEM images obtained at high magnification show that in PLA/OMMT/GNP samples (**Figure B.5**), the montmorillonite is well dispersed similarly to PLA/OMMT samples with the coexistence of quasi-individual sheets, small and middle size tactoïds. The presence of graphene is difficult to observe due to the very high content of montmorillonite compared to graphene and to the similar shape of these two lamellar fillers.

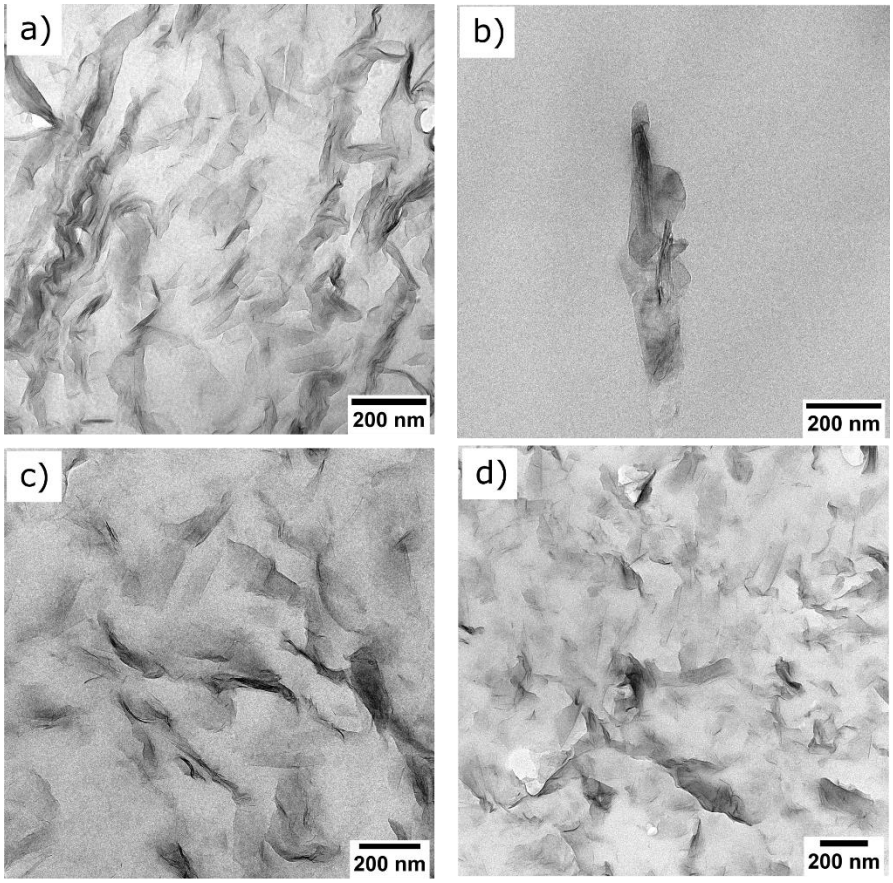


Figure B.5 - TEM micrographs from the cross section of (a) PLA/OMMT/10, (b) PLA/GNP/0.5, (c), PLA/GNP_0.1 /OMMT and (d) PLA/GNP_0.5/OMMT_10.

4.2.b) Water vapor permeability of graphene/montmorillonite nanocomposites

First it can be noticed that all nanocomposites have a permeability lower than the reference PLA (P_{PLAref} = 3600 ± 150 barrer). The addition of graphene in the PLA leads to a great decrease of permeability with a minimum value of 2,200 barrer for only 0.1 vol% of graphene, however beyond this content the permeability increases as seen in **Figure B.6**. The existence of an optimum graphene content in the same range has also been reported by Li *et al.* [12] and Pinto *et al.* [11] for optimized barrier properties. For montmorillonite, a significant decrease of the permeability up to 1,500 barrer is observed for 10 vol%. Concerning the nanocomposites containing graphene and montmorillonite, the permeability coefficient is below the one of PLA/GNP/0.1 and PLA/GNP/0.5 (**Figure B.6**). This means that the addition of montmorillonite enables to decrease the permeability of the graphene nanocomposites reaching 1,550 barrer for PLA/OMMT_10/GNP_0.1. However, the permeability of the

graphene/montmorillonite nanocomposites are close to the permeability of PLA/OMMT/10 ($P_{PLA/OMMT/10}$ = 1,500 ± 70 barrer).

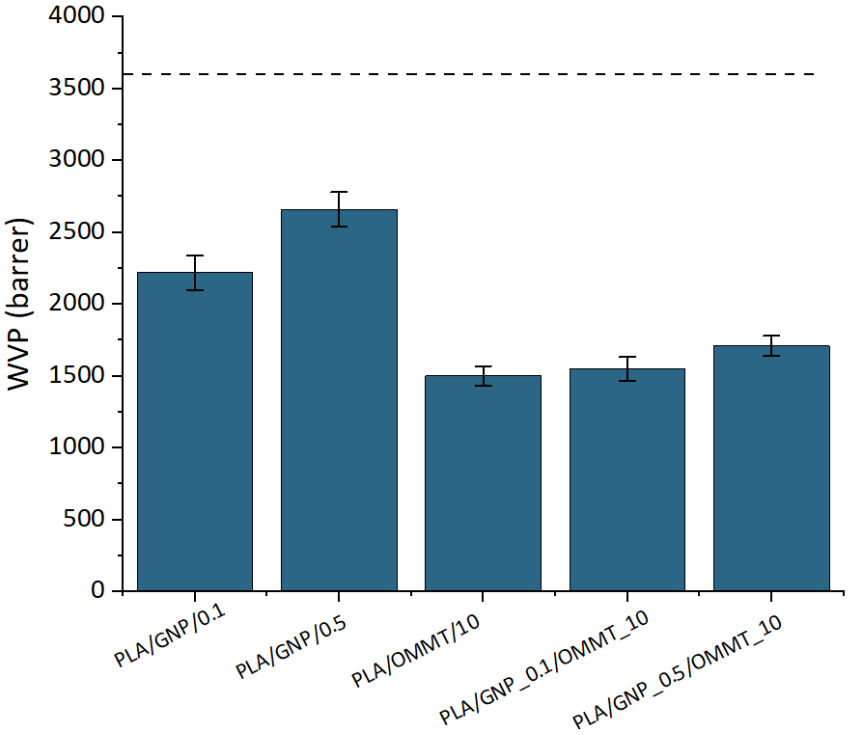


Figure B.6 - Water vapor permeability coefficient (WVP) at 23 °C, 90 %RH of the PLA/GNP, PLA/GNP/OMMT and PLA/OMMT/10 nanocomposites. The dotted line stands for the permeability of the unfilled PLA.

5. Discussion

In this part, the evolution of permeability of each system is related to the filler dispersion and the *RAF*, which are the two main factors changing significantly between the samples. Experimental permeability of the two-fillers systems will be compared to permeability models. This will enable to investigate whether the introduction of montmorillonites, as a second filler, has an independent effect regarding the other one, eg : silica or graphene.

The addition of montmorillonite in silica nanocomposites, for a global content of 10 vol% of fillers, leads to lower permeability compared to sample containing only 10 vol% of silica. However, the permeability of PLA/$SiCH_3$_5.5/OMMT/5 is a little bit higher than the permeability of PLA/OMMT/5, which is an unexpected result if we consider an additive contribution of each filler to the permeability decrease. To go deeper in the analysis of the

results in a extended range of silica/montmorillonite nanocomposite composition, a two step analysis was made.

First, the permeability of the PLA nanocomposites containing only silica (P_{SiCH3}) was calculated from the Maxwell model [25] (equation (B.6)) which has been shown to well describe the permeability of PLA/silica nanocomposites in our previous study [20].

$$P_{SiCH3} = P_{PLAref} \frac{1 - \Phi_v}{1 + 0.5\Phi_v} \qquad (B.6)$$

P_{PLAref} is the permeability of the unfilled PLA and Φ_v the volume fraction of silica.

Then the theoretical permeability of PLA/$SiCH_3$/OMMT samples has been determined by considering the role of the montmorillonite filler in a matrix whose permeability is P_{SiCH3}. As a random orientation of montmorillonite was evidenced by TEM analysis, Bharadwaj law [26] is used (equation (B.7)).

$$\frac{P}{P_{SiCH3}} = \frac{1 - \Phi_v}{1 + \frac{\alpha}{2}\Phi_v \frac{2}{3}\left(S + \frac{1}{2}\right)} \qquad (B.7)$$

The *S* parameter has been fixed to 0, corresponding to a random orientation of the montmorillonites in the matrix, Φ_v corresponds to the volume content of OMMT and α *is* the mean aspect ratio of the montmorillonite domains inside the matrix, previously determined by TEM analysis ($\alpha = 85$).

Figure B.7 shows in full line the theoretical permeability of the silica/montmorillonite nanocomposites ratioed to the theoretical permeability of the silica nanocomposite obtained by Maxwell law. The dotted line located at P/P_{SiCH3} equal to 1 is representative of the lonely effect of silica. Thus, the difference between these two curves represents the contribution of OMMT assuming an additive contribution of $SiCH_3$ and OMMT to the permeability. The points are representative of the experimental data obtained for silica/montmorillonite nanocomposites.

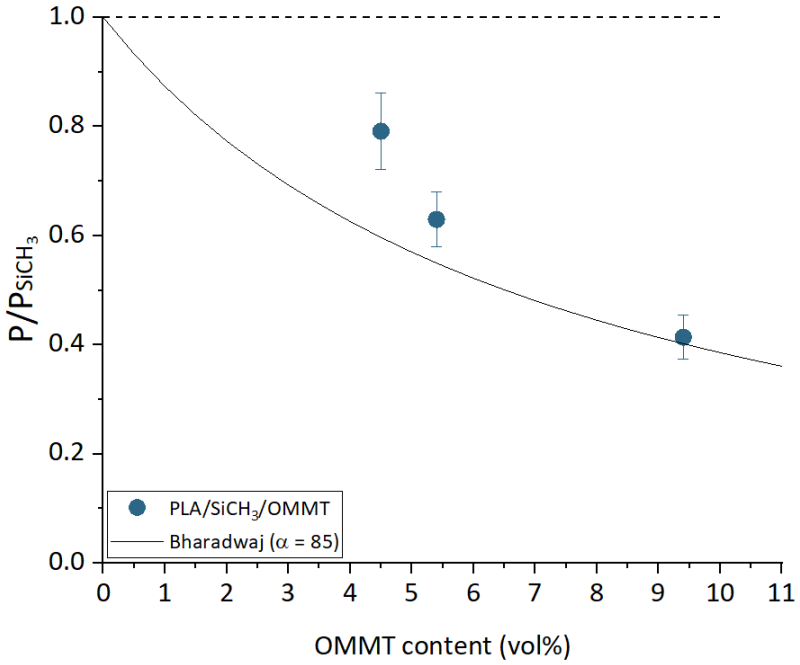


Figure B.7 - P/P_{SiCH3} of PLA/$SiCH_3$/OMMT nanocomposites. The solid line stands for the relative permeability calculated with the Bharadwaj model for an aspect of 85. The dotted line corresponds to a relative permeability of 1, which means no contribution of the montmorillonite.

It can be seen that the experimental values are below the dotted line, showing that OMMT brings an efficient contribution for permeability decrease, but above the curve in full line, meaning that the OMMT contribution is less than expected from an additivity law. These results can be related to the type of dispersed domains which consist in OMMT embedded in silica domains as reported by TEM observations, which would lead to a decrease of the tortuosity compared to samples containing only montmorillonite. Moreover, the increase of the *RAF* reported previously could be assigned in part to the polymer chains located in these domains, between the fillers, which could finally not play a role as important as expected.

Concerning the nanocomposites based on graphene and montmorillonite, it has been shown that the addition of 10 vol% montmorillonite in nanocomposites based on 0.1 or 0.5 vol% GNP allows to decrease further the permeability with respect to PLA/GNP. However, the permeability of the PLA/GNP/OMMT nanocomposite is equal or slightly higher than the permeability of the PLA/OMMT having the same montmorillonite content (i.e: 10 vol%) which could appear as surprising. One of the hypotheses to explain this result would be that the dispersed filler domains could contain both graphene and montmorillonite. This hypothesis is supported by the fact that GNP are graphene oxide and thus some hydrogen bonds can be

formed between the OMMT and GNP [27]. In that case, the aspect ratio of the dispersed filler domains would be much less important than that of individual graphene platelets but in the same order of magnitude than pure OMMT domains. Here again, the slight increase of *RAF* appears to not play a major role on permeability.

6. Conclusion

In this work, the addition of montmorillonite in amorphous PLA nanocomposites films has been investigated, focusing on two distinct systems: silica/montmorillonite and graphene/montmorillonite. The morphology and permeability of these hybrid nanocomposites have been compared those of the films containing exclusively either silica, montmorillonite or graphene. All the systems were prepared via melt-blending and thermo-compression. The presence of two fillers results in a slight increase of the *RAF* for both systems, which reflects a decrease of the chain mobility in comparison with the respective one filler-based nanocomposites. Concerning the nanocomposite morphology, it was observed a homogeneous dispersion of small filler domains for all samples. Whereas some montmorillonite platelets were clearly observed within the silica domains, it was more challenging to distinguish the graphene sheets from the montmorillonites. The permeability of silica/montmorillonite samples containing 10 vol% of total fillers was systematically lower than the permeability of the nanocomposite containing 10 vol% of silica. However, the effect of adding OMMT was less important than the one predicted by additive law. This behavior was related to the presence of both montmorillonite and silica in the filler domains which decreases the tortuosity compared to the presence of only montmorillonite. The graphene/montmorillonite nanocomposites had enhanced barrier properties with respect to nanocomposites only based on graphene. This is an interesting behavior as increasing the graphene content usually leads to a loss of barrier properties. Thus, by adding another type of lamellar filler, it was possible to increase both the filler content and barrier properties. Nevertheless, no additive effect was observed and the graphene/montmorillonite nanocomposites exhibited permeability close to the sample filled with only montmorillonite. One of the hypotheses to explain this result is that the dispersed filler domains could contain both graphene and montmorillonite leading to filler domain aspect ratio close to the one of

purely montmorillonite domains. All in all, although the addition of montmorillonite does not lead to an additive effect on permeability, it enables to bring a significant contribution to barrier properties enhancement of hydrophobic silica and graphene nanocomposites.

7. References

[1] M. Labonté, C. Dubois, Processing of Impact Modifed PLA in a Continous Process at High Speed: Comparison with PET Molding Conditions – A New Era, Polymer-Plastics Technology and Engineering 54 (2015) 368–374. https://doi.org/10.1080/03602559.2014.958774.

[2] S. Farah, D.G. Anderson, R. Langer, Physical and mechanical properties of PLA, and their functions in widespread applications — A comprehensive review, Advanced Drug Delivery Reviews 107 (2016) 367–392. https://doi.org/10.1016/j.addr.2016.06.012.

[3] S. Singha, M.S. Hedenqvist, A Review on Barrier Properties of Poly(Lactic Acid)/Clay Nanocomposites, Polymers 12 (2020) 1095. https://doi.org/10.3390/polym12051095.

[4] F. Morel, E. Espuche, V. Bounor-Legaré, O. Persynn, M. Lacroix, Impact of coated calcium carbonate nanofillers and annealing treatments on the microstructure and gas barrier properties of poly(lactide) based nanocomposite films, Journal of Polymer Science Part B: Polymer Physics 54 (2016) 649–658. https://doi.org/10.1002/polb.23957.

[5] M.A. Ortenzi, L. Basilissi, H. Farina, G. Di Silvestro, L. Piergiovanni, E. Mascheroni, Evaluation of crystallinity and gas barrier properties of films obtained from PLA nanocomposites synthesized via "in situ" polymerization of l-lactide with silane-modified nanosilica and montmorillonite, European Polymer Journal 66 (2015) 478–491. https://doi.org/10.1016/j.eurpolymj.2015.03.006.

[6] C. Fan, H. Chi, C. Zhang, R. Cui, W. Lu, M. Yuan, Y. Qin, Effect of multiscale structure on the gas barrier properties of poly(lactic acid)/Ag nanocomposite films, Polymers for Advanced Technologies 30 (2019) 1709–1715. https://doi.org/10.1002/pat.4601.

[7] Y. Guo, K. Yang, X. Zuo, Y. Xue, C. Marmorat, Y. Liu, C.-C. Chang, M.H. Rafailovich, Effects of clay platelets and natural nanotubes on mechanical properties and gas permeability of Poly (lactic acid) nanocomposites, Polymer 83 (2016) 246–259. https://doi.org/10.1016/j.polymer.2015.12.012.

[8] W.L. Tham, B.T. Poh, Z.A. Mohd Ishak, W.S. Chow, Transparent poly(lactic acid)/halloysite nanotube nanocomposites with improved oxygen barrier and antioxidant properties, J Therm Anal Calorim 126 (2016) 1331–1337. https://doi.org/10.1007/s10973-016-5834-7.

[9] N. Tenn, N. Follain, J. Soulestin, R. Crétois, S. Bourbigot, S. Marais, Effect of Nanoclay Hydration on Barrier Properties of PLA/Montmorillonite Based Nanocomposites, J. Phys. Chem. C 117 (2013) 12117–12135. https://doi.org/10.1021/jp401546t.

[10] E. Picard, E. Espuche, R. Fulchiron, Effect of an organo-modified montmorillonite on PLA crystallization and gas barrier properties, Applied Clay Science 53 (2011) 58–65. https://doi.org/10.1016/j.clay.2011.04.023.

[11] A.M. Pinto, J. Cabral, D.A.P. Tanaka, A.M. Mendes, F.D. Magalhães, Effect of incorporation of graphene oxide and graphene nanoplatelets on mechanical and gas permeability properties of poly(lactic acid) films, Polymer International 62 (2013) 33–40. https://doi.org/10.1002/pi.4290.

[12] F. Li, C. Zhang, Y. Weng, X. Diao, Y. Zhou, X. Song, Enhancement of Gas Barrier Properties of Graphene Oxide/Poly (Lactic Acid) Films Using a Solvent-free Method, Materials 13 (2020) 3024. https://doi.org/10.3390/ma13133024.

[13] E. Espino-Pérez, J. Bras, V. Ducruet, A. Guinault, A. Dufresne, S. Domenek, Influence of chemical surface modification of cellulose nanowhiskers on thermal, mechanical, and barrier properties of poly(lactide) based bionanocomposites, European Polymer Journal 49 (2013) 3144–3154. https://doi.org/10.1016/j.eurpolymj.2013.07.017.

[14] R. Kumar, S. Kumari, B. Rai, R. Das, G. Kumar, Effect of nano-cellulosic fiber on mechanical and barrier properties of polylactic acid (PLA) green nanocomposite film, Mater. Res. Express 6 (2019). https://doi.org/10.1088/2053-1591/ab5755.

[15] A. Bendahou, H. Kaddami, E. Espuche, F. Gouanvé, A. Dufresne, Synergism Effect of Montmorillonite and Cellulose Whiskers on the Mechanical and Barrier Properties of Natural Rubber Composites, Macromolecular Materials and Engineering 296 (2011) 760–769. https://doi.org/10.1002/mame.201000444.

[16] S.A. Oleyaei, H. Almasi, B. Ghanbarzadeh, A.A. Moayedi, Synergistic reinforcing effect of TiO2 and montmorillonite on potato starch nanocomposite films: Thermal, mechanical and barrier properties, Carbohydrate Polymers 152 (2016) 253–262. https://doi.org/10.1016/j.carbpol.2016.07.040.

[17] P. Cheviron, F. Gouanvé, E. Espuche, Preparation, characterization and barrier properties of silver/montmorillonite/starch nanocomposite films, Journal of Membrane Science 497 (2016) 162–171. https://doi.org/10.1016/j.memsci.2015.09.039.

[18] J. Trifol, D. Plackett, C. Sillard, P. Szabo, J. Bras, A.E. Daugaard, Hybrid poly(lactic acid)/nanocellulose/nanoclay composites with synergistically enhanced barrier properties and improved thermomechanical resistance, Polymer International 65 (2016) 988–995. https://doi.org/10.1002/pi.5154.

[19] B.S. Bouakaz, I. Pillin, A. Habi, Y. Grohens, Synergy between fillers in organomontmorillonite/graphene–PLA nanocomposites, Applied Clay Science 116–117 (2015) 69–77. https://doi.org/10.1016/j.clay.2015.08.017.

[20] A. Jullin, G. Sudre, N. Hascoët, F. Chinesta, E. Espuche, Influence of different type of impermeable phase on the permeability of PLA films : nanofillers versus crystalline phase, Polymer Testing (Submitted) (2024).

[21] B. Kalb, A.J. Pennings, General crystallization behaviour of poly(l-lactic acid), Polymer 21 (1980) 607–612. https://doi.org/10.1016/0032-3861(80)90315-8.

[22] E. Kontou, M. Niaounakis, P. Georgiopoulos, Comparative study of PLA nanocomposites reinforced with clay and silica nanofillers and their mixtures, Journal of Applied Polymer Science 122 (2011) 1519–1529. https://doi.org/10.1002/app.34234.

[23] B. Tan, N.L. Thomas, A review of the water barrier properties of polymer/clay and polymer/graphene nanocomposites, Journal of Membrane Science 514 (2016) 595–612. https://doi.org/10.1016/j.memsci.2016.05.026.

[24] S. Sinha Ray, K. Yamada, M. Okamoto, Y. Fujimoto, A. Ogami, K. Ueda, New polylactide/layered silicate nanocomposites. 5. Designing of materials with desired properties, Polymer 44 (2003) 6633–6646. https://doi.org/10.1016/j.polymer.2003.08.021.

[25] J.C. Maxwell, A Treatise on Electricity and Magnetism, Clarendon Press, 1873.

[26] R.K. Bharadwaj, Modeling the Barrier Properties of Polymer-Layered Silicate Nanocomposites, Macromolecules 34 (2001) 9189–9192. https://doi.org/10.1021/ma010780b.

[27] Y.-X. An, W.-J. Qu, P.-Z. Yu, J.-G. Lü, The assembly of a composite based on nano-sheet graphene oxide and montmorillonite, Pet. Sci. 15 (2018) 366–374. https://doi.org/10.1007/s12182-018-0216-3.

Conclusion

Ce chapitre était consacré à l'étude de la perméabilité dans des matrices PLA contenant deux phases imperméables.

Une première partie a permis d'étudier l'influence du procédé sur la perméabilité de nanocomposites semi-cristallins. L'incorporation de charges par voie solvant a conduit à de plus faibles perméabilités que le PLA non chargé préparé avec le même procédé. Au contraire, le traitement thermique de films nanocomposites amorphes n'a pas permis de diminuer la perméabilité par rapport au PLA semi-cristallin, à l'exception de films chargés avec des montmorillonites. La dispersion des charges n'a pas suffi à expliquer les différences de perméabilité. Une interface charge/matrice faible pour les nanocomposites semi-cristallins à base de silice, d'halloysite ou d'oxyde de graphène ayant subi un traitement thermique de cristallisation froide a été avancée comme la cause probable de perte de propriétés barrière. Ainsi, en fonction du type de charge et du procédé utilisé pour élaborer des nanocomposites semi-cristallins, on peut avoir soit un effet additif de la phase cristalline et des charges, soit au contraire un effet antagoniste dû à la dégradation de l'interface charge/matrice. Par ailleurs, les nanocomposites semi-cristallins obtenus après traitement thermique ont tout de même une perméabilité plus faible que les échantillons préparés par voie solvant, sauf pour le graphène, en particulier dû à un taux de cristallinité plus élevé de la matrice PLA.

Puis, une seconde partie a comparé l'effet de l'association de montmorillonite à de la silice ou à de l'oxyde de graphène sur la perméabilité pour un taux de charges global proche de 10 %vol. Cette étude a montré que l'ajout de montmorillonite permet d'améliorer, pour les nanocomposites étudiés, les propriétés barrière des systèmes PLA/silice et PLA/graphène. Cependant l'effet relevé sur la perméabilité est inférieur à un effet additif. En effet, de par la création de domaines dispersés mixtes, il s'avère que l'effet de tortuosité est moins marqué.

Ainsi la présence de deux phases imperméables n'est pas forcément favorable pour les propriétés barrière sauf dans le cas de nanocomposites semi-cristallins chargés avec des montmorillonites élaborés par mélange en voie fondue puis traité à 120 °C pendant 24 h. Dans ce cas une diminution de la perméabilité du PLA par un facteur 10 est obtenue.

Les résultats des deux chapitres expérimentaux III et IV concernent seulement des matériaux à base de PLA, qui ont permis de comparer différents procédés de mise en œuvre ainsi que de jouer sur la cristallinité. De ce fait, un large panel de morphologies et de microstructures a pu être étudié et mis en lien avec la perméabilité. Mais observe-t-on les mêmes tendances avec d'autres matrices ? Est-ce que la diminution de perméabilité obtenue avec l'ajout de charges dépend de la perméabilité initiale de la matrice et par conséquent de la nature de la matrice? Le prochain chapitre s'attachera à répondre à ces questions en utilisant des modèles machine learning déjà utilisés avec succès dans le cas du PLA (cf. chapitre III.C). Dans ce cadre, il a également été incorporé à la base de données des données relatives à des nanocomposites à charges nanocellulosiques.

Supporting information Chapitre IV :

Design de nanocomposites PLA contenant deux phases imperméables

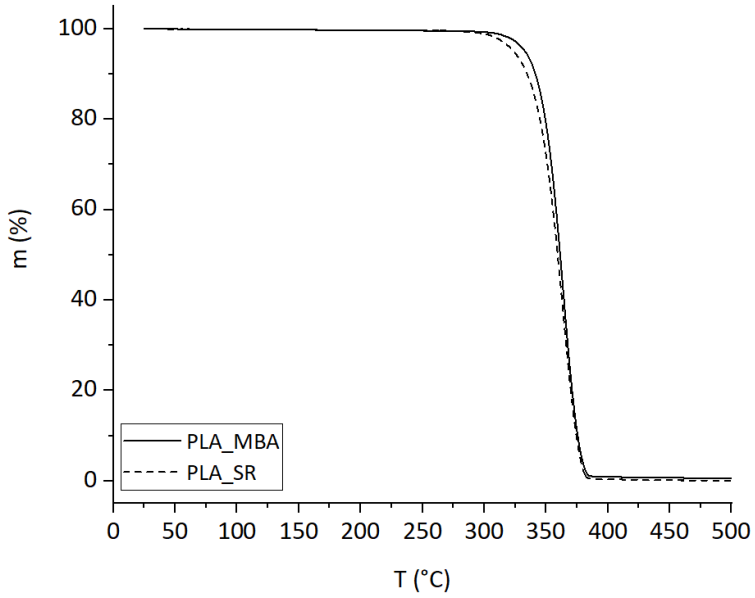
Supplementary information IV.A _____ *286*

Supplementary information IV.B _____ *290*

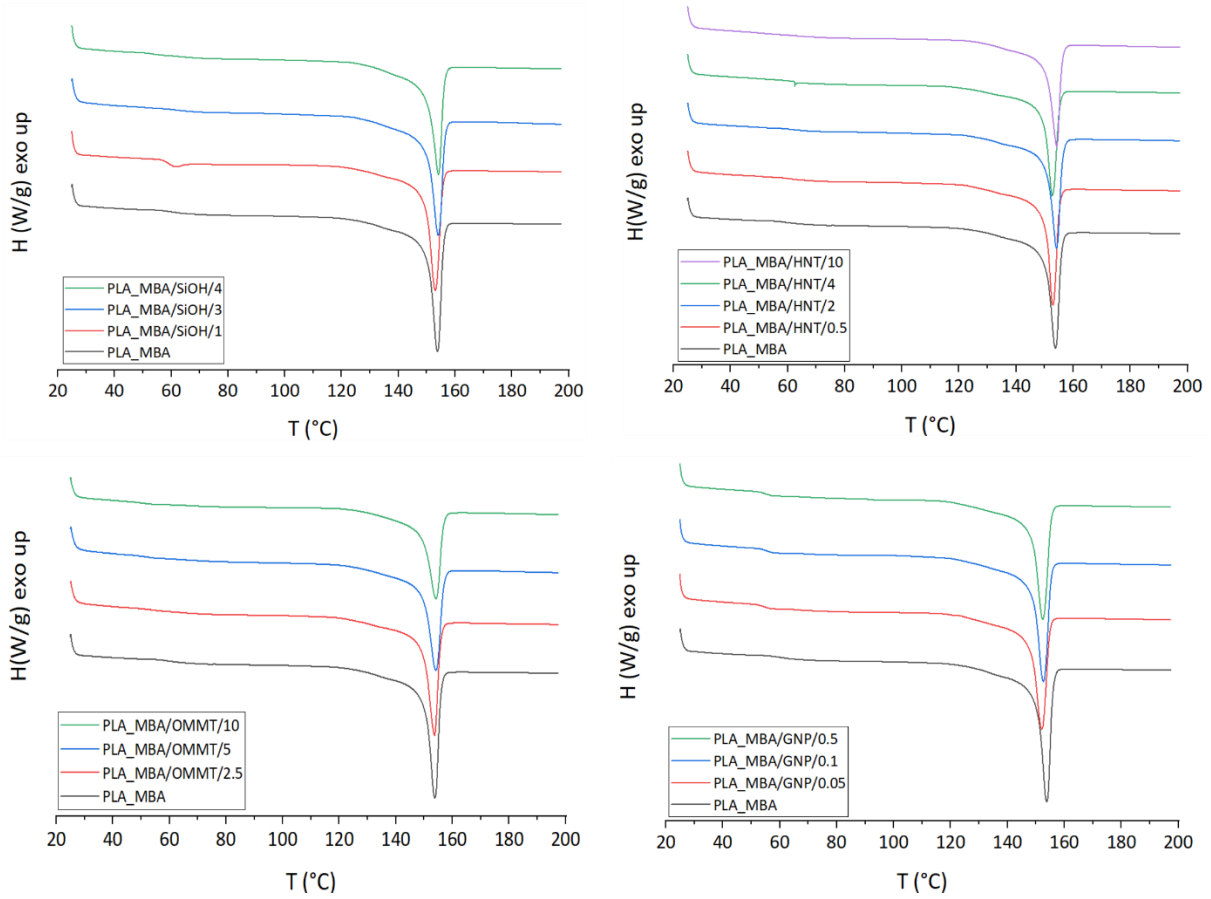
Supplementary information IV.A:

Influence of the process on the permeability of semi-crystalline PLA nanocomposites: solvent casting versus annealing of melt-blended films

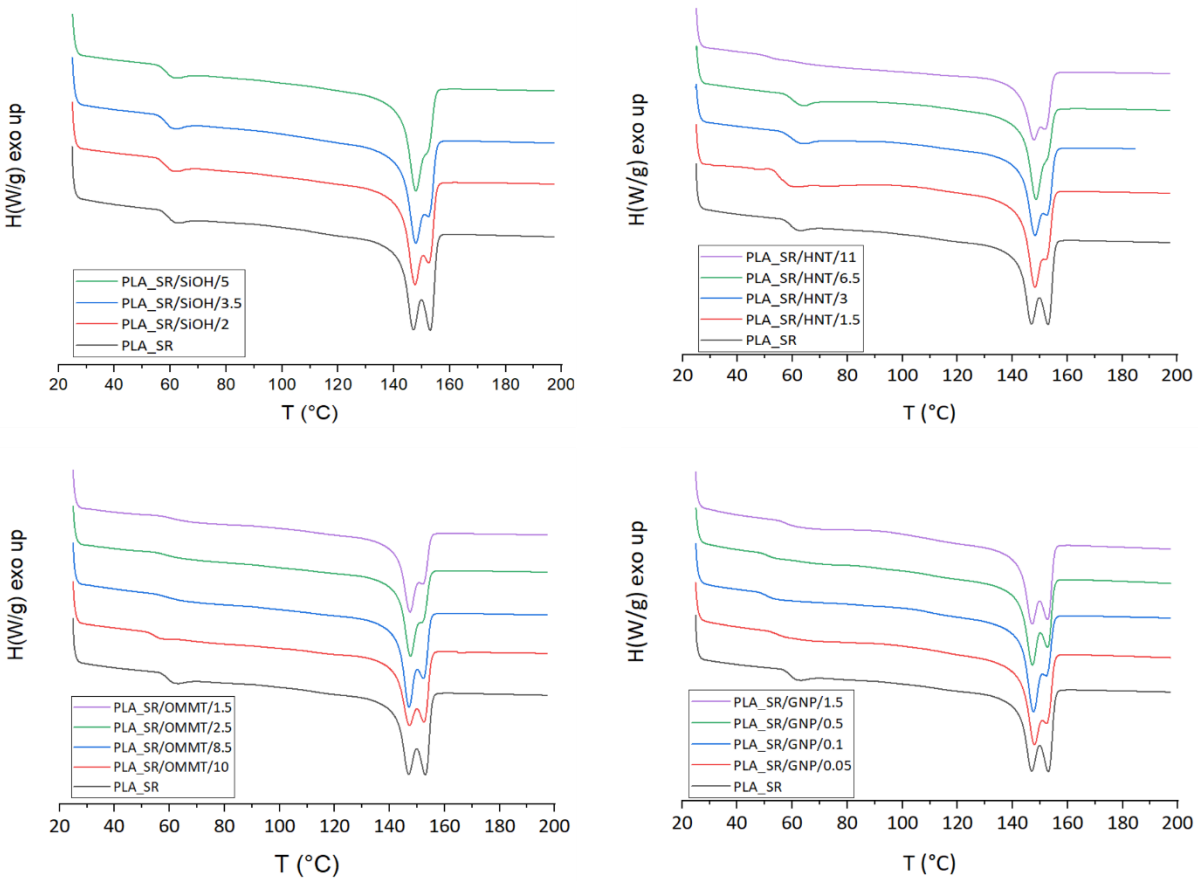
---



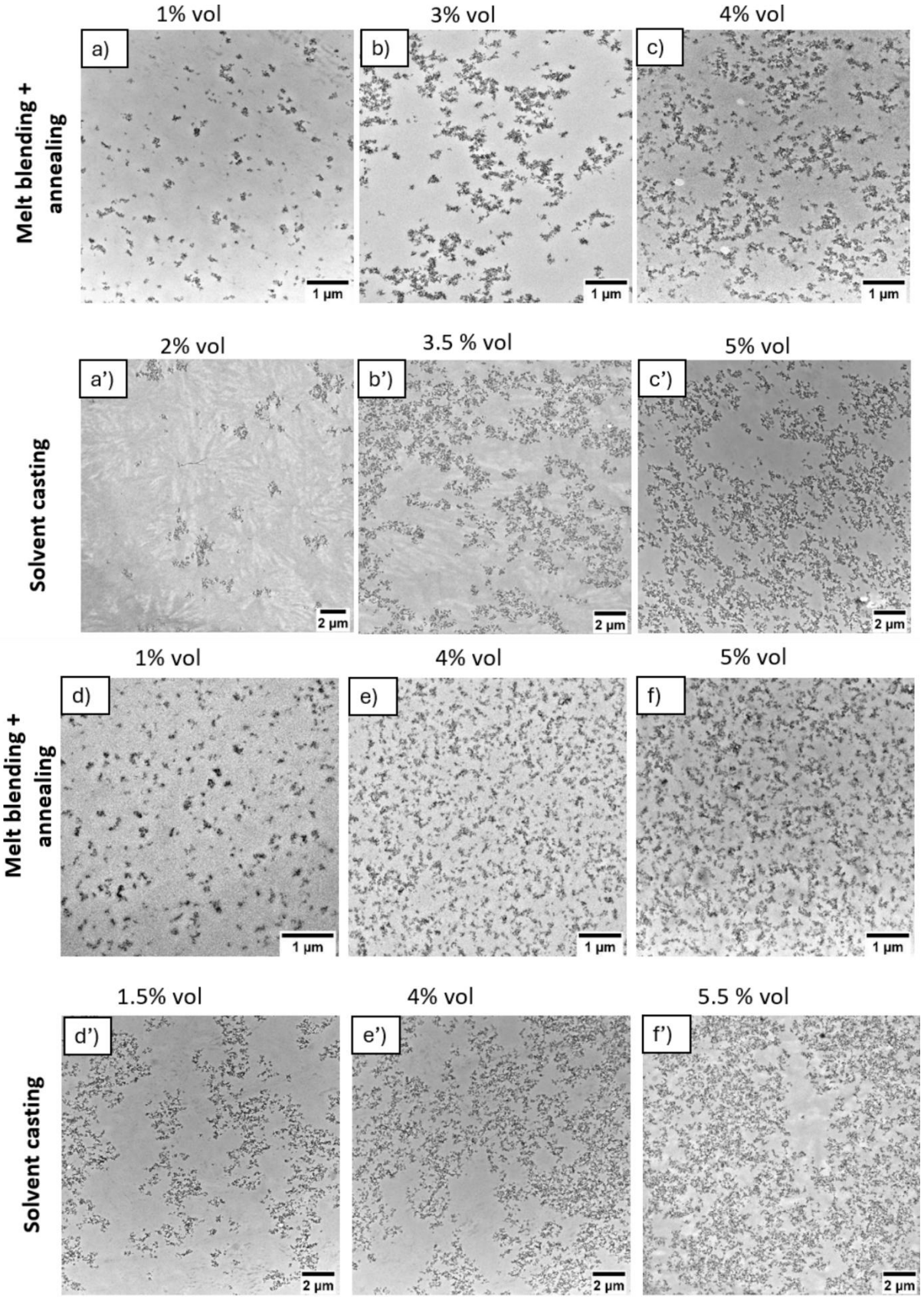
Supplementary Figure A.1- TGA thermogram under nitrogen @ 10 °C/min of the PLA films prepared by met-blending/annealing (PLA_MBA) and by solvent casting (PLA_SR).



Supplementary Figure A.2 - DSC thermograms @10 °C/min of nanocomposites prepared by melt-blending and annealed (PLA_MBA series).



Supplementary Figure A.3 - DSC thermograms @10 °C/min of nanocomposites prepared by solvent route (PLA_SR series).

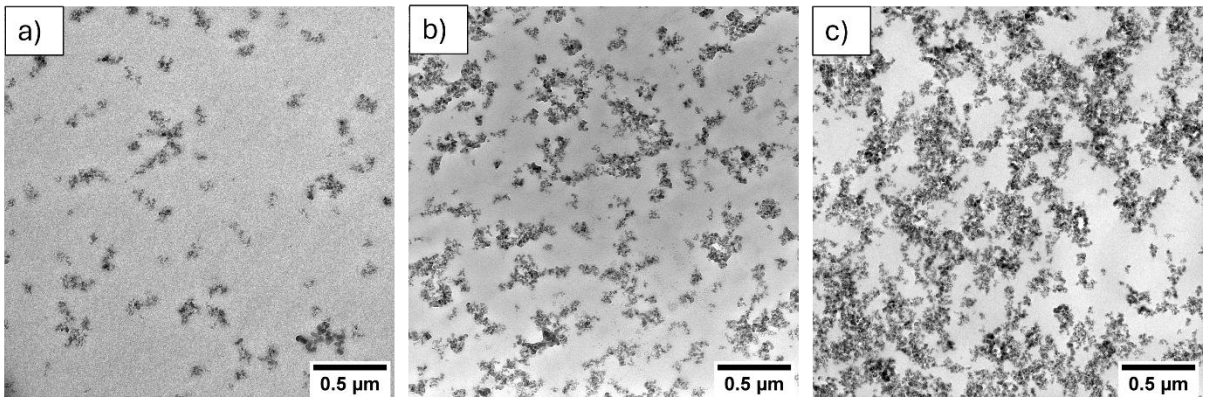


Supplementary Figure A.4 - TEM micrographs of cross sections of nanocomposites containing hydrophilic silica: a, b, c) PLA_MBA/SiOH and a', b', c') PLA_SR/SiOH; or hydrophobic silica d ,e, f) PLA_MBA/$SiCH_3$ d', e', f') PLA_SR/$SiCH_3$.

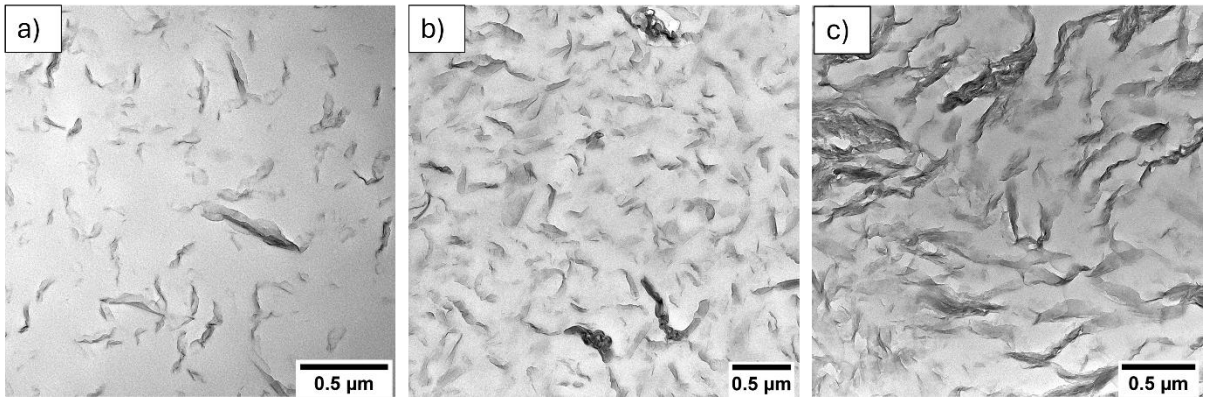
Supplementary information IV.B:

Adding montmorillonite in PLA/silica and PLA/graphene nanocomposites: influence on nanocomposite morphology and barrier properties

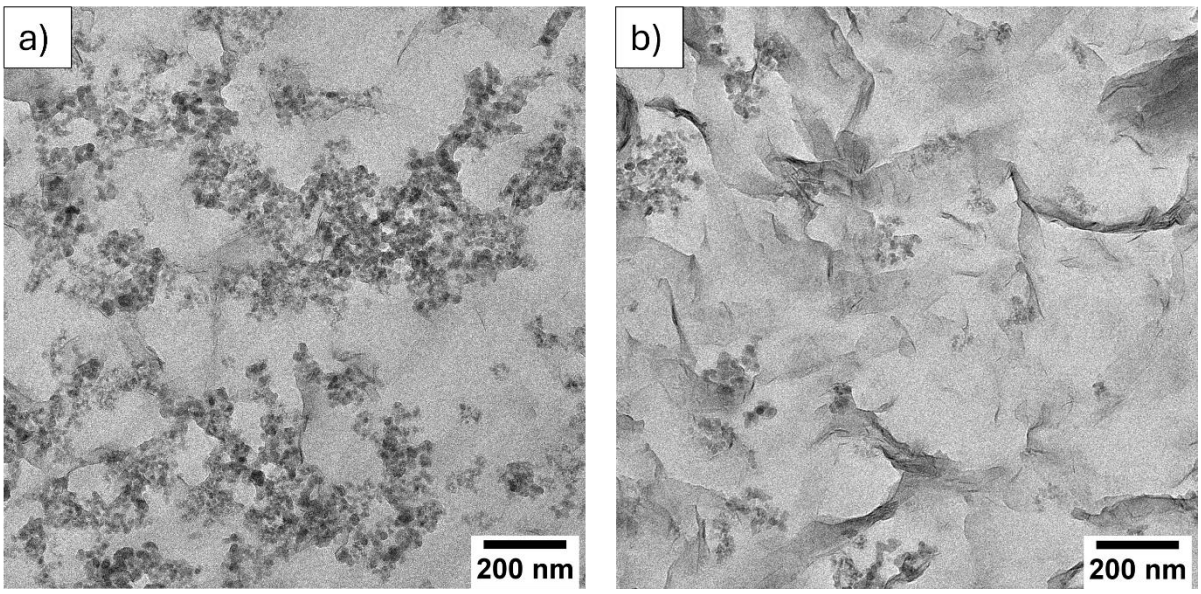
---



Supplementary Figure B.1 - TEM micrographs of hydrophobic silica nanocomposite containing (a) 1 vol%, (b) 5 vol% and (c) 10 vol% of silica.



Supplementary Figure B.2 - TEM micrographs of montmorillonite nanocomposite containing (a) 2.5 vol%, (b) 5 vol% and (c) 10 vol% of filler.



Supplementary Figure B.3 - TEM micrograph of silica/montmorillonite nanocomposites at high magnification (a) PLA/$SiCH_3$_7/OMMT_4 and (b) PLA/$SiCH_3$_2/OMMT_9.

Chapitre V

Design of high barrier properties polymer nanocomposites with machine learning

Chapitre V - Design of high barrier properties polymer nanocomposites with machine learning

1. Objectif ____ *295*

2. Abstract ____ *296*

3. Introduction ____ *296*

4. Methods ____ *298*

4.1. Dataset ____ 298

4.2. Modelling ____ 301

5. Results and discussion ____ *302*

5.1. Statistical analysis of the data set ____ 302

5.2. Machine learning predictions of relative permeability ____ 305

5.3. Assisted design of polymer nanocomposites with the Random Forest ____ 308

6. Conclusion ____ *311*

7. References ____ *313*

1. Objectif

L'objectif de ce chapitre est d'étudier la perméabilité de nanocomposites pour des matrices polymères de différentes compositions chimiques dans une approche de machine learning. Pour cela, des données ont été collectées dans la littérature permettant de couvrir une vaste gamme de nanocomposites. Il est à noter que pour cette étude, nous nous sommes limités à l'effet d'une seule charge introduite dans les échantillons.

Les études précédentes ont montré que la perméabilité dépend de multiples facteurs comme la fraction volumique de charges, le facteur de forme, le type de charges, mais aussi de paramètres relatifs à la dispersion des charges, à la mobilité des chaines polymères, à la masse molaire, au bout de chaines, à l'interface charge/matrice… Cependant ces données ne sont pas forcément disponibles dans la littérature, il a donc fallu choisir des paramètres plus généraux qui décrivent et discriminent au mieux chacun des systèmes.

Ainsi les charges ont été décrites par leur forme (sphères, formes allongées, lamelles) et leur facteur de forme initial ainsi que la fraction volumique. De plus, la polarité des charges a été ajoutée pour rendre compte des possibles affinités avec les matrices polymère pour lesquelles les propriétés ont été résumées à l'énergie de surface et à la perméabilité au dioxygène. Le procédé de mise en oeuvre des nanocomposites a également été renseigné. Il est à noter le manque d'informations accessibles quant à la morphologie des systèmes. La démarche adoptée en machine learning est similaire à celle présentée précédemment dans le chapitre III.C qui traite du cas du PLA. Ainsi, une base de données de 220 échantillons a été construite à partir de données collectées, issues de 31 publications, et de notre plateforme de nanocomposites.

Ce chapitre s'attachera donc à entrainer des modèles de machine learning, à partir de la base de données constituée, afin d'essayer de prédire au mieux la perméabilité de nanocomposites à partir des paramètres évoqués précédemment. Enfin le but sera d'utiliser ces modèles pour suggérer des combinaisons de paramètres permettant d'atteindre une certaine perméabilité. Ce chapitre est écrit sous la forme d'un article.

2. Abstract

In this study, two machine learning models, namely Random Forest and Support Vector Machine, have been trained to predict the relative permeability of polymer-based nanocomposites. A large range of matrices have been used in this work, going from amorphous to semi-crystalline polymers and from rubbery to glassy polymers. Moreover, different fillers with distinct shape (spherical, elongated, lamellar), size and chemical nature have been considered. Additionally, the most prevalent techniques for the synthesis of nanocomposites (eg: melt-blending, solvent casting and *in situ* polymerization) were also studied. The Random Forest gives the better accurate predictions with a mean absolute error of 10% and a R^2 of 0.78. The model was then employed to suggest some design of nanocomposites for targeted relative permeability. To the best of our knowledge, it is the first time that machine learning (ML) is used to predict the permeability of such a diverse range of polymer nanocomposites.

3. Introduction

Currently, there is a considerable demand for high-gas barrier polymer materials as this specific property is required for a large range of applications including packaging, gas storage, gas distribution… [1]. The incorporation of fillers into polymer matrices appears to be an efficient way for enhancing the barrier properties. Indeed, it has been shown that the incorporation of impermeable fillers is an effective method to create a tortuosity effect which results in a reduction of the permeability [2], [3]. Nevertheless, the performance of the nanocomposites depends on numerous parameters going from the choice of the polymer/filler couple, the filler shape and content, the method of preparation, the morphology…. [4] which must be optimized without harming others. Testing the effect of each parameter and the possible interrelations in an experimental approach, consisting in the preparation of designed materials and their deep characterization, is time consuming and expensive. Alternatively, an estimation of the permeability can be calculated from empirical permeability models (Nielsen, Bharadwaj...)[5], [6] or by using finite element modelling [7], [8], [9]. However, although these models are suitable for ideal systems, they generally fail to take account of the complexity of real materials. Thus, the ability to predict permeability of nanocomposite materials from a minimal number of parameters is a significant challenge

either to adapt the material design to the required function or even to extend the material performance in terms of barrier properties. Machine learning (ML) is more and more used to solve complex problems depending on lot of parameters and where some of them can be potentially interrelated. In the polymer nanocomposites field, ML has already been reported to be an efficient method to predict different targeted properties [10] . For example ML was successfully used for the predictions of mechanical properties of low density polyethylene/graphene [11], polyethertherketone/graphene [12] and epoxy/alumina [13] or thermal conductivity of low density polyethylene/graphene nanocomposites [11]. The targeted properties are predicted from the content of each component and/or from the processing conditions by using Artificial Neural Network and some encouraging results with high correlation coefficient have been obtained [11], [12], [13]. Furthermore, ML can also be used to predict the possible parameters that may lead to a targeted permeability. Indeed, ML methods have already been used to predict permeability to a variety of gas of a wide range of homopolymer or copolymer from their chemical structure or "fingerprint" [14], [15]. The authors show good accuracy of predictions compared to experimental values. Moreover, a first study has been realized on the use of ML to predict the permeability of a platform of polylactic acid (PLA) nanocomposites. It has been shown that ML is a promising tool to predict permeability from a set of carefully selected parameters [16].

The objective of this study is to take advantage of ML models to extend the prediction of nanocomposites permeability across a broader range of matrices. To achieve this goal, a wide range of polymer matrices and nanofillers, as well as different nanocomposites processing routes, are considered. To this end, a large amount of data has been collected from the literature as well from our own nanocomposite platform and two ML regression models, Random Forest regression and Support Vector Machine regression, successfully used with PLA nanocomposites [16], are chosen. The first step consists in selecting the appropriate descriptors concerning the matrix, the filler and the process to be able to fully describe the systems with the most accessible parameters and further be able to predict the nanocomposite's permeability. In a second step, Random Forest regression and SVM regression are trained with a database to predict relative permeability from a wide range of nanocomposites characteristics. Subsequently, permeability values predicted with the other part of the database are compared with experimental ones. At last, ML was utilized to propose

a design for nanocomposites that would facilitate the achievement of a relative permeability level. The possible combinations of parameters suggested by the model are presented and the differences obtained between high and low permeable matrices are discussed.

4. Methods

4.1. Dataset

The dataset used in this study is composed of 220 samples and has been built by using our own experimental data and by collecting a wide amount of data in the literature [17], [18], [19], [20], [21], [22], [23], [24], [25], [26], [27], [28], [29], [30], [31], [32], [33], [34], [35], [36], [37], [38], [39], [40], [41], [42], [43], [44], [45], [46], [47], [48]. All samples are composed of a polymer matrix and of an impermeable nanotype filler. The extensive collection of data enables us to cover a wide range of polymer matrices and then a large range of oxygen permeability coefficients as detailed in **Table 1**. A total of 20 different polymer matrices have been used in this work, going from amorphous (PMMA, PS as examples) to semi-crystalline polymers (PE, PA as examples) and from rubbery (PP, PP+EPDM, PCL) to glassy polymers (PI, PET, PS, PLA as examples). Moreover, a large range of fillers have been considered with different shape (spherical, elongated, lamellar), different size and different chemical nature (metals, silicate, graphene, cellulose…).

Relative oxygen permeability has been considered to investigate the gain of barrier properties brought by the addition of fillers. The relative permeability (P/P_0) corresponds to the permeability of the samples containing fillers (P) over the permeability of the polymer matrix (P_0) and it will be taken as the output parameter.

Table 1 - Acronym of the matrices used in this study and their respective detailed name and their range of oxygen permeability coefficient in barrer unit (1 barrer = 10^{-10} cm^3_{STP} .cm.cm².s^{-1}.cm_{Hg}^{-1} = 3.36x10^{-16} mol.m.m^{-2}.s^{-1}.Pa^{-1})

ACRONYM	DETAILED NAME	P (O_2) RANGE
PVA	Poly (vinyl alcohol)	< 0.1 barrer
EVOH	Ethylene vinyl alcohol copolymer	
PA6	Polyamide 6	
PET	Polyethylene terephthalate semi-crystalline	
PMMA	Polymethyl methacrylate	
PVDF	Poly (vinylidene fluoride)	
PLA	Poly (lactic acid) amorphous	0.1-1 barrer
PLA sc	Poly (lactic acid) semi-crystalline	
PI	Polyimide	
PHBV	Poly(3-hydroxybutyrate-*co*-3-hydroxyvalerate)	
PCL	Polycaprolactone	
HPDE	High density polyethylene	
PE + HPDE-g-MA	Polyethylene + high density polyethylene grafted with maleic acid	1-10 barrer
LPDE + HPDE-g-MA	Low density polyethylene + high density polyethylene grafted with maleic acid	
PS	Polystyrene	
PVC	Polyvinyl chloride	
LPDE	Low density polyethylene	
PP+ EPDM	Polypropylene + ethylene-propylene-diene rubber (50:50 wt%)	

Figure 1 represents the relative permeability values of the samples of the dataset as a function of the filler volume content. A cloud of experimental points is obtained with relative permeability values ranging from 0.2 to 1.2. It can also be noticed that a wide range of relative permeability values can be achieved depending on the systems at a fixed content of fillers. Thus, no simple relation can be established between the filler content and the relative permeability, showing that other parameters have to be considered to give a more detailed description of each sample. **Table 2** summarizes the input parameters used in this study with their respective range of values.

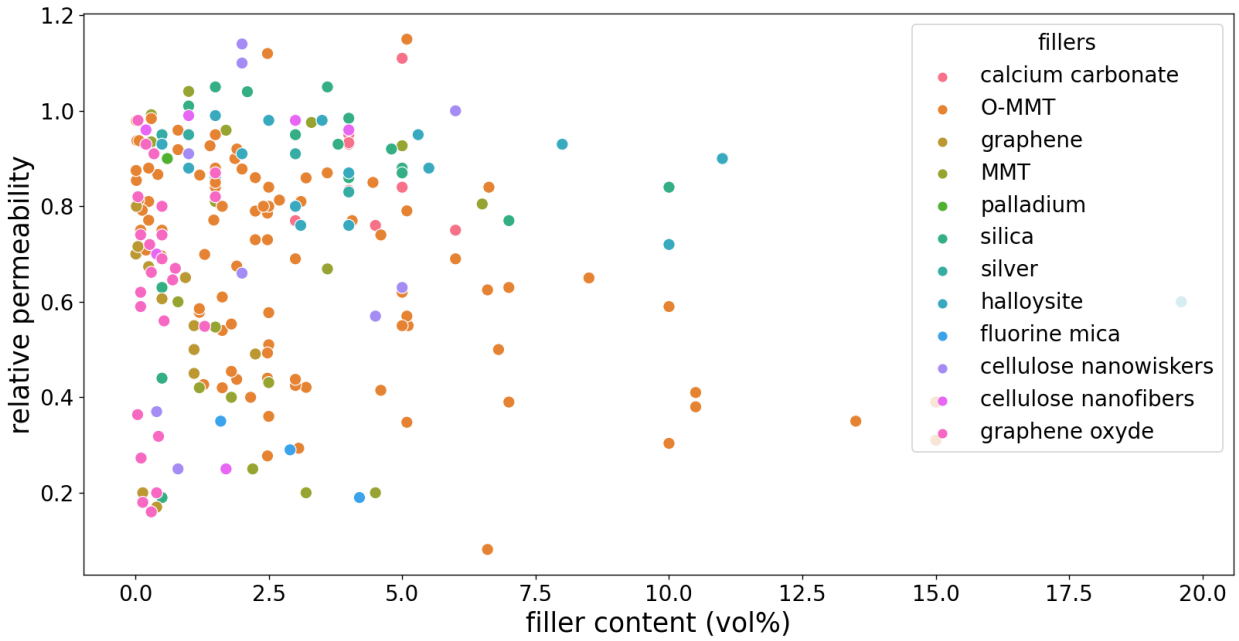


Figure 1- Relative permeability as a function of the filler volume content for the different fillers which constitute the dataset of 220 samples. MMT stands for montmorillonites and O-MMT for organo-modified montmorillonites.

The *filler_type* corresponds to the initial shape of the fillers. The *volume_content* corresponds to the volume fraction of the fillers in the material. The *aspect_ratio* is equal to the average value of ratio of the length over the thickness (or diameter) of the unitary raw filler. The *filler_polarity is attributed in a discrete scale from 0 to 4 with* 0 corresponding to non-modified apolar filler and 4 corresponding to the polar fillers which have the most polar groups at the surface. We also considered the *matrix_surface_energy* (in mJ/m²) [49] and the *matrix_perm(O_2)* input parameter which corresponds to the permeability coefficient expressed in barrer units (1 barrer = 10^{-10} cm^3_{STP} .cm.cm^{-2}.s^{-1}.cm_{Hg}^{-1}) of the unfilled polymer prepared in the same conditions as the nanocomposite. The process (*Process*) to elaborate the nanocomposites has also been considered.

Table 2 - Input parameters used and their range values.

PARAMETERS	*Parameter type for ML*	*VALUES*
type_filler	Input parameters	1: sphere 2: tubes 3: random platelets 4: oriented platelets
volume_content		0 - 20 % vol
aspect_ratio		1 - 500
filler_polarity		0 : non-modified apolar filler 1: apolar filler modified with a polar group 2: non-modified polar filler 3: polar filler modified with an apolar group 4: polar filler modified with a polar group
Matrix_surface_energy		30 - 60 mJ/m²
Matrix_perm(O2)		From 5.10^{-4} to 10 barrer
Process		1: melt-blending 2: solvent casting 3 : *in situ* polymerization
P/P_0	Output parameter	0 - 1

4.2. Modelling

In this work, two ML regression models have been used and compared. The first one is the Random Forest (RF), which gives the average results of several decision trees based on binary data sorting [50], [51]. This model is well appropriate when there is a wide variety of input parameters. The second regression model is the Support Vector Machine (SVM), which uses a hyperplane to describe the data with. We used a radial basis functional kernel to recognize the data pattern [50], [51], [52], [53]. This second model has been chosen because of its efficiency for nonlinear regression.

The machine learning models were trained on 80% of the randomly selected samples from the dataset using the *train-test-split* procedure. Subsequently, the remaining 20% of samples were employed to assess the model accuracy by comparing the predicted outputs with the experimental results. The performance of the model was evaluated based on the mean

absolute error (MAE) as well as on the coefficient of determination (R^2) given by equation (1) and (2).

$$MAE = \frac{\sum_{i=1}^{n} |yi - \hat{y}i|}{n} \quad (1)$$

$$R^2 = 1 - \frac{\sum_{i=1}^{n} (yi - \hat{y}i)^2}{\sum_{i=1}^{n} (yi - \overline{y})^2} \quad (2)$$

with n the number of samples, yi the experimental relative permeability, $\hat{y}i$ the predicted relative permeability and $\overline{y}$ the mean of the experimental permeability values.

The robustness of the models was assessed with the cross validation which consists in repeating the splitting procedure, changing the subsets for training and validation, 40 times to select samples used for training data and testing data. The cross validation has been done by using *Shuffle Split* strategy. The MAE and the R^2 of the predicted relative permeability are calculated with splitting procedure.

5. Results and discussion

5.1. Statistical analysis of the data set

One of the challenges when working with machine learning in material science is to choose the appropriate material descriptors to assess the target physical properties.

The dataset is composed of a wide range of polymer matrices, but some of them are present in significant numbers and thus will weigh heavily in the model. As an example, **Figure 2** shows a large proportion of amorphous PLA (PLA: 87 samples) and semi-crystalline PLA (PLAsc: 44 samples) in the database. Consequently, the ability to predict relative permeability from the minority matrices would be questionable. Thus, it has been chosen not to work with the type of polymer matrices but rather with characteristic parameters of the polymer matrices which can influence the permeability.

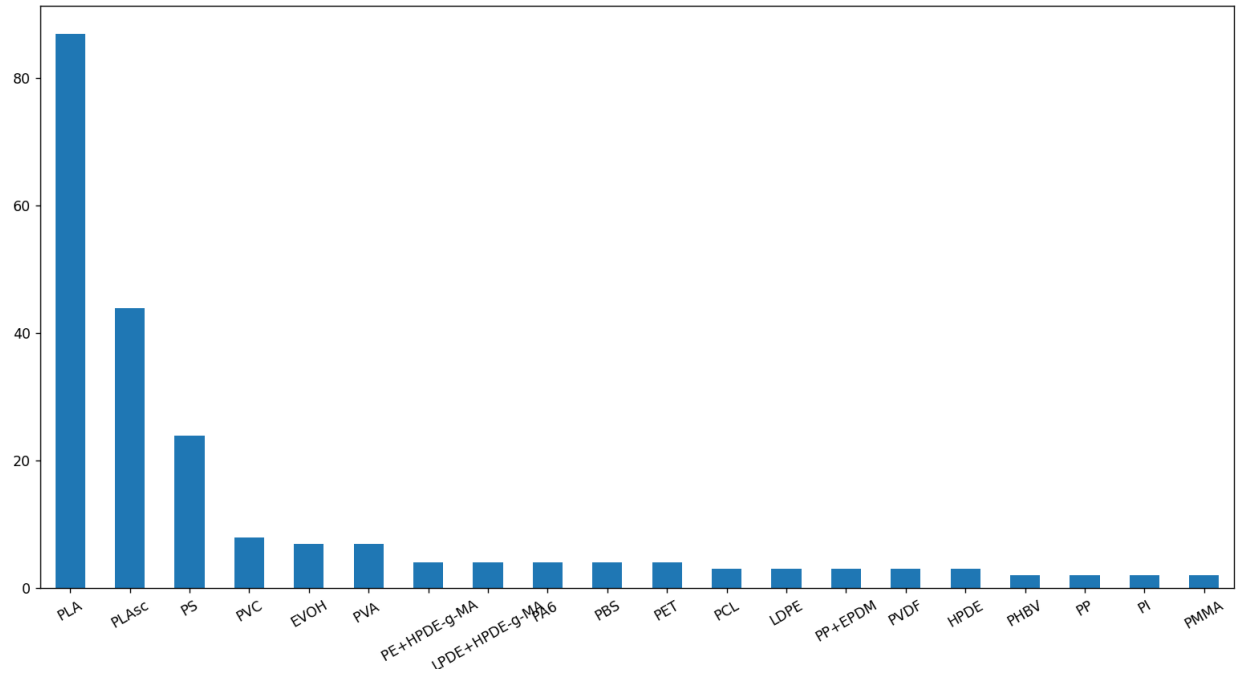


Figure 2 - Number of samples for each polymer matrix in the database composed of 220 samples.

To appropriately select the parameters, we first analyzed the values of the oxygen permeability coefficient of the matrices contained in the data set (**Figure 3a**). The permeability levels depend on the cohesive energy density of a polymer, which is linked to its polarity/apolarity [1], [54]. Moreover, the polarity of the matrix can modify the filler dispersion and the filler/matrix interface which influences therefore the permeability of the nanocomposites. Thus, the surface energy has been added to the dataset for each matrix. The range of surface energy goes from 30 to 60 mJ/m² (**Figure 3b**) with the highest value for polyvinyl alcohol (PVA), a polar polymer and the lowest for polypropylene (PP), an apolar polymer [49].

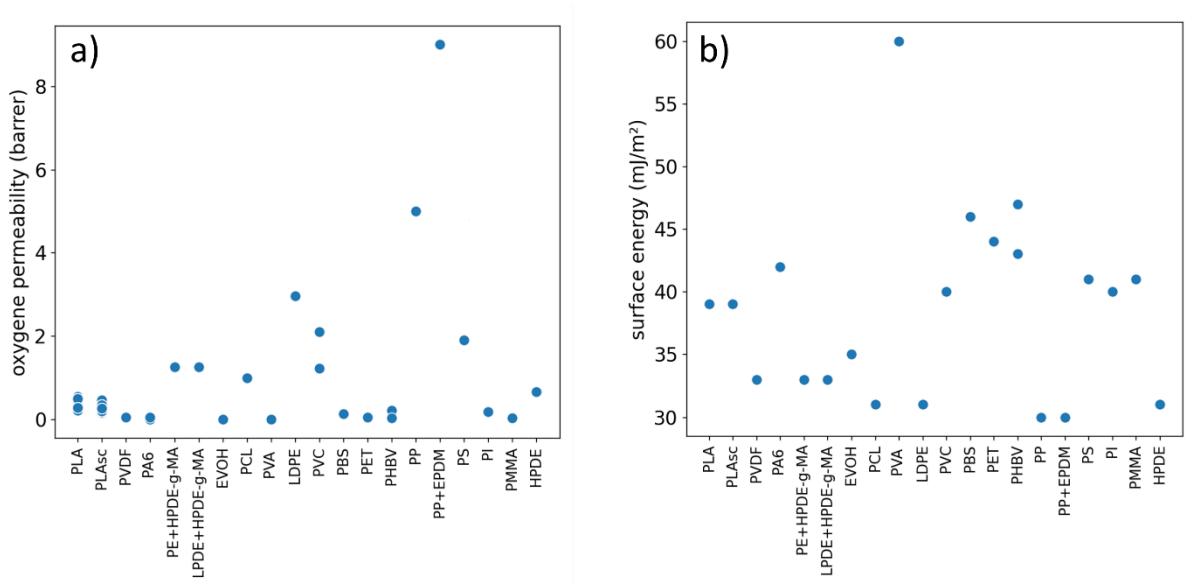


Figure 3 - (a) oxygen permeability coefficient (in barrer units) and (b) surface energy values (in mJ/m²) of the matrix in the dataset.

Furthermore, the database gathers a wide range of fillers as seen previously (**Figure 1**). To simplify the problem, the fillers were sorted by their initial shape (eg: sphere, tubes, lamellae). For lamellae, the fillers orientation in the nanocomposite sample has also been considered as it has been shown to have an influence on the permeability [6]. **Figure 4a** shows the partition of the different filler shapes and orientation in the dataset. Random lamellae count for half of the dataset whereas the oriented lamellae, tubes and sphere represent each about 15% of the samples. Moreover, to complete the dataset the order of magnitude of initial filler aspect ratio has been added. The aspect ratio of spherical fillers has been fixed to 1. For tubes it was set at 10 for the halloysites nanotubes [55], [56], [57], 20 for cellulose nanocrystals [41], [42], [58] and 100 for cellulose nanofibrils [43], [59]. For lamellae it has been taken equal to 100 for montmorillonites [35], [56], [60] and 500 for graphene [25], [47], [56]. Finally, to completely describe the fillers, the polarity of the surface of the fillers has been considered. For that purpose, the fillers were sorted from 0 to 5 going from the less polar filler surfaces to the more polar ones. The volume fraction of fillers is also a parameter which has been taken into account.

Finally, the process used to prepare the nanocomposites (e.g: melt-blending, solvent casting, in situ polymerization) has been added to the data set. **Figure 4b** shows the partition concerning the process in the dataset. It can be seen that melt-blending and solvent casting are present in large majority with respectively 48% and 46% of the samples.

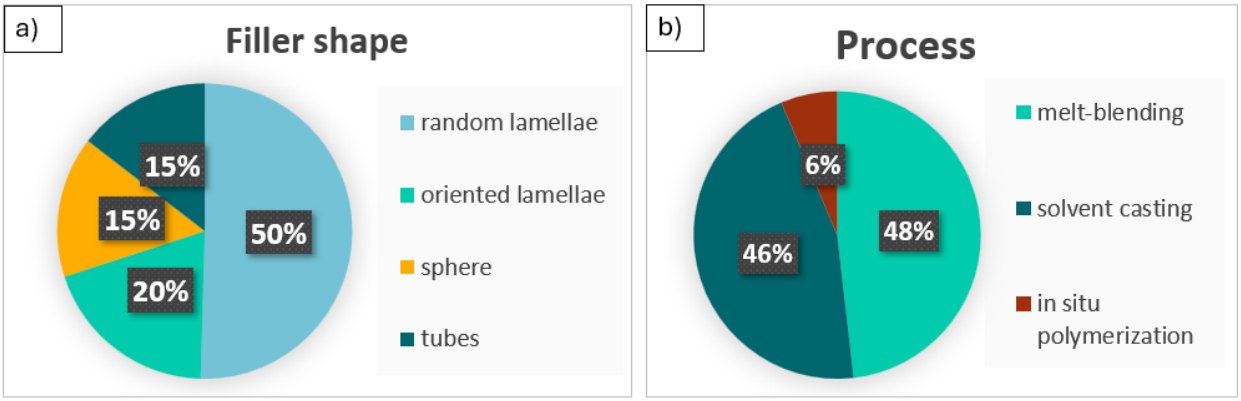


Figure 4 - Partition of the filler shape (spheres, tubes, random lamellae, oriented lamellae) and of the process (melt-blending, solvent casting, *in situ* polymerization) in the dataset.

The set of the chosen input parameters allows us to have, from an experimental point of view, a sufficient description of the wide range of nanocomposites that can be prepared from polymer matrices and preformed nanofillers.

5.2. Machine learning predictions of relative permeability

The database was randomly split into two datasets: one for training the ML models and one for testing the models. The training dataset contains 80% of the database (176 samples) which are used to build the ML model. The remaining 20%, which represents 44 samples (testing dataset) are used to check the accuracy of the model predictions. Predicted P/P_0 values are compared to the experimental P/P_0 values of the database in the confusion graph shown in **Figure 5**. When using Random Forest regression (**Figure 5a**), the P/P_0 *predicted* values are close to the P/P_0 *experimental* values for the samples used to train the model (blue point) and for the samples used to test the model (red point). The mean absolute error value for the test is 0.10 and the R^2 value is 0.78 which show a good accuracy of the predictions. For the SVM regression, P/P_0 *predicted* values are less consistent with the P/P_0 *experimental* values both for training and testing (**Figure 5b**). The mean absolute error value (*MAE*) is equal to 0.11 and the R^2 score is 0.63 for the testing dataset which reflects less accuracy for the predictions than with the Random Forest regression model. However, it can be noted that the predictions of the testing samples are as far from the perfect fit as the training samples, which means that the model is not overfitted.

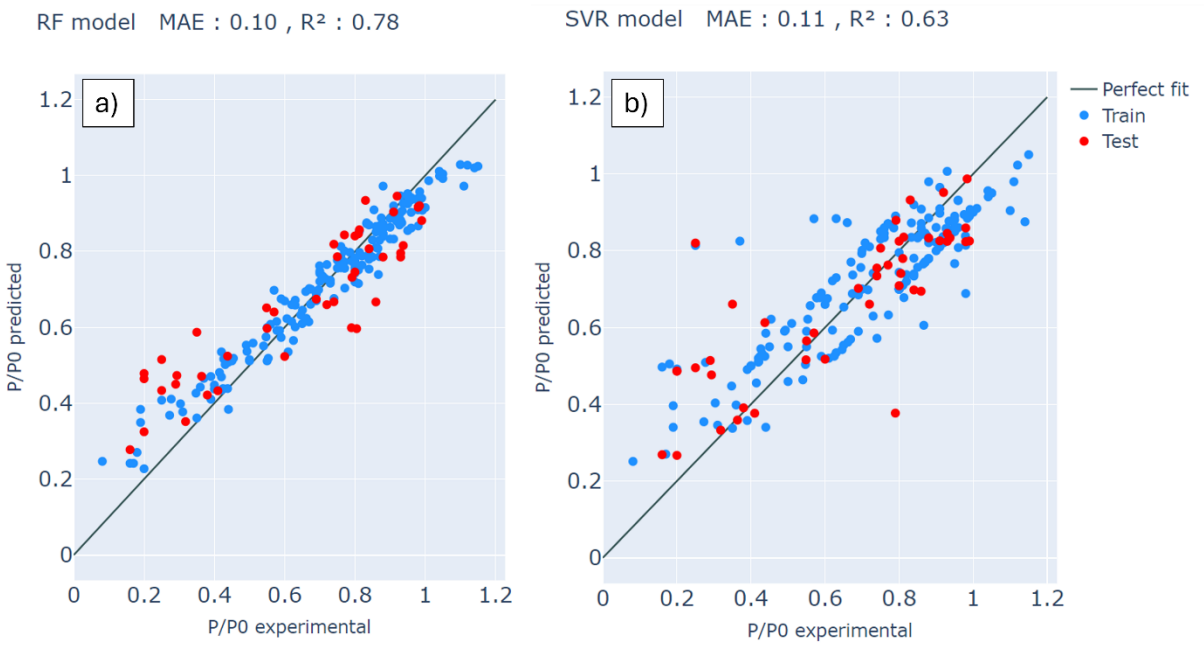


Figure 5 - Confusion graph of the *P/P₀ predicted* versus the *P/P₀ experimental* for (a) Random Forest regression and (b) SVM regression.

To confirm that the obtained score is not dependent on the data used to train the model, cross validation is performed on the whole database. As already explained, it consists in splitting randomly 40 times the whole database into a training and testing dataset and looking at the predictions for each split. The mean absolute error and the R^2 score of the predicted P/P_0 values are calculated for the testing samples. For the Random Forest, *MAE* is equal to 0.11 ± 0.01 and the R^2 has a value of 0.64 ± 0.09. The low standard deviation values show that the accuracy of the predictions is not dependent on the data selected to train the model. SVM exhibits less accuracy and higher standard deviation value with a *MAE* of 0.13 ± 0.02 and a R^2 score of 0.48 ± 0.17.

More specifically, it can be observed on **Figure 5b** that some outlier points have a high predicted P/P_0 value whereas their experimental P/P_0 values are much lower as it the case of the sample with a P/P_0 *experimental* = 0.81 and P/P_0 *predicted* = 0.25. On the contrary, a sample with a predicted P/P_0 of 0.79 has an experimental P/P_0 of 0.44.

Regarding these results, it has been decided to train separately the samples having a high relative permeability ($P/P_0 > 0.8$) and those having a low relative permeability ($P/P_0 \leq 0.8$). For this goal, we add a step in the model building which consists in separating the samples exhibiting a relative permeability value higher than 0.8 and the ones having a permeability value equal or less than 0.8 by using Random Forest Classification on the previously used input

parameters. Then the two groups were trained separately with a different SVM regression. To summarize, a new model was created with a first step of classification between high and low relative permeability, and then the relative permeability value is predicted with the corresponding most suitable SVM regression.

To evaluate this new model, the predicted sample categories ($P/P_0 \leq 0.8$ and $P/P_0 > 0.8$) are first compared to the experimental respective ones in the confusion matrix (**Figure 6**). The '0' category corresponds to samples with a $P/P_0 \leq 0.8$ while '1' corresponds to samples with a $P/P_0 > 0.8$. Predictions are very good as only 6 samples (e.g. in fact 3 samples for each category) over 44 are classified in the wrong category.

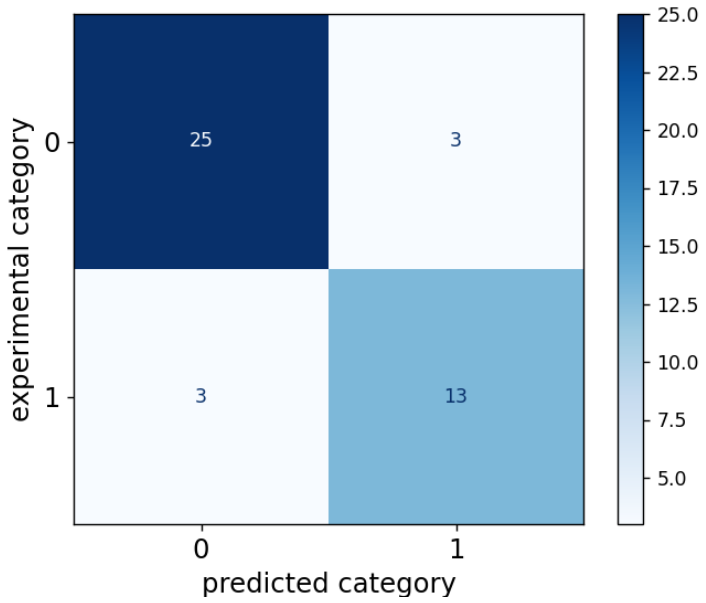


Figure 6 – Confusion matrices of the *predicted versus experimental* P/P_0 class: '0' corresponds to samples with a $P/P_0 \leq 0.8$ while '1' corresponds to samples with a $P/P_0 > 0.8$.

In a second step, the results of the predicted relative permeability values with this new model are compared with the results of the previous non splitter model (**Figure 7**). For the relative permeability higher than 0.8, predictions are much better compared to the first model, with predicted values close to the experimental ones both for training and testing samples. The circled points correspond to the samples which were not classified in the right category and resulting then from an unsuited SVR regression. For the relative permeability lower than 0.8, the predictions are also better than the first ones, although there is still one testing point for which the predicted P/P_0 value is equal to 0.44 which is far from the experimental value of 0.8. This outlier point can be attributed to uncertainty in the experimental data or to data

scarcity for similar systems. The overall mean absolute error on the testing samples is equal to 0.11 which is similar to the first SVM model but the R^2 is higher (R^2 = 0.71).

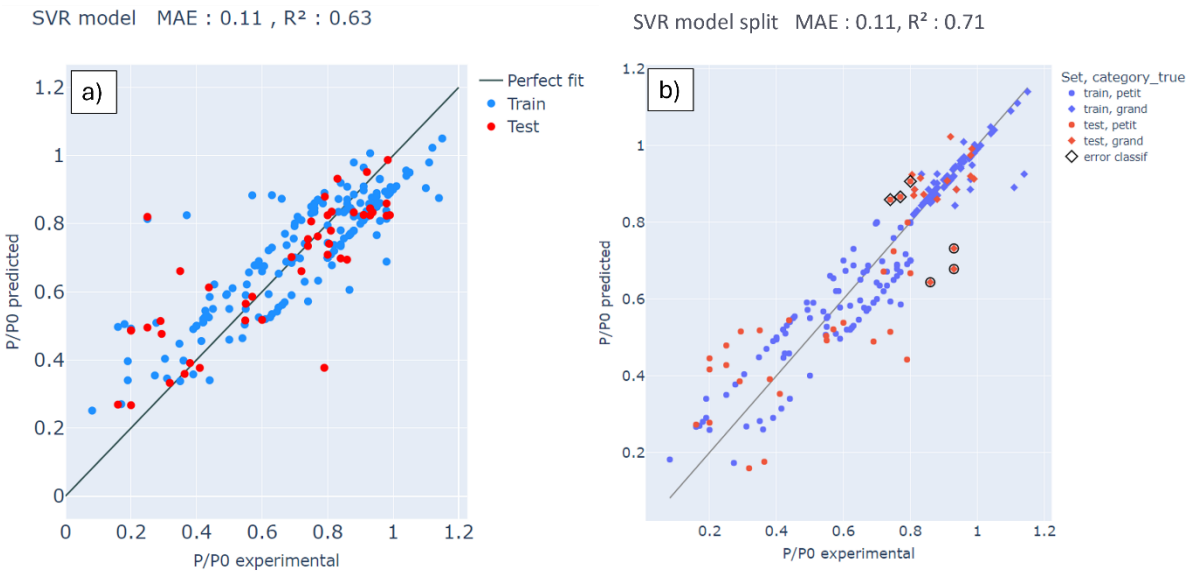


Figure 7 - Confusion graph of the predicted P/P_0 over the experimental P/P_0 with the SVM model a) before splitting and b) after splitting.

Thus, by training the model separately between the high and low relative permeability, we have improved the accuracy of the predictions. Although this new model shows promising results, the accuracy of the predictions is still better with the Random Forest regression (R^2 = 0.78 versus 0.71).

5.3. Assisted design of polymer nanocomposites with the Random Forest

In the last part of our work, machine learning was used to predict the values of the possible combinations of parameters (eg: process, filler shape, initial filler aspect ratio, filler volume content, matrix surface tension and matrix oxygen permeability) that could achieve a specified range of P/P_0. Only predictions from Random Forest regression model have been used as this model exhibits the highest determination coefficient (R^2 = 0.78). In order to remove proposed solutions that could lead to inappropriate materials, notably considering mechanical properties, the following criterion has been taken into account. The filler content (whatever the filler shape: spheres, tubes or lamellae) has to be below 15 vol% as beyond this content the material should become too brittle. The relative permeability values were fixed at 0.6 and 0.4 and the possibilities suggested by the model are presented and discussed.

For a P/P_0 value of 0.6, all types of fillers are given as possibilities. However, we know that from a physical point of view, it is not possible to reach such relative permeability with a spherical filler content below 15 %vol. Indeed, the Maxwell model [61], often used to have an approximated value of the permeability with spherical fillers, indicates that a relative permeability of 0.6 would be possible with 30 %vol of such filler. In that case, the only possibility is an increase in the polymer matrix crystallinity with the introduction of filler.

The possible combinations suggested by the model for lamellar fillers randomly oriented in the matrix are more deeply investigated. For these fillers the three processes are in the possible combinations (eg: melt-bending, solvent route *in situ* polymerization). **Figure 8** compared the possibilities (represented in grey lines) for different matrix permeability. **Figure 8a,b** exhibit the results for matrix having high oxygen permeability (between 5 and 9 barrer) and a low surface energy (≤ 30 mJ/m²) which corresponds to matrix such as polyolefins. In the contrary **Figure 8c,d** shows the results for matrix having low oxygen permeability (<0.1 barrer) and a higher surface energy (between 35 and 45 mJ/m²) which corresponds to matrix such as PET, EVOH or PA6. First it can be noted that the number of possibilities (grey lines) seems to be comparable for matrix with high and low permeability. To go deeper in the analysis of the results, we look at to the possibilities suggested by the model for an aspect ratio value of 100, corresponding to the order of magnitude of montmorillonites, prepared by melt-blending. Then the suggested combinations have been split between the one corresponding to non-modified polar lamellae (**Figure 8a,c**) and lamellae modified with an agent having polar groups, such as methyl tallow bis-2-hydroxyethyl quaternary ammonium (**Figure 8b,d**) . These combinations are highlighted with the blues line on the graphs. For unmodified polar lamellae, high volume factions are suggested in case of matrix having high permeability (**Figure 8a**) whereas the entire volume count range is suggested in case of matrix having low permeability (**Figure 8c**). These results highlight the fact that a matrix having low permeability, and logically higher surface energy, enables a better dispersion of the fillers and so lower filler content for same permeability. However such large range of volume content is surprising. For lamellae modified with polar groups, the volume content is comparable whatever the matrix permeability and is rather low (<6 %vol). This is consistent with the fact that the polar groups of the modification agent enhance the filler dispersion and thus lower content is needed compared to non-modified lamellae.

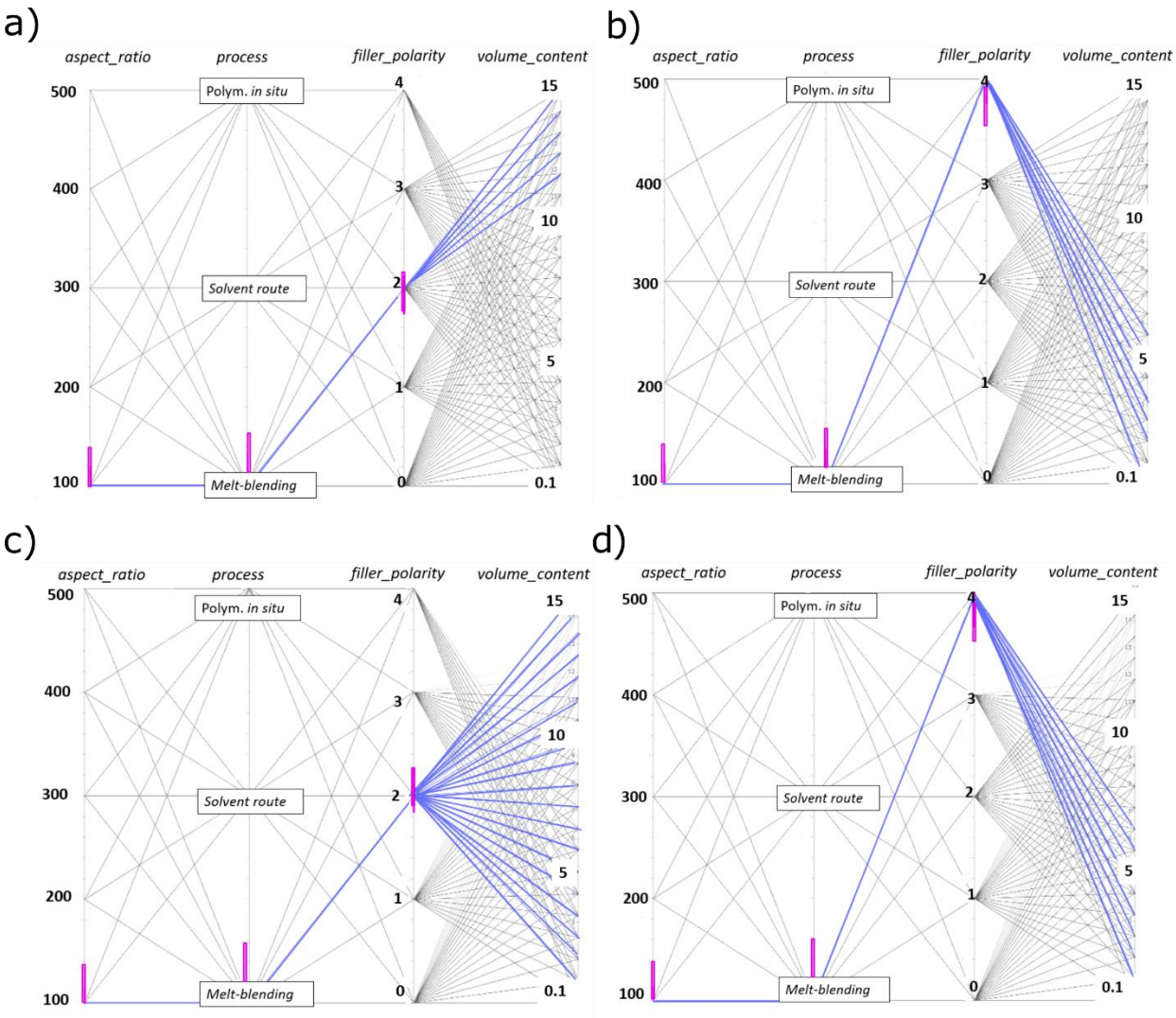


Figure 8- Predicted possibilities for a P/P_0 value of 0.6 with an absolute error of 0.05 in case of lamellar filler with the Random Forest regression model for a,b) matrix having high oxygen permeability (5-9 barrer) and low surface energy (30 mJ/m²) and c,d) matrix having low oxygen permeability (<0.1 barrer) and high surface energy (35 - 45 mJ/m²). The blue line corresponds to the possibilities for a filler aspect ratio value of 100 with the melt-blending and a,c) non modified polar lamellae or b,d) lamellae modified with agent having polar groups (as Cloisite 30B) .

For a relative permeability of 0.4, the number of suggested combinations decreased. Only polar lamellar fillers modified with molecules having polar groups are given as possibilities. **Figure 9** shows the possibilities for randomly oriented lamellar fillers for matrix having high oxygen permeability (between 5 and 9 barrer) and a low surface energy (≤ 30 mJ/m²) (**Figure 9a**) and the results for matrix having low oxygen permeability (< 0.1 barrer) and a higher surface energy (between 35 and 45 mJ/m²) (**Figure 9b**). Whatever the matrix permeability, the number of possibilities is lower than in the case of P/P_0 = 0.6 and indicates that the aspect ratio of the lamellar fillers must be superior or equal to 200. Moreover, for matrix having a

high permeability and low surface energy, the solvent route is not in the possibilities. However, it is not significant because such matrices are not really suited for this process. Furthermore, the range of filler content is smaller for matrix with high permeability (filler content range between 6.5 to 15 vol%) than for matrix having low permeability (filler content range between 2.5 and 15 vol%). However, as mentioned previously, we know that high volume content is not experimentally possible when working with high aspect ratio fillers.

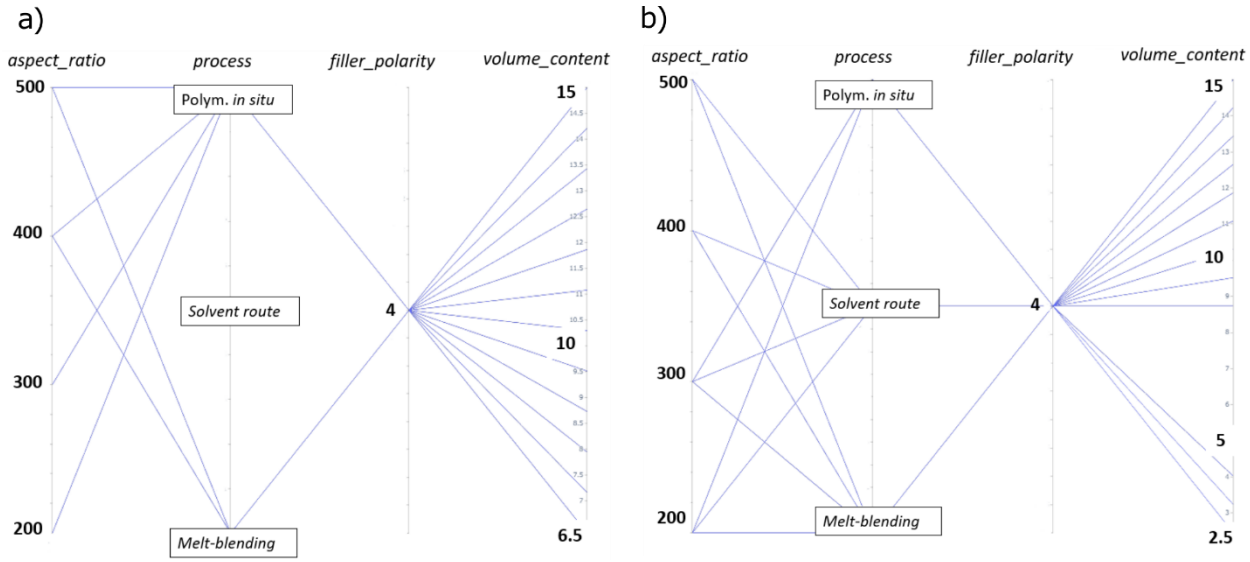


Figure 9 - Predicted possibilities for a P/P_0 value of 0.4 with an absolute error of 0.05 in case of lamellar filler with the Random Forest regression model for a) matrix having high oxygen permeability (5 - 9 arrer) and low surface energy (30 mJ/m²) and b) matrix having low oxygen permeability (< 0.1 barrer) and low surface energy (35 - 45 mJ/m²).

6. Conclusion

In this work, two machine learning models (Random Forest and Support Vector Machine regression) have been trained to predict the relative permeability of nanocomposites with diverse matrices, fillers and processes. A substantial number of input parameters concerning the fillers (filler shape, filler mean aspect ratio, filler content, filler polarity), the matrix (matrix surface energy, matrix oxygen permeability) and the process have been investigated through a consequent amount of data. The mean absolute error for the Random Forest model was 0.10, with an R^2 of 0.78. In comparison, the Support Vector Machine model exhibited less accurate predictions (R^2 = 0.63). Nevertheless, we succeeded to enhance the SVM predictions (R^2 = 0.71) by the introduction of a classification step within the model, whereby the input data was initially separated into two categories: high and low relative permeability. Finally, the most accurate model (Random Forest) was used to suggest combinations of input parameters

for achieving a chosen level of relative permeability values. The results for matrices with high and low oxygen permeability were compared for two targeted relative permeabilities: $P/P_0 = 0.6$ and $P/P_0 = 0.4$. The model gives fewer possibilities for matrices with high permeability, such as polyolefins, which have lower affinity with the fillers. From these predictions, a variety of materials can be prepared for a specific permeability, allowing some flexibility in material composition. Therefore, it would be interesting to train the model with a larger number of data, to see if the predictions could be enhanced. All in all, ML is a promising tool for assisting the design of nanocomposites with high barrier properties, but it is essential to keep a critical eye on the results.

7. References

[1] M.-H. Klopffer, P. Berne, É. Espuche, Development of Innovating Materials for Distributing Mixtures of Hydrogen and Natural Gas. Study of the Barrier Properties and Durability of Polymer Pipes, Oil Gas Sci. Technol. – Rev. IFP Energies Nouvelles 70 (2015) 305–315. https://doi.org/10.2516/ogst/2014008.

[2] G. Choudalakis, A.D. Gotsis, Permeability of polymer/clay nanocomposites: A review, European Polymer Journal 45 (2009) 967–984. https://doi.org/10.1016/j.eurpolymj.2009.01.027.

[3] B. Tan, N.L. Thomas, A review of the water barrier properties of polymer/clay and polymer/graphene nanocomposites, Journal of Membrane Science 514 (2016) 595–612. https://doi.org/10.1016/j.memsci.2016.05.026.

[4] C. Wolf, H. Angellier-Coussy, N. Gontard, F. Doghieri, V. Guillard, How the shape of fillers affects the barrier properties of polymer/non-porous particles nanocomposites: A review, Journal of Membrane Science 556 (2018) 393–418. https://doi.org/10.1016/j.memsci.2018.03.085.

[5] L.E. Nielsen, Models for the Permeability of Filled Polymer Systems, Journal of Macromolecular Science—Chemistry (1967). https://doi.org/10.1080/10601326708053745.

[6] R.K. Bharadwaj, Modeling the Barrier Properties of Polymer-Layered Silicate Nanocomposites, Macromolecules 34 (2001) 9189–9192. https://doi.org/10.1021/ma010780b.

[7] S. Zid, Finite element modeling and experimental approach of gas transport in polymer-based multimaterials and complex systems, Thèse de doctorat, Univsersité Lyon 1, 2019.

[8] S. Zid, M. Zinet, E. Espuche, Modeling diffusion mass transport in multiphase polymer systems for gas barrier applications: A review, Journal of Polymer Science Part B: Polymer Physics 56 (2018) 621–639. https://doi.org/10.1002/polb.24574.

[9] T. Htira, S. Zid, M. Zinet, E. Espuche, Finite Element Analysis of Gas Diffusion in Polymer Nanocomposite Systems Containing Rod-like Nanofillers, Polymers 13 (2021) 2615. https://doi.org/10.3390/polym13162615.

[10] E. Champa-Bujaico, P. García-Díaz, A.M. Díez-Pascual, Machine Learning for Property Prediction and Optimization of Polymeric Nanocomposites: A State-of-the-Art, International Journal of Molecular Sciences 23 (2022) 10712. https://doi.org/10.3390/ijms231810712.

[11] P.N. Khanam, M. AlMaadeed, S. AlMaadeed, S. Kunhoth, M. Ouederni, D. Sun, A. Hamilton, E.H. Jones, B. Mayoral, Optimization and Prediction of Mechanical and Thermal Properties of Graphene/LLDPE Nanocomposites by Using Artificial Neural Networks, International Journal of Polymer Science 2016 (2016) 5340252. https://doi.org/10.1155/2016/5340252.

[12] M. Zakaulla, Y. pasha, S. kesarmadu Siddalingappa, Prediction of mechanical properties for polyetheretherketone composite reinforced with graphene and titanium powder using artificial neural network, Materials Today: Proceedings 49 (2022) 1268–1274. https://doi.org/10.1016/j.matpr.2021.06.365.

[13] E. Kosicka, A. Krzyzak, M. Dorobek, M. Borowiec, Prediction of Selected Mechanical Properties of Polymer Composites with Alumina Modifiers, Materials 15 (2022) 882. https://doi.org/10.3390/ma15030882.

[14] A. Zhu, H. Diao, Q. Rong, A. Cai, Preparation and properties of polylactide–silica nanocomposites, Journal of Applied Polymer Science 116 (2010) 2866–2873. https://doi.org/10.1002/app.31786.
[15] J.W. Barnett, C.R. Bilchak, Y. Wang, B.C. Benicewicz, L.A. Murdock, T. Bereau, S.K. Kumar, Designing exceptional gas-separation polymer membranes using machine learning, Science Advances 6 (2020) 1-7. https://doi.org/10.1126/sciadv.aaz4301.
[16] A. Jullin, N. Hascoët, F. Chinesta, E. Espuche, Data Driven modelling as a new route to design PLA based materials with high barrier properties, Food Packaging and Shelf Life (Submitted) (2024).
[17] F. Morel, Compréhension des phénomènes interfaciaux dans les composites à base de charges carbonate de calcium précipité: influence du traitement de surface et du procédé de mise en œuvre, Thèse de doctorat, Université Lyon 1 (2010).
[18] E. Picard, A. Vermogen, J.-F. Gérard, E. Espuche, Barrier properties of nylon 6-montmorillonite nanocomposite membranes prepared by melt blending: Influence of the clay content and dispersion state: Consequences on modelling, Journal of Membrane Science 292 (2007) 133–144. https://doi.org/10.1016/j.memsci.2007.01.030.
[19] E. Jacquelot, E. Espuche, J.-F. Gérard, J. Duchet, P. Mazabraud, Morphology and gas barrier properties of polyethylene-based nanocomposites, Journal of Polymer Science Part B: Polymer Physics 44 (2006) 431–440. https://doi.org/10.1002/polb.20707.
[20] O. Gain, E. Espuche, E. Pollet, M. Alexandre, Ph. Dubois, Gas barrier properties of poly(ε-caprolactone)/clay nanocomposites: Influence of the morphology and polymer/clay interactions, Journal of Polymer Science Part B: Polymer Physics 43 (2005) 205–214. https://doi.org/10.1002/polb.20316.
[21] A. Blanchard, F. Gouanvé, E. Espuche, Influence of the Graphene Filler Nature on the Morphology and Properties of Melt Blended EVOH Based Nanocomposites, Polymers 13 (2021) 3546. https://doi.org/10.3390/polym13203546.
[22] S. Clemenson-Simon, Nanostructuration de membranes polymère-métal pour applications fonctionnelles, Thèse de doctorat, Lyon 1, 2009.
[23] A. Kalendova, D. Merinska, J.F. Gerard, M. Slouf, Polymer/clay nanocomposites and their gas barrier properties, Polymer Composites 34 (2013) 1418–1424. https://doi.org/10.1002/pc.22541.
[24] S.W. Kim, S.-H. Cha, Thermal, mechanical, and gas barrier properties of ethylene–vinyl alcohol copolymer-based nanocomposites for food packaging films: Effects of nanoclay loading, Journal of Applied Polymer Science 131 (2014). https://doi.org/10.1002/app.40289.
[25] R. Cosquer, S. Pruvost, F. Gouanvé, Improvement of Barrier Properties of Biodegradable Polybutylene Succinate/Graphene Nanoplatelets Nanocomposites Prepared by Melt Process, Membranes 11 (2021) 151. https://doi.org/10.3390/membranes11020151.
[26] A. García, S. Eceolaza, M. Iriarte, C. Uriarte, A. Etxeberria, Barrier character improvement of an amorphous polyamide (Trogamid) by the addition of a nanoclay, Journal of Membrane Science 301 (2007) 190–199. https://doi.org/10.1016/j.memsci.2007.06.018.
[27] M.D. Sanchez-Garcia, E. Gimenez, J.M. Lagaron, Novel PET Nanocomposites of Interest in Food Packaging Applications and Comparative Barrier Performance With Biopolyester Nanocomposites, Journal of Plastic Film & Sheeting 23 (2007) 133–148. https://doi.org/10.1177/8756087907083590.

[28] Sh. Hamzehlou, A.A. Katbab, Bottle-to-bottle recycling of PET via nanostructure formation by melt intercalation in twin screw compounder: Improved thermal, barrier, and microbiological properties, Journal of Applied Polymer Science 106 (2007) 1375–1382. https://doi.org/10.1002/app.26730.

[29] J.P.G. Villaluenga, M. Khayet, M.A. López-Manchado, J.L. Valentin, B. Seoane, J.I. Mengual, Gas transport properties of polypropylene/clay composite membranes, European Polymer Journal 43 (2007) 1132–1143. https://doi.org/10.1016/j.eurpolymj.2007.01.018.

[30] J. Gaume, C. Taviot-Gueho, S. Cros, A. Rivaton, S. Thérias, J.-L. Gardette, Optimization of PVA clay nanocomposite for ultra-barrier multilayer encapsulation of organic solar cells, Solar Energy Materials and Solar Cells 99 (2012) 240–249. https://doi.org/10.1016/j.solmat.2011.12.005.

[31] M. Frounchi, S. Dadbin, Z. Salehpour, M. Noferesti, Gas barrier properties of PP/EPDM blend nanocomposites, Journal of Membrane Science 282 (2006) 142–148. https://doi.org/10.1016/j.memsci.2006.05.016.

[32] S. Nazarenko, P. Meneghetti, P. Julmon, B.G. Olson, S. Qutubuddin, Gas barrier of polystyrene montmorillonite clay nanocomposites: Effect of mineral layer aggregation, Journal of Polymer Science Part B: Polymer Physics 45 (2007) 1733–1753. https://doi.org/10.1002/polb.21181.

[33] V.E. Yudin, J.U. Otaigbe, S. Gladchenko, B.G. Olson, S. Nazarenko, E.N. Korytkova, V.V. Gusarov, New polyimide nanocomposites based on silicate type nanotubes: Dispersion, processing and properties, Polymer 48 (2007) 1306–1315. https://doi.org/10.1016/j.polymer.2007.01.012.

[34] N. Tenn, N. Follain, J. Soulestin, R. Crétois, S. Bourbigot, S. Marais, Effect of Nanoclay Hydration on Barrier Properties of PLA/Montmorillonite Based Nanocomposites, J. Phys. Chem. C 117 (2013) 12117–12135. https://doi.org/10.1021/jp401546t.

[35] S. Sinha Ray, P. Maiti, M. Okamoto, K. Yamada, K. Ueda, New Polylactide/Layered Silicate Nanocomposites. 1. Preparation, Characterization, and Properties, Macromolecules 35 (2002) 3104–3110. https://doi.org/10.1021/ma011613e.

[36] S. Sinha Ray, K. Yamada, M. Okamoto, K. Ueda, New polylactide-layered silicate nanocomposites. 2. Concurrent improvements of material properties, biodegradability and melt rheology, Polymer 44 (2003) 857–866. https://doi.org/10.1016/S0032-3861(02)00818-2.

[37] M.A. Ortenzi, L. Basilissi, H. Farina, G. Di Silvestro, L. Piergiovanni, E. Mascheroni, Evaluation of crystallinity and gas barrier properties of films obtained from PLA nanocomposites synthesized via “in situ” polymerization of l-lactide with silane-modified nanosilica and montmorillonite, European Polymer Journal 66 (2015) 478–491. https://doi.org/10.1016/j.eurpolymj.2015.03.006.

[38] J.-H. Chang, Y.U. An, G.S. Sur, Poly(lactic acid) nanocomposites with various organoclays. I. Thermomechanical properties, morphology, and gas permeability, Journal of Polymer Science Part B: Polymer Physics 41 (2003) 94–103. https://doi.org/10.1002/polb.10349.

[39] H.C. Koh, J.S. Park, M.A. Jeong, H.Y. Hwang, Y.T. Hong, S.Y. Ha, S.Y. Nam, Preparation and gas permeation properties of biodegradable polymer/layered silicate nanocomposite membranes, Desalination 233 (2008) 201–209. https://doi.org/10.1016/j.desal.2007.09.043.

[40] E. Espino-Pérez, J. Bras, G. Almeida, C. Plessis, N. Belgacem, P. Perré, S. Domenek, Designed cellulose nanocrystal surface properties for improving barrier properties in polylactide nanocomposites, Carbohydrate Polymers 183 (2018) 267–277. https://doi.org/10.1016/j.carbpol.2017.12.005.

[41] E. Fortunati, M. Peltzer, I. Armentano, L. Torre, A. Jiménez, J.M. Kenny, Effects of modified cellulose nanocrystals on the barrier and migration properties of PLA nano-biocomposites, Carbohydrate Polymers 90 (2012) 948–956. https://doi.org/10.1016/j.carbpol.2012.06.025.

[42] S.S. Karkhanis, N.M. Stark, R.C. Sabo, L.M. Matuana, Water vapor and oxygen barrier properties of extrusion-blown poly(lactic acid)/cellulose nanocrystals nanocomposite films, Composites Part A: Applied Science and Manufacturing 114 (2018) 204–211. https://doi.org/10.1016/j.compositesa.2018.08.025.

[43] B.N. Jung, H.W. Jung, D.H. Kang, G.H. Kim, M. Lee, J.K. Shim, S.W. Hwang, The fabrication of flexible and oxygen barrier cellulose nanofiber/polylactic acid nanocomposites using cosolvent system, Journal of Applied Polymer Science 137 (2020) 49536. https://doi.org/10.1002/app.49536.

[44] O.C. Compton, S. Kim, C. Pierre, J.M. Torkelson, S.T. Nguyen, Crumpled Graphene Nanosheets as Highly Effective Barrier Property Enhancers, Advanced Materials 22 (2010) 4759–4763. https://doi.org/10.1002/adma.201000960.

[45] S. Morimune, T. Nishino, T. Goto, Ecological Approach to Graphene Oxide Reinforced Poly (methyl methacrylate) Nanocomposites, ACS Appl. Mater. Interfaces 4 (2012) 3596–3601. https://doi.org/10.1021/am3006687.

[46] F. Li, C. Zhang, Y. Weng, X. Diao, Y. Zhou, X. Song, Enhancement of Gas Barrier Properties of Graphene Oxide/Poly (Lactic Acid) Films Using a Solvent-free Method, Materials 13 (2020) 3024. https://doi.org/10.3390/ma13133024.

[47] A.M. Pinto, J. Cabral, D.A.P. Tanaka, A.M. Mendes, F.D. Magalhães, Effect of incorporation of graphene oxide and graphene nanoplatelets on mechanical and gas permeability properties of poly(lactic acid) films, Polymer International 62 (2013) 33–40. https://doi.org/10.1002/pi.4290.

[48] H.-D. Huang, P.-G. Ren, J.-Z. Xu, L. Xu, G.-J. Zhong, B.S. Hsiao, Z.-M. Li, Improved barrier properties of poly(lactic acid) with randomly dispersed graphene oxide nanosheets, Journal of Membrane Science 464 (2014) 110–118. https://doi.org/10.1016/j.memsci.2014.04.009.

[49] D.W. Van Krevelen, K. Te Nijenhuis, Interfacial Energy Properties, Properties of Polymers, Elsevier Science (2009) 229–244. https://doi.org/10.1016/B978-0-08-054819-7.00008-X.

[50] M. Somvanshi, P. Chavan, S. Tambade, S.V. Shinde, A review of machine learning techniques using decision tree and support vector machine, International Conference on Computing Communication Control and Automation (2016) 1–7. https://doi.org/10.1109/ICCUBEA.2016.7860040.

[51] D.M. Dutton, G.V. Conroy, A review of machine learning, The Knowledge Engineering Review 12 (1997) 341–367. https://doi.org/10.1017/S026988899700101X.

[52] C.-C. Chang, C.-J. Lin, LIBSVM: A library for support vector machines, ACM Trans. Intell. Syst. Technol. 2 (2011) 1–27. https://doi.org/10.1145/1961189.1961199.

[53] S. Ray, A Quick Review of Machine Learning Algorithms, International Conference on Machine Learning, Big Data, Cloud and Parallel Computing (2019) 35–39. https://doi.org/10.1109/COMITCon.2019.8862451.

[54] J. Crank, Diffusion in Polymers, Academic Press, 1968.
[55] W.L. Tham, B.T. Poh, Z.A. Mohd Ishak, W.S. Chow, Transparent poly(lactic acid)/halloysite nanotube nanocomposites with improved oxygen barrier and antioxidant properties, J Therm Anal Calorim 126 (2016) 1331–1337. https://doi.org/10.1007/s10973-016-5834-7.
[56] A. Jullin, G. Sudre, N. Hascoët, F. Chinesta, E. Espuche, Influence of different type of impermeable phase on the permeability of PLA films : nanofillers versus crystalline phase, Polymer Testing (Submitted) (2024).
[57] Y. Guo, K. Yang, X. Zuo, Y. Xue, C. Marmorat, Y. Liu, C.-C. Chang, M.H. Rafailovich, Effects of clay platelets and natural nanotubes on mechanical properties and gas permeability of Poly (lactic acid) nanocomposites, Polymer 83 (2016) 246–259. https://doi.org/10.1016/j.polymer.2015.12.012.
[58] E. Espino-Pérez, J. Bras, V. Ducruet, A. Guinault, A. Dufresne, S. Domenek, Influence of chemical surface modification of cellulose nanowhiskers on thermal, mechanical, and barrier properties of poly(lactide) based bionanocomposites, European Polymer Journal 49 (2013) 3144–3154. https://doi.org/10.1016/j.eurpolymj.2013.07.017.
[59] R. Kumar, S. Kumari, B. Rai, R. Das, G. Kumar, Effect of nano-cellulosic fiber on mechanical and barrier properties of polylactic acid (PLA) green nanocomposite film, Mater. Res. Express 6 (2019) 125108. https://doi.org/10.1088/2053-1591/ab5755.
[60] F. Li, C. Zhang, Y. Weng, Improvement of the Gas Barrier Properties of PLA/OMMT Films by Regulating the Interlayer Spacing of OMMT and the Crystallinity of PLA, ACS Omega 5 (2020) 18675–18684. https://doi.org/10.1021/acsomega.0c01405.
[61] J.C. Maxwell, A Treatise on Electricity and Magnetism, Clarendon Press (1873)

Conclusion générale

Ce travail, intégré au projet ANR BANCODEMM, avait pour objectif la compréhension des mécanismes gouvernant la perméabilité dans les nanocomposites et les polymères semi-cristallins. Les enjeux étaient i/d'identifier les paramètres microstructuraux les plus pertinents et de les corréler avec la perméabilité et ii/ de proposer des outils pour optimiser le design de matériaux ayant de hautes propriétés barrière, afin de ne pas devoir multiplier les formulations, de ne pas avoir à réaliser des caractérisations expérimentales systématiques et ainsi aboutir à une meilleure efficience et avoir *in fine* un gain de temps.

L'étude bibliographique (chapitre I) a d'abord rappelé l'intérêt d'introduire une phase imperméable (phase cristalline ou charges imperméables) pour diminuer la perméabilité des films polymères. La phase imperméable permet en effet de diminuer le nombre de volumes libres et de créer de la tortuosité au sein du matériau. L'évolution de la perméabilité au sein de ces matériaux a été présentée à travers différents modèles théoriques, s'appuyant sur la fraction volumique de phase imperméable et un ensemble de facteurs géométriques. Cependant, il a été montré que ces modèles ne permettent pas de prendre en compte l'ensemble des paramètres matériaux qui gouvernent la perméabilité. Cette étude bibliographique a ensuite mis en avant l'intérêt de l'apprentissage automatique dénommé le plus souvent machine learning, qui s'appuie uniquement sur des données expérimentales, comme nouvelle approche pour modéliser la perméabilité. Face à la diversité des systèmes nanocomposites envisageables, il a été décidé de se concentrer dans un premier temps sur une seule matrice, le PLA, ce qui permettait de s'affranchir de paramètres spécifiquement liés à la structure chimique de la phase continue du matériau tout en autorisant la prise en compte d'un nombre important de facteurs d'intérêt tels que le taux de cristallinité, le procédé de mise en œuvre ainsi qu'un large éventail de nanocharges. L'analyse d'un nombre conséquent d'études expérimentales a montré, comme attendu, la complexité de décrire la perméabilité en fonction uniquement des informations liées à la phase imperméable (composition chimique, forme initiale) et le manque d'informations détaillées sur certains aspects. Ainsi, il s'est avéré essentiel de disposer d'informations supplémentaires à la fois sur la matrice, sur l'interface charge/matrice et sur l'état de dispersion des charges. C'est pourquoi il a été décidé de préparer et caractériser une large plateforme de nanocomposites PLA (présentée dans le chapitre II) qui a été pensée i/ pour pouvoir

prendre en compte la diversité des procédés, des taux de cristallinité de la matrice polymère pouvant varier ainsi qu'un large éventail de charges et ii/pour pouvoir compléter un certain nombre de données peu présentes dans la littérature.

Un premier chapitre expérimental (chapitre III) a été consacré à la perméabilité de systèmes de type matrice PLA contenant une seule phase imperméable. Une première étude a permis d'étudier et de comparer l'effet de différentes charges sur la perméabilité de PLA amorphe. La perméabilité au dioxygène et à la vapeur d'eau des différents systèmes a pu être reliée à la forme initiale des charges ainsi qu'à leur fraction volumique, mais aussi à la dispersion des charges au sein de la matrice qui a pu être finement décrite. De plus pour ces systèmes, les mêmes tendances ont été observées pour le dioxygène et la vapeur d'eau. À partir de ces observations, différents modèles théoriques de perméabilité ont pu être ajustés pour décrire au mieux les données expérimentales. Par ailleurs l'effet des charges a pu être comparé à l'effet de la phase cristalline du PLA, qui de par sa densité plus élevée est également imperméable au gaz et à la vapeur d'eau.

Puis, une deuxième étude s'est attachée à comparer deux procédés, le procédé de mélange en voie fondue et la polymérisation *in situ*, sur la perméabilité de PLA contenant de la silice hydrophobe ou une montmorillonite modifiée avec un cation organique à caractère polaire. Cette étude a montré que la différence majeure à laquelle conduisent ces deux procédés concerne la microstructure de la matrice (masse molaire, bouts de chaines, interface charge/matrice…). Ces changements ont été mis en relation avec les différences de perméabilité observées sur les matériaux obtenus par les deux procédés, mais les modèles théoriques n'ont pas pu décrire ces différences.

Par la suite, des modèles de machine learning ont été utilisés pour prédire la perméabilité de matériaux PLA contenant une phase imperméable. Pour cela il a fallu construire une base de données à partir de données de la littérature et de notre propre plateforme de matériaux, en veillant à équilibrer au mieux les différentes catégories de systèmes. Deux modèles (*Random Forest* et *Support Vector Machine*) ont été entrainés sur 80% des échantillons pris au hasard dans la base de données. Le nombre de paramètres a pu être réduit en identifiant les intercorrélations. Malgré un nombre limité d'échantillons utilisé pour entrainer ces modèles, la perméabilité de nouveaux systèmes a pu être prédite avec une erreur proche de l'erreur expérimentale, et à l'inverse ces modèles ont permis de proposer les choix possibles de combinaisons de paramètres matériaux pour une perméabilité donnée, ce qui permet d'imaginer la conception de nouveaux matériaux avec un guide tout en conservant un certain degré de liberté.

Un troisième chapitre s'est intéressé à l'effet de l'introduction de deux phases imperméables sur la perméabilité du PLA. Dans un premier temps, l'étude a porté sur la combinaison charge/matrice PLA semi-cristalline, pour des matériaux préparés par deux procédés différents, en utilisant une large gamme de charges. La comparaison entre les matériaux élaborés par traitement thermique de nanocomposites amorphes obtenus par mélange en voie fondue a montré une meilleure dispersion de charges que pour les matériaux obtenus par voie solvant. Cependant, cette différence n'a pas eu de relation directe avec la perméabilité. En effet les nanocomposites semi-cristallins obtenus après traitement thermique ont montré une perméabilité supérieure à celle de PLA semi-cristallins (sauf dans le cas des montmorillonites) alors qu'une diminution de la perméabilité a bien été observée pour les nanocomposites préparés par voie solvant. Une dégradation de l'interface charge/matrice induite par des contraintes lors de la cristallisation à l'état caoutchoutique pourrait être à l'origine de cette dégradation des propriétés barrière. Néanmoins, le traitement thermique de nanocomposites chargés avec de la montmorillonite a mené à une diminution maximum de la perméabilité, avec une réduction d'un facteur 10 par rapport au PLA amorphe, montrant l'importance du choix du type de charge.

Puis dans un deuxième temps, des nanocomposites amorphes contenant deux charges imperméables ont été préparés par voie fondue pour une fraction volumique totale de charges de 10%. L'association de montmorillonites avec de la silice ou du graphène a montré une diminution de la perméabilité par rapport aux échantillons contentant uniquement de la silice ou du graphène. Cependant l'additivité des contributions n'a pas été obtenue par la combinaison de deux charges. Ce résultat a été attribué à la formation de domaines de charges mixtes qui conduit *in fine* à une diminution des effets de tortuosité.

Enfin dans un dernier chapitre, l'étude de la perméabilité dans les nanocomposites a été étendue à un grand nombre de matrices polymères de natures différentes et ayant des valeurs de perméabilité initiales s'étendant de 10^{-5} à 10 barrer pour le dioxygène. Une base de données de plus de 200 échantillons a été constituée à partir d'une trentaine de publications permettant également de considérer un large éventail de nanocharges. Deux modèles de machine learning ont été utilisés pour prédire la perméabilité des échantillons. Les *Random Forest* ont permis d'obtenir les meilleures prédictions avec une erreur absolue de 10% et un coefficient de corrélation de 0.78. À partir de ces modèles, des combinaisons de paramètres ont pu être suggérées pour la préparation de

nanocomposites répondant à une valeur de perméabilité donnée et les résultats ont été globalement validés d'un point de vue physique.

D'un point de vue expérimental cette thèse a permis de réaliser et finement caractériser une large plateforme de matériaux à base de PLA contenant une ou deux phases imperméables et d'étudier leur perméabilité, de modéliser cette propriété et d'établir des lois d'équivalence expérimentales concernant les effets de phases imperméables différentes en considérant diverses nanocharges mais également la phase cristalline. Par ailleurs, ce travail a montré l'efficacité du machine learning pour prédire la perméabilité de nanocomposites, qui implique des relations non linéaires et multidimensionnelles. Cependant, quelques résultats obtenus restent surprenants c'est pourquoi il est nécessaire de garder un regard critique et de s'appuyer sur les mécanismes/modèles physiques qui régissent les propriétés ciblées. Par ailleurs, même si les résultats issus de l'approche machine learning sont très convaincants, il subsiste la question de savoir si l'apprentissage pourrait être amélioré en enrichissant davantage la base donnée, notamment pour les paramètres les moins représentés. Il serait également intéressant de disposer de davantage de paramètres microstructuraux, comme ceux identifiés dans le cas des analyses fines menées pour notre plateforme expérimentale de systèmes à base de PLA, et de voir leur degré d'importance sur les prédictions en machine learning. Une autre perspective de ce travail serait de tester expérimentalement des combinaisons de paramètres suggérées en machine learning et de comparer la perméabilité expérimentale avec la perméabilité prédite. Par ailleurs, la démarche présentée dans cette thèse pourrait être appliquée pour prédire d'autres propriétés de matériaux appartenant à la classe des nanocomposites dans le domaine du transport (séparation et sélectivité par exemple) ou dans des domaines élargis (propriétés thermiques, électriques, mécaniques...).